



## DISSERTATION

# Human Cochlear Nerve Model

ausgeführt zum Zwecke der Erlangung des akademischen Grades einer  
Doktorin der technischen Wissenschaften unter der Leitung von

Ao.Univ.Prof. Dipl.-Ing. DDDr. Frank Rattay  
E101 - Institut für Analysis und Scientific Computing

eingereicht an der Technischen Universität Wien  
Fakultät für Mathematik und Geoinformatik  
von

Dipl.-Ing. Cornelia Wenger  
Matrikelnummer: 0326222  
Pramergasse 1/17B, 1090 Wien

Wien, am 4. Mai 2012

---

Unterschrift

# Acknowledgments

First of all I want to thank my advisor Prof. Rattay, who has been a great motivation to progress with a topic with been working on very closely for the last 5 years. I really appreciate his patience and advice and I admire his passion for discussing any idea or suggestion on any possible topic. Furthermore I'm really grateful to Prof. Mayr, who agreed to review my thesis on short notice.

I definitely have to mention Thomas Potrusil, MSc, who has always been a very good team player and even more, a congenial colleague. He not only provided me with great data of enormous size while also explaining its acquisition and relevance, but also shared good conversation on- and off-topic!

Still the biggest gratitude goes out to all the people who inspired me, no matter if close friends, family members or enjoyable acquaintances. It's the time spent sharing happy moments and enjoying mother nature, that I highly regard and won't forget. I'm so grateful to all my close friends who helped me keep going, each of them having their own individual way of connecting with me. Thanks to all of you!

For financial support, I am indebted to the Austrian Science Foundation (FWF- Fond zur Förderung der wissenschaftlichen Forschung).

*Cornelia Wenger*

# Abstract

**Objectives.** The human auditory system certainly differs from other species, e.g., human spiral ganglion cell bodies are unmyelinated and often arranged in functional units covered by common satellite glial cells. This unique morphology has often been speculated to affect excitability and spiking pattern of cochlear neurons. Since vital human spiral ganglion cells are not experimentally accessible, theoretical analysis concerning single neuron response has to be performed with consideration of fundamental anatomical data. Nonetheless the physiology of hearing is not fully understood, e.g., complex coding strategies as speech recognition and perception in noisy environment, attenuation effects and the temporal fine structure of the neural pattern.

**Methods.** The electrical activity of neurons can be deduced from solving systems of differential equations which will enhance our understanding of action potential initiation and propagation of nerve impulses. Using MatLab 2011a (MathWorks, Natick, MS, USA) new anatomical and histological findings (partly provided by the Medical University of Innsbruck) will be incorporated in a new model approach for simulating the natural spiking behavior of human cochlear neurons as well as their excitability to microstimulation by electrodes.

**Results.** The unmyelinated soma region reduces the safety factor of AP transmission whereas certain sensitive parameter can be identified leading to divergent excitation profiles. The clustering of human cochlear neurons has two basic consequences. For successful ephaptic stimulation the spikes of adjacent neurons get synchronized. Some inhibiting effects can also be observed due to large current loss on the sensitive human soma region. Previously reported sensitivity pattern of human auditory fibers to electrical stimulation could be replicated with a 2D model neuron. Furthermore the findings with 3D data suggest highly diverging excitation pattern of tonotopically aligned neurons.

**Conclusions.** Mathematical modeling and computer simulation have become important and decisive tools for many clinical and medical applications. Especially further development for electrical prosthesis leading to better implant user performance is achieved by adapting stimulation strategies according to results obtained by computer simulation. Still, the results of the thesis predict that contemporary models shall be adapted according to the unique human in order to improve pending studies.

# Kurzfassung

**Motivation.** Das menschliche Hörsystem zeigt im Vergleich zu anderen Säugetieren einige Besonderheiten. Die Somata der Cochlearneuronen sind unmyelinisiert und bilden auch gelegentlich funktionelle Einheiten, die von gemeinsamen Satellitenzellen umgeben sind. Man vermutet, dass beide Einzigartigkeiten die neuronalen Muster wesentlich beeinflussen. Nachdem vitale humane Spiralganglien nicht experimentell zugänglich sind, müssen Modelle der elektrischen Aktivität eines Neurons Abhilfe leisten, die speziell an die menschlichen Besonderheiten angepasst sind. Bis heute bleiben einige Ungeklärtheiten bezüglich der physiologisch spezifischen Hörleistung und der humanen akustischen Signalcodierung.

**Methoden.** Um die Entstehung und Weiterleitung eines Nervenimpulses zu untersuchen, wird die elektrische Aktivität der Neuronen mit Differentialgleichungen beschrieben, die mit Hilfe von MatLab 2011a (MathWorks, Natick, MS, USA) gelöst werden. Angepasst an die neuesten Daten über Morphologie und Anatomie der menschlichen Cochlearneuronen (teilweise bereitgestellt von der Medizinischen Universität Innsbruck) wurde ein Modell entwickelt um sowohl die natürliche Nervenübertragung als auch die Erregbarkeit bei elektrischer Stimulation zu simulieren.

**Resultate.** Die unmyelinisierte Somaregion reduziert den Sicherheitsfaktor für erfolgreiche AP Weiterleitung, wobei kleine Änderungen von gewissen sensitiven Parametern unterschiedliche Erregungsprofile erzeugen. Das Clustering der Spiralganglien hat zwei Konsequenzen. Bei erfolgreicher ephaptischer Erregung kommt es zur Synchronisierung der berührenden Neuronen. Allerdings können wegen dem großen Stromverlust am Soma auch inhibitorsche Effekte beobachtet werden. Messungen der Reizempfindlichkeit von humanen Hörnerven unter elektrischer Stimulation konnten mit einem 2D Modell bestätigt werden. Die ersten Resultate mit einem neuen 3D Modell verdeutlichen die Unterschiede der Erregung von Neuronen unterschiedlicher Cochlearregionen.

**Folgerung.** Mathematische Modellbildung und Computer Simulation sind wichtige Instrumente zur Weiterentwicklung von elektrischen Neuroprothesen. Erhobene Resultate tragen dazu bei die Hörleistung von Cochlear Implantat Patienten zu verbessern. Die Resultate der Dissertation verdeutlichen, dass es für zukünftige Studien unumgänglich ist, die menschlichen Besonderheiten bei der Modellierung zu berücksichtigen.

# Contents

Acknowledgments . . . . .	i
Abstract . . . . .	ii
Kurzfassung . . . . .	iii
Contents . . . . .	iv
List of Abbreviations . . . . .	vi
<b>1 Introduction</b>	<b>1</b>
<b>2 The cochlea</b>	<b>7</b>
2.1 Physiology of hearing, sensory pathway . . . . .	7
2.2 Human anatomy and histology . . . . .	12
<b>3 Modeling of nervous structure</b>	<b>15</b>
3.1 The membrane and its electrical properties . . . . .	16
3.2 Electrical circuits and mathematical modeling . . . . .	22
3.2.1 Compartment model - Functional subunits . . . . .	24
3.3 Ion channels . . . . .	26
3.3.1 Comparison of sodium channel gating kinetics . . . . .	32
3.3.2 Comparison of potassium channels gating kinetics . . . . .	35
3.4 Action potential modeling . . . . .	37
<b>4 Models of human cochlear neurons</b>	<b>47</b>
4.1 Afferent single neuron model . . . . .	47
4.1.1 Soma region . . . . .	50
4.1.2 Central and peripheral process . . . . .	54
4.1.3 Channel kinetics . . . . .	62
4.2 Cluster modeling . . . . .	66
4.2.1 Cluster 1 . . . . .	69
4.2.2 Cluster 2 . . . . .	74
4.2.3 Cluster 3 . . . . .	78
4.2.4 Cluster 4 . . . . .	84

## CONTENTS

---

<b>5</b>	<b>Extracellular stimulation</b>	<b>94</b>
5.1	Extracellular stimulation excitation profiles . . . . .	95
5.2	Soma size . . . . .	98
5.2.1	Extracellular stimulation with electrodes E1 and E2 . . . . .	99
5.2.2	Extracellular stimulation with electrodes E3 and E4 . . . . .	101
5.3	Micro CT 3D data . . . . .	106
5.3.1	Apical 2 neuron . . . . .	107
5.3.2	Middle 1 neuron . . . . .	116
5.3.3	Basal 7 neuron . . . . .	122
<b>6</b>	<b>Discussion</b>	<b>127</b>
	<b>Bibliography</b>	<b>132</b>
	<b>Curriculum Vitae</b>	<b>142</b>

# List of Abbreviations and Symbols

CI	cochlear implant
SGC	spiral ganglion cell
NRT	neural response telemetry
eCAP	electrically evoked compound action potential
SEM	Scanning Electron Microscope
TEM	Transmission Electron Microscope
MedUni IBK	Medical University of Innsbruck, Austria
IHC	inner hair cell
OHC	outer hair cell
ISC	intracellular space
ESC	extracellular space
HH	Hodgkin-Huxley model
RGC	retinal ganglion cell
CA5	pyramidal cells of the fifth layer
CA3	pyramidal cells of the third layer
$Na^+$	sodium ion
$K^+$	potassium ion
$Ca^{2+}$	calcium ion
$Na$	sodium channel
$K$	potassium channel
$Na_v1.1, \dots$	sodium channel isoforms
$K_v1, \dots$	potassium channel isoforms
$K_v$	fast potassium ion channel
$K_m$	slow non-inactivating potassium ion channel
$t_{adj}$	multiplicative temperature adjustment coefficient
$T$	absolute temperature [°C]
$T_0$	initial model temperature [°C]
$Q_{10}$	coefficient for a temperature increase of 10°C
$m, n, h$	gating variables, probability for a membrane gating process
$\alpha_m, \alpha_n, \alpha_h$	transfer rates from closed to open state [1/ms]
$\beta_m, \beta_n, \beta_h$	transfer rates open form to closed state [1/ms]

## LIST OF ABBREVIATIONS AND SYMBOLS

---

$m_\infty, n_\infty, h_\infty$	steady state of the gating variables
$\tau_m, \tau_n, \tau_h$	time constant of the gating variables [ms]
$V_{1/2}$	half-(in)activation voltage [mV]
$k$	slope factor for transfer rates [mV/e-fold]
$E_m, V_m$	transmembrane potential and corresponding reduced potential [mV]
$\phi_i, V_i$	intracellular potential and corr. reduced potential [mV]
$\phi_e, V_e$	extracellular potential and corr. reduced potential [mV]
$E_{rest}, V_{rest}$	resting membrane potential and corr. reduced potential [mV]
$E_{Na}, V_{Na}$	sodium reversal potential and corr. reduced potential [mV]
$E_K, V_K$	potassium reversal potential and corr. reduced potential [mV]
$E_L, V_L$	leakage reversal potential and corr. reduced potential [mV]
$I_{mem}$	membrane current [ $\mu\text{A}/\text{cm}^2$ ]
$I_{cap}$	capacitive current [ $\mu\text{A}/\text{cm}^2$ ]
$I_{ion}$	ionic current [ $\mu\text{A}/\text{cm}^2$ ]
$I_{ohm}$	ohmic current [ $\mu\text{A}/\text{cm}^2$ ]
$I_{ax}$	axial current [ $\mu\text{A}/\text{cm}^2$ ]
$I_{stim}$	stimulation current [ $\mu\text{A}/\text{cm}^2$ ]
$IC_{amp}$	amplitude of intracellular injected current [ $\mu\text{A}/\text{cm}^2$ ]
$IC_{dur}$	duration of intracellular injected current [ms]
$I_{El}$	stimulation current of an extracellular electrode [ $\mu\text{A}$ ]
$I_{ephap}$	ephaptic current [ $\mu\text{A}/\text{cm}^2$ ]
$I_{Na}$	sodium current [ $\mu\text{A}/\text{cm}^2$ ]
$I_K$	potassium current [ $\mu\text{A}/\text{cm}^2$ ]
$I_L$	current of other ions, leakage current [ $\mu\text{A}/\text{cm}^2$ ]
$C_{mem}$	membrane capacitance [ $\mu\text{F}/\text{cm}^2$ ]
$R_{mem}$	membrane resistance [ $\text{k}\Omega/\text{cm}^2$ ]
$C_n$	membrane capacitance of the $n$ -th compartment [ $\mu\text{F}$ ]
$R_n$	intracellular resistance of the $n$ -th compartment [ $\text{k}\Omega$ ]
$g_{Na}$	sodium conductance [ $\text{mS}/\text{cm}^2$ ]
$g_K$	potassium conductance [ $\text{mS}/\text{cm}^2$ ]
$g_L$	leakage conductance [ $\text{mS}/\text{cm}^2$ ]
$g_{my}$	internode conductance of one layer of membrane [ $\text{mS}/\text{cm}^2$ ]
$g_E$	cluster conductance of one layer of myelin [ $\text{mS}/\text{cm}^2$ ]
$l$	length
$d$	diameter
$A$	surface
$nm$	number of myelin layers
$\rho_i$	intracellular resistivity [ $\text{k}\Omega\cdot\text{cm}$ ]
$\rho_e$	extracellular resistivity [ $\text{k}\Omega\cdot\text{cm}$ ]



## LIST OF ABBREVIATIONS AND SYMBOLS

---

AP	action potential
$AP_{height}$	local parameter: maximal overshoot of membrane potential [mV]
$AP_{amp}$	local parameter: difference between maximum and minimum value of membrane potential [mV]
$AP_{width}$	local parameter: half-height width of an AP [ms]
$AP_{dur}$	global parameter: duration or traveling time of the spike, i.e., difference between peak of the first and last compartment [ms]
E1	electrode position 1
E2	electrode position 2
E3	electrode position 3
E4	electrode position 4
CAT	monophasic cathodic pulse [0.1 ms]
BIC	biphasic cathodic first pulse [0.05 ms/phase]
ANO	monophasic anodic pulse [0.1 ms]
BIA	biphasic anodic first pulse [0.05 ms/phase]
IS	compartment index of initiation site
PT	voltage peak time at the IS compartment [ms]
PTS	voltage peak time at the soma compartment [ms]
ET	voltage peak time at the last compartment [ms]

# Chapter 1

## Introduction

Within the past few decades mathematical modeling and computer simulation have become a benchmark in several disciplines, especially within the fields of neuroscience and biomedical engineering computational investigation are of great importance. With the help of neuron modeling techniques a greater understanding of the nervous system and its functioning can be achieved. Among many other applications, computer simulation has been beneficial to the development and further improvement of neural prosthesis. Although many assistive devices that restore functions lost as a result of neural damage have been produced, the *cochlear implant* (CI) is the most successful and effective of all neural prosthesis developed to date.

In the healthy human ear the auditory receptor cells called hair cells communicate their responses to the central nervous system through afferent cochlear neurons, called *spiral ganglion cells* (SGC). These bipolar neurons have a peripheral and a central axon whereby approx. 35.000 afferent neurons are found in young individuals and 29.000 in adults (Otte et al. 1978, Spoendlin and Schrott 1990). Causes of deafness or severe hearing loss are numerous, still some cases of profound sensorineural hearing loss can be treated with the application of an CI. Pfingst et al. (2011) gives a good summary of what is currently known about conditions in the cochlea of deaf and furthermore suggests optimization of the pattern of electrical stimulation.

CIs differ not only with respect to the number, position and spacing of electrodes. For example Shepard et al. (2011) compared the Cochlear Ltd's Hybrid-L to a standard 8 ring array and reported differences in the excitation profiles of the stimulated SGCs and also changing stimulus thresholds for their activation. Another crucial decision has to be faced on the configuration of the electrodes with respect to the placement of the reference electrode. The performed monopolar, bipolar, tripolar and recently suggested partial tripolar configurations all show varying spatial pattern of neural activation. The single- and two-channel responses induced by these configurations were evaluated by Bierer (2007) and the resulting channel interactions have been discussed. Furthermore Goldwyn et al. (2010) suggest that focused partial tripolar

## 1. Introduction

---

configurations could be used in regions of the cochlea with the most surviving SGCs, and the monopolar mode could be applied in the vicinity of a neural dead region. Even a four-electrode stimulation pattern has been analyzed by [Landsberger and Srinivasan \(2009\)](#) who state that this quadrupolar virtual channels might provide the best combination of the previous modes by improving the number of spectral channels while reducing interactions.

However, along with other special features of varying implants, the key element concerns the processing strategies used by the implant to stimulate the neurons. Many strategies have been developed and further improved, whereby the most important strategies in the history of these prosthesis are the Compressed Analog and the Continuous Interleaved Sampling strategy. The latest strategies involve the similar n-of-m, Spectral Peak and the Advanced Combination Encoder strategies, as well as the HiResolution methods and a novel simulated phase-locking stimulation strategy by [Chen et al. \(2009\)](#). The psychological measurements and performed test trials with different implants among patients are numerous. [Wilson and Dorman \(2008\)](#) gives a very good summary of the contemporary CIs and compares their designs and points out future possibilities.

Nonetheless, our knowledge about the neural coding principles in mammalian SGCs is primarily based on animal experiments. Single cell recordings enlightened our understanding of how an acoustical signal is represented in the spiking pattern of the auditory nerve ([Kiang 1965](#), [Brugge et al. 1969](#), [Sachs and Abbas 1974](#), [Shamma 1985](#), [Javel 1994](#), [Rattay and Lutter 1997](#)). Essential anatomic differences between man and mammalian species are observed of the neural elements responsible for signal transport from the cochlea to the brain.

These peculiarities of human SGCs are not considered so far while a growing amount of studies on CI strategies, electrode positioning within the cochlea, psychological measurements and recorded audiograms emerge. Nonetheless, the physiology of hearing is not yet fully understood, e.g., complex coding strategies as speech recognition and perception in noisy environment ([Drennan et al. 2007](#)), attenuation effects ([Smit et al. 2009a](#)) and the temporal fine structure of the neural pattern. This leads to several non tested and unapproved hypotheses concerning functional consequences. Due to missing fundamental computational investigations addressing the specific human anatomy and morphology of crucial neural elements, even the latest signal processing strategies for CI users are de facto designed for cats instead for humans.

As an alternative to single fiber recordings which are not available for humans, a general biophysical model of SGCs will be developed including cluster properties in order to understand the functional consequences of neuron variability seen in men by analyzing the influence of relevant geometric and electric parameters.

The human ear shows two distinct anatomical features which have not been reported for other mammalian species. Both human particularities are expected to essentially

affect the neural pattern, resulting in a specific human physiologic hearing performance. Especially the somatic region of afferent human cochlear neurons are quite unique as has been already reported in early studies, e.g. in [Nadal \(1988\)](#). Also [Liu et al. \(2009\)](#) state that the human auditory nerve obviously presents unique structural and also most likely physiological characteristics that need further elucidation.

The cell bodies differ not only in size (compare [Spoendlin and Schrott \(1989\)](#) and [Liberman and Oliver \(1984\)](#)), but also in the number of myelin layers surrounding them. According to [Ota and Kimura \(1980\)](#) 94% of human SGC somata are unmyelinated and mostly surrounded by one to several layers of satellite cells. Additionally the pre- and postsomatic areas, the lengths of which vary a lot, are not shielded by myelin. By contrast, in all adult mammals studied so far 90-95% of the SGCs are large and myelinated, thus representing almost a reverse proportion between man and cat.

Prior research has led to speculation that the unique human morphology of SGC somata ([Tylstedt and Rask-Andersen 2001](#), [Glueckert et al. 2005b](#)) affects excitability and spiking pattern ([Rattay et al. 2001](#), [Rusznák and Szücs 2009](#)) since these unmyelinated neuronal parts are the first energy barrier for an action potential traveling from the sensory epithelium to the auditory cortex. To overcome this barrier the nerve impulse must load the membrane capacitance of the cell body, which is directly proportional to its surface ([Rattay 1995](#), [Rattay et al. 2001](#)). Nevertheless, ever since [Hodgkin and Huxley \(1952\)](#) developed their model of a nonmyelinated squid axon, functional electrical stimulation has focused on myelinated nerve structures and nodes of Ranvier. Thus, in order to simulate the response of single SGCs to micro stimulation, some modelers have considered the soma to be myelinated ([Frijns et al. 1994](#)) or passive ([Woo et al. 2009b](#)), while others have completely neglected the presence of a soma ([Mino et al. 2004](#)). Thus within this thesis, the model of [Rattay et al. \(2001\)](#) will be adapted according to latest findings on soma size of human SGCs ([Potrusil et al. 2012](#)) since it is the only model which includes an unmyelinated soma region.

The second outstanding peculiarity also concerns the soma region of afferent cochlear neurons. A *transmission electron microscope* (TEM) study of [Tylstedt et al. \(1997\)](#) first revealed 'unit-like' formations of somata from different SGCs. Their findings suggest that within the upper basal and middle turn, the cell bodies of neurons were frequently ensheathed by the same Schwann cell so that they are gathered to clusters with 2-4 neurons. Thus these SGCs showed signs of physical interaction, so that the membranes of adjacent somata were in direct apposition. In another study this group investigated distinct membrane specializations of these 'gaps' ([Tylstedt and Rask-Andersen 2001](#)). They speculate whether unique formations of SGCs may constitute interactive electrotonic or electronic transmission pathways. These may be in the low frequency region and may increase plasticity and signal acuity related to the coding of speech. [Tylstedt and Rask-Andersen \(2001\)](#) further indicated the relevance of the cell cluster concerning nerve cell survival after hair cell loss, thus also explaining the slow

rate of retrograde degeneration of human cochlear neurons. For detailed information on degeneration see [Felder et al. \(1997\)](#).

Within more recent studies [Liu et al. \(2009\)](#) observed certain connexin proteins appearing in single neurons what raises the possibility of the existence of gapjunction-based electrical circuits within the human spiral ganglion. They suggest that apart from abundant chemical synapses in the auditory pathway, another important way that local population of neurons may code information might be through the synchrony of their nerve signals. Although they speculate that such rapid processing mechanism could play a role for coding elaborate speech, they also state that more studies are needed on the possible modulating role of the unique satellite cells surrounding the human spiral ganglion which may allow electric currents to spread between groups of neurons ([Liu et al. 2012](#)).

The term *ephaptic* is derived from the Greek meaning 'touching onto' where ephaptic interactions were observed to occur in neurons that are coupled by current loops in the extracellular space. Since such interactions are mostly negligible in comparison to chemical and electrical synaptic interactions, the functional significance of ephaptic coupling is often not considered ([Neske and Rinzel 2010](#)). Still certain physical situations, such as close packing of neurons may increase the efficacy of ephaptic interactions, e.g., [Holt and Koch \(1999\)](#) also state that while extracellular action potentials outside axons are small in amplitude and spatially spread out, they are larger in amplitude and much more spatially confined near cell bodies. Thus ephaptic interactions between a neuron and axons or dendrites passing by its cell body can be more significant than ephaptic interactions among axons in a fiber tract.

Some modeling studies did comprehend with ephaptic coupling between neural elements although most theoretical studies of ephaptic interactions have been performed for parallel axons ([Binczak et al. 2001](#)) due to the simple geometry as summarized in [Holt and Koch \(1999\)](#). [Anastassiou et al. \(2011\)](#) stimulated and recorded from rat cortical pyramidal neurons and found that extracellular fields induced ephaptically mediated changes in the somatic membrane potential that were less than 0.5 mV under subthreshold conditions.

In order to comprehend with this topic, our cooperation partners from the *Medical University of Innsbruck* (MedUni IBK) acquired 3D - Confocal image stacks of the SGC clusters as explained in detail at the beginning of Sec. 4.2. With the evaluated diameter of cluster-sharing somata and their calculated contact areas, a new model approach was developed to account for possible additional current flow between adjacent SGCs.

Still another option to study the neural response induced by micro stimulation is provided by contemporary CIs since recording tools like the *neural response telemetry* (NRT) provide easy acquisition to the *electrically evoked compound action potential* (eCAP) of the auditory nerve fibers. Contrary to the *electrically evoked auditory brainstem responses* (eABR), the ECAP can be recorded through the implant system

itself without the need of additional electrodes. Still the eABR is not only used during CI surgery especially for fitting children (Westen et al. 2011) but also investigated for test trials. For example Bahmer et al. (2010) analyzed the eABR evoked by bi- and triphasic stimulation within 10 CI patients.

However as Miller et al. (2004) summarized, the eCAP is characterized as a response occurring shortly after stimulus onset which is dominated by a relatively large-amplitude negative peak followed by a smaller positive peak (compare Fig. 5.1). The eCAP is a direct result of the auditory nerve activity in response to an electrical stimulus and according to Westen et al. (2011) its threshold is the most commonly determined parameter as an indication to program the speech processor of the CI.

The common assumption that the eCAP has a linear relationship with the number of excited nerve fibers which is called unitary response concept has been turned around by Briaire and Frijns (2005). Anyway the clinical utility of eCAP measures, including possible application to adjusting device parameters to individual users, predicting nerve survival, and using repeated measures for longitudinal monitoring of nerve status is investigated by many groups, e.g., explained in Miller et al. (2004) and Smit et al. (2009a).

## THESIS ORGANIZATION

The basic anatomy of the human ear is presented in **Chapter 2** including a detailed description of the cochlear neurons which will be subsequently modeled within this thesis. The human peculiarities and the variations among individuals are outlined in order to provide an overview of the possible parameter ranges required to deduce a model of the excitation of a human cochlear neuron.

**Chapter 3** initially outlines the electrical properties of the cell membrane which enable the propagation of a resting potential at the surface of the cell as well as the generation of a nerve impulse which is considered to be a change in the transmembrane potential deviating from its resting state. Furthermore this section summarizes modeling approaches for the response of a local model neuron induced by intracellular current injection. The electrical circuit considered to describe the membrane is presented and with the use of basic physical laws the differential equations are derived. Additionally compartment modeling used to describe the neuron as a network of isopotential elements is explained in order to describe the excitation pattern of a single SGC in more detail.

Within **Chapter 4** the discussed specific human anatomical features will be tested systematically whereas the first section 4.1 deals with the unmyelinated soma region, the variations of electrical and geometrical properties of the two cell process and different ion channel representation. The second part, section 4.2, demonstrates four detected neuron clusters which have been just recently investigated by our cooperation partner of the MedUni IBK. The effect of ephaptic coupling between the SGCs sharing

a common myelin layer over their somata will be analyzed.

The case of extracellular stimulation, which is applicable for CI studies, is discussed in **Chapter 5**. First, the basics of mathematical modeling are outlined in section 5.1. The two-dimensional arrangement of a model SGC and possible sites of the stimulating electrode are discussed in section 5.2. The neuron has been varied with respect to the soma diameter according to a recently detected data set of two specimen ([Potrusil et al. 2012](#)). Furthermore four different electrode positions have been tested for varying configurations, including monophasic and biphasic pulses of varying polarities. The just recently evaluated three dimensional traced neuron data of a Micro-CT examined cochlea will be analyzed in section 5.3. Three different model neurons, each of which originates in another cochlear turn, are systematically tested concerning different electrode positions in the scala tympani.

In conclusion the results are discussed and summarized in **Chapter 6**. Furthermore a comparison with previous findings will be included and further model adaption or pending simulation experiments which could enhance our understanding of the hearing physiology will be suggested. Additionally shortcomings of the presented modeling approaches will also be discussed.

# Chapter 2

## The cochlea

This chapter provides the physiological background information needed to comprehend the topic of the thesis. Initially the basic anatomy of the human ear with emphasis on the organ of hearing, the cochlea, is presented in Section 2.1 and the auditory sensory pathway will be shortly outlined. Thus the first section is concerned with auditory perception, i.e. it will be explained how sound information is processed into neural activity.

The nervous structure involved in the process will be described while focusing on the sensory cells responsible for initiating the sensory transduction. Additionally their companion afferent neurons are discussed which comprise the primary pathway for auditory perception. Those primary auditory neurons are called *spiral ganglion cells* (SGCs). Their relevant geometrical and electrical properties which are essential for the computational models used within the thesis will be outlined. Since the peripheral auditory system shows refined mechanical and electrical specializations to enhance frequency-specific coding (Davis and Liu 2011), some of these tonotopic features along the cochlea are pointed out within this chapter.

Furthermore human cochleae show some anatomical variations among individuals (Erixon et al. 2009) which will also be shortly surveyed. Still the aforementioned human peculiarities will be the main interest in Section 2.2. Again the summary will focus on specializations of the SGCs which will be examined in detail using computer simulation. The influence of those parameters on the natural spiking behavior of SGCs will be discussed in Chapter 4. Consequences for extracellular stimulation, i.e., artificial stimulation by electrodes, will be presented in Chapter 5.

### 2.1 Physiology of hearing, sensory pathway

The human ear is divided in the outer, middle and inner ear which is illustrated in Fig. 2.1. The outer ear, responsible for collecting sound waves, consists of the pinna and the external auditory canal and finally ends at the surface of the ear drum, also called tympanic membrane. The sound is then amplified in the middle ear, which is an



## 2.1 Physiology of hearing, sensory pathway

air-filled cavity with the three contained ear bones, called the malleus (or hammer), incus (or anvil) and stapes (or stirrup). This chain of ossicles starts to vibrate when the waves have reached the tympanic membrane.

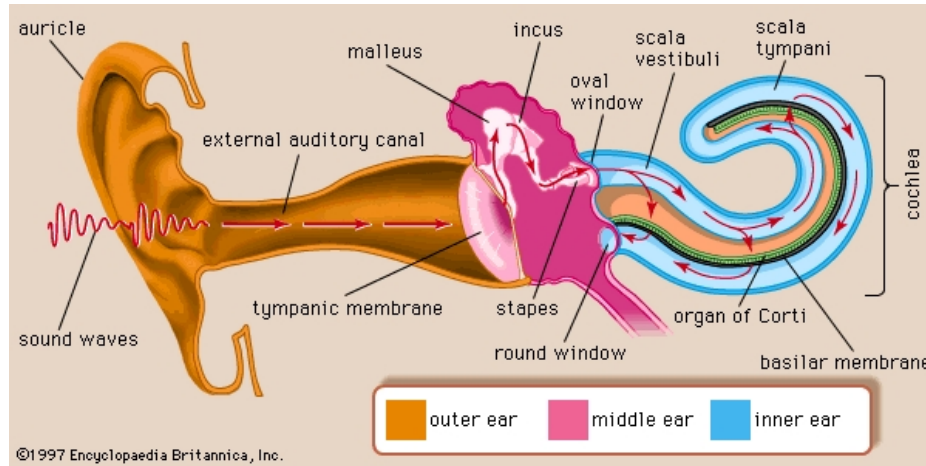


Figure 2.1: The schematic drawing illustrates the main elements of the outer, the middle and the inner ear ([Encyclopædia Britannica 2012a](#)).

The inner ear on the one hand consists of the labyrinth which represents the vestibular system. Furthermore the inner ear contains the cochlea, where the sound is actually converted into nerve signals, thus also referred to as the organ of hearing. Both parts of the inner ear are fluid-filled and contain sensory cells, which transmit the motion of the fluids into electrical nerve signals.

The cochlea is a spiraled hollow embedded in the temporal bone where about  $2\frac{1}{2}$  coils are predicted in humans. [Erixon et al. \(2009\)](#) studied 73 human inner ears and their results showed that the human cochlea is individually shaped, varying greatly in dimensions. Their measurements predict that actually the number of quadrants varied from slightly more than 8 to 12. Furthermore the outer cochlear wall length ranged from 38.6 to 45.6 mm within the observed cochleae, even showing variational height of the cochlear tube itself (1.6-2.6 mm in the first turn).

Basically the cochlea consists of three fluid filled chambers (scalae) separated through certain membranes as represented in the schematic drawing of the cross section in Fig. 2.2A. The stapes of the middle ear connect the outside of the cochlea at the oval window, adjacent to the scala vestibuli which is the upper chamber of the cochlea. The scala vestibuli is filled with perilymph, a solution of electrolytes and proteins, which starts to move in waves away from the oval window through the turns of the cochlea when it is stimulated by the stapes.

The lower cavity is called scala tympani and ends in the round window. The scala tympani is also filled with perilymph and is separated from the scala vestibuli by the cochlea duct on the whole length of the coiled tube except at the communication

## 2.1 Physiology of hearing, sensory pathway

area located at the end, the apex of the cochlea which is called the helicotrema. At the helicotrema the fluid waves traveling from the oval window through the scala vestibuli continue in the perilymph of the scala tympani ending at the round window.

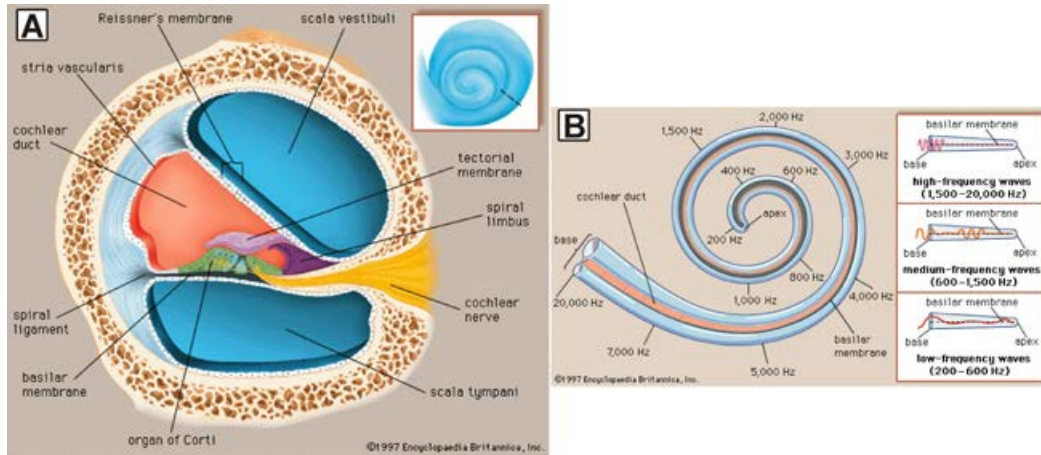


Figure 2.2: (A) Schematic drawing of the cross section through one cochlea turn showing the three scalae described in the text ([Encyclopædia Britannica 2012c](#)). (B) Model showing the distribution of frequencies along the basilar membrane of the cochlea ([Encyclopædia Britannica 2012b](#)).

The cochlea duct, also called scala media is the third scala which is filled with endolymph, a fluid similar to perilymph but with a higher concentration of potassium and less sodium. The scala media is separated from the scala vestibuli by the Reissner's membrane while the basilar membrane, which contains the organ of Corti, disunites the scala media from the scala tympani. Furthermore the basilar membrane decreases in width and stiffness from base to apex ([Davis and Liu 2011](#)).

The organ of Corti carries the sensory or also called receptor cells, the hair cells, responsible for conducting motion of endolymph, resulting from motion of perilymph in the scala media and the scala vestibuli, into electrical signals. The organ of Corti contains about 15000 hair cells per human ear which are divided into *inner hair cells* (IHCs) and *outer hair cells* (OHCs) ([Spoendlin and Schrott 1990](#)). This distinction is based on differences in shape and function. The hair cells are basically said to be organized in four rows along the whole length. There are three rows of OHC, which mainly receive signals from the brain via the medial olivocochlear bundle, and one row of IHC, which basically transmit nerve impulses to the brain via the vestibulocochlear nerve. A very good illustration of the hair cell's arrangement can be found in [Glueckert et al. \(2005c, Fig.8\)](#), who also observed the presence of a fourth row of OHC, irregularly distributed with seemingly missing OHCs and additionally supernumerary IHCs in adult human cochlea.

The IHC is responsible for the transmission of the sound vibration in the peri- and endolymph to electrical signals. Roughly most publications suggest that there exist about 3500 IHCs per human ear, whereas [Nayagam et al. \(2011, Table 1\)](#) predicts 3700. Since their function is basically to transport the coded information to the brain they are mainly afferently innervated. Actually, more than 90% of the afferent neurons are myelinated and connected to IHC via synaptic junctions. These radial afferents are called type I ganglion cells which will be the main purpose for the simulation within this thesis. While one afferent fiber only innervates one single IHC, one IHC forms in average 8-11 synaptic complexes to send neural signals to the brain ([Nayagam et al. 2011, Table 2](#)). A synaptic complex consists of the synapse with a dendrite of a type I cell and one lateral synaptic ending of an efferent fiber, i.e., there is no direct contact to the IHC, acting as a feedback for the afferent fibers.

The function of the OHC with an amount of about 12000 per human ear was uncertain for a long time. Note that again [Nayagam et al. \(2011, Table 1\)](#) predicts a higher number of 14600 OHC per ear. Studies revealed that they receive signals from the brain, i.e., show mainly efferent innervation and act as an amplifier of low to medium-level sound with an up to hundredfold increase of perception. OHCs are only present in mammals. Although the innervation pattern of OHC certainly changes along the cochlea turns from base to apex, the OHC are mainly innervated by medial efferents. These fibers need to cross the Tunnel of Corti to reach the synaptic ends of the OHCs. According to [Glueckert et al. \(2005a\)](#) the diameter of these efferents varied extensively from 0.2 to 1.5  $\mu\text{m}$ . Their findings on the course of these fibers are a valuable extensions to the pioneering work of [Spoendlin and Schrott \(1989\)](#). Nevertheless the OHC are also innervated by at least 5% of the afferent fibers with an increasing amount in apical regions. These spiral afferents are nonmyelinated and called type II SGCs. In contrast to the IHC, one type II neuron innervates ten or more OHCs, sometimes also from different rows, although usually they innervate the same row. The typical synaptical arrangement consists of a large synapse with the medial efferent and a undersized one with the small afferent. Increasing afferent innervation is only present in the very apical region of the cochlea.

A very good illustration obtained with fluorescence confocal microscopy of the hair cell's innervation pattern can be found in [Nayagam et al. \(2011\)](#). Furthermore there exist a tonotopic arrangement of the hair cells, i.e., the hair cells are tuned to certain frequencies and lined up from the oval window for high frequency (20000 Hz) tones to the apex of the cochlea for low frequencies (20 Hz). This pattern is illustrated in Fig. 2.2B and along with the mentioned decrease in stiffness of the basilar membrane some more properties of the neural elements in the cochlea show tonotopic arrangement.

As mentioned before the electrically coded information from the cochlea is transmitted via the cochlear nerve to the brain. The cochlear nerve is part of the vestibulocochlear nerve, also called the VIII cranial nerve. The cochlear neurons are synap-

tically connected to the hair cells, then bundled together to form the cochlear nerve with its spiral ganglion, i.e., the packed cell bodies, to finally enter the brainstem and form synapses to the cochlear nucleus.

A human ear has 30000 to 35000 cochlear neurons which all are basically classified as bipolar nerve cells (Spoendlin and Schrott 1990, Nayagam et al. 2011). Otte et al. (1978) reported 35000 afferents in young individuals and 29000 in adults and Spoendlin and Schrott (1989) found from 32000 to 31000 myelinated nerve fibers in the cochlear nerve of normal hearing individuals and a lower number in case of sensory neural deafness. Still note that Davis and Liu (2011) also report other possible morphological appearances of SGCs including pseudounipolar and lemon-like shapes.

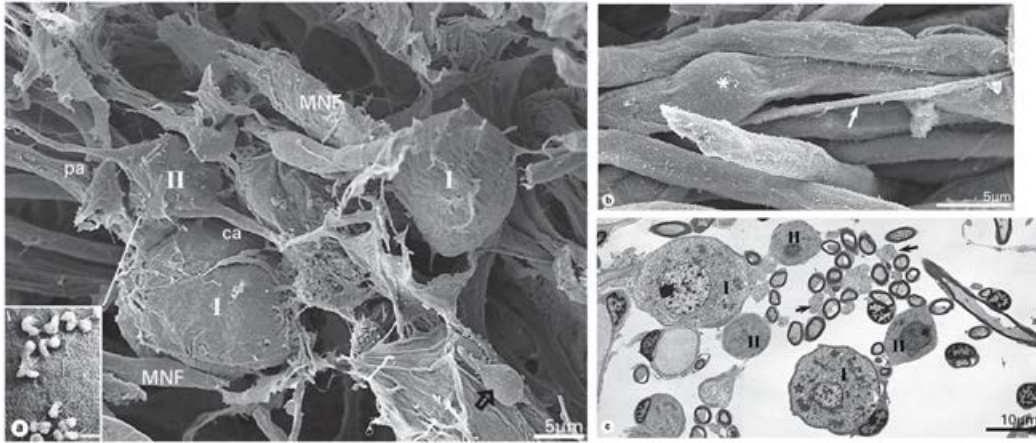


Figure 2.3: Left: *Scanning Electron Microscope* (SEM) picture with type I (I) and type II (II) cells in the upper basal turn of the cochlea. Central (ca) and peripheral (pa) axons of a type II cell are much thinner than myelinated nerve fibers (MNF) from type I cells. The insert shows a higher magnification of the surface coat of a Schwann cell covering a type II neuron; scale bar = 500 nm. Top right: SEM picture of myelinated nerve fibers and an unmyelinated (arrow) one. Asterisk shows bulging of a Schwann cell nucleus. Bottom right: TEM showing both myelinated and unmyelinated (arrows) nerve fibers. Small type II SGCs (II) and large type I SGCs (I) can be seen. Lower type I cell is wrapped by only a thin myelin sheath (star) [Glueckert et al. (2005b)].

Observing cochlear neurons commonly two types of cells are distinguished. Although the types are often categorized by their soma size and degree of myelination of their cell processes, actually the functional difference is concerned. Thus the majority of cells, with an amount of more than 90% are the type I cochlear neurons, which innervate single IHC of the organ of corti in contrast to the other 5-10% of cochlear neurons which are called type II SGCs and innervate as many as ten or more OHCs usually in one row at the same time by crossing the tunnel of Corti.

Still very often the type I neurons are categorized as 'large' and with myelinated fibers as can be seen in Fig. 2.3. Thus the peripheral and central processes of type I cells are ensheathed with glial cells. Due to the numerously contained mitochondria in the cell body, type I cells are believed to be highly metabolic and older studies predict a diameter of about 30  $\mu\text{m}$  (Glueckert et al. 2005b). On the other hand, the type II cochlear cells are said to be small in size compared to type I cells, e.g., the diameter of the perikarya was reported to be about 15  $\mu\text{m}$  (Glueckert et al. 2005b). Furthermore Hossain et al. (2005) suggested that the lack of myelinization of type II afferents cause a decay in OHC outputs compared to type I cells.

Rusznák and Szücs (2009) reported problems making the differentiation between type I and type II cells according to their size, since there is evidence for a 'large type II' group. A recent study of Potrusil et al. (2012) found variational soma diameters of SGCs from different tonotopic regions suggesting four populations of SGCs concerning their soma size. Additionally the detected mean value of about 19  $\mu\text{m}$  for the soma diameter indicates that the predicted diameter value of 30  $\mu\text{m}$  might be too large.

Due to their structural classification cochlear neurons consists of the soma and two distinct processes symmetric to the cell body. One is called the peripheral process or peripheral axon and can also be defined as the dendrite, the other one is called axon, central axon or is referred to as the central process. Usually the central process has twice the diameter of the peripheral process and according to Spoendlin and Schrott (1989) the average diameter of the central axons is 2.5  $\mu\text{m}$  but range of calibers increase with age. There exist a wide variety of cochlear neurons concerning their lengths, diameters, myelinization of the two processes and the soma which is the topic of our current research paper.

## 2.2 Human anatomy and histology

Many authors reported distinct differences between the human cochleae and those of other mammals, e.g., Tylstedt and Rask-Andersen (2001), Tylstedt et al. (1997), Glueckert et al. (2005b). Although Nadal (1988) reports major differences among species concerning the length and width of the BM, the number and length of IHCs and OHCs as well as the number of nerve terminals per hair cell, the two outstanding human specialties concern the spiral ganglion, i.e., the soma region of human SGCs. These morphometric specialties are speculated to be related to the speech processing and coding mechanism in the human cochlea (Tylstedt and Rask-Andersen 2001). Some more suggestions on the functional consequences of the special human anatomy of the spiral ganglion are summarized in chapter 1.

Among others Tylstedt and Rask-Andersen (2001) reported that whereas the cell bodies of the acoustic ganglion are myelinated in other animals, the spiral ganglion perikarya in humans are unmyelinated (Liu et al. 2012). Only 5% of the neurons are surrounded by several loose myelin layers (Ota and Kimura 1980, Spoendlin and



Schrott 1989). Conforming with these observations, according to Glueckert et al. (2005b) the majority of the population, with about 94% are nonmyelinated, with an increasing rate of myelination in aged individuals (Ota and Kimura 1980).

As a first consequence a slower conductance rate in man is expected. Previously performed computer simulations showed problems resulting from the human nonmyelinated soma, caused by the current loss at the soma region due to the large diameter of the soma in comparison with the presomatic region. Because  $N$  layers of myelin act as  $N$  capacitors in series, most of the current is needed to load the capacitor of the soma. Rattay et al. (2001) reported a larger time delay of the traveling AP from the peripheral to the central axon compared to the cat or other mammals with myelinated soma, e.g., 330  $\mu\text{s}$  in man and 118  $\mu\text{s}$  in the cat. Furthermore according to Rattay et al. (2001) the safety factor for the generation of an AP is reduced by this human peculiarity, i.e., small changes in certain sensitive parameters cause the absence of AP propagation.

Another specialty of human cochlear neurons was investigated by Tylstedt et al. (1997). With their TEM studies they described unit-like structures of neurons in the regions where ganglion cells lay close to each other, i.e., in the middle and upper turn of the cochlea.

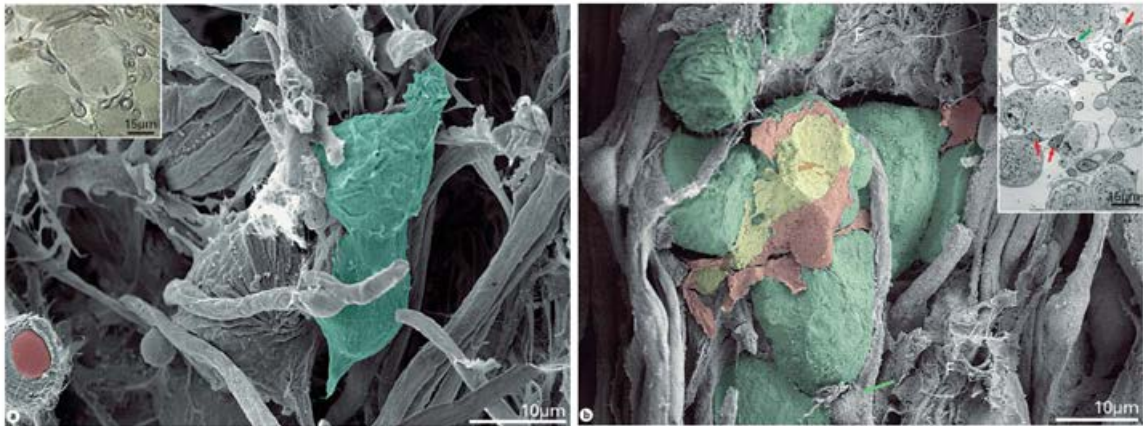


Figure 2.4: Left: (SEM) view of type I cells in the upper basal turn at approximately 2 kHz region. Two cells are wrapped by the same Schwann cells forming a structural unit (colored green). The inset shows also neurons wrapped by common Schwann cells (arrow). Right: Type I human SGCs, colored green in the middle turn at approximately 500 Hz to 1 kHz region. Neurons are arranged in dense clusters. Spaces between are filled with cell bodies from surrounding satellite cells (selected Schwann cells are colored yellow and red). The inset shows a TEM section of an undecalcified human cochlea. Cells between spiral ganglion neurons may belong to Schwann cells surrounding perikarya of neurons (red arrows) or Schwann cells surrounding nerve fibers (green arrows) [Glueckert et al. (2005b)].

In the apical turn, e.g., Pamulova et al. (2006) found 3694 myelinated fibers representing 10% of the total number of fibers innervating the cochlea. At this sites adjacent neurons often faced each other and were ensheated by the same Schwann cells at the soma region. This structural or metabolic unit is called neuronal cluster and illustrated in Fig. 2.4.

Tylstedt et al. (1997) reported that as many as four neurons could share one cluster and that up to 20% of the type I neurons make direct physical contact with neighbouring nerve cells, with an intercellular cleft of approximately 15 to 20 nm (Tylstedt and Rask-Andersen 2001). At these contact sites certain membrane specialisations can be observed (Liu et al. 2009). It remains unknown if the neurons in one cluster innervate the same group of hair cells. At these contact sites electric transmission is believed to occur between nerve elements with a resulting ephaptic neural interaction between enclosed neurons, as suggested by Tylstedt and Rask-Andersen (2001) and Liu et al. (2012).

The distribution of certain ion channels (see Sec. 3.3) along the SGC plays a key role of its activity pattern. Rusznák and Szücs (2009) investigate the distribution of certain channels with a detailed description of potassium channel isoforms of murine SGCs (see Table 4 Rusznák and Szücs 2009) and guinea pig SGCs (see Table 5 Rusznák and Szücs 2009) which are related to divergent conduction properties of SGCs from different frequency regions. Furthermore Davis and Liu (2011) report different channel expression varying from base to apex. Differences in sodium channel distribution among type I and type II cells can also be observed (Hossain et al. 2005).

# Chapter 3

## Modeling of nervous structure

This chapter primary provides an overview of the structure and function of nerve cells, whereby especially the surrounding cell membrane with its electrical properties will be discussed. Thus Sec. 3.1 explains the underlying mechanisms for the generation and transmission of nerve impulses which can be understood as traveling electrical signals. The characteristics of this so called *action potential* (AP) will be explained and furthermore some basic physical concepts are outlined which are used to describe the passive and active electrical properties of the cell membrane.

A nerve impulse can be described as the temporal change of the transmembrane potential  $V_m$ . Thus electrical circuits are used to simulate the excitability of neurons which will be explained in Sec. 3.2. The basic physical laws which are required to describe the electrical currents across the cell membrane will be pointed out in order to derive the differential equation for  $V_m$ . In a next step this model approach is extended to a compartment model, where the neuron will be divided into functional subunits and thus again describes an electrical network of electrical currents across the membrane and also currents between these isopotential elements. The derivation of the system of differential equation for  $V_m$  of each compartment of a single bipolar model neuron will be presented. Furthermore Sec. 3.2 provides a listing of the geometric and electrical parameters which are needed to simulate the excitability of a neuron and therefore also the propagation of a nerve impulse.

The variety of different model approaches for the voltage-dependent ion channels responsible for the change of transmembrane potential is enormous. Thus Sec. 3.3 explains how the complex gating kinetics can be quantitatively described and again the derivation of suitable differential equations will be presented. Within literature, many different sets of equations for these gating kinetics of certain ion channels are used. This thesis provides detailed information of 6 different model approaches for electrically excitable membrane in order to compare their individual characteristics.

Summing up the presented modeling approaches for the spiking pattern of a neuron, Sec. 3.4 evaluates the local model of a patch of active membrane for the 6 different sets of equations. The resulting APs will be analyzed and compared concerning their spike properties.



## 3.1 The membrane and its electrical properties

Nerve cells, also called neurons, are cells in the nervous system which enable the processing and transmission of information. Although neurons consist of the same principal elements as all other cells in the human body, together with muscle cells they are the only electrically excitable cells. Thus, information processing or communication between neurons, can be understood as traveling electrical neural signals.

Nerve cells consist of different functional subunits, i.e., the cell body, also called the soma or perikaryon, the axon and the dendritic tree. Neurons communicate with up to 7000 other neurons via certain junctions called synapses. A neuron receives information represented by an electrical neuronal impulse mostly at the dendrites and also at the soma. The nerve impulse of the neuron is only transmitted to other target neurons by one distinct output region, the axon.

In man the axon has a length ranging from a few  $\mu\text{m}$  up to 1 m and a varying diameter from 0.1 to 20  $\mu\text{m}$  depending on the presence of several surrounding satellite cells forming the myelin layer. This layer consists of either one of two types of glial cells, where Schwann cells supply peripheral neurons and oligodendrocytes enwrapping those of the central nervous system. Therefore axons can be classified into the so called unmyelinated axons which are only supported by one single layer of satellite cells and the larger myelinated axons. These nerve fibers may have up to 300 sheets of myelin as reported by [Ritchie \(1995\)](#).

The main difference between myelinated and unmyelinated axons is their velocity of signal conduction. Unmyelinated axons which are found in vegetative nervous system show a continuous propagation with a velocity in the range of  $v = 1 - 3 \text{ m/s}$  depending on the fiber diameter. Myelinated nerve fibers are found in the peripheral nervous system, their myelin layers are intermitted by so called nodes of Ranvier, where the interaction with the extracellular fluid is possible. These nodes are periodically organized along the axon (every 0.1-2 mm) and enable the fast saltatory conduction velocity of up to  $v = 120 \text{ m/s}$ . The relation between velocity and diameter is linear within myelinated nerve fibers and quadratic for unmyelinated nerve fibers. (for detailed information about the velocity see, e.g., [Malmivuo and Plonsey \(1995\)](#) and also Sec. 4.1.2 and 5.1). Although the myelin sheet is often assumed to be an electrically insulating layer, [Ritchie \(1995\)](#) reported that it has become increasingly clear that myelin itself is not a very good insulator, but its crucial role is to reduce dramatically the capacitive load of internodal axolemma between the nodes of Ranvier which is going to be discussed later on.

The biological membrane surrounds all cells and therefore disunites the intracellular and the extracellular space. Its electrical properties enable the generation and transmission of information coded in a nerve impulse, represented by an AP. Due to the certain structure of the membrane, it has passive and active electrical properties.

### 3.1 The membrane and its electrical properties

---

The passive properties enable the propagation of an equilibrium state of the transmembrane voltage which can be described with the use of the Nernst and Goldman equations. The active properties are responsible for the development and previous transmission of a nerve impulse along the nerve fiber.

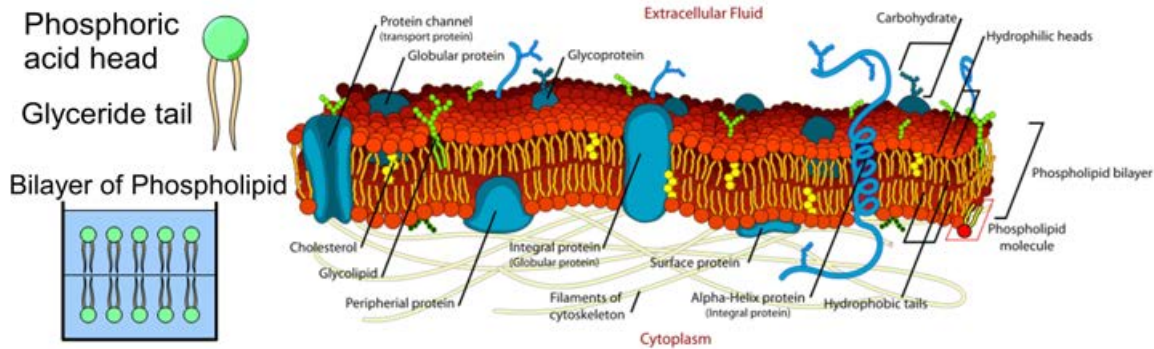


Figure 3.1: One phospholipid and the arrangement of some in aqueous solution to a bilayer at the left (Malmivuo and Plonsey 1995). Schematic picture of the cell membrane with an included transmembrane protein at the right (Hill 2008).

The membrane is a semipermeable bilayer of different phospholipids which are molecules composed of a hydrophobic lipid tail and a hydrophilic phosphate head (Fig. 3.1). Due to the aqueous fluids inside and outside the cell the phospholipids arrange spontaneously to the stable floating equilibrium of a bilayer, i.e., the lipid tails face each other and the phosphate heads confront the intra- and extracellular space. The membrane also contains different proteins which differ in their location. There are proteins attached to the membrane inside and outside the cell, proteins which are embedded in one lipid layer and the channel proteins which pass the whole membrane connecting the intracellular space and the extracellular space. A single lipid molecule has a length of 3 nm and consequently the membrane is about 7 nm thick. By taking the attached proteins into account some authors report a membrane thickness of 7.5-10 nm (Malmivuo and Plonsey 1995).

Some types of ions are able to pass the mentioned channels if they are in an open state. These membrane channels are specific for certain ions, i.e., only one type of ion is able to pass one specific channel. They show distinct distribution along the neuron and also differ in their permeabilities. In the resting state the membrane is permeable to  $K^+$  and  $Cl^-$  and almost not permeable to  $Na^+$  and  $Ca^{2+}$ . The opening process of these channels are of complex chemical nature, however ions are only able to diffuse through the channel from the *intracellular space*(ICS) to the *extracellular space*(ECS) or in the other direction if the voltage-dependent activation and inactivation gates are open.  $10^6$  ions per second are able to pass through one open channel.

The ICS and ECS contain many types of dissolved ions with different concentra-

### 3.1 The membrane and its electrical properties

---

tions on each side. Among others the most important ions concerning the electrical properties are sodium  $Na^+$  which is numerous especially in the ECS, potassium  $K^+$  with a greater amount in the ICS, chloride  $Cl^-$  predominant in the ECS and large anions  $A^-$  only present in the ICS. These ions move freely in the aqueous fluids and are able to cross the membrane from the ICS to the ECS or in the other direction with exception of the immobile, impermeable  $A^-$  which are important for the electro neutrality.

Due to their movement, the electrically charged ions tend to concentrate on the inner and outer surface of the membrane resulting in an electrical field. It is predicted that the ions are endeavored to reach an equilibrium by influx of  $Na^+$  and efflux of  $K^+$ . Thus the electric work to cause transmission of ionic concentrations must equal the osmotic work to compress those ion volumes, i.e.,  $W_{electric} = W_{osmotic}$ . Using the relation between gas constant  $R = 8.31441 \text{ J/mol} \cdot K$  and the absolute temperature  $T$ , the osmotic work  $W_{osmotic}$  can be described. For the electric work  $W_{electric}$ , the electric charge  $Q$  and its relation to the Faraday constant  $F = 9.64845 \cdot 10^4 \text{ C/mol}$  is used. Setting  $W_{osmotic} = W_{electric}$  thus leads to the Nernst Equation

$$V = \frac{R \cdot T}{z \cdot F} \ln \frac{c_2}{c_1}.$$

In the resting state the concentration gradient of  $K^+$  is of special interest, because of the permeable channels. Due to the sparsely permeable channels of  $Na^+$  and  $Ca^{2+}$  and the high concentration gradients across the membrane,  $Na^+$  leakage influx needs to be also considered while deriving the equilibrium. In order to prevent these leakage flux and to maintain the equilibrium potential an enzyme, the sodium-potassium pump ( $Na^+/K^+$ -ATPase), is located in the membrane. This pump corresponds to an active transport which consumes energy in form of ATP. For each ATP molecule three  $Na^+$  ions are transported back to the ECS and two  $K^+$  ions to the ICS.

This steady state where no signal is applied, i.e., no AP is present is not truly a passive state, but more of a stable active state. Because of the selective membrane channels and the existing concentration, gradients of the ions an equilibrium potential may develop. The ion concentrations  $[K^+]$ ,  $[Na^+]$  and  $[Cl^-]$  of potassium, sodium and chloride play the most important part concerning electrical properties. Therefore an extension of the Nernst Equation for one ionic type is given by the Goldman Equation for calculating the resting membrane potential, defined as the difference between the intra- and extracellular potential, i.e.,  $V_m = \phi_i - \phi_e$ , which is given as

$$V_m = \frac{R \cdot T}{F} \ln \frac{P_K[K]_e + P_{Na}[Na]_e + P_{Cl}[Cl]_i}{P_K[K]_i + P_{Na}[Na]_i + P_{Cl}[Cl]_e}.$$

The suffix i stands for intracellular, e corresponds to the extracellular. The ECS concentrations of  $Na^+$  and  $K^+$  appear in the numerator, because they both are anions in contrast to the cathodic  $[Cl^-]$ .  $P_i$  stands for the permeability of either  $Na^+$ ,  $K^+$  or  $Cl^-$  (induced by the suffix i) and is measured in cm/s.

### 3.1 The membrane and its electrical properties

---

The resting potential of neurons certainly varies among species and also for neurons of different origin and type with reported values between -40 and -85 mV. As the Goldman equation indicates, the specific distribution of ion channels and their distinct permeability are crucial parameters. Nonetheless, the resting potential of many neurons and therefore also for the simulations within this thesis is assumed to be about -70 mV.

When a neuron receives a signal from another nerve cells, e.g., due to synaptic currents, the transmembrane potential  $V_m$  certainly changes from the measured resting value. If an excitatory stimulus is applied the potential is depolarized, in case of an inhibitory signal the magnitude of the membrane voltage increases, i.e., the cell is hyperpolarized. This change of potential is caused by the opening of ion channels.

If the stimulus remains below a certain threshold, i.e., it is not strong enough, the membrane is not activated. Under this subthreshold condition the potential will recover with the help of the  $Na^+/K^+$ -ATPase. The neuron is activated if an excitatory stimulus reaches the threshold of about 20 mV, i.e., a transmembrane voltage of -50 mV. This change of potential, irrespective of the strength of the suprathreshold stimulus, leads to a sequence of opening and closing of the different channels resulting in ion flow. Therefore every AP is said to follow the all-or-nothing principle and has a uniform shape when conducted along the axon.

During the initiation phase the membrane is depolarized and the threshold for the voltage dependent sodium channels is reached. At a voltage of about -60 mV a bit more sodium channels open leading to the following rising phase and subsequent overshoot. The resulting  $Na^+$  influx depolarizes the membrane and therefore more sodium channels are activated because of the rapid increase in sodium permeability. As a consequence an overshoot, i.e., a positive inside potential of about 20-40 mV is observed. Before the maximum potential is reached, the sodium channels begin to inactivate spontaneously and the potassium channels slowly increase their permeability. During the repolarization phase the  $Na^+$  influx stops and the  $K^+$  ions flow from the ICS to the ECS decreasing the membrane potential. Often a hyperpolarization is also present resulting from the still increased potassium permeability and pump rate of the  $Na^+/K^+$ -ATPase. After stimulation the membrane potential returns again to its resting state. Although the duration of the whole AP in neurons is often assumed to last for about 1 ms, much shorter APs appear in the mammalian peripheral nerve fiber (see Section 5.1).

Although the AP follows the all-or nothing principal, its characteristics change within species and also for different functional subunits (compare Fig. 3.2). Certain properties can be evaluated in order to describe the AP's appearance, namely one can calculate the *AP height* ( $AP_{height}$ ) or *AP amplitude* ( $AP_{amp}$ ) as well as the *AP*

### 3.1 The membrane and its electrical properties

*duration or half-duration* ( $AP_{width}$ ). These parameter are described in detail e.g. in [Bean \(2007\)](#). The calculations within this thesis follow this definition.

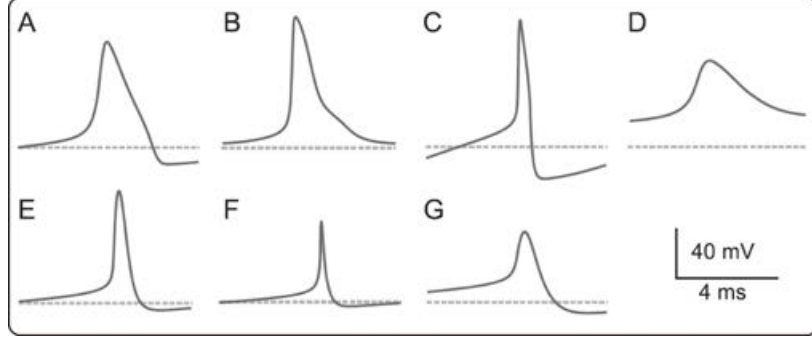


Figure 3.2: The shapes of APs, adapted from [Sengupta et al. \(2010\)](#): (A) Hodgkin-Huxley type models from the squid giant axon, (B) crab motor neuron axon, (C) mouse fast-spiking neuron, (D) honeybee Kenyon cell, (E) rat hippocampal interneuron, (F) rat granule cell and (G) mouse thalamo-cortical relay neuron.

Thus the  $AP_{height}$  is defined as the maximal overshoot of membrane potential, whereas in this context the  $AP_{amp}$  defines the difference between the minimum and maximum of membrane potential, which also takes afterhyperpolarization into account. The AP half-duration is measured as the width at half-maximal spike amplitude. Since for this spike width, which is commonly discussed in many scientific publications, different notation are confusingly used, [Bean \(2007\)](#) is right so suggest that 'half-height width' would be the clearest term. However, within this thesis, two values are presented, one is calculated with the  $AP_{height}$ , which would mean the actual 'half-height width', and one is evaluated with the  $AP_{amp}$ , therefore corresponding to the 'half-amplitude width'.

The electrical properties of the membrane vary tremendously among different cells and also among functionally different parts of one neuron. Thus not only altering ion channel densities are observed, also the resting membrane potential changes, e.g. [Bean \(2007\)](#) state that for pyramidal neurons in CA1 region of rat hippocampus typical values range from -85 mV to -60 mV. Their recordings reveal an  $AP_{width}$  of about 1 ms, while recordings of guinea-pig cortical neurons ([Gutfreund et al. 1995](#)) show a mean value of 1.4 ms. They further report a quite low spike height of about 88 mV and a resting potential of -66 mV.

Corresponding values of the resting membrane potentials for cochlear neurons of guinea pig, mouse, rat and gerbil can be found in [Rusznák and Szűcs \(2009, Table 1\)](#). They report varying values among type I and type II neurons ranging for about -53 mV for gerbil and up to -77 mV for the rat type I cells. Furthermore [Santos-Sacchi \(1993\)](#) studied type I neurons of guinea pigs what revealed varying values of this resting membrane potentials at different sites of the neuron with about -70 mV

### 3.1 The membrane and its electrical properties

---

near the cell soma while previous examinations report measured membrane potentials in type I afferent terminals in the guinea pig, which ranged from -40 to -60 mV.

Furthermore a detailed characterization of the firing pattern produced by mouse SGCs, including latencies of AP, adaption and the duration of an AP, was performed by Reid et al. (2004). Rusznák and Szücs (2009, Table 3) summarize these results which predict the shortest AP duration of about 1.25 ms for basal type I neurons and the longest value of 1.9 ms for apical type II cells.

A recent modeling study of Sengupta et al. (2010) unravels the great difference of APs with different shapes and varying heights and widths. They used single compartment models to assess the energy consumption of APs from seven neurons from both vertebrates and invertebrates. The energy costs of these APs vary by over an order of magnitude from the most economical, the rat granule cell and mouse thalamo-cortical interneuron, to the most profligate, the squid giant axon. Sengupta et al. (2010) state, that energy consumption can increase by more than ten-fold simply by changing the overlap of the  $Na^+$  and  $K^+$  currents during the AP without changing the AP's shape essentially.

Although Hodgkin and Huxley (1952) stated that their equations in the present form only apply to the isolated squid axon, a long-held supposition, based on their theoretical analysis, established that APs are energetically wasteful. This hypothesis has recently been overturned by studies that measured the currents contributing to the AP in several mammalian neurons. Patch-clamp recordings at 36° to 37°C from rat hippocampal mossy fiber boutons revealed brief APs of a half-duration of 0.25 ms with  $Na$  currents showing rapid activation and fast decay and significantly delayed  $K$  current onset (Alle et al. 2009).

The high dependency of the AP properties on the temperature is extensively discussed in Fohlmeister et al. (2010). The recorded impulse trains from a rat retinal ganglion cell for 5 different temperature values show distinct differences in their AP kinetics, with a significant decrease in  $AP_{width}$  for higher temperatures. While, they observed the highest AP amplitudes and lowest threshold for temperatures of 13-16°C, the spiking becomes noisy at mammalian temperatures (37.1°C).

Different recording techniques reveal the specific AP properties of cochlear neurons, e.g., see collected NRT data explained in Chapter 1. The NRT data of Miller et al. (2004) suggest that the whole spike of a cochlear neuron stimulated with anodic monophasic pulses lasts about 0.5 ms, i.e., the quite short AP duration measured at the bottom sums up to 0.5 ms. Also recordings of cat auditory nerve fibers (Zhang et al. 2007) suggest quite similar AP durations for certainly different pulse train stimulation, although the  $AP_{amp}$  significantly changes.

While many different approaches exist to model the single neuron response for cochlear neurons (see Section 4.1), the approach of Rattay et al. (2001) allows a very good description of the human AP properties. In Rattay (2004) modeled APs



following biphasic extracellular stimulation produce an  $AP_{width}$  of about 0.25 ms with a total spike duration of about 0.5 ms in accordance with the previously mentioned observations.

Artificial activation of a neuron is triggered with a strong short stimulus and also follows an adequate longer weaker current, i.e., excitation is strength-duration dependent, which can be illustrated with the strength-duration curve. The weakest pulse amplitude which would need theoretically infinite duration to initiate activation is called the rheobase. The chronaxy is defined as the minimum pulse duration needed to excite the cell with twice rheobase current.

When repetitive stimuli are applied the neuron shows refractory behavior, characterized by a rise in the excitation threshold. The absolute refractory period is denoted as the time when the neuron is activated and therefore unable to trigger a following impulse caused by inactive, closed sodium channels. When these channels return to active, open state in the onwardly repolarization phase the neuron is able to be activated by a much stronger current with a resulting smaller depolarization and is said to be relatively refractory.

## 3.2 Electrical circuits and mathematical modeling

As indicated previously, the AP interpreted as electrical signal can be described as temporal change in the transmembrane potential which deviates from its resting potential  $E_{rest} \approx -70$  mV. The transmembrane potential is defined as the potential difference between ICS and ECS, i.e.,  $E_m = V_i - V_e$ . The reduced transmembrane potential  $V_m = E_m - E_{rest}$  is of special interest, because it is generally used in modeling and simulation studies. Nonetheless the difference shall be recognized.

In order to derive a differential equation for  $\frac{dV_m(t)}{dt}$  or  $\frac{dE_m(t)}{dt}$ , the membrane will be describe with an electrical circuit. Although different approaches with altering degree of complexity exist, a very common attempt is presented in Fig 3.3.

There are two ways to interpret a patch of membrane, either as passive (Fig. 3.3A) or active model (Fig. 3.3B). Generally, parts of a neuron which are covered in myelin are considered to be of the passive type which are most likely internodes. This means that no voltage-gated ion channels are present, so that the membrane is considered to be a simple RC circuit with a constant resistance. Therefore, it follows for the membrane current per unit area  $I_{mem}(t) = I_{cap}(t) + I_{ohm}(t)$ , measured in  $[\mu\text{A}/\text{cm}^2]$ . The capacitance is given as  $C = \frac{Q}{V}$  and the current can be expressed by means of the charge  $Q$  as  $I = \frac{dQ}{dt}$ . Thus, the capacitive current  $I_{cap}(t)$  can be described as  $C_{mem} \frac{dV_m}{dt}$  where  $C_{mem}$  denotes the membrane capacitance per unit area  $[\mu\text{F}/\text{cm}^2]$ . When a stimulus current is present which changes the potential  $E_m(t)$ ,  $I_{stim}(t) + I_{mem}(t) = 0$  holds and with the inclusion of Ohm's law for the membrane resistance per unit area

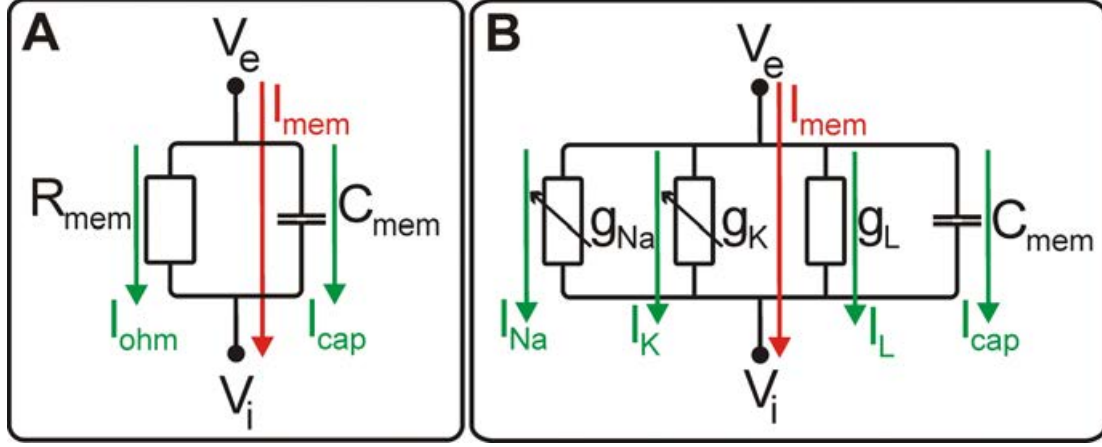


Figure 3.3: Schematic drawing of the equivalent circuit model for a patch of membrane. (A) passive model of the membrane with constant membrane resistance  $R_{mem}$ . (B) active model with ionic currents, the nonlinear conductances of  $Na$  and  $K$  which are voltage dependent are indicated with an arrow in contrast to the constant leakage conductance  $g_L$ .

$R_{mem}$  [ $k\Omega \cdot cm^2$ ] it follows

$$\begin{aligned} \frac{dE_m(t)}{dt} &= \frac{-I_{stim}(t) - \frac{1}{R_{mem}} \cdot E_m(t)}{C_{mem}} \\ \frac{d(V_i - V_e)(t)}{dt} &= \frac{-I_{stim}(t) - \frac{1}{R_{mem}} \cdot (V_i(t) - V_e(t))}{C_{mem}} \end{aligned}$$

This differential equation can be solved with an initial value of  $E_m(t = 0) = E_{rest}$ , if the equation is solved for the reduced transmembrane potential,  $V_m(0) = E_m(0) - E_{rest} = 0$  holds.

In contrast to this, active patches are regions without a myelin shield cover, where ion channels are exposed to the extracellular fluid. The linear ohmic current  $I_{ohm}$  is replaced by a nonlinear ionic term  $I_{ion}$ . For this thesis we will focus solely on sodium and potassium channels, i.e.,  $I_{ion} = I_{Na} + I_K + I_L$ . The constant membrane resistance  $R_m$  is replaced by voltage-dependent conductance  $G_{mem} = \frac{1}{R_{mem}}$ , measured in [ $mS/cm^2$ ]. No sodium current is present, if the reduced transmembrane voltage  $V_m$  equals the reduced Nernst Potential of sodium  $V_{Na} = E_{Na} - E_{rest}$ , concluding that the driving voltage for the sodium flow is given as  $(V_m - V_{Na})$  [ $mV$ ]. Thus, the following equations hold for  $I_{Na}$  and  $I_K$ , the electric currents per unit area [ $\mu A/cm^2$ ]

$$\tilde{G}_{Na}(t) = \frac{I_{Na}(t)}{V_m(t) - V_{Na}}, \quad \tilde{G}_K(t) = \frac{I_K(t)}{V_m(t) - V_K}.$$

Each type of ion channel acts differently when the membrane voltage changes. The dependency of the conductance is described with gating variables which indicate if



the channel is either open or closed. For sodium channels even an inactivating and non-inactivating state is distinguished. For details see section 3.3.

The leakage current  $I_L$  compensates other ion flux and is considered to be of the linear type, i.e.,  $G_L$  is chosen to be constant and  $I_L(t) = \frac{1}{R_{mem}} \cdot (V_m(t) - V_L)$  holds. The parameter  $V_L$  will be therefore calculated in order to account for minimal initial ionic currents.

The differential equation for the temporal change of the reduced transmembrane potential  $\frac{dV_m(t)}{dt}$  for an active patch of membrane can be written as

$$\frac{d(V_i - V_e)(t)}{dt} = -\frac{I_{stim}(t)}{C_{mem}} - \frac{\tilde{G}_{Na}(t) \cdot (V_m(t) - V_{Na})}{C_{mem}} - \frac{\tilde{G}_K(t) \cdot (V_m(t) - V_K)}{C_{mem}} - \frac{G_L \cdot (V_m(t) - V_L)}{C_{mem}}.$$

#### 3.2.1 Compartment model - Functional subunits

In order to develop a more complex model of the excitability of a neuron, it is divided into functional subunits of uniform geometrical and electrical properties. A compartment model defines different regions as isopotential elements which are connected through intracellular axial currents. The equivalent circuit diagram of the soma region of a bipolar neuron, with only two processes, is illustrated in Fig. 3.4. The schematic drawing helps to derive a mathematical model based on physical laws concerning electrical circuits.  $V_{i,n}$  denotes the intracellular potential at the n-th compartment and  $V_{e,n}$  the corresponding extracellular potential.

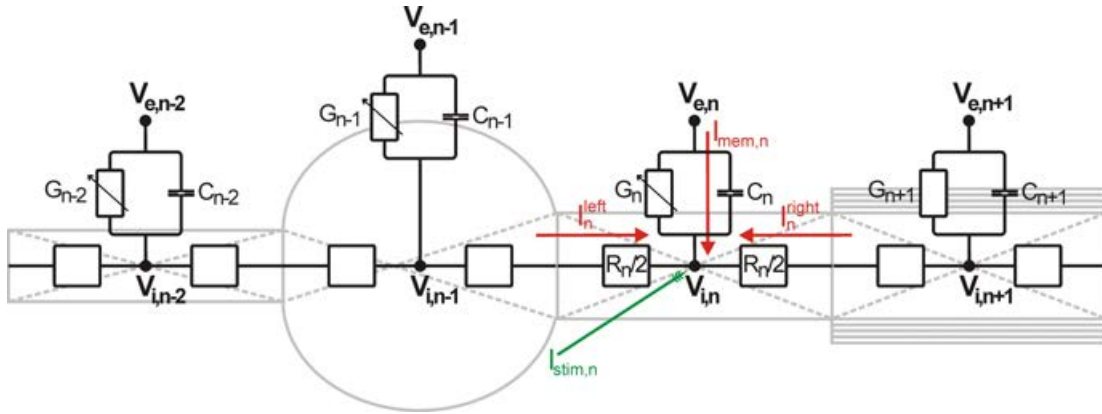


Figure 3.4: Schematic drawing of the equivalent circuit around a spherical active soma of a bipolar neuron. Note the myelin sheet at the first postsomatic passive internode and the resulting constant resistance, in contrast to the nonlinear conductances indicated by arrows of active compartments [adapted from Rattay et al. (2001)].

Investigating the current to the central point of the n-th compartment in Fig. 3.4 shows that the total current consists of the capacitive current  $I_{cap,n}$ , the ionic trans-

### 3.2 Electrical circuits and mathematical modeling

---

membrane current  $I_{ion,n}$  and the axial ohmic currents  $I_{ax,n}$  to the adjacent compartments. Therefore if a stimulus current is present and by applying Kirchhoff's law, which states that the sum of the total current must equal zero, it follows

$$I_{stim,n}(t) + I_{cap,n}(t) + I_{ion,n}(t) + I_{ax,n}(t) = 0, \quad \forall n \in \{1, \dots, n_{Comp}\}.$$

The axial current  $I_{ax,n}$  consists of two components except for the first and last compartment which only have one neighbor.

$$I_{ax,n}(t) = I_n^{left}(t) + I_n^{right}(t) = \frac{V_{i,n}(t) - V_{i,n-1}(t)}{R_n/2 + R_{n-1}/2} + \frac{V_{i,n}(t) - V_{i,n+1}(t)}{R_n/2 + R_{n+1}/2}$$

$R_n$  describes the axoplasmatic resistance to its neighbors and is calculated by  $R_n/2 = (2\rho_i l_n)/(d_n^2 \pi)$  with the exception of the spherical soma (Rattay et al. 2003).  $\rho_i$  denotes the specific intracellular resistivity,  $l_n$  the length and  $d_n$  the diameter of the n-th cylindrical compartment.

Also the the membrane capacitance  $C_n$  has to be calculated for each of the  $n_{Comp}$  compartments with a surface  $A_n$  by  $C_n = \frac{C_{mem} \cdot A_n}{nm_n}$ , where  $C_{mem}$  denotes the specific membrane capacitance which is reverse proportional to the numbers of myelin layers of the n-th compartment  $nm_n$ .

As already mentioned, we will focus on two types of assumptions for the ionic currents of a compartment depending on its electrical behavior. For the ionic currents of the active compartments  $I_{ion,n}(t) = G_{Na,n}(t) \cdot (V_{m,n}(t) - V_{Na}) + G_{K,n}(t) \cdot (V_{m,n}(t) - V_K) + G_{L,n} \cdot (V_{m,n}(t) - V_L)$  the conductances have to be calculated again with the densities and the compartments surface  $A_n$ .

The internodes are myelinated and therefore considered to be of the passive type, i.e.,  $I_{ion,n}(t) = \frac{g_{my} \cdot A_n}{nm_n} \cdot (V_{i,m}(t) - V_{e,m}(t))$ .  $g_{my}$  denotes the conductance of one layer of membrane and again  $nm_n$  the number of myelin layers enwrapping the internode.

With the notation  $V_{m,n} = V_{i,n} - V_{e,n} - E_{rest,n}$  using the reduced membrane potential of the n-th compartment the derived differential equation for this membrane potential can be written as

$$\begin{aligned} \frac{dV_{m,n}(t)}{dt} = & \left[ -I_{ion,n}(t) + \frac{V_{m,n+1}(t) - V_{m,n}(t)}{R_{n+1}/2 + R_n/2} + \frac{V_{m,n-1}(t) - V_{m,n}(t)}{R_{n-1}/2 + R_n/2} \right. \\ & \left. + \frac{V_{e,n+1}(t) - V_{e,n}(t)}{R_{n+1}/2 + R_n/2} + \frac{V_{e,n-1}(t) - V_{e,n}(t)}{R_{n-1}/2 + R_n/2} \right] / C_n. \end{aligned}$$

If no stimulating electrode is present in the ESC it is assumed that  $V_{e,n} = 0, \forall n$  holds and therefore the equation reduces to

$$\frac{dV_{m,n}(t)}{dt} = \left[ -I_{ion,n}(t) + \frac{V_{m,n+1}(t) - V_{m,n}(t)}{R_{n+1}/2 + R_n/2} + \frac{V_{m,n-1}(t) - V_{m,n}(t)}{R_{n-1}/2 + R_n/2} \right] / C_n.$$

### 3.3 Ion channels

Making a decision on the active electrical properties is a critical task. Not only one has to know which ion channels are present on the nervous structure of interest, also appropriate models for the gating mechanisms of these channels have to be chosen. Although our knowledge concerning single ion channels and their distribution has certainly improved within the past few decades, no uniform equations representing the electrical properties have been presented in order to describe the voltage dependency of the activation and inactivation of channels.

Although for this thesis we will focus on sodium  $Na$  and potassium  $K$  channels, within the mammalian nervous systems many more voltage-dependent ion channels are present which are selective to only one type of ion. Furthermore for each ion many subtypes exist which differ with respect to their structure and therefore also function and as well with respect to their location.

[Yu and Catterall \(2003\)](#) state that mammalian sodium channels also have varying expression profiles during development and different subcellular localizations, consistent with a distinct role for each channel in mammalian physiology. Their findings reveal that voltage-dependent sodium channels  $Na_v1.1$  and  $Na_v1.3$  are localized to the soma of the neuron probably controlling neuronal excitability through integration of synaptic impulses to set the threshold for AP initiation and propagation to the dendritic and axonal compartments. Furthermore [Yu and Catterall \(2003\)](#) report that during development, in maturing nodes of Ranvier  $Na_v1.6$  replaces  $Na_v1.2$  which is also expressed in the unmyelinated axons, where it conducts the AP. Although  $Na_v1.1$  and  $Na_v1.6$  are also significantly expressed in the peripheral nervous system the most abundantly expressed isoform is  $Na_v1.7$ , localized to axons, where it may function in initiating and conducting the AP. The other isoforms  $Na_v1.8$  and  $Na_v1.9$  are expected to have a key role in the perception of pain and finally the  $Na_v1.4$  and  $Na_v1.5$  isoforms are muscle sodium channels ([Yu and Catterall 2003](#)).

Generally voltage-gated sodium channels are critical elements of AP initiation and propagation in excitable cells because they are responsible for the initial depolarization of the membrane ([Goldin et al. 2000](#)). The nine mammalian sodium channel isoforms that have been identified and functionally expressed are all greater than 50% identical in amino acid sequence in the transmembrane and extracellular domains. In contrast, for potassium channels ([Chandy 1991](#), [Chandy and Gutman 1993](#)) all the membranes of distinct subfamilies are less than 50% identical to those of other families, and there is much closer sequence similarity within families.

[Coetzee et al. \(1999\)](#) comprehend with the variety of potassium channels which constitute a highly diverse class of ion channel and thus participate in multiple modulatory functions. There are several functional types of  $K$  channel, including voltage-gated  $K$  channels,  $Ca^{2+}$ -activated  $K$  channels, inward rectifiers, leak  $K$  channels and  $Na^+$ -activated  $K$  channels. Their detailed work ([Coetzee et al. 1999](#)) includes a co-

herent schematic representation of the three groups of  $K$  channel principal subunits as well as a description of their location within the nervous system.

Many different approaches for modeling the gating of ion channels have been proposed, all of which have different degrees of complexity. The model of *Hodgkin and Huxley (1952)* (HH) suggests hypothetical gating particles to explain the channel's function, by describing their motion with respect to the electric field across the membrane. Beside this well known approach, discrete-state Markov models have been used to describe the different states of the ion channel (*Kienker 1989*). Fractal models of ion channel gating (e.g., *Liebovitch et al. 2001*) provide a different description of the underlying mechanism with equations having continuous rather than discrete states. *Francis et al. (2010)* gives a very good overview of further modeling approaches.

However, for this thesis only models are used which follow the ansatz of HH who introduced a physical basis for their mathematical description. For the potassium channels they presented n-gates which are responsible for opening and closing the selective potassium channels, i.e., an n-gate may be in the open state with the probability  $n$  and change to the closed state with the probability  $(1-n)$ , where  $0 \leq n \leq 1$ . Although HH assumed that a potassium channel is open if there exist four open n-gates, i.e.,  $n^4$ , other models only assume one opening gate as will be discussed subsequently. The changes in the parameter  $n$  describe the alteration of the state of the n-gates. These changes from  $n$  to  $(1-n)$  are explained with voltage-dependent transfer rates, i.e.,  $\alpha_n$  [1/ms] which describe the transfer from  $(1-n)$  to  $n$  and  $\beta_n$  [1/ms] from  $n$  to  $(1-n)$ .

The opening and closing of the  $Na$  channel is typically described with the parameter  $m$ . Additionally HH supposed h-gates, equivalent to the inactivation gates, where  $h$  is the probability for the fraction of h-gates to be in the non-inactivating state, and  $(1-h)$  the probability to be in the inactivating state. Again corresponding voltage-dependent transfer rate describe the change from one state to the other. Most models predict that a selective sodium channel is open if there are three open m-gates and one non-inactivating h-gate, therefore the probability of an open, active channel is proportional to  $m^3h$ .

All gating variables  $\alpha$  and  $\beta$  describe the rate of change of one parameter  $p = \{m, h, n, \dots\}$  from the open (inactivating) to closed (non-inactivating) state and therefore  $p$  obeys a first order differential equation with time constant  $\tau_p$  and a steady state  $p_\infty$ , generally described directly by the gating variables.

Furthermore the model temperature, at which the equations are derived, has to be taking into account, especially when different models shall be compared. Previous simulation studies also dealt with this critical topic (*Fohlmeister et al. 2010, Smit et al. 2009b,c*). Usually a multiplicative factor, the temperature adjustment coefficient, is applied for each gating variable  $\alpha$  and  $\beta$  which is calculated via  $t_{adj} = Q_{10}^{0.1 \cdot (T - T_0)}$ , where  $Q_{10}$  is a factor describing the temperature increase for 10°C,  $T_0$  is the original

### 3.3 Ion channels

---

model temperature and  $T$  the new temperature. The  $Q_{10}$  factors vary for different models and sometimes also for the type of channel.

These assumptions lead to a differential equation for each gating parameter which represents the fraction of the gates in the open state (or non-inactivating state):

$$\text{with } \tau_p = \frac{1}{\alpha_p + \beta_p} \text{ and } p_\infty = \tau_p \cdot \alpha_p : \quad \frac{dp(t)}{dt} = t_{adj} \cdot \frac{p_\infty(t) - p(t)}{\tau_p(t)} \quad (3.1)$$

Furthermore by defining  $G_{K,max}$  as the maximum value of potassium conductance per unit area [mS/cm<sup>2</sup>] and  $n$  solves equation 3.1, the conductance is given as  $\tilde{G}_K = G_{K,max} \cdot n^4$ . For the sodium channel  $G_{Na,max}$  denotes the maximum value of sodium conductance per unit area [mS/cm<sup>2</sup>] and with parameters  $m$  and  $h$  obeying the equation 3.1, the sodium conductance can be written as  $\tilde{G}_{Na} = G_{Na,max} \cdot m^3 \cdot h$ .

Conclusively the ionic current  $I_{ion}$  of an active patch of membrane can be rewritten to:

$$\begin{aligned} I_{ion}(t) &= I_{Na}(t) + I_K(t) + I_L(t) = \\ &= G_{Na,max} \cdot m(t)^3 \cdot h(t) \cdot (V_m(t) - V_{Na}) \\ &\quad + G_{K,max} \cdot n(t)^4 \cdot (V_m(t) - V_K) \\ &\quad + G_L \cdot (V_m(t) - V_L) \end{aligned}$$

Patch clamp techniques and single channel recordings reveal the voltage dependency of each parameter for different ion channels. HH found their equations for the gating variables through curve fitting techniques. All models used in this thesis follow this approach, which basically is fitting measured voltage dependency to Boltzmann-Function parameters (Dubois et al. 2009).

$$(\alpha, \beta) = \frac{A \cdot k \cdot (V - V_{1/2})}{1 - e^{-[r] \cdot k \cdot (V - V_{1/2})}}$$

The two properties, i.e.,  $k$  denotes the slope factor and  $V_{1/2}$  the half-activation potential, are often discussed in scientific publications and their values are distinct for certain ion channels. A very good explanation of the derivation of those parameters can be found in Osorio et al. (2010) who investigate  $Na_v1.2$  and  $Na_v1.6$  cerebellar granule cells of mice. The presented Fig.4 illustrates the curve fitting technique.

Cummins et al. (1994) studied sodium channels of neocortical pyramidal neurons using whole-cell voltage clamp in both rats and humans and evaluated the amount of persistent and transient sodium currents. When the current magnitudes are divided by the capacitance, cells of different size can be compared. Thus they report a  $Na$  current density of  $595 \pm 65$  pA/pF in humans (Cummins et al. 1994, Table 1). The two property values are predicted to be for activation  $V_{1/2} = -29.6 \pm 1.0$  mV and  $k = 6.0 \pm 0.2$  mV/e-fold, and for the inactivation  $V_{1/2} = -66.5 \pm 1.3$  mV and  $k = 6.7 \pm 0.2$  mV/e-fold.

### 3.3 Ion channels

---

The somatic and axonal outside-out patches of [Hu et al. \(2009\)](#) revealed different properties for two subtypes,  $Na_v1.2$  believed to be dominant at the soma and  $Na_v1.6$  only expressed at axonal sites. Their recordings showed the following parameter values for activation at the axon  $V_{1/2} = 43.9 \pm 1.3$  mV,  $k = 5.7 \pm 0.2$ ; at the soma:  $V_{1/2} = 29.7 \pm 1.0$  mV,  $k = 5.8 \pm 0.2$ . The inactivation values are at the axon  $V_{1/2} = 80.0 \pm 1.0$  mV,  $k = 5.4 \pm 0.2$ ; at the soma:  $V_{1/2} = 67.0 \pm 1.7$  mV and  $k = 7.1 \pm 0.3$ .

For potassium currents similar recordings exist, although the variety of reported values certainly increases. [Hoffman et al. \(1997\)](#) studied the  $K$  channel regulation of signals and derived potassium channel equations with recordings of whole-cell patch-clamp recordings of rat hippocampal slices. [Kole et al. \(2007\)](#) analyzed  $K_v1$  channels with paired recordings between rat layer 5 pyramidal neurons and fitted their results to Boltzmann equations.

Not only the patch-clamp recording examinations differ, also the sets of equations for the gating kinetic parameters  $\alpha$  and  $\beta$  reported within literature are highly divergent. Even more, since many authors adapt older models whereas others develop their own set of equations or combine their results with previously used models, studying the ion channel models and comparing them is a very difficult task. Within this thesis 6 commonly used models of the two ion channels of interest, i.e.,  $Na$  and  $K$  channels, are presented. In the following the gating kinetics of these models will be discussed and the original model parameters are indicated. In order to compare these 6 models two parameters are essential, i.e., the initial transmembrane voltage  $V(t=0)$  and the original model temperature  $T$  vary and thus have to be addressed in detail.

#### SQUID AXON BY HH

The well known model of [Hodgkin and Huxley \(1952\)](#) incorporates one sodium and one potassium channel and corresponds to recordings of a squid axon. Thus the model was developed for an initial transmembrane voltage of  $V(0) = \phi_i(0) - \phi_o(0) = -60$  mV and a very low original temperature of  $T = 6.3^\circ\text{C}$ . Although [Hodgkin and Huxley \(1952\)](#) suggest a  $Q_{10}$  of 3 for all  $\alpha$ 's and  $\beta$ 's, for this thesis a  $Q_{10}$  of 2.2466 was chosen, to match the results for the cochlear neuron model of [Rattay et al. \(2001\)](#), which uses a multiplicative factor of  $k = 12$  for  $T = 37^\circ\text{C}$ .

$$\begin{aligned}\alpha_m &= \frac{2.5 - 0.1 \cdot V}{e^{2.5 - 0.1 \cdot V} - 1} & \beta_m &= 4 \cdot e^{\frac{-V}{18}} \\ \alpha_h &= 0.07 \cdot e^{\frac{-V}{20}} & \beta_h &= \frac{1}{e^{3 - 0.1 \cdot V} + 1} \\ \alpha_n &= \frac{0.1 - 0.01 \cdot V}{e^{1 - 0.1 \cdot V} - 1} & \beta_n &= 0.125 \cdot e^{\frac{-V}{80}}\end{aligned}$$

#### RGC BY FOHLMEISTER

Fohlmeister et al. (2010) intracellularly recorded trains of APs of rat and cat *retinal ganglion cells* (RGC) across a temperature range of 7 – 37°C. In their previous study Fohlmeister (2009) they modified the original HH model in order to reduce the large ion currents and thus increase energy efficiency of the AP.

The included calcium current was omitted for this thesis. The listed equations correspond to an initial transmembrane voltage  $V(0) = \phi_i(0) - \phi_o(0) = -60$  mV. The original temperature of  $T = 13.9^\circ\text{C}$  is adjusted with a  $Q_{10}$  of 2 for all  $\alpha$ 's and  $\beta$ 's.

$$\begin{aligned}\alpha_m &= \frac{-0.3753 \cdot (V + 35)}{e^{-0.1 \cdot (V+35)} - 1} & \beta_m &= 12.51 \cdot e^{\frac{-(V+60)}{20}} \\ \alpha_h &= 0.2502 \cdot e^{\frac{-(V+52)}{20}} & \beta_h &= \frac{3.753}{e^{-0.1 \cdot (V+22)} + 1} \\ \alpha_n &= \frac{-0.01319 \cdot (V + 37)}{e^{-0.1 \cdot (V+37)} - 1} & \beta_n &= 0.2638 \cdot e^{\frac{-(V+47)}{80}}\end{aligned}$$

#### CA5 BY MAINEN AND SEJNOWSKI

Mainen and Sejnowski (1996) simulate *pyramidal cells of the fifth layer* (CA5) with different geometry of the dendritic tree. They include sodium, potassium and calcium currents. For this study, only the  $Na$ , the fast  $K_v$  and the slow non-inactivating  $K_m$  currents were used. The corresponding equations, except the  $K_m$  current, have been formalized in an earlier paper (Mainen et al. 1995).

This modeling and simulation study is very often used by many authors as a basis for the adaption to their certain circumstances. The equations correspond to an initial transmembrane voltage  $V(0) = \phi_i(0) - \phi_o(0) = -70$  mV and to the original temperature of  $T = 23^\circ\text{C}$  with a  $Q_{10}$  of 2.3 for all  $\alpha$ 's and  $\beta$ 's.

$$\begin{aligned}\alpha_m &= \frac{0.182 \cdot (V + 25)}{1 - e^{-(V+25)/9}} & \beta_m &= \frac{-0.124 \cdot (V + 25)}{1 - e^{(V+25)/9}} \\ \alpha_h &= \frac{0.024 \cdot (V + 40)}{1 - e^{-(V+40)/5}} & \beta_h &= \frac{-0.0091 \cdot (V + 65)}{1 - e^{(V+65)/5}} \\ h_\infty &= \frac{1}{1 + e^{(V+55)/6.2}} \\ \alpha_{n1} &= \frac{0.02 \cdot (V - 25)}{-e^{-(V-25)/9}} & \beta_{n1} &= \frac{-0.002 \cdot (V - 25)}{1 - e^{(V-25)/9}} \\ \alpha_{n2} &= \frac{10^{-4} \cdot (V + 30)}{1 - e^{-(V+30)/9}} & \beta_{n2} &= \frac{-10^{-4} \cdot (V + 30)}{1 - e^{(V+30)/9}}\end{aligned}$$

An interesting fact about the sodium current is the separate equation for the steady state of inactivation variable  $h$ , although the time constant  $\tau_h$  will still be calculated with  $\alpha_h$  and  $\beta_h$ . This evaluation has to be used since the usual calculation results in



### 3.3 Ion channels

---

the opposite monotony behavior, i.e., the inactivation curve would also be increasing for increasing membrane potential as it is the case for the steady state of the activation variable.

This discrepancy has been analyzed (data not shown) in earlier simulation runs, which revealed problems with repolarization to an initial transmembrane value.

#### CA3 BY MEEKS AND MENNERICK

[Meeks and Mennerick \(2007\)](#) investigated basic properties of spike initiation and propagation in *pyramidal cells of the third layer* (CA3) of juvenile rat hippocampus with paired intracellular/extracellular recordings. They constructed one sodium channel for an initial transmembrane voltage  $V(0) = \phi_i(0) - \phi_o(0) = -70$  mV.

Their potassium channel was adapted from [Mainen et al. \(1995\)](#). Therefore again the original temperature of  $T = 23^\circ\text{C}$  has to be corrected with a  $Q_{10}$  of 2.3 for all  $\alpha$ 's and  $\beta$ 's.

$$\begin{aligned}\alpha_m &= \frac{1.15 \cdot 0.111 \cdot (V + 35)}{1 - e^{-0.111 \cdot (V+35)}} & \beta_m &= \frac{1.688 \cdot (-0.111) \cdot (V + 40)}{1 - e^{0.111 \cdot (V+40)}} \\ \alpha_h &= \frac{0.045 \cdot (-0.15) \cdot (V + 75)}{1 - e^{0.15 \cdot (V+75)}} & \beta_h &= \frac{0.12 \cdot 0.2 \cdot (V + 50)}{1 - e^{-0.2 \cdot (V+50)}} \\ \alpha_n &= \frac{0.18 \cdot 0.111 \cdot (V - 20)}{1 - e^{-0.111 \cdot (V-20)}} & \beta_n &= \frac{0.018 \cdot (-0.111) \cdot (V - 20)}{1 - e^{0.111 \cdot (V-20)}}\end{aligned}$$

#### CA5 BY HU ET AL

[Hu et al. \(2009\)](#) performed patch clamp recordings from the axon cut end on layer 5 pyramidal neurons of the rat prefrontal cortex. They distinguish two types of sodium ion channels, the low-threshold  $Na_v1.6$  and high-threshold  $Na_v1.2$  channel. With a detailed study of the distribution of channels, axonal and somatic APs properties are compared.

The equations for the sodium currents are adapted from [Mainen et al. \(1995\)](#) with alterations concerning the half-activation potential  $V_{1/2}$  and the slope factor  $k$ . Their model includes the  $K_v$  and the  $K_m$  current of [Mainen and Sejnowski \(1996\)](#) and also calcium currents for somatodendritic compartments. The initial transmembrane voltage is again  $V(0) = \phi_i(0) - \phi_o(0) = -70$  mV and to the original temperature of



$T = 23^\circ\text{C}$  is adjusted with a  $Q_{10}$  of 2.3 for all  $\alpha$ 's and  $\beta$ 's.

$$\begin{aligned}
\alpha_{m12} &= \frac{0.182 \cdot (V + 28)}{1 - e^{-(V+28)/7}} & \beta_{m12} &= \frac{-0.124 \cdot (V + 28)}{1 - e^{(V+28)/7}} \\
\alpha_{h12} &= \frac{0.024 \cdot (V + 35)}{1 - e^{-(V+35)/5}} & \beta_{h12} &= \frac{-0.0091 \cdot (V + 60)}{1 - e^{(V+60)/5}} \\
\alpha_{m16} &= \frac{0.182 \cdot (V + 41)}{1 - e^{-(V+41)/6}} & \beta_{m16} &= \frac{-0.124 \cdot (V + 41)}{1 - e^{(V+41)/6}} \\
\alpha_{h16} &= \frac{0.024 \cdot (V + 48)}{1 - e^{-(V+48)/5}} & \beta_{h16} &= \frac{-0.0091 \cdot (V + 73)}{1 - e^{(V+73)/5}} \\
h12_\infty &= \frac{1}{1 + e^{(V+57)/6.2}} & h16_\infty &= \frac{1}{1 + e^{(V+70)/6.2}} \\
\alpha_n &= \frac{0.02 \cdot (V - 25)}{-e^{-(V-25)/9}} & \beta_n &= \frac{-0.002 \cdot (V - 25)}{1 - e^{(V-25)/9}}
\end{aligned}$$

#### MOS BY ENGEL

The modeling studies of [Schmidt-Hieber et al. \(2008\)](#) and [Engel and Jonas \(2005\)](#) about mossy fibers are very similar. [Engel and Jonas \(2005\)](#) quantitatively described sodium currents in rat hippocampal mossy fiber buttons for an initial transmembrane voltage  $V(0) = \phi_i(0) - \phi_o(0) = -80$  mV. Although there was no indication on temperature dependency, the standard values were used for the sodium current. Surprisingly [Engel and Jonas \(2005\)](#) used an adaption of the HH potassium current. [Schmidt-Hieber et al. \(2008\)](#) performed simultaneous somatic and axonal whole-cell recordings from granule cells in hippocampal slices of adult mice at  $23^\circ\text{C}$ . For their comparison between axonal and somatic AP properties, they used the equations of [Engel and Jonas \(2005\)](#).

$$\begin{aligned}
\alpha_m &= \frac{-93.8285 \cdot (V - 117.023)}{e^{-\frac{V-117.023}{17.7094}} - 1} & \beta_m &= 0.168396 \cdot e^{-\frac{V-12}{23.2707}} \\
\alpha_h &= 0.000354 \cdot e^{-\frac{V-12}{18.706}} & \beta_h &= \frac{6.62694}{e^{-\frac{V+5.6769}{13.3097}} + 1} \\
\alpha_n &= \frac{0.01 \cdot (V - 50)}{e^{-\frac{V+55}{10}} - 1} & \beta_n &= 0.125 \cdot e^{-\frac{V+55}{80}}
\end{aligned}$$

#### 3.3.1 Comparison of sodium channel gating kinetics

Since the CA5 model of [Hu et al. \(2009\)](#) includes two different sodium channels, seven different sets of equations are compared. Initially the gating kinetic parameters  $\alpha$  and  $\beta$  were studied for the activating variable  $m$  and the inactivating variable  $h$ . Therefore the original equations were examined for changing membrane potential  $E_m$  as can be seen in Fig 3.5.

### 3.3 Ion channels

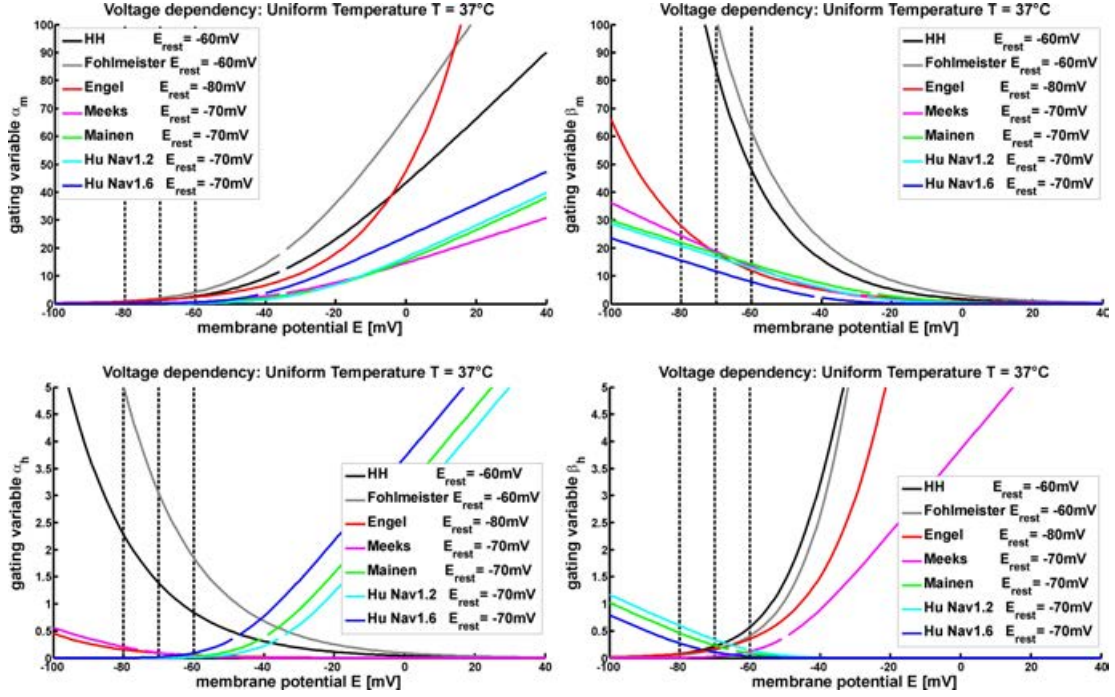


Figure 3.5: The seven different equations for the gating kinetics are plotted for changing membrane potential  $E_m$ . The model temperature  $T = 37^\circ\text{C}$  was used for all models. Values of the opening variable  $m$  are illustrated in the top panels,  $\alpha_m$  at the left,  $\beta_m$  at the right. Corresponding graphs of the inactivation variable  $h$  are plotted at the bottom. The vertical dotted black lines indicate the three different values of resting membrane potential  $E_{rest} = -60, -70 \wedge -80$  mV.

The parameter  $\alpha$  for the activating variable  $m$  describes a change from closed to open state (left top panel in Fig 3.5). The Fohlmeister model is the first to open up the sodium channels since the rise begins first for the gray line. The slope is lowest for the Meeks model. By contrast the Engel model rises faster than the other models, i.e., the red line crosses the black HH model at about  $-5$  mV and even the gray line at about  $E_m = 10$  mV.

However, the critical range for AP initiation starts around  $E_m = -55$  mV to  $E_m = -40$  mV, where the models act quite similar if all equations are temperature corrected. Note that for a lower temperature range the line's appearance certainly changes and the differences among the models increase.

The discrepancies for the parameter  $\beta_m$  are more pronounced, especially within the range of the neuron's resting potentials, the models certainly predict different rates of change from open to closed state. Again the gray Fohlmeister model shows the highest values for low values of membrane potential. This time the  $Na_v1.6$  channel of Hu displays the lowest slope.

Observing the bottom panels of Fig 3.5, the first conspicuousness concerns the

### 3.3 Ion channels

---

different monotony pattern of the lines for the inactivating variable  $h$ . The Mainen model, and therefore also the two sodium channels of the Hu model, are evaluated with a different attempt, where the time constant of  $h$  will be calculated with  $\alpha$  and  $\beta$ , but the steady state  $h_\infty$  is computed with a separate equation. As already mentioned the usual calculation would lead to a rising inactivation curve for increasing membrane potential, which is a result of the set of equations used for  $\alpha_h$  and  $\beta_h$ .

For the other four models, again the Fohlmeister model shows the highest rates, closely followed by the HH model. The  $\alpha_h$  values of the Meeks and the Engel model are almost identical (magenta and red lines), but with certainly lower values compared to the HH and Fohlmeister values. This behavior is still obvious but less pronounced for the variable  $\beta_h$ .

The time constant  $\tau = \frac{1}{\alpha+\beta}$  and the steady state of the two sodium parameters  $m$  and  $h$  are displayed in Fig 3.6. The model temperature was set to 37°C for each of the seven models. Note that the steady state will not change with temperature since the adjustment coefficient appears in the denominator and in the numerator.

The left panels of Fig 3.6 show the evaluated time constants. For both parameters the Fohlmeister and the HH model certainly have lower values than the other models, although their peaks appear at approximately the same membrane potential of about  $E_m \approx -35$  mV for  $\tau_m$  around -60 mV for  $\tau_h$ . The  $Na_v1.6$  channel of Hu shows the earliest and highest peak of  $\tau_m$ , for  $\tau_h$  the red line has the earliest peak, but lacks the steep rising and falling phases.

On the right side of Fig 3.6 the steady state values are plotted, i.e.,  $m_\infty$  on top and  $h_\infty$  at the bottom. The discrepancies seem marginal at first sight, although note that the sigmoidal shape of the red Engel line is less pronounced. The other models have a higher slope factor, where the Mainen and also Hu models are the steepest. The early onset of the low threshold  $Na_v1.6$  is clearly obvious. The HH, Fohlmeister and Meeks model values of  $m_\infty$  are very similar.

For the steady state of  $h$  (bottom right) the Engel and the Mainen model are exactly the same, and also the HH and the  $Na_v1.2$  channel of Hu are very similar. The  $Na_v1.6$  channel values appear for the lowest values of membrane potential  $E_m$ , shortly afterwards follows the steepest magenta Meeks curve. The highest values of membrane potential are needed for the Fohlmeister model.

A very important fact while comparing different sets of equations is the distinction between the notations of membrane potential  $E_m$  and reduced potential  $V_m = E_m - E_{rest}$ . During simulation also the graphs have been studied for the deviation from the resting potential. That means, using  $V_m$  starting from 0 mV as the command potential, i.e., the x-axis will be shifted with the individual resting potentials of the seven different models.

This certainly changes the relation among the model equations since three different values of the resting potential  $E_{rest}$  are reported. The red and green line of the previously discussed parameter  $\tau_h$  correspond to models with different values of  $E_{rest}$ ,

### 3.3 Ion channels

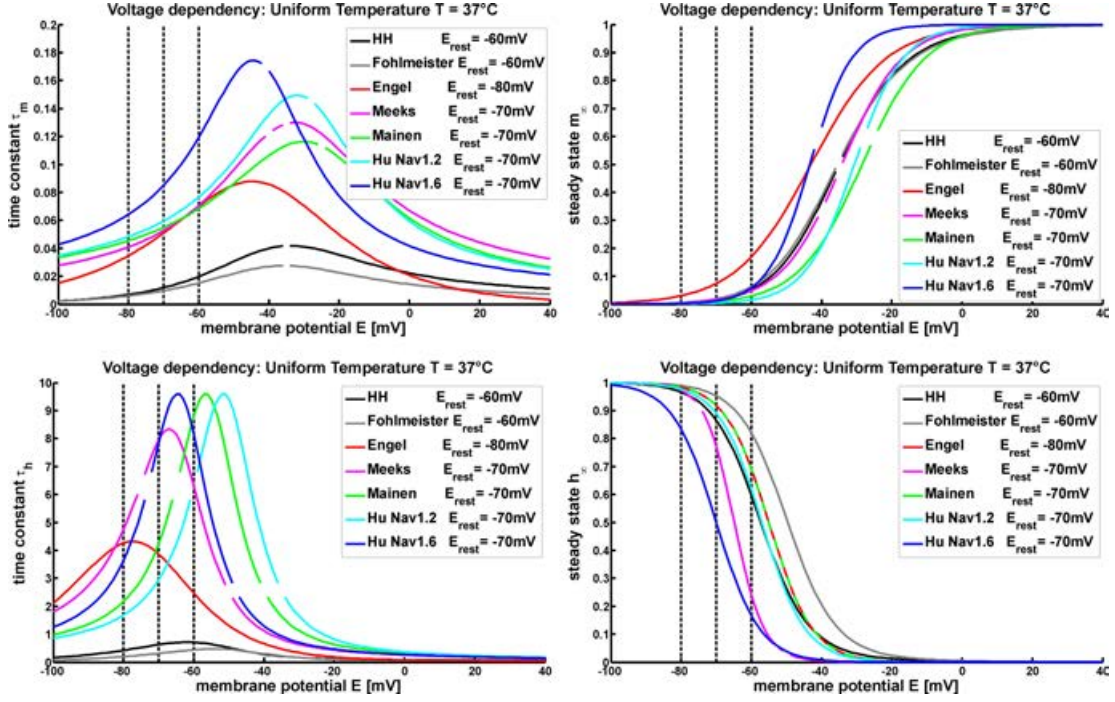


Figure 3.6: The time constants and steady states of the two variables  $m$  and  $h$  are plotted for changing membrane potential  $E_m$ . The model temperature  $T = 37^\circ\text{C}$  was used for all models, although note that the steady state is not affected by the temperature coefficient. The time constants  $\tau_m$  and  $\tau_h$  are plotted at the left, the steady states  $m_\infty$  and  $h_\infty$  are illustrated at the right. The vertical dotted black lines indicate the three different values of resting membrane potential  $E_{rest} = -60, -70 \wedge -80$  mV.

so that if plotted for the deviation from the resting potential, the Engel model needs 10 mV more and therefore the highest values of  $V_m$ . The Fohlmeister model with its low value  $E_{rest} = -60$  mV will appear earlier than the Mainen and  $Na_v1.2$  value. The black HH model will be very similar to the still fastest inactivating model, the blue  $Na_v1.6$  model (data not shown).

#### 3.3.2 Comparison of potassium channels gating kinetics

The same comparisons and evaluations have been performed for the seven different sets of equations for potassium channels. This time the CA5 model of [Mainen and Sejnowski \(1996\)](#) includes two potassium currents, i.e.,  $K_v$  and  $K_m$ . Fig 3.7 summarizes the results for the gating kinetic parameters  $\alpha$  and  $\beta$  of the activating variable  $n$ .

The electrical behavior of the potassium channels differs tremendously even if the model temperature is held on  $T = 37^\circ\text{C}$  for all models. Although for the  $K_m$  current of Mainen it is no surprise that the blue graphs for  $\alpha_n$  and  $\beta_n$  are definitely

### 3.3 Ion channels

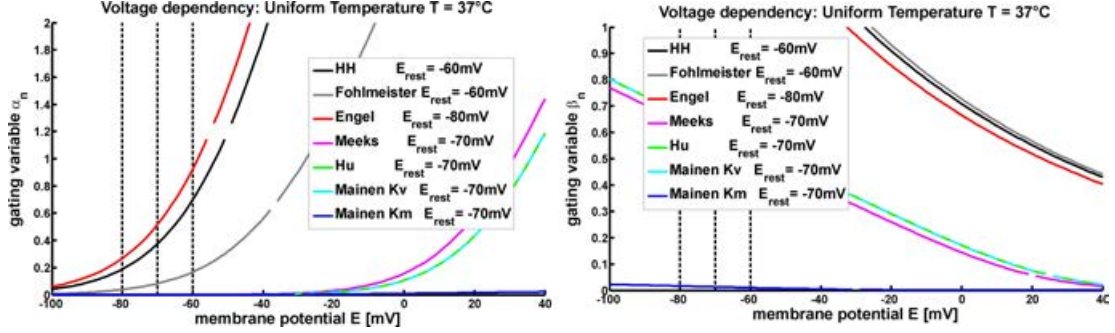


Figure 3.7: The seven different equations for the gating kinetics are plotted for changing membrane potential  $E_m$ . The model temperature  $T = 37^\circ\text{C}$  was used for all models. Values of the gating kinetic parameter  $\alpha_n$  are plotted at the left,  $\beta_n$  at the right. The vertical dotted black lines indicate the three different values of resting membrane potential  $E_{rest} = -60, -70 \wedge -80$  mV.

outsiders. This current is only used at somatodendritic compartments and with a very low density as will be shortly discussed in the next section.

The Hu model uses the unchanged Mainen  $K_v$  channel kinetics, and Meeks only slightly adapted their equations, which is why the cyan and blue lines are identical and the magenta line is very close (Fig 3.7). It is also obvious that Engel made minor changes of the HH potassium current, i.e., the black and red lines appear almost for the same values of membrane potential  $E_m$ .

This observations are valid for both variable of the activation parameter  $n$ . Only the gray Fohlmeister model shows altering relation the the other models for  $\alpha_n$  and  $\beta_n$ . For the rate of change from open to closed state, i.e., on the left side of (Fig 3.7), the onset appears later compared to the HH model. While for  $\beta_n$  the the gray line is almost identical with the black curve.

Summarizing the results, one can observe that the slopes of each current, of course without the exception of  $K_m$ , seem to be comparable, although for  $\alpha_n$  lower values of  $E_m$  are needed for the HH, Fohlmeister, Engel group, while for  $\beta_n$  exactly the opposite behavior holds.

The time constant  $\tau_n$  and the steady state  $n_\infty$  of the activating potassium parameter are displayed in Fig 3.8. The model temperature was set to  $37^\circ\text{C}$  for each of the seven models and again the great discrepancies among the potassium gating kinetics of the equations are obvious.

The time constant of the  $K_m$  channel displayed outstanding high values, so that an own y-axis was used for the  $\tau_h$  plot, i.e., the blue axis on the right side of Fig 3.8 only corresponds to the blue  $K_m$  channel of Mainen. The other channels reach values of less than 4, where the higher magenta Meeks and the Mainen  $K_v$  channel are very similar and the lower values appear for the HH, Engel and Fohlmeister potassium



### 3.4 Action potential modeling

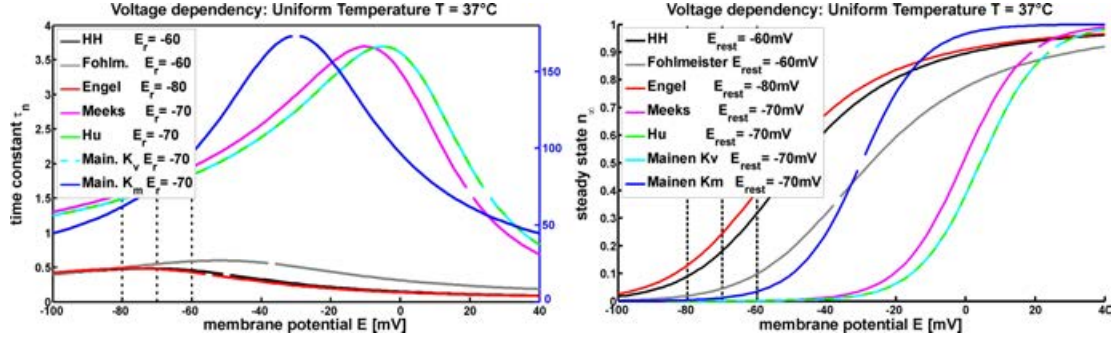


Figure 3.8: The time constant and steady state of the variable  $n$  are plotted for changing membrane potential  $E_m$ . The model temperature  $T = 37^\circ\text{C}$  was used for all models, although note that the steady state is not affected by the temperature coefficient. The time constant  $\tau_n$  are plotted at the left, the steady states  $n_\infty$  is illustrated at the right. The vertical dotted black lines indicate the three different values of resting membrane potential  $E_{rest} = -60, -70 \wedge -80$  mV.

current. Also the membrane potential  $E_m$  at which the maximum appears is different for the two groups of channels. Although these peaks are less pronounced for the black, gray and red line, they appear earlier than those of the other models.

The right side of Fig 3.8 shows the steady state of the activation variable  $n$  of the potassium channels. Again a certain difference can be observed for the different groups of models, i.e., the HH, Fohlmeister and Engel group have a lower slope factor. Although the Meeks and the Mainen  $K_v$  channels rise faster, they need higher values of  $E_m$  with a shift of 60 mV compared to the HH and Engel model. The gray Fohlmeister model is the middle model concerning the needed membrane potential  $E_m$  for channel activation onset. The blue  $K_m$  channel acts for similar values, but shows a higher slope factor comparable with those of the Meeks and  $K_v$  group.

Still it should be noted, that the potassium channels not only display great differences in their sets of equations, the potassium current  $I_K$  is also evaluated differently for two groups of models. The HH, Fohlmeister and Engel models evaluate the potassium currents via  $I_K = n^4 \cdot (E_m - E_K)$ , while the others use  $I_K = n \cdot (E_m - E_K)$ . Thus, resulting discrepancies of ionic currents and their influence on the AP properties are discussed in the next section.

### 3.4 Action potential modeling

Summing up the previously mentioned model approaches the AP of a patch of membrane will be simulated. Thus a system of differential equations has to be solved. In order to evaluate the transmembrane potential  $V_m$  and the parameters  $m$ ,  $h$  and  $n$ , initial values are needed to derive the unique solution of the subsequently presented system of differential equations. Note that actually only the parameters  $V_{Na}$ ,

### 3.4 Action potential modeling

---

$V_K$ ,  $V_L$ ,  $G_L$  and  $C_{mem}$  are constant within the equations. Beside the transmembrane potential  $V_m$  also the injected stimulus current  $I_{stim}$  are functions of time  $t$ . The gating variables  $m$ ,  $h$  and  $n$  are voltage-dependent, and thus actually functions of  $t$  and  $V_m$ , i.e.,  $m(V_m(t))$ . Recall that the sodium conductance is calculated via  $G_{Na} = G_{Na,max} \cdot m^3 \cdot h$  for all models, the potassium conductance follows as either  $G_K = G_{K,max} \cdot n^4$  or  $G_K = G_{K,max} \cdot n$ , with constant values of  $G_{Na,max}$  and  $G_{K,max}$ .

$$\begin{aligned}\frac{dV_m}{dt} &= \frac{-I_{stim} - G_{Na} \cdot (V_m - V_{Na}) - G_K \cdot (V_m - V_K) - G_L \cdot (V_m - V_L)}{C_{mem}} \\ \frac{dm}{dt} &= \frac{m_\infty - m}{\tau_m} \\ \frac{dh}{dt} &= \frac{h_\infty - h}{\tau_h} \\ \frac{dn}{dt} &= \frac{n_\infty - n}{\tau_n}\end{aligned}$$

Not only the used set of equations for the gating kinetics is crucial, several other parameters determine the neuron's active spiking behavior. Starting from the adjusted model of HH, i.e., using the temperature coefficient for  $T = 37^\circ\text{C}$ , recursive testing revealed the individual values of parameters for each of the other five models which fit best with the HH model.

The membrane capacitance is very often assumed to be  $1 \mu\text{F}/\text{cm}^2$ , although it should be stated that this value was reduced to  $0.75 \mu\text{F}/\text{cm}^2$  in [Meeks and Mennerick \(2007\)](#) and [Mainen and Sejnowski \(1996\)](#). In order to produce comparable results this value was set to the standard value of the HH model, i.e.,  $C_{mem} = 1 \mu\text{F}/\text{cm}^2$ .

Stronger discrepancies appear among the six models for the value of the leakage conductance  $G_L$ . The highest value of  $0.3 \text{ mS}/\text{cm}^2$  is used by the HH model which will also be held constant for the subsequent simulations of matching APs. Still the Fohlmeister model originally considers a value of  $0.1 \text{ mS}/\text{cm}^2$  which is also partly predicted by the Engel models unless they use a value of  $0.03 \text{ mS}/\text{cm}^2$  which is also common for the Meeks and the Hu model. The lowest value of  $0.01 \text{ mS}/\text{cm}^2$  occurs for the Meeks model.

Of course the conductance values of  $g_{Na}$ ,  $g_K$  and  $g_L$  are of main importance. For compartment models, their distribution commonly varies along the neuron, so that the magnitude and composition of ion channels, and therefore also ion flow, certainly differ. Usually the somatodendritic compartments possess lower conductance values than those of the axon, especially the nodes of Ranvier which are hot spots for  $Na$  channels. If modeling studies include  $Ca$  currents, they are also regularly restricted to somatodendritic compartments.

Also the reversal potentials of  $Na$  and  $K$  vary within publications. If the values of  $V_{Na}$  or  $V_K$  are altered, also the corresponding ionic current will change. Especially the HH model, developed for the cold squid axon, uses an atypical value for the reversal potential of potassium, i.e.,  $V_K = -72 \text{ mV}$ . Table 3.1 gives an overview of original values for those potentials.

### 3.4 Action potential modeling

The parameter  $V_L$  decides the resting state of the transmembrane potential  $V_m$ , i.e., if no stimulus current is present or the neuron repolarizes after an AP, the value of  $V_m$  adjusts to  $V_L$ . That is an important fact to understand when one wants to comprehend the obtained results. When HH developed their model they evaluated a value of  $V_L = 10.6$  mV which is not randomly chosen but calculated. As mentioned before, one has to state initial conditions to solve the differential equations. With a fixed value for  $V_m(0) = V_0$  the initial values of  $m$ ,  $h$  and  $n$  can be computed, via  $p_0 = p_\infty(V = V_0)$ . Furthermore these values enable the calculation of the initial current flow of  $Na$  and  $K$ . With these assumptions and the condition that the temporal change of transmembrane potential at the beginning equals zero, i.e.,  $\frac{dV_m(0)}{dt} = 0$  the leakage potential can be evaluated with the following equation.

$$E_L = \frac{-I_{Na}(V_0) - I_K(V_0)}{G_L} + V_0$$

With this equation and the use of  $V_0 = -60$  mV for the HH model and standard values of the conductances, i.e.,  $g_{Na} = 120$  mS/cm<sup>2</sup> and  $g_K = 36$  mS/cm<sup>2</sup>, the leakage potential results as  $E_L = 10.5989$  mV or  $V_L = -49.4011$  mV. If the starting value of the membrane potential is changed to  $V_0 = -70$  mV, it follows  $E_L = -69.9$  mV (see Tab. 3.1).

		HH	Fohlm.	Engel	Meeks	Hu	Mainen
$g_{Na}$	[mS/cm <sup>2</sup> ]	120	80	90	120	90	100
$g_K$	[mS/cm <sup>2</sup> ]	36	50	20	80	40	60
$g_L$	[mS/cm <sup>2</sup> ]	0.3	0.3	0.3	0.3	0.3	0.3
$E_{Na}$	[mV]	55	54.96	60	60	60	50
$E_K$	[mV]	-72	-91.9	-85	-80	-80	-80
$E_L$	[mV]	-69.90	-70.22	-80.88	-67.71	-69.34	-68.99

Table 3.1: Listing of the conductance values of  $g_{Na}$  and  $g_K$  for axon models used to produce matching APs for a common leakage conductance of  $g_L = 0.3$  mS/cm<sup>2</sup>. Note that the sodium channel of Hu corresponds to the  $Na_v1.6$  channel and the potassium channel of Mainen to the  $K_v$  channel. The resulting leakage potentials  $E_L$  are also presented.

In order to produce best matching APs according to their  $AP_{height}$  and temporal spike parameters like the  $AP_{width}$ , the conductance values of  $Na$  and  $K$  have been altered. The leakage conductance, the initial value of transmembrane potential  $V_0 = -70$  mV as well as a temperature of  $T = 37^\circ\text{C}$  are fixed for all models. With the use of the original values of reversal potentials, the individual leakage potentials are calculated. The deviation from the initial value  $V_0$  is highest for the Engel model which occurs due to their prediction of  $E_{rest} = -80$  mV.

Suprathreshold current injection leads to the initiation of an AP on the patch of membrane. The properties of this AP differ for varying stimulus amplitude and



### 3.4 Action potential modeling

duration. Initially the threshold current of the temperature adjusted HH model were evaluated for stimulus duration ranging from  $IC_{dur} = 0.01 \dots 10$  ms. With this wide range of threshold values for the current amplitude, also the chronaxy can be evaluated which will be present subsequently.

However, as a starting point for fitting the conductance values of the other five models, a stimulus with  $IC_{dur} = 0.05$  ms was chosen with an amplitude of  $IC_{amp} = 800 \mu\text{A}/\text{cm}^2$  which is about twice the threshold value of  $349 \mu\text{A}/\text{cm}^2$  for this pulse duration. The best fitting conductance values which appeared during testing are summarized in Tab. 3.1, the APs are plotted in Fig. 3.9. The spike of the temperature adjusted HH model, i.e. the red curve, is very short with an  $AP_{height}$  of 108.4 mV appearing 0.157 ms after stimulus onset. Due to the lack of hyperpolarization, the  $AP_{amp}$  has about the same magnitude, and both values for the half-duration are computed to be about 0.19 ms.

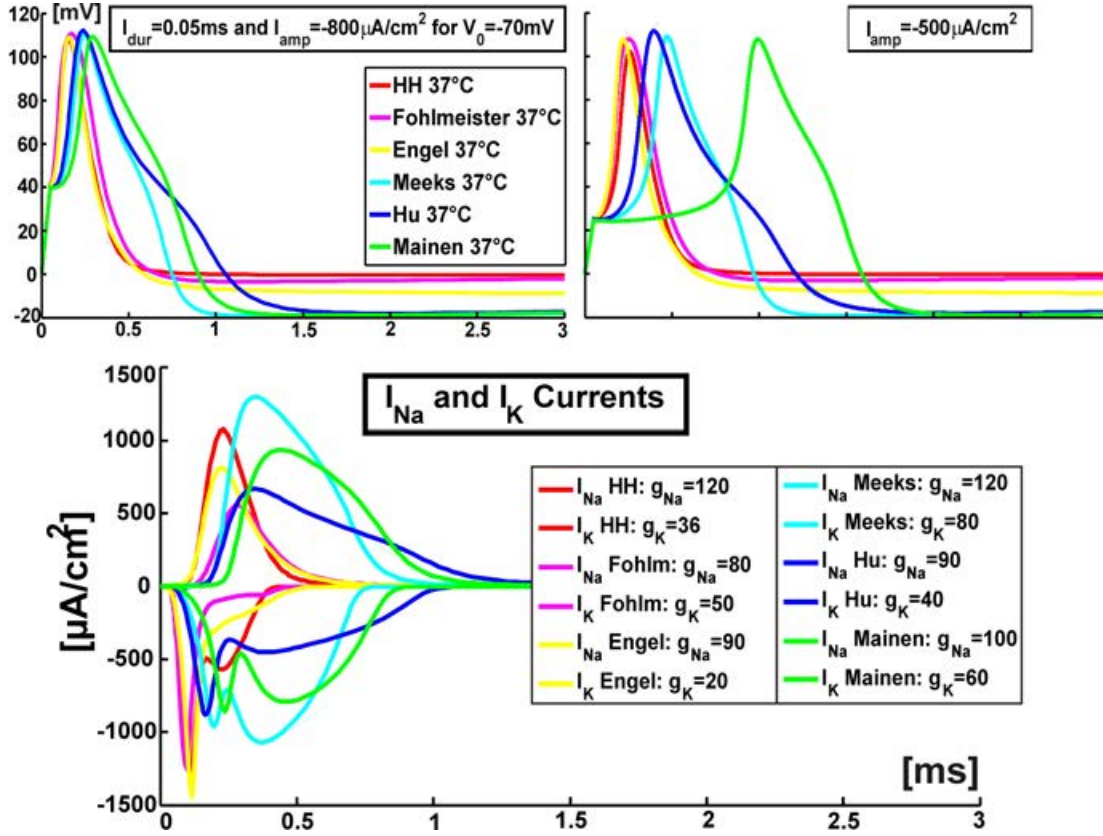


Figure 3.9: The upper panels represent the temporal change of transmembrane potential of the six different models. Conductance values of  $Na$  and  $K$  where fitted for an impulse amplitude with twice the threshold value of the HH model. Thus the congruence decreases for stimuli of different magnitude (right upper panel). The corresponding ionic currents for the matching case are shown at the bottom.

Furthermore it should be noted that the reported onset of the AP appears very

early, i.e., the patch of membrane initiates the spike without almost any delay. This behavior is very difficult to replicate with at least some of the other models. Not only the gating variables suggest that the six models can be divided into two groups, also the following experiments further strengthen this classification.

The magenta Fohlmeister curve and the yellow Engel curve in the left upper panel of Fig. 3.9 are very good matches to the red HH line, since they are almost congruent, at least during the AP. Note that because individual values of  $E_L$  are computed for the different models the transmembrane voltages level up at their leakage potentials which can be found in Tab. 3.1 after the AP is over. The Fohlmeister model is an adjustment of the HH model which is also derived for a resting potential  $E_{rest} = -60$  mV and a quite similar value of  $E_{Na} = 54.96$  mV. Conspicuously the reversal potential of potassium is certainly changed from the HH value of -72 mV to  $E_K = -91.9$  mV which is the highest presumed value for this parameter among all six models. During testing conductance values of  $g_{Na} = 80$  mS/cm<sup>2</sup> and  $g_K = 50$  mS/cm<sup>2</sup> resulted in a very good fit compared to the HH model for an 0.05 ms long intracellular current stimulation with an amplitude of 800  $\mu$ A/cm<sup>2</sup>. Probably even a more congruent curve would have been possible for uneven values of the conductances, but the  $AP_{height}$  of 110.6 mV appearing at  $t = 0.171$  ms offers enough conformity. Although it should be stated that the corresponding half-duration of about 0.24 to 0.25 ms is slightly longer than that of the HH model, but still short enough to simulate spikes of human cochlear neurons.

Observing the values of the individual leakage potentials in Tab. 3.1 it is obvious that the highest value, i.e.,  $E_L = -80.88$  mV, occurs for the Engel model which is close to the presumed resting potential  $E_{rest} = -80$  mV. The sodium reversal potential is  $E_{Na} = 60$  mV which is a very common value in recent modeling studies. For the potassium current they only adapted the HH channel by shifting the equations for the gating variables and also the reversal potential to  $E_K = -85$  mV. The conductance value of  $g_{Na} = 90$  mS/cm<sup>2</sup> is well within the range of the other models, but only  $g_{Na} = 20$  mS/cm<sup>2</sup> is needed to produce the best matching spike. The AP properties are surprisingly similar to those of the HH model, i.e., the  $AP_{amp}$  of 109.1 mV is not even 1mV apart and appearing at exactly the same time as the HH model, namely 0.157 ms after stimulus onset. Both half-durations are only slightly smaller than the corresponding values of the HH model (compare Tab. 3.2), showing the shortest  $AP_{width}$ 's of about 0.17 to 0.18 ms. Only the  $AP_{height}$  which sums up to 117.9 mV is certainly higher, because the transmembrane potential hyperpolarizes after the spike and levels up at leakage potential. This is not the only difference in the spiking behavior of the modeled patch of membrane which comes along with this discrepancy.

The spikes appearance is obviously altered for the cyan Meeks, the blue Hu and the green Mainen model which could not be forced to initiate the spike earlier. Furthermore the duration of the spikes are certainly longer which as well could not be prevented with only changing the conductance values without further modification of the model equations and parameters. These are the models which constitute the

### 3.4 Action potential modeling

---

second group, because their  $K$  conductance is modeled as  $\tilde{G}_K \approx G_{K,max} \cdot n$ , contrary to the previously mentioned models for which  $\tilde{G}_K \approx G_{K,max} \cdot n^4$  is valid. Additionally, the six different transmembrane potentials are only plotted for a duration of 3 ms which is why the cyan, blue and green line are still below their initial value, i.e., the corresponding transmembrane potentials are still hyperpolarized. In contrast to the group of the first three models (displayed in red, magenta and yellow) which level up to their resting state quite fast, the Meeks, Hu and Mainen models need about 15 ms to fully accommodate at their values of  $V_L$ .

All three leakage potentials  $E_L$  are within an acceptable range, although all three are slightly lower than the value of the HH model. The lowest computed value of  $E_L = -67.61$  mV originates from the Meeks model. The value of the sodium reversal potential equals the generally reported 60 mV, except the Mainen model which uses 50 mV. Still the potassium reversal potential of  $E_K = -80$  mV is common for all three models. All the sodium conductance values are comparable to the other three models. The highest and identical HH value of  $g_{Na} = 120$  mS/cm<sup>2</sup> obeys the Meeks model which also has the highest potassium conductance of  $g_K = 80$  mS/cm<sup>2</sup>. The Hu and the Mainen model have lower values which are similar to the first three models. Further increasing the potassium conductances for the Hu and Mainen models only slightly changes the half-duration values and do not support earlier repolarization, but it undesirably reduces the  $AP_{height}$ . Furthermore it should be noted that for the Hu model no  $Na_v1.2$  current was inserted, since the AP will appear even later according to the higher threshold. Additionally, when the same value of  $Na_v1.2$  is used instead of  $Na_v1.6$  the  $AP_{height}$  increases. For the Mainen model the  $K_m$  current was also omitted, since for almost matching spikes the inclusion of this ion channel will only shift the AP to the right, but lacks any positive effect on the AP properties, i.e., the appearance of the graph of the transmembrane potential will not change.

The values of  $AP_{amp}$  still represent a good match to the HH model, but again higher values of  $AP_{height}$  can be observed due to hyperpolarization. Additionally, the onset of the spikes are delayed, i.e., the peak of transmembrane potential of the Meeks and Hu model appears at about 0.24 ms, but the highest value occurs for the Mainen model which is twice the value of the HH model. The striking difference is the larger magnitude of the half-durations which could not be reduced with altering channel densities. The lowest half-duration value of these three models occurs for the Meeks model of about 0.28 ms which is still in the desirable range of a quarter millisecond. Again the Mainen model with a value of 0.37 ms represents the longest spike duration. When computed with the  $AP_{height}$  even values up to 0.46 ms are possible.

The upper right panel shows the effect of changing the pulse amplitude to 500  $\mu$ A/cm<sup>2</sup> which is only slightly higher than the lowest of the six individual threshold values. Interestingly the red HH, the magenta Fohlmeister and the yellow Engel curves stay comparable. The other three models certainly show a larger delay in the AP onset, where the latest spike to appear is the green Mainen model with the highest

### 3.4 Action potential modeling

threshold value for this pulse duration. This time the blue Hu model spike with its lower threshold appears shortly before the cyan Meeks model which for short stimuli has almost the same threshold values as the HH model.

		$IC_{amp} = 800 \text{ } \mu\text{A}/\text{cm}^2 \text{ } IC_{dur} = 0.05 \text{ ms}$					
		HH	Fohlm.	Engel	Meeks	Hu	Mainen
$V_m^{max}$	[mV]	108.4	114.1	117.9	129.9	130.1	128.2
	[mV]	108.2	110.6	109.1	110.6	112.1	109.3
$t(V_m^{max})$	[ms]	0.1568	0.1714	0.1571	0.2464	0.2393	0.2966
$AP_{width}$	[ms]	0.1969	0.2445	0.1860	0.3510	0.3922	0.4553
	[ms]	0.1965	0.2393	0.1721	0.2764	0.3165	0.3675
$I_{Na}^{min}$	$[\frac{\mu\text{A}}{\text{cm}^2}]$	-1296	-1239	-1430	-1071	-881.7	-855.4
$t(I_{Na}^{min})$	[ms]	0.1103	0.0941	0.1163	0.3720	0.1680	0.2400
$I_K^{max}$	$[\frac{\mu\text{A}}{\text{cm}^2}]$	1073	557.6	813.4	1294	669.1	936.3
$t(I_K^{max})$	[ms]	0.2288	0.2843	0.2246	0.3484	0.3491	0.4440
		$IC_{amp} = 500 \text{ } \mu\text{A}/\text{cm}^2 \text{ } IC_{dur} = 0.05 \text{ ms}$					
		HH	Fohlm.	Engel	Meeks	Hu	Mainen
$V_m^{max}$	[mV]	102.3	110.9	116.8	128.4	129.6	126.6
	[mV]	102.1	107.8	107.9	109.2	111.6	107.8
$t(V_m^{max})$	[ms]	0.2576	0.2550	0.2198	0.4718	0.3960	0.9919
$AP_{width}$	[ms]	0.1984	0.2468	0.1841	0.3488	0.3904	0.4511
	[ms]	0.1976	0.2415	0.1702	0.2745	0.3157	0.3634
$I_{Na}^{min}$	$[\frac{\mu\text{A}}{\text{cm}^2}]$	-1161	-1144	-1440	-995.1	-875.5	-800.4
$t(I_{Na}^{min})$	[ms]	0.2107	0.1766	0.1792	0.5966	0.3225	0.9326
$I_K^{max}$	$[\frac{\mu\text{A}}{\text{cm}^2}]$	1011	533.2	821.4	1223	655.4	875.9
$t(I_K^{max})$	[ms]	0.3229	0.3664	0.2854	0.5704	0.5051	1.1314

Table 3.2: Listing of the AP properties of all six models for two different stimulus amplitudes. The two rows for the parameter  $V_m^{max}$  correspond to the  $AP_{height}$  in the top row and the values for the  $AP_{amp}$  are listed in the second row. The same pattern is valid for the  $AP_{width}$  which is calculated for both parameters.

The corresponding values of the AP properties for the six models and reduced stimulus intensity of  $500 \text{ } \mu\text{A}/\text{cm}^2$  are displayed in the bottom part of Tab. 3.2.

Deeper insight into the individual spiking behavior offers the lower part of Fig. 3.9 which displays both ionic currents, i.e., negative inward  $I_{Na}$  and positive outward  $I_K$ , for the six different models. Again the temporal properties as well as the magnitude of the currents can be studied and compared. There are only two models which lack a second rising phase of the sodium current, namely the magenta Fohlmeister and the yellow Engel model. Observing the negative red HH  $I_{Na}$ , a second peak occurs which has to compensate the large  $K$  current with the earliest peak. The same behavior

### 3.4 Action potential modeling

---

occurs for the Meeks, Hu and Mainen models, where the second peak of the cyan  $Na$  current of Meeks is even higher than the first one.

The maximum of the potassium currents and the minimum of the sodium currents are also presented in Tab. 3.2, corresponding temporal values are displayed in the row below. For the stimulation with  $IC_{amp} = 800 \mu A/cm^2$ , the highest peak of  $Na$  current with a magnitude of  $1430 \mu A/cm^2$  occurs for the Engel model at  $t = 0.12$  ms almost at the same time as the peak of the HH model. Generally the peaks of  $I_{Na}$  are lower for the Meeks, Hu and Mainen models, i.e., lower than  $1000 \mu A/cm^2$ . The slightly higher value and the corresponding highest values of peak time are expected for the cyan Meeks curve, because this Model has to compensate the largest potassium current, i.e.  $I_K^{max} = 1294 \mu A/cm^2$  even greater than  $I_{Na}^{min} = -1071 \mu A/cm^2$ . This second higher peak is also the reason why the Meeks model is the only one where the peak of potassium occurs before that of sodium.

The potassium currents certainly differ and the great discrepancies between the two groups is obvious. For the Meeks, Hu and Mainen model the peak of the potassium current appears a bit later than those of the HH, Fohlmeister and Engel model. But especially the duration is highly increased which causes the larger amount of total ionic current. Furthermore it is interesting to compare the proportion between the peak of the  $Na$  current and the generally lower peak of the  $K$  current. Beside the mentioned Meeks exception, also the Mainen model has a 10% lower peak of  $I_{Na}$  compared to that of  $I_K$ . For the other models the minimum of  $Na$  exceeds the maximum of  $K$  with the highest disparity for the Engel model, i.e., 222% increase. The next one with 176% is the Fohlmeister model followed by the quite similar 132% of the Hu and 121% for the HH model.

Also the gap between the corresponding peak times can be compared, but the overall behavior stays the same for all models. The widest gap, i.e., the longest duration between the peaks of  $Na$  and  $K$  currents appear for the Engel model and the shortest 'inter-peak' duration occurs for the Mainen model. The bottom part of Tab. 3.2 also lists the reported values for a stimulation with an amplitude of  $500 \mu A/cm^2$ . Interestingly the ratio between current peak amplitudes stays the same, although the gap between the corresponding time values reduces.

During the test runs for matching APs to the adjusted HH model, also the threshold values for different pulse durations ranging from  $IC_{dur} = 0.01 \dots 10$  ms were calculated. The chronaxy and the rheobase have been evaluated for all models by computing threshold values for different pulse duration and subsequent interpolation.

The strength duration curves for all six models are presented in Fig. 3.10. For the HH model the highest rheobase can be observed which is between 16 and 17  $\mu A/cm^2$ . At first sight it is difficult to spot the threshold, since, contrary to the all-or-nothing principle, the  $AP_{height}$  of the HH model continuously reduces to very low values without changing the spikes shape, i.e., the curve of the transmembrane

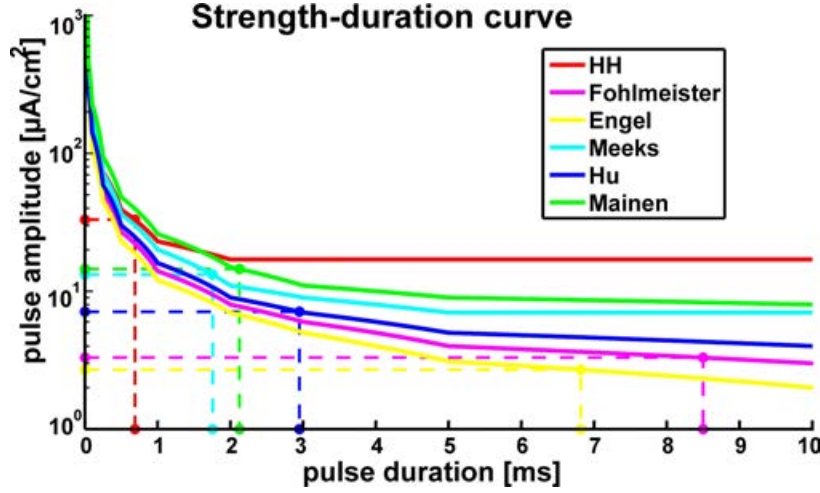


Figure 3.10: The threshold values of stimulus amplitude are plotted against stimulus duration. Note the logarithmic scale of the y-axis and the restriction of the x-axis to  $[0 \dots 10]$  for better visualization. The dotted lines indicate the chronaxy values on the x-axis and twice the rheobase on the y-axis.

potential rather shrinks down than showing altering subthreshold behavior. Still, the threshold can be easily realized when observing the ionic currents. While comparing the excitation profiles for threshold stimulation and stimulation with an impulse that is only  $1 \mu\text{A}/\text{cm}^2$  less than threshold, the transmembrane potential is only doubled while the ionic currents undergo a 10-fold increase. Another peculiarity can be observed while looking for the threshold, especially for long impulse duration. Very often several spikes are initiated when the threshold is reached, where the proceeding spikes are higher than the first. Depending on model, the delay of the first spike and the interspike-interval differ.

The previous simulations indicated some discrepancies in the model equations of the Engel model, i.e., most striking  $E_{rest} = -80 \text{ mV}$  highly influences the spiking behavior. Since the Engel model as it was used before displayed such small threshold values irrespective of the pulse duration, the model had to be slightly adapted for the strength-duration tests. Therefore the equations of the gating variable  $\alpha$  and  $\beta$  of each parameter, namely  $m$ ,  $h$  and  $n$  were adapted, according to a  $10 \text{ mV}$  shift. The models rheobase value is still the smallest and was calculated to be  $1.35 \mu\text{A}/\text{cm}^2$ . If this value is doubled, i.e.,  $IC_{amp} = 2.7 \mu\text{A}/\text{cm}^2$  a stimulus duration of  $6.82 \text{ ms}$  is needed to initiate a spike at a patch of membrane modeled with the adapted Engel equations. Thus the chronaxy of the  $6.82 \text{ ms}$ , which is indicated as yellow circle at the x-axis, corresponds to a pulse amplitude of  $2.7 \mu\text{A}/\text{cm}^2$ , yellow dot on the y-axis (Fig. 3.10). Obviously, although the Engel model has the smallest value of rheobase, the chronaxy is the second highest after the Fohlmeister model.

The rheobase of the Fohlmeister model is  $1.65 \mu\text{A}/\text{cm}^2$  which is the second smallest value closely after the Engel model. The doubled value, magenta dot on y-axis, leads to

### 3.4 Action potential modeling

---

a chronaxy of 8.5 ms which is the longest chronaxy among the six models and therefore also is the last circle at the x-axis. The blue Hu model has the third smallest rheobase and the third longest chronaxy value, i.e., the Hu model needs a very long pulse with  $IC_{amp} = 3.55 \mu\text{A}/\text{cm}^2$  to initiate a spike and for a pulse with twice the amplitude  $IC_{dur} = 2.95 \text{ ms}$  has to hold in order to generate an AP. The cyan Meeks and the green Mainen model have quite similar strength-duration curves. The rheobase of the Meeks model is  $6.6 \mu\text{A}/\text{cm}^2$  which is a bit smaller than the rheobase of the Mainen model  $7.25 \mu\text{A}/\text{cm}^2$ . The corresponding chronaxy values are 1.76 ms for the Meeks and 2.13 ms for the Mainen model. As mentioned before, the HH model shows the highest rheobase which is between 16 and 17  $\mu\text{A}/\text{cm}^2$ . For the calculation of the chronaxy  $IC_{amp} = 33 \mu\text{A}/\text{cm}^2$  was assumed resulting in the smallest chronaxy of 0.69 ms.

Still it should be noted that the values of rheobase and chronaxy not only differ between different models, also for studying a single set of equations for the gating variable the behavior can change significantly. The strength-duration calculations strongly depend on the assumed parameter values, i.e., if the conductance values or the reversal potentials are altered, also the rheobase and chronaxy values change.



# Chapter 4

## Models of human cochlear neurons

The presented modeling techniques of the previous chapter shall now be applied to human cochlear neurons. It will be described which of the detailed morphological and anatomical data (chapter 2) is needed to fully describe a traveling AP along an afferent cochlear neuron. Special interest will be paid to the human peculiarities, i.e., the almost unmyelinated soma region as well as the clustering of cochlear neurons.

The natural spiking behavior which means that a nerve impulse conducts a spike from the dendritic ending, over the soma region, to the axonal end, can be simulated with intracellular current injection into the first compartment. Still, the excitation profile of different cochlear neurons certainly varies and depends on distinct assumptions of model parameter. Therefore at first, Sec. 4.1 addresses the single neuron response of afferent cochlear neurons followed by current injection and enlightens the influence of changing geometrical and electrical properties. More precisely, in Sec. 4.1.1 the soma region and local spike properties are examined. The overall conduction properties of the whole neuron is certainly altered by specific parameters for the dendrite and the axon which will be discussed in Sec. 4.1.2. Results for varying electric properties of the model neuron are discussed in Sec. 4.1.3, where again different representations of the ion channels will be compared.

Furthermore in order to comprehend with new morphological findings on the clustering of cochlear neurons, a new approach for modeling the ephaptic coupling of spiral ganglion cells is presented in Sec. 4.2. An extended electrical circuit will be deduced to derive adapted differential equations for the corresponding transmembrane potentials. With the inclusion of restricted current flow from one soma region to another, the possible interactions between these two neurons sharing a common myelin layer will be discussed.

### 4.1 Afferent single neuron model

There are many ways to simulate the response of a cochlear neuron to acoustical as well as to electrical stimulation. Thus a variety of different models is found within

literature which are developed for various reasons and altering applications.

Some groups work with complete composite models of the middle ear, the basilar membrane, the IHC and the auditory nerve. Just one example can be found in [Sumner et al. \(2002\)](#) where a revised computational model of the inner-hair cell auditory-nerve complex is able to reproduce quantitatively phase-locking characteristics, relative refractory effects, mean-to-variance ratio, and first- and second-order discharge history effects.

There also exist dynamical point-process models in order to simulate the response of an auditory neuron. The model of [Trevino et al. \(2010\)](#) uses the intensity function to speech input which gives an accurate representation of the spiking pattern at the auditory nerve in response to a complex speech sound.

Other modelers follow a stochastic approach like [Bruce et al. \(1999\)](#) who presented a simple and computationally efficient stochastic model of single-fiber response to single biphasic electrical pulses, based on a deterministic threshold model of action potential generation. Even more, others use integrate-and fire models of auditory nerve fibers, characterized by its computation ease and efficiency, e.g., [Chen and Zhang \(2007\)](#) propose a new computation-efficient auditory nerve model, which can be also utilized to investigate its response to the high-rate electrical stimulation.

In order to approximate physiological properties measured in the auditory nerve such as spike latency, jitter, chronaxie, relative refractory period and conduction velocity, [Imenkov and Rubinstein \(2009\)](#) used a Markov process to simulate the stochastic nature of the sodium and potassium channels, while gating parameters governing the opening and closing kinetics were chosen based on values obtained from biophysical literature.

Despite of single fiber simulation, [Lütkenhöner \(2008\)](#) focuses on the response of a population of auditory nerve fibers by using the approach of [Sachs and Abbas \(1974\)](#) with some further modifications. Based on assumptions about the rate-intensity functions of single auditory-nerve fibers and the pattern of cochlear excitation caused by a tone, a model for the gross response of the population of auditory nerve fibers was developed.

Another tool for creating population responses is presented in [Zhang et al. \(2001\)](#) who use their model to study the roles of nonlinearities in the encoding of simple and complex sounds. The implementation of this model represents a relatively simple phenomenological description of a single mechanism that underlies several important nonlinear response properties of auditory nerve fibers.

This model approach has often been used and extended, like e.g. by [Heinz et al. \(2001\)](#) who include an implementation of three auditory nerve fibers groups concerning their spontaneous-rate. Their model has a modified description of frequency resolution as a function of characteristic frequency that is derived from estimates of human rather than cat tuning.

However, within this thesis a more detailed representation of the cochlear neuron itself is required, since the effect of special human properties shall be clarified. Thus

#### 4.1 Afferent single neuron model

the main goal was to better understand the activity pattern of the SGCs and to offer more insights in the fundamentals underlying the neural response.

In order to simulate the response of single SGCs to microstimulation, most modelers consider the soma to be myelinated (Frijns et al. 1994) or passive (Woo et al. 2009b), while others have completely neglected the presence of a soma (Mino et al. 2004). Since the effect of varying soma size will be examined, the model of Rattay et al. (2001) was adapted for the following computer simulations, because apart from Smit et al. (2009a, 2008) who only changed the peripheral process, it is the only model which accounts for this human specialty.

As already mentioned an impulse detected by the hair cells will activate the inner-activating afferent cochlear neuron in order to transmit a spike to the brain. There exist a wide variety of geometrical and electrical properties of these afferent neurons which makes it difficult to suggest a simple classification (see chapter 2). Concerning their innervation pattern, a vast majority of 90 - 95% innervate the IHCs which are categorized as 'large' type I cells while only 5 - 10% which are connected to OHCs are assigned to 'small' type II SGCs. Especially the two prominent human peculiarities are believed to essentially effect the excitation pattern of SGCs (see chapter 1).

The subsequent sections will step-by-step comprehend with the variation of SGCs, since the excitation profile of a cochlear neuron certainly changes when the relevant parameters are varied, e.g., alterations of the soma size or its degree of myelinization leads to a delay of information processing or even to AP propagation failure in extreme cases. The specific differences are examined for changes in geometrical parameters as well as electrical parameters. By systematically testing relevant parameter ranges the alterations of excitation profiles are analyzed.

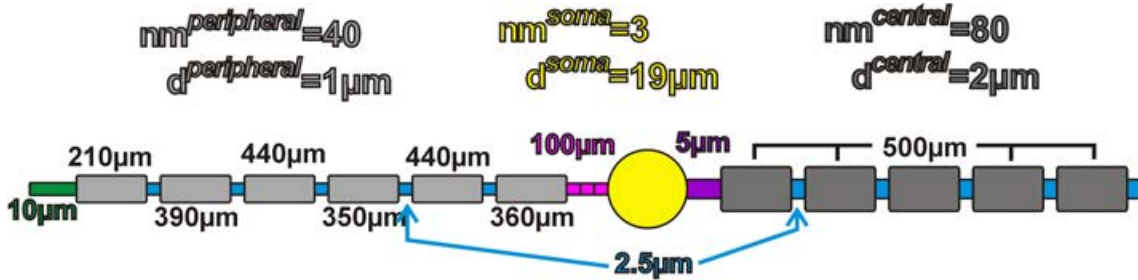


Figure 4.1: Schematic drawing of the standard compartment model used within this thesis, illustrating the bipolar type I neuron with adapted soma size. See text for further explanation.

It is convenient and less difficult to follow the results when a standard model is defined which is used as a starting point for all simulation. Thus the arrangement of the typical compartment model of a SGC is illustrated in Fig. 4.1 which follows the model of Rattay et al. (2001) with some adaptations. The peripheral process of

the bipolar cochlear neuron remained unchanged, i.e., six peripheral internodes of varying length are intersected by 2.5  $\mu\text{m}$  long nodes of Ranvier. The first dendritic compartment, the terminal region is 10  $\mu\text{m}$  long. For the presomatic region which is split up into three compartments originally  $l_{pre} = 100 \mu\text{m}$  was necessary, since enough current had to be supplied to obey the large capacitive load of the soma. The diameter of all dendritic compartments remained at the original value of  $d_{peripheral} = 1 \mu\text{m}$  unless otherwise stated. Note that this is rather thin for human type I neurons according to more recent studies (see Sec. 2.1), thus test trials for different values are presented in Sec. 4.1.2. Still also for higher values, the often reported relation of doubled diameter for the central process holds. Thus for the standard model  $d_{central} = 2 \mu\text{m}$  holds. For this axon five 500  $\mu\text{m}$  long internodes are considered with intersecting nodes of again 2.5  $\mu\text{m}$  length. Although the actual length of the central process is certainly longer, in order to analyze the case of intracellular current injection at the first compartment a reduced model axon length is sufficient and time-saving. Therefore also a longer or split up axon terminal region is omitted. The postsomatic region is only 5  $\mu\text{m}$  long which also was the original model value.

The essential difference compared to Rattay et al. (2001) is the diameter of the soma which was considered to be 30  $\mu\text{m}$ . Although there is a wide range of  $d_{soma}$ , in Fig. 4.1 the approximate mean value of 19  $\mu\text{m}$  is presented. Along with extensive testing concerning this parameter the mentioned  $l_{pre}$  has been varied for simulations of this thesis, since the reduced soma size allows for shorter presomatic compartments which would be more accurate and realistic.

Only the internodes are considered to be passive compartments which are represented in gray color in Fig. 4.1. According to the original model the peripheral internodes have 40 layers of myelin whereas  $nm = 80$  holds for the axon. Thus different membrane conductances are calculated for  $g_{my} = 1 \text{ mS/cm}^2$ , the conductance of one layer of membrane. All other compartments are considered to be active and only surrounded by one layer except the whole soma region including the three presomatic and the postsomatic compartment where  $nm = 3$  holds. All active compartments are modeled with HH kinetics for  $T = 37^\circ\text{C}$  with 10-fold ion channel densities (see Sec. 3.4) but again except the soma where the original conductance values are used, i.e.,  $g_{Na} = 120$ ,  $g_K = 36$  and  $g_L = 0.3 \text{ mS/cm}^2$ .

The overall electrical properties of the intracellular specific resistivity and the specific membrane capacity which are valid for the whole neuron remain at their original values, i.e.,  $\rho_i = 50 \text{ k}\Omega\cdot\text{cm}$  and  $C_{mem} = 1 \mu\text{F/cm}^2$ .

### 4.1.1 Soma region

Recent research concerned the soma size of human afferent cochlear neurons for different positions along the cochlear turns (Potrusil et al. 2012). Two specimen have been tested for volumetric data of perikarya and nuclei identifying 4 populations of SGC concerning their soma size. The report focuses on testing the effect of changing soma size of a neuron stimulated by varying electrode configurations. Thus special

## 4.1 Afferent single neuron model

---

interest has been paid to the overall spiking behavior of the neuron's excitation profile, such as peak times of different sites of the neuron (see Sec. 5.2). But within this section we will now focus on the local properties of the AP at the soma, i.e., the magnitude ( $AP_{height}$  and  $AP_{amp}$ ) and temporal properties ( $AP_{width}$  and onset of AP) will be discussed.

Nonetheless it should be stated, that only changing the soma diameter, while leaving all other geometric and electric properties to their standard values, has no profound effect on the conductance velocity of an AP induced by intracellular stimulation of the first dendritic compartment. When the soma diameter is varied from its minimum of 10.05  $\mu\text{m}$  to the standard value of 30  $\mu\text{m}$  the threshold amplitude for a 0.1 ms pulse is either 0.06 nA or 0.07 nA. The traveling time of the spike for threshold current injection is only slightly changed, i.e., 0.58 ms for the smallest cell to 0.66 ms for the standard value. The  $AP_{height}$  at the soma shows a spread of only 2.3 mV, when all other parameters are held constant. The  $AP_{width}$  at the soma is always about 0.13 ms and its small variations do not correlate with soma diameter.

Still, the unmyelinated soma region which is typical for human SGCs displays certain difficulties for APs traveling from the beginning to the axonal branching region. Rattay et al. (2001) reported certain sensitive model parameters for the signal transmission of a spike, e.g., the number of membrane layers at the soma, the length of the presomatic region or diameter of the peripheral process. Even small deviation from their standard values can reduce the safety factor for successful information processing.

Since the model of Rattay et al. (2001) assumed a quite large soma diameter of  $d_{soma} = 30 \mu\text{m}$ , these investigations have been repeated for the detected mean, maximum and minimum values of the soma size for the three regions, i.e., apical, middle turn and basal. The performed experiments show that the effect of systematically changing either the number of myelin layer,  $nm$ , the length  $l_{pre}$  or diameter  $d_{pre}$  of the presomatic region is more pronounced for neurons with larger cell bodies. Thus neurons with bigger somata are more sensitive to parameter changes and will be more restricted concerning small variations as will be quantitatively described in the following.

Initially the number of myelin layers has been varied from  $nm = 1 \dots 5$  for the soma compartment of ten different cells with individual  $d_{soma}$ . The trial for the myelination has also been repeated for the original value of 30  $\mu\text{m}$ . The other nine cases correspond to the detected diameter values of Potrusil et al. (2012), i.e., for each of three regions the minimum, the mean and the maximum detected soma diameter have been tested (see Table 4.1).

Contrary to findings of Rattay et al. (2001), the amount of myelin layers at the soma can be reduced to one for all possible diameters and still the neuron conducts the AP to its axonal end. Although the changes only concern the soma itself, also

#### 4.1 Afferent single neuron model

the overall conduction properties of the neuron are altered. Thus, when the amount is decreased from 5 to only one layer, the whole traveling time of the AP from the first to the last compartment, i.e., the spike duration, is elevated (up to 14% longer for large cells and about 8% for small cells) which is a result of the longer  $AP_{width}$  at the soma for unmyelinated cells (up to 40% longer for large cells and about 15% for small cells).

No matter which neuron is tested, the values of the AP parameters monotonically increase when the number of layers is increased from 1 to 5. The observed general trend is, that the  $AP_{height}$  at the soma significantly changes for more layers of myelin with amplitudes 25 mV higher for large cells and 10 mV increased values for small cells. The same is valid for the  $AP_{amp}$  and accordingly also for the temporal parameters, the corresponding  $AP_{width}$ 's which decrease for increasing myelinization. Although the absolute difference between corresponding values of  $AP_{width}$  is only small, the  $AP_{width}$  is more than 30% longer for less myelinization of bigger cells, and at least 10% longer for small cells.

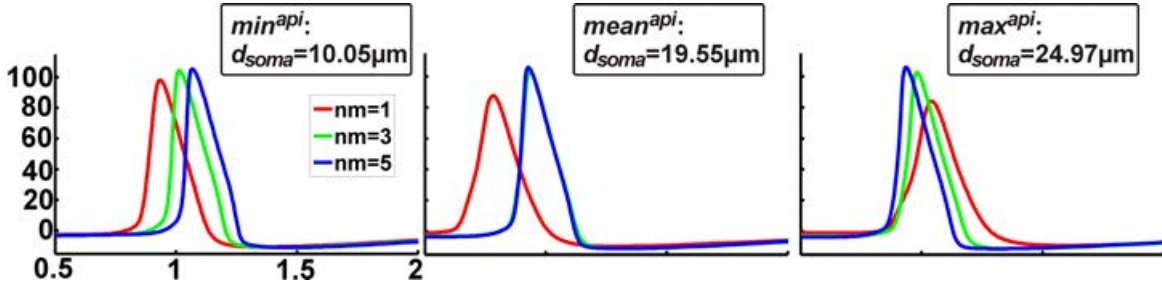


Figure 4.2: Each panel shows three different transmembrane potentials at the soma  $V_m^{soma}$  which correspond to different amount of myelin layers covering the soma compartment. The minimum (left panel), the mean (middle) and the maximum value of soma diameter from apical neurons are displayed.

Results for the minimum, the mean and the maximum value of soma diameter of the apical turn are presented in Fig. 4.2. For each of the three neurons the spike of the unmyelinated soma, i.e., the red line which corresponds to  $nm = 1$ , shows the smallest  $AP_{amp}$  and also has slightly longer values of  $AP_{width}$ . Interestingly the time at which the peak appears and the order varies for different soma sizes. For the smallest detected cell in the apical turn (left panel of Fig. 4.2) the peak of the unmyelinated soma appears earlier than the corresponding peak of the neuron which has 5 layers of myelin at the soma compartment. Contrary if the biggest detected cell is observed, the increased myelinization allows earlier AP onset at the soma.

Changing also the degree of myelinization of pre- and postsomatic compartments increases the described effect. Usually  $nm = 3$  also holds for the three presomatic and the single postsomatic region. If additionally these values are altered according to the number of layers at the soma, also the traveling time of the spike from the first to the last compartment certainly changes. For apical neurons, this spike duration of a cell



## 4.1 Afferent single neuron model

---

with a totally unmyelinated soma region ( $nm = 1$  for pre- and postsomatic and soma) is 0.3 ms longer compared to the same cell with 3 layers of myelin for the pre- and postsomatic region. Another consequence is the decrease of  $AP_{height}$  and also  $AP_{amp}$  at the soma itself which can lead to reductions of more than 6 mV. The  $AP_{width}$  at the soma compartment is only slightly changed. The variations are greater for less degree of myelination, i.e., if a cell with a soma with  $nm = 5$ , also gets 5 layers instead of 3 on the whole region, the reported effects are less pronounced, but still obvious. The cell size does not really matter, because the consequences were comparable for the maximum, the mean and the minimum values of soma diameter.

The conduction limit for the diameter of the presomatic region is well beneath the standard value of 1  $\mu\text{m}$ , i.e., even 0.15  $\mu\text{m}$  for small cells and still 0.5  $\mu\text{m}$  for the largest ones produces satisfactory excitation. This minimum value for successful AP propagation reduces since less current is needed to load smaller cell bodies. The spike properties are only slightly modified, but it should be noted that the APs of neurons with thicker dendrites tend to propagate faster with higher amplitudes for all cell sizes, but with a stronger effect on larger diameters.

The reported value fluctuations are most obvious for representative middle turn neurons, e.g. the minimum diameter of the middle turn allows a reduction to a diameter of 0.15  $\mu\text{m}$ , but the  $AP_{height}$  at the soma therefore reduces for more than 12 mV if compared to a presomatic diameter of 0.75  $\mu\text{m}$ . This would be even more pronounced if the standard value of 1  $\mu\text{m}$  was used. The mean and maximum soma diameter both allow the process diameter to be as small as 0.25  $\mu\text{m}$ , but comparing the corresponding values shows, that the effect of  $AP_{height}$  reduction is higher on bigger cells. If the diameter of the cell with the mean soma size is raised to 0.75  $\mu\text{m}$ , the difference in spike height is about 6 mV but even 9 mV for the maximum soma size (see Tab. 4.1).

The most outstanding result concerns the length of the presomatic region. This is also a parameter which has not been determined among the variety of cells and might be much shorter than predicted by the [Rattay et al. \(2001\)](#) model. Interestingly there exist one certain cell size underneath which the length of this presomatic region becomes dispensable for successful propagation, i.e., for cells with a soma diameter smaller than 18.75  $\mu\text{m}$  the presomatic compartment can get as short as 1.5  $\mu\text{m}$  and the AP will still cross the somatic barrier. All cells above this value need the presomatic area to be of a minimum length to further conduct the spike. The minimum values are fluctuating between 50 to 65  $\mu\text{m}$  without any monotonic pattern for increasing soma diameters.

The overall behavior for changing this parameter is that for cells above the limit a longer presomatic region will produce higher  $AP_{amp}$ 's at the soma and will conduct spikes faster (up to 40% faster) to the axonal end, although the  $AP_{width}$  at the soma reduces. For cells beneath the limit diameter this reduction is more pronounced



#### 4.1 Afferent single neuron model

		$nm$		$l_{pre}$		$d_{pre}$	
	$d_{soma}$	$AP_{height}$	$AP_{width}$	$AP_{height}$	$AP_{width}$	$AP_{height}$	$AP_{width}$
$min^{bas}$	10.29	107.26%	114.23%	106.91%	104.55%	103.89%	102.4%
$mean^{bas}$	19.04	119.46%	124.8%	104.97%	111.74%	106.96%	105.55%
$max^{bas}$	25.05	125.92%	128.05%	101.02%	102.77%	106.86%	106%
$min^{mid}$	12.29	109.77%	111.43%	107.51%	106.05%	113.02%	106.96%
$mean^{mid}$	19.90	119.17%	125.82%	103.96%	108.95%	106.66%	103.7%
$max^{mid}$	22.91	123.49%	131.95%	103.32%	107.62%	109.85%	104.34%
$min^{api}$	10.05	106.98%	110.35%	107.11%	102.67%	108.36%	107.49%
$mean^{api}$	19.55	120.47%	127.32%	107.09%	107.11%	103.73%	103.34%
$max^{api}$	24.97	125.82%	133.9%	101.06%	101.15%	106.72%	105.52%

Table 4.1: Changes of local spike properties  $AP_{height}$  [mV] and  $AP_{width}$  [ms] at the soma for nine cells with different soma diameter. The minimum, maximum and mean values of soma diameter from basal, middle and apical turn SGCs (Potrusil et al. 2012) are given in [ $\mu$ m]. Percentaged difference between maximum and minimum value for altering the number of myelin layers at the soma from  $nm = 1 - 5$ . For the length and diameter of the presomatic region the values display the difference between the standard value, i.e.,  $l_{pre} = 100 \mu$ m and  $d_{pre} = 1 \mu$ m, and the minimum possible value for successful AP transmission.

with a difference of about 10 mV, but the traveling time of the spike remains almost unchanged, although the  $AP_{width}$  at the soma certainly decreases to extreme values when the presomatic region is only 2  $\mu$ m long.

Although the intracellular resistivity  $\rho_i$  is an electrical parameter which holds for the whole neuron, not only at the soma region, it has also been examined for the reported minimum, mean and maximum values of soma diameter from basal, middle and apical turn. Different sensitivity can be observed for varying soma size.  $\rho_i$  cannot exceed a certain maximum value which is distinctive of the soma size, where smaller cells can transmit APs till  $\rho_i = 0.22 \text{ k}\Omega\cdot\text{cm}$ , but larger ones cannot conduct successfully when the value surpasses  $0.16 \text{ k}\Omega\cdot\text{cm}$ . This parameter certainly has the strongest effect on the spike duration with almost doubling for the maximum values of  $\rho_i$  compared to its standard value of  $0.05 \text{ k}\Omega\cdot\text{cm}$ . Although the  $AP_{width}$  at the soma slightly reduces, its  $AP_{amp}$  remains approximately the same.

##### 4.1.2 Central and peripheral process

Beside the special human soma region, a wide variety of geometrical and electrical properties of the two processes, i.e., the peripheral dendrite and the central axon, can be observed. Depending on the cochlear turn of the SGC the length of the peripheral process alters, so that the spike has to travel varying distances until it reaches the

#### 4.1 Afferent single neuron model

---

soma region. Therefore also the number of internodes as well as their length certainly changes.

Furthermore different diameter values of the two processes are found within literature (see Sec. 2.1). This parameter has a striking effect on the conduction velocity of the neuron, as has been very often observed and previously described. Along with this fact comes the dependency of myelination. Certainly different degree of myelination at the processes alters the excitation profile and strongly affects the overall spiking behavior of the neuron, i.e., the conduction properties and peak times of certain compartments are changed.

A recent study with confocal laser-scanning microscope images from human and cat cochleae revealed different degrees of myelination on the cell processes. Still within this study other correlating parameters could not be evaluated at the same time, that is why some uncertainties within parameter values were investigated as well. Thus again most of the parameters from the standard model are used which is explained in detail in Sec. 4.1, although the length of the pre- and postsomatic region were changed to  $l_{pre} = 10 \mu\text{m}$  and  $l_{post} = 8 \mu\text{m}$  (see Table 4.2).

	peripheral process	presomatic region	soma	postsomatic region	central process
length	0.22 cm	10 $\mu\text{m}$	$d_{soma}$	8 $\mu\text{m}$	0.35 cm
diameter	$d_{peripher}$		$d_{soma}$	$d_{central} = 2 \cdot d_{peripher}$	
$nm$	1N   40IN	$nm_{pre}$	$nm_{soma}$	$nm_{post}$	1N   80IN

Table 4.2: Summary of model parameters for afferent cochlear neurons. Red values are varied during the simulation experiments, green values are fixed.

In contrast to the standard model now the short presomatic region is represented by only one compartment. With the predicted standard values, the length of the total peripheral process sums up to 2212.5  $\mu\text{m}$  and that of the central process to 3525.5  $\mu\text{m}$  as indicated in Table 4.2 which illustrates which parameter values will be involved for subsequent test trials (printed in red).

Additionally our cooperation partner from the MedUni IBK were recently able to detect one specific type II SGC in its full dimension, i.e., the specific lengths and diameter values could be obtained from a single neuron rather than using mean values of reported parameter ranges. Thus in order to account for the usually unmyelinated cell processes, both are modeled as two active uniform fibers with a compartment length of 25  $\mu\text{m}$ .

Furthermore our partners suggested to perform test trials concerning the excitation profile of efferent fibers with varying diameter and degree of myelination, since recent investigations revealed a probably wider variety of these parameters than expected. Therefore also a short discussion of different model approaches is presented.

#### 4.1 Afferent single neuron model

---

For all simulations the previously mentioned global spike parameter, i.e., its traveling time, has been investigated. The *AP duration* ( $AP_{dur}$ ) is defined as the difference between the peak time of the transmembrane potential  $V$  at the first excited compartment and the peak time of  $V$  at the compartment on the other end of the neuron. Note that this is not the delay of information processing, since the peak time at the first excited compartment will occur shortly after stimulus onset. The delay can be calculated by adding the peak time of the initiating compartment to the  $AP_{dur}$ .

Additionally the mean axonal conduction velocity is calculated. The evaluation involves the distance between two axonal nodes from the middle of the process ( $\bar{N}$  denotes the nodal index in the middle of the axon), and the difference between the two corresponding peak times.

$$AP_{dur} = t(\max(V_{end}) - t(\max(V_1)), \quad v^{axon} = \frac{dist(comp_{\bar{N}}, comp_{\bar{N}-1})}{t(\max(V_{\bar{N}})) - t(\max(V_{\bar{N}-1}))}$$

Note that with the evaluation of the axonal velocity  $v^{axon}$ , different values of  $AP_{dur}$  can be calculated with extrapolation for arbitrary length of the central process since the predicted length of 0.35 mm for the central process of the model neuron is rather short. This extrapolation will also be applied for the evaluations of the type II neuron in order to reduce computational effort for the solely active SGC and also for the uniform efferent fiber simulations.

The simulation trials involve alterations for three different varying parameters. Four different soma diameters are tested,  $d_{soma} = 10 \mu\text{m}$ ,  $d_{soma} = 15 \mu\text{m}$ ,  $d_{soma} = 20 \mu\text{m}$  and  $d_{soma} = 25 \mu\text{m}$ . The diameter of the cell process is varied with four different values,  $d_{peripher} = 1 \mu\text{m}$ ,  $d_{peripher} = 1.5 \mu\text{m}$ ,  $d_{peripher} = 2 \mu\text{m}$ ,  $d_{peripher} = 2.5 \mu\text{m}$ . Note that the central process will always have doubled value. The degree of myelination at the soma region has been varied from completely unmyelinated, i.e., only one layer for the three compartments, over different degrees of myelination ( $nm = 3|3|3$ ,  $nm = 7|7|7$  and  $nm = 11|11|11$ ) to a completely myelinated soma region, i.e., 40 layers for the presomatic region, 60 for the soma itself and 80 sheets for the postsomatic region (Table 4.3).

For each of the four different soma diameters, the neuron has varying thresholds for successful stimulation when the diameter of the processes is increased from  $d_{peripher} = 1 \mu\text{m}$  to  $d_{peripher} = 2.5 \mu\text{m}$ . Some configurations result in the failure of AP propagation over the somatic region no matter what stimulus amplitude is used (This behavior mostly occurs for certain degrees of myelination and thin processes, see (-) in Table 4.3). Interestingly, if the stimulation is successful, the corresponding threshold values are the same for all four soma diameters. For afferent stimulation, the smallest threshold value of 0.07 nA appears for the thinnest dendrite with  $d_{peripher} = 1 \mu\text{m}$ , the highest value of 0.3 nA is needed for the thickest dendrite of  $d_{peripher} = 2.5 \mu\text{m}$ . To produce comparable results the pulse amplitude is chosen to be  $IC_{amp} = 0.5$  nA for a duration of  $IC_{dur} = 0.1$  ms.

#### 4.1 Afferent single neuron model

$d_{peri}$	$d_{cent}$	$nm$	$d_{soma} = 10 \mu m$		$d_{soma} = 15 \mu m$		$d_{soma} = 20 \mu m$		$d_{soma} = 25 \mu m$	
			$AP_{dur}$	$v^{axon}$	$AP_{dur}$	$v^{axon}$	$AP_{dur}$	$v^{axon}$	$AP_{dur}$	$v^{axon}$
1	2	1	-	-	-	-	-	-	-	-
		3	2.3	12.84	2.408	14.34	-	-	-	-
		7	2.244	12.34	2.287	12.03	2.345	13.48	2.486	12.34
		11	2.231	15.15	2.26	13.62	2.299	14.28	2.347	13.18
		60	2.207	13.04	2.22	11.95	2.23	14.39	2.247	13.57
1.5	3	1	1.947	17.16	-	-	-	-	-	-
		3	1.846	15.57	1.891	14.17	1.955	15.93	2.095	20.29
		7	1.82	20.25	1.84	16.23	1.868	16.04	1.897	16.19
		11	1.809	16.35	1.827	20.14	1.845	15.91	1.867	15.69
		60	1.798	16.04	1.802	16.12	1.809	16.13	1.818	20.25
2	4	1	1.655	17.12	1.745	20.66	-	-	-	-
		3	1.591	16.17	1.62	16.26	1.653	21.14	1.703	21.98
		7	1.568	16.14	1.581	17.9	1.599	15.69	1.622	18.17
		11	1.562	18.58	1.569	17.12	1.582	21.05	1.596	21.08
		60	1.55	24.07	1.553	19.74	1.558	16.29	1.566	16.06
2.5	5	1	1.469	24.66	1.523	23.87	1.62	23.7	-	-
		3	1.415	20.76	1.436	20.62	1.461	23.96	1.495	25.31
		7	1.399	24.26	1.407	18.39	1.42	18.74	1.438	20.94
		11	1.393	19.92	1.398	21.04	1.409	21.06	1.421	21.2
		60	1.385	21.27	1.385	18.03	1.387	17.84	1.395	18.21

Table 4.3: Summary of all trials for  $v^{axon}$  in [m/s] and  $AP_{dur}$  in [mV] which correspond to a total SGC length of 2.737 cm. Changing values are presented for varying soma and process diameters as well as for altering degree of myelination. (-) indicates AP propagation failure.

Table 4.3 shows that a completely unmyelinated soma region, with only one layer covering the pre- and postsomatic region including the soma, will not be able to produce solid AP conduction. The required amount of myelin layers of the somatic region for successful propagation increases with increasing soma diameter (Table 4.3).

The presented values of  $AP_{dur}$  in Table 4.3 have been simulated for a 2.513 cm long central process as suggested by recent findings of our partners of the MedUni IBK. This corresponds to 50 central internodes of a fixed length of 500  $\mu m$  and sums up to a total length of the SGC of 2.737 cm. The mean value among all 16 trials of the  $AP_{dur}$  is 1.764 ms. The maximum value of 2.486 ms appears for  $d_{soma} = 25 \mu m$  and  $d_{peripher} = 1 \mu m$ ,  $nm = 7$ , the minimum of 1.385 ms for  $d_{soma} = 10 \& 15 \mu m$  and  $d_{peripher} = 2.5 \mu m$ ,  $nm = 60$ . The mean value among all 16 trials of the axonal conduction velocity is 17.85 m/s. The maximum value of 25.31 m/s appears for  $d_{soma} = 25 \mu m$  and  $d_{peripher} = 2.5 \mu m$ ,  $nm = 3$ , the minimum of 11.95 m/s for  $d_{soma} = 15 \mu m$  and  $d_{peripher} = 1 \mu m$ ,  $nm = 60$ .

### Comparison degree of myelinization

The  $AP_{dur}$  values decrease when the amount of myelin layers is increased, while the soma and the process diameters are held constant. Five different degrees of myelinization are considered for every simulation sequence. One sequence for increasing amount of myelin sheets involves fixed soma and process diameters. The mean gap between minimum and maximum value of  $AP_{dur}$  of all sequences is 0.149 ms (minimum gap of 0.084 ms for  $d_{soma} = 10 \mu\text{m}$  and  $d_{peripher} = 2.5 \mu\text{m}$ ; maximum gap of 0.277 ms for  $d_{soma} = 25 \mu\text{m}$  and  $d_{peri} = 1.5 \mu\text{m}$ ). The myelinization at the soma region which is only 28 to 43  $\mu\text{m}$  long therefore has a visible but minor effect on the total  $AP_{dur}$  of the neuron with a length of about 2.72 cm.

The degree of myelinization at the soma region has minor effect on the axonal conduction velocity. The values are fluctuating not favoring any degree of myelinization. Although no monotonic behavior can be observed, it shall be stated, that the mean value of the difference between maximum velocity and minimum velocity for a cell with fixed diameters but varying amount of myelin sheets at the soma is 4.39 m/s. The minimum gap of 0.22 m/s appears for  $d_{soma} = 20 \mu\text{m}$  and  $d_{peripher} = 1.5 \mu\text{m}$ ; the maximum gap of 7.93 m/s for  $d_{soma} = 10 \mu\text{m}$  and  $d_{peripher} = 2 \mu\text{m}$ .

### Comparison different soma diameters

The  $AP_{dur}$  values increase for increasing soma diameter, while the process diameters and the number of myelin sheets at the soma are held constant. Four cases are distinguished:  $d_{soma} = 10 \mu\text{m}$ ,  $d_{soma} = 15 \mu\text{m}$ ,  $d_{soma} = 20 \mu\text{m}$ ,  $d_{soma} = 25 \mu\text{m}$  while the other parameters are held constant. Therefore one series of 4 trials has to be performed for the four process diameters, the six possible degrees of myelinization. The mean value of the difference between the shortest and longest  $AP_{dur}$  for all sequences is 0.085 ms. The minimum gap of 0.01 ms appears for  $d_{peripher} = 2.5 \mu\text{m}$  and  $nm = 60$ ; the maximum gap of 0.249 ms for  $d_{peripher} = 1.5 \mu\text{m}$  and  $nm = 3$ .

Also varying soma diameters has no significant effect on the axonal conduction velocity without any monotonic behavior for fixed process diameters and fixed number of myelin sheets. The mean value of the difference between the fastest and slowest axonal velocity for all sequences is 3.69 m/s. The minimum gap of 0.96 m/s appears for  $d_{peripher} = 2.5 \mu\text{m}$  and  $nm = 1$ ; the maximum gap of 8.01 m/s for  $d_{peripher} = 2 \mu\text{m}$  and  $nm = 60$ .

### Comparison diameter of cell processes

The strongest effect on the spike conduction time has the increase of both diameters of the two processes what causes the  $AP_{dur}$  values to decrease. (4 cases:  $d_{peripher} = 1 \mu\text{m}$ ,  $d_{peripher} = 1.5 \mu\text{m}$ ,  $d_{peripher} = 2 \mu\text{m}$ ,  $d_{peripher} = 2.5 \mu\text{m}$  while the other parameters are held constant.) Therefore one series of 4 trials has to be performed for one of the

four soma diameters and one of the six possible degrees of myelination. For each sequence the values of the  $AP_{dur}$  monotonically decrease for increasing diameter of the processes. The difference between the highest value (corresponding to the thinnest processes) and the lowest value (corresponding to the thickest processes) has been compared for every sequence. The mean detected difference for an increased diameter is 0.887 ms. The minimum gap of 0.822 ms appears for  $d_{soma} = 10 \mu\text{m}$  and  $nm = 60$ ; maximum gap of 1.048 ms for  $d_{soma} = 25 \mu\text{m}$  and  $nm = 7$ .

The axonal conduction velocity is certainly affected by the diameter of the processes. In most of the cases the axonal velocity increases for increasing diameter. Some exceptions appear for the highest degree of myelination of the soma region, i.e.,  $nm = 60$ . The mean detected difference for an increased diameter is 7.01 m/s. The minimum gap of 3.21 m/s appears for  $d_{soma} = 10 \mu\text{m}$  and  $nm = 7$ ; maximum gap of 11.92 m/s for  $d_{soma} = 15 \mu\text{m}$  and  $nm = 1$ .

### Test run: afferent neuron with unmyelinated fibers

As already mentioned one specific type II SGC with unmyelinated cell processes was investigated with the following evaluated diameters:  $d_{soma} = 10 \mu\text{m}$ ,  $d_{peripher} = 0.65 \mu\text{m}$ ,  $d_{central} = 1.4 \mu\text{m}$ . Both processes were modeled as uniform active fibers with varying degree of myelination. To compare  $AP_{dur}$ 's of such a cell with one neuron with a myelinated central axon, the same stimulation current  $IC_{amp} = 0.5 \text{ nA}$  for a duration of  $IC_{dur} = 0.1 \text{ ms}$  is used.

Five trials have been performed for varying amount of myelin layers for the whole neuron which also corresponds to the previous notation. Fig. 4.3 shows the traveling spike of each configuration of the cell. The temporal change of transmembrane potential of the peripheral process are plotted in yellow, the corresponding soma curve is red. Note that the green central lines only display the traveling AP till the last model compartment, 0.5 cm after the soma. The  $AP_{dur}$  values which are given in the inset of each panel are therefore higher than the displayed traveling time, i.e., note that the x-axis only displays the first 5 ms of the spike on its way to the central end.

Certainly the  $AP_{dur}$  values are higher than the mean value of 1.764 ms for afferent SGCs with myelinated fibers. Increasing amount of myelin layers leads to reduced values of  $AP_{dur}$  and mean axonal conduction velocity. Of course it should be noted that the case of  $nm = 60$  which is presented in the bottom panel of Fig. 4.3 is purely hypothetical since actually a neuron with unmyelinated processes is examined. Still the simulation trial has been included to demonstrate the high influence of the myelination.

### Test run: efferent fibers

Although efferent conduction is not the main topic of this thesis and some histological and anatomical parameters of efferent cochlear neurons still have to be clarified, two

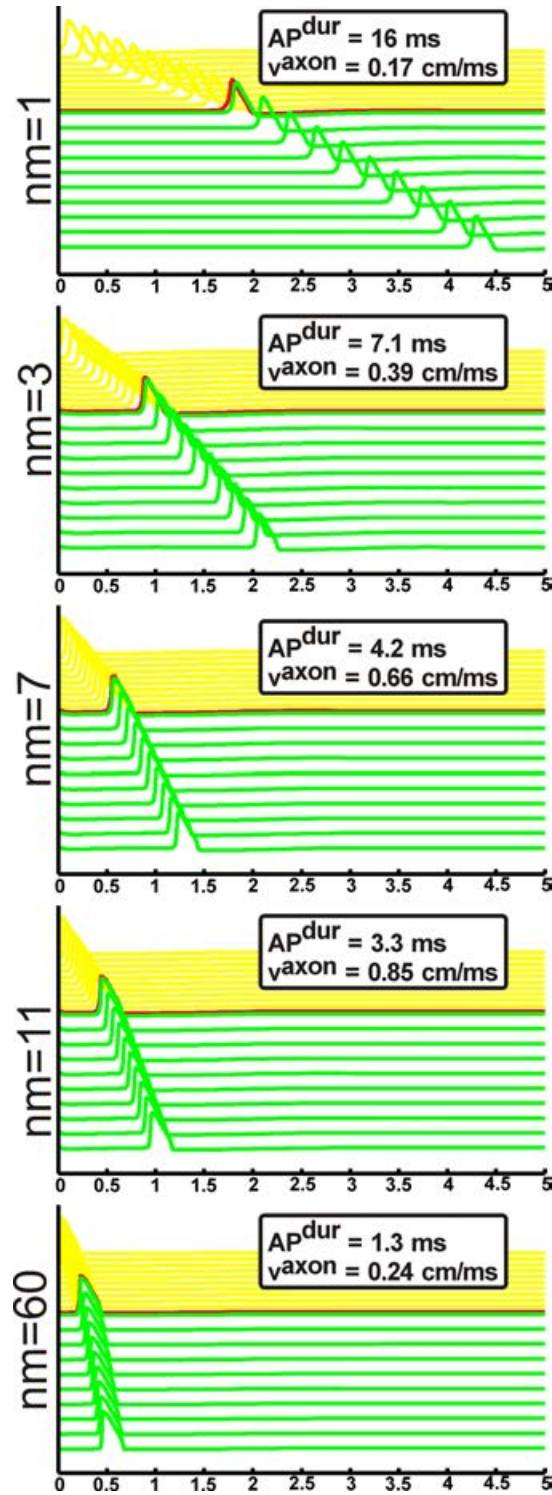


Figure 4.3: The excitation profiles of the type II model neuron are presented for different degrees of myelination of the two processes. For details see text.



#### 4.1 Afferent single neuron model

---

different types of uniform fibers have been tested for conduction velocity. Six possible diameters have been evaluated for one unmyelinated fiber, solely modeled as active compartments. Additionally the corresponding simulations have been repeated for a uniform node-internode sequence of different degree of myelination at the internodes.

		uniform active $nm = 1$	node- internode $nm = 20$	node- internode $nm = 40$	node- internode $nm = 60$	node- internode $nm = 80$
$d = 0.1 \mu\text{m}$	$AP_{dur}$ $v^{fiber}$	55.8 ms 0.45 m/s	- -	- -	- -	- -
$d = 0.3 \mu\text{m}$	$AP_{dur}$ $v^{fiber}$	28.7 ms 0.87 m/s	- -	- -	- -	16.6 ms 1.51 m/s
$d = 0.6 \mu\text{m}$	$AP_{dur}$ $v^{fiber}$	20.6 ms 1.21 m/s	12.5 ms 1.99 m/s	9 ms 2.79 m/s	7.8 ms 3.22 m/s	7.2 ms 3.48 m/s
$d = 1 \mu\text{m}$	$AP_{dur}$ $v^{fiber}$	14.2 ms 1.76 m/s	7.6 ms 3.31 m/s	6 ms 4.17 m/s	5.4 ms 4.67 m/s	5.1 ms 4.92 m/s
$d = 1.5 \mu\text{m}$	$AP_{dur}$ $v^{fiber}$	13.7 ms 1.82 m/s	5.8 ms 4.33 m/s	4.5 ms 5.6 m/s	4.1 ms 6.15 m/s	3.9 ms 6.42 m/s
$d = 2 \mu\text{m}$	$AP_{dur}$ $v^{fiber}$	11.8 ms 2.11 m/s	4.7 ms 5.35 m/s	3.8 ms 6.65 m/s	3.4 ms 7.47 m/s	3.3 ms 7.55 m/s

Table 4.4: Summary of  $AP_{dur}$  and  $v^{fiber}$  for 2.5 cm long efferent fibers. Six different diameters of the process are tested. An uniform active fiber is compared to a node-internode sequence of different degree of myelination.

The results are presented in Table 4.4. The unmyelinated fiber is the slowest, although for this type of compartment model the thinnest fiber with a diameter of only  $0.1 \mu\text{m}$  is able to successfully transmit a spike. For the node internode sequence no matter how high the stimulus current and how many covering myelin layers at the internodes, the AP fails to propagate.

The values of the unmyelinated axon have been calculated with extrapolation since the initial simulation values correspond to a 0.5 cm long model fiber with a compartment length of  $25 \mu\text{m}$  summing up to 200 active compartments which is very time-consuming. By contrast, the node internode sequence can be simulated for the total length of 2.5 cm. Again  $IC_{amp} = 0.5 \text{ nA}$  with  $IC_{dur} = 0.1 \text{ ms}$  is used (only for  $d = 2 \mu\text{m}$  0.8 nA).

Obviously the velocity of the unmyelinated fiber is smaller than that of the myelinated fiber, which allows for the fast saltatory conduction on the nodes of Ranvier. Moreover for increasing values of myelin layers the conduction velocity increases as expected.

This evaluation involves intracellular current injection and therefore shall mimic

the natural spiking behavior. Calculations have also been performed for extracellular stimulation by a point-electrode (see Sec. 5.1), where a quite linear velocity-diameter relation for well wrapped myelinated fibers can be observed. Anyway for this kind of simulations no linear relations can be deduced, neither for the diameter nor for the amount of myelin layers.

Still for unmyelinated fibers, theoretical investigations demands for a quadratic velocity - diameter relation for homogeneous fibers (Rattay 1990). The reported relation  $v [\text{mm/s}] = 1.5 \cdot \sqrt{d} [\mu\text{m}]$  holds for simulation of the unmyelinated fiber case with small deviations.

Conclusively it should be stated, that during experimental testing the reported short  $AP_{dur}$ 's of auditory neurons predicted by NRT data can be replicated by the adapted cochlear neuron model of Rattay et al. (2001). Furthermore this traveling time of the spike propagating from the beginning to the central end can be distinguished into 4 characteristic phases whereas some details are presented in Sec. 5.1.

### 4.1.3 Channel kinetics

Beside the great diversity among the mentioned electrical and geometrical parameters, another crucial point is the choice of ion channel kinetics. Of course, initially one has to decide which types of voltage-dependent ion channel should be incorporated for modeling the excitation behavior of the neuronal structure of interest. For the bipolar cochlear neurons, the inclusion of sodium and potassium channels is sufficient to model the response to intra- and extracellular stimulation.

In Sec. 3.3 six different sets of equations are presented each of which models a patch of active membrane with one  $Na$  and one  $K$  channel following the HH ansatz. As extensive testing with these local models has outlined the great differences among them, which especially result of the diverse  $K$  channel representation, the following short section shall clarify the effect for modeling the spike transmission on a whole SGC, i.e., the excitation profiles for the standard compartment model of a human cochlear neuron are repeated for the six models. Previous testing revealed certain distribution of ion channel conductances to produce the best matching APs corresponding to the standard values of the HH model, i.e.,  $g_{Na} = 120 \text{ mS/cm}^2$ ,  $g_K = 36 \text{ mS/cm}^2$  and  $g_L = 0.3 \text{ mS/cm}^2$ .

The standard model of a human cochlear neuron of Rattay et al. (2001) uses 10 fold conductance values for all other active compartments except the soma, i.e., the nodes of Ranvier have the following conductance values,  $g_{Na} = 1200 \text{ mS/cm}^2$ ,  $g_K = 360 \text{ mS/cm}^2$  and  $g_L = 3 \text{ mS/cm}^2$ . By assuming the same adaption for the other 5 models and using the same model temperature for all models of  $T = 37^\circ\text{C}$ , a 0.1 ms long intracellular current injection at the first compartment with an amplitude of  $IC_{amp} = 0.3 \text{ nA}$  leads to the excitation profiles presented in Fig. 4.4

At first sight the previously mentioned classification of two groups is still obvious, whereas the HH, the RGC and the Fohlmeister model constitute to the first group and the Meeks, the Hu and the Mainen model with their different  $K$  channel representation

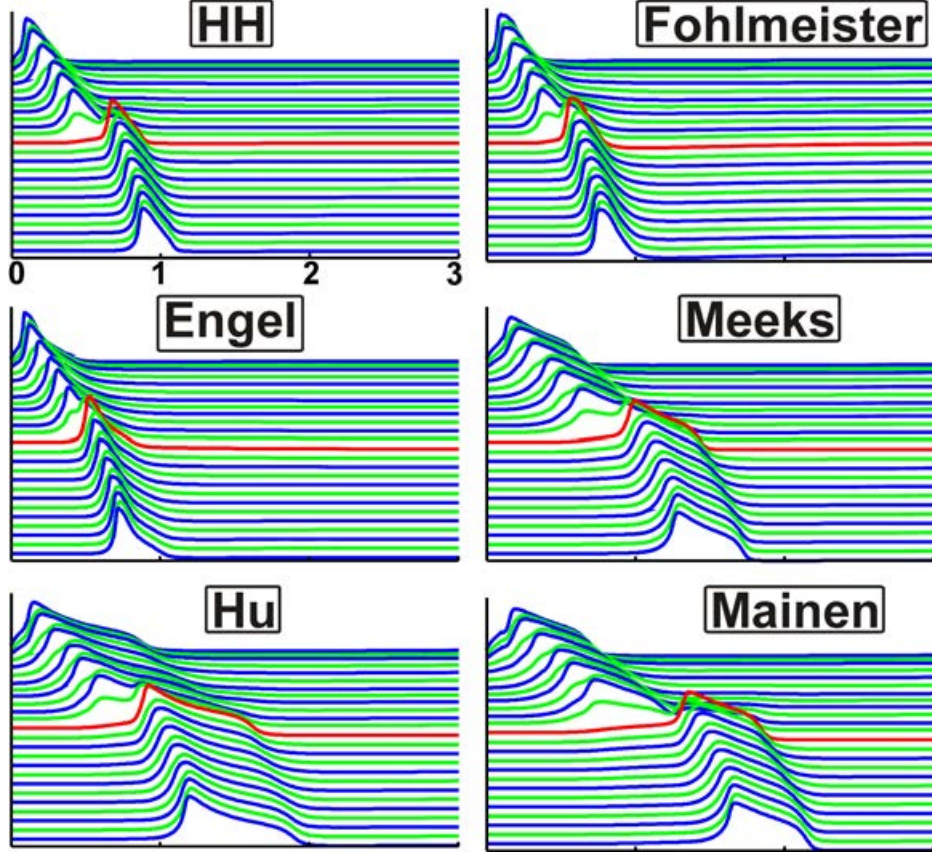


Figure 4.4: The standard model neuron was stimulated by intracellular current injection into the first compartment with  $IC_{amp} = 0.3$  nA. Blue lines are internodal transmembrane potentials, the intersecting nodes are plotted in green. The presomatic compartment is the magenta line and the soma is displayed in red.

make up the second group. The earliest peak appears at 0.094 ms for the Engel model, although the HH and the RGC model both with 0.099 ms generate the spike quite simultaneously (compare values in Table 4.5). The onset of the spike of the second group is delayed and the latest shows a doubled value compared to the Engel model, i.e., the first peak of the Mainen model appears quite late 0.193 ms after stimulus onset.

The longer repolarization phase of the second group of models causes also a delay of the transmission of the spike which is especially crucial in the peripheral and the soma region. The constant conduction velocity in the central axon would still be satisfactory, since note that between the red soma line and the last graph of each model only a small delay can be observed. This can be also examined with the individual peak time values in Table 4.5 where the last row derived the  $AP_{dur}$  of the spike, i.e., the difference in peak times of the first and the last compartment. Between the minimum of 0.626 ms corresponding to the Engel model and the Mainen maximum

of 1.476 ms is a large gap of 0.859 ms. But if one only analyzes the conduction time of the central model axon, i.e., the difference between the peak time of the soma and that of the last compartment, this gap reduces to 0.117 ms. This time the Fohlmeister model is the fastest with 0.19 ms for the transmission of the spike from the soma to the end, whereas the slowest Mainen model needs 0.307 ms for conduction.

However Fig. 4.4 clearly illustrates the varying arrival times of the six different model approaches. As mentioned before, the Engel model is the fastest which will arrive at the end 0.719 ms after stimulus onset, shortly followed by the Fohlmeister model with a delay of 0.7651 ms. The standard HH model produces a peak time at the last compartment of 0.882 ms which is the latest of this first group of models. From the second group the Hu kinetics lead to the earliest arrival at the end of 1.199 ms and also the peak of the Meeks model appears shortly afterwards at 1.288 ms. The latest is again the Mainen model which arrives at the end at 1.361 ms which is slightly more than the doubled value of the standard HH model.

For better visualization the pre- and postsomatic compartments were not plotted in the previously described excitation profiles, since for the first group of models the spike displays the typical short  $AP_{width}$  (compare Sec. 3.4) which means that the corresponding lines of the transmembrane potentials are almost congruent. Therefore the individual lines of only three compartments, namely the first, the soma and the last compartment, are illustrated in Fig. 4.5.

The first panel in Fig. 4.5 compares the temporal change of transmembrane potentials of the first compartment for all six models where the same colors are used as in Sec. 3.4. The typical appearance of the individual lines clearly resembles those observed before, although note that now the 10-fold densities are used and therefore the ionic current demand essentially increases (data not shown).

Still some examinations have been performed to test if other distribution of channels could lead to successful spike transmission especially over the critical soma region. Lower values which would be preferable concerning the energy consumption of an AP and different relation between  $Na$  and  $K$  conductance values did not result in satisfactory excitation. The possible variations are overwhelming, but again it seems that especially the equations of the  $K$  channel and additionally the parameter  $g_L$  are crucial to produce faithful results.

Furthermore it should be noted that the reversal leakage potential  $E_L$  is a parameter that is evaluated for the local model in order to maintain stability. An unsuitable choice of this parameter can lead to 'self-reactive' behavior, i.e., a spike is induced without any present stimulus current. Certainly the value depends on the conductance densities since  $E_L$  compensates the primary ionic currents which are present for an initial value of the transmembrane potential  $V_m(0)$ . Furthermore it should be noted that physiologically the resting potential of the membrane  $V_{rest}$  varies along a nerve structure, i.e., this value actually differs for altering sites.

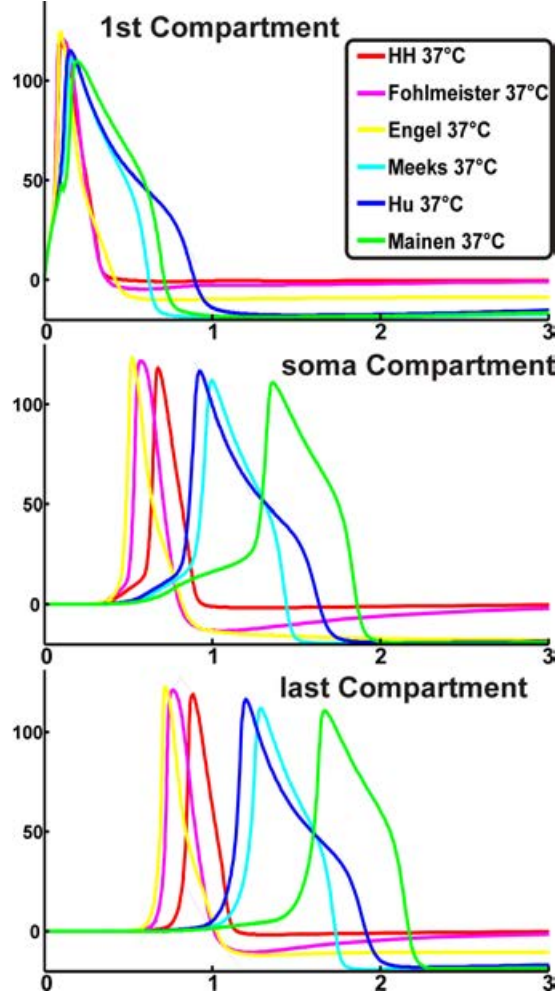


Figure 4.5: The transmembrane potentials of the first (top), the soma (middle) and the last (bottom) model neuron compartments are plotted for each of the six different models.

Anyway, when one studies the excitation behavior of a compartment model, varying channel densities would cause altered  $E_L$  values. For the observed case, where only two different active compartments are used for the model of the cochlear neuron, also two values of  $E_L$  are computed, i.e., the soma compartment would have another equilibrium state than the nodes of Ranvier. Generally, the value of  $E_L$  is assumed to be a fixed value along the whole structure. Both cases, i.e., a fixed value of  $E_L$  or two different possible values, were evaluated. Corresponding values are summarized in Table 4.5 where values for a uniform  $E_L$  distribution are given in parentheses.

The peak time values of the first compartment (PT in Table 4.5) are not effected, but the effect of changing  $E_L$  becomes obvious for the time at which the peak appears at the soma as presented in the second PTS column. The HH, RGC, Meeks and Hu values remain almost unchanged, either slightly smaller or larger, but the spike of the

Model	PT	PTS	ET	$AP_{dur}$
HH	0.0994	0.6775 (0.6804)	0.8821 (0.8845)	0.7827 (0.7851)
RGC	0.0997	0.5748 (0.5726)	0.7651 (0.7627)	0.6654 (0.663)
Engel	0.0935	0.5223 (0.38)	0.7199 (0.5708)	0.6264 (0.4758)
Meeks	0.1612	0.9968 (1.0448)	1.2879 (1.3368)	1.1267 (1.175)
Hu	0.154	0.9246 (0.9334)	1.1995 (1.2116)	1.0455 (1.0576)
Mainen	0.1929	1.3613 (1.2481)	1.6683 (1.6181)	1.4754 (1.4252)

Table 4.5: Different ion channel kinetics lead to strong variations of the peak time values of different neuronal sites. The evaluated values are given in ms and correspond to intracellular current injection of the first dendritic compartment.

Engel model appears significantly earlier at the soma for uniform  $E_L$ . This leads of course also to alterations of the arrival times of the spike (ET) and the corresponding  $AP_{dur}$ 's of the spike.

## 4.2 Cluster modeling

One of the most interesting peculiarities of human cochlear neurons is the sometimes observed 'clustering' of somata from more than one cell (Tylstedt et al. 1997, Liu et al. 2012). This means that neurons are found which share a common myelin layer over their cell bodies and also show some membrane specializations on a certain common contact area (Tylstedt and Rask-Andersen 2001, Liu et al. 2009). The significance of this anatomical feature is unclear to the present which leaves room for speculations, i.e., the effect of this clustering on the excitation profiles of neurons sharing a common myelin layer over their somata shall be addressed within this section.

Therefore a recent study, realized by the project's cooperation partners of the MedUni IBK, acquired confocal data of nervous structure showing this human peculiarity. Immunohistochemical sections were scanned on a Zeiss LSM 510 Meta confocal laser-scanning microscope equipped with a 63x/1.4 NA oil immersion lens. For detecting perikarya and their corresponding cell nuclei a 488 nm line of an argon ion laser and a 405 nm diode laser were used simultaneously. The pixel-sizes of the acquired 3D-stacks were chosen and calculated according the Nyquist theorem resulting in the following resolutions: x=38 nm, y=38 nm, z=122 nm.

Subsequently, for the sake of image processing, the acquired 3D - confocal image stacks of the SGC clusters were processed with Amira 5.3.3 (Mercury Computer Systems Inc., San Diego, CA, USA). Each stack was separated subsequently in its single channels allowing individual deconvolution for image restoration. Therefore, a theoretical point spread function was computed for each channel. The point spread functions were then used to deconvolute each channel using a non-blind maximum-likelihood image restoration algorithm for 40 iterations. To enhance signal-to-noise-ratio a median filter was applied to data prior to segmentation. Perikarya, their corresponding



nuclei as well as their direct contact area within a cluster were manually segmented using Amira's 'Segmentation Editor'. Segmentation data were saved in a label field which was used to quantify the volume of each structure as well as the contact area between cell bodies. For visualization data were smoothed by producing a surface from a resampled label field. Within this thesis four different clusters have been examined which are plotted in the following (see Fig. 4.7, Fig. 4.11, Fig. 4.14, Fig. 4.18).

In order to integrate this clustering to the model of the excitation of a neuron, the electrical circuit has to be adapted for the soma compartment of the neuron where the neurons face each other at a certain contact area. A new approach is presented in order to simulate the effect of ephaptic coupling. As explained in chapter 1 this term refers to electrical field interactions between neural elements and is deduced from the Greek term 'touch-onto'. Some more details are outlined in chapter 6.

The extended circuit is presented in Fig. 4.6 where  $V$  denotes the potential of the first cell and  $W$  denotes that of the second cell. The red arrows correspond to the electrical currents of the soma compartment of the first cell, whereas the blue ones indicate those of cell 2. This representation shall help to derive the equations for the two and three neuron cluster.

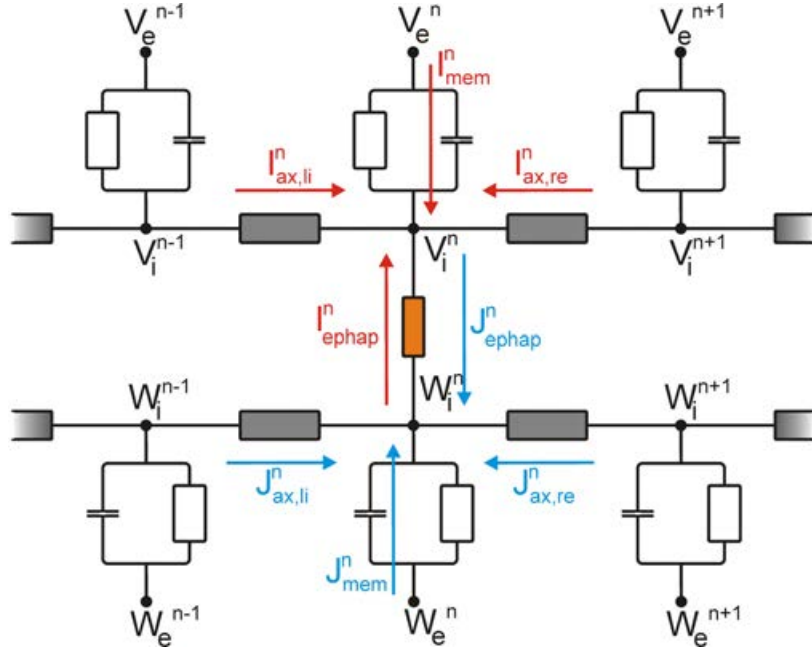


Figure 4.6: The electrical circuit shows the soma region of two neurons which are surrounded by one common sheet of myelin.  $I$  currents correspond to the first cell in the neuron cluster, whereas  $J$  currents describe those of the second cell.

Thus, the equations for the soma compartments will be again deviated by applying Kirchhoff's Law. This time the ephaptic current has to be included, i.e.,  $I_{ephap}^n$  denotes



the current from the inside of the first cell with an internal potential denoted as  $V_i^n$ . The corresponding current of the second cell is denoted as  $J_{ephap}^n$ . The extended equation therefore can be written as

$$\begin{aligned} I_{ephap}^n + I_{ax,re}^n + I_{ax,li}^n + I_{mem}^n &= 0 \\ J_{ephap}^n + J_{ax,re}^n + J_{ax,li}^n + J_{mem}^n &= 0. \end{aligned}$$

If ephaptic connections are considered to allow electrical current flow through a resistor from one intracellular soma compartment to the other intracellular soma compartment it follows

$$\begin{aligned} I_{ephap}^n &= G_E^n \cdot (V_i^n - W_i^n), \\ J_{ephap}^n &= G_E^n \cdot (W_i^n - V_i^n) = -I_{ephap}^n. \end{aligned}$$

Critical assumptions have to be made for the parameter  $G_E^n = g_E^n \cdot A_{contact}^n$  [mS/cm<sup>2</sup>] · [cm<sup>2</sup>] = [mS]. One layer of membrane typically has a conductance of  $g_E = 1$  mS/cm<sup>2</sup>. If two cells have direct contact one could assume two layers of membrane (summing up to  $g_E = 0.5$  mS/cm<sup>2</sup>) or also consider possible ionic flow through certain membrane specializations which might increase the value of  $g_E$ .

Depending on the number of neurons sharing a cluster these equations have to be further adapted. Within this theses basically two different neuron clusters are examined. On the one hand, three clusters have been reported where two neurons show membrane specialization on a certain common contact area. On the other hand, one three neuron cluster has been found where one middle neuron is connected to both other cells, each connecting at one side. Thus the outer two neurons only have one contact area to the cell in the middle, not having direct contact to each other.

For this kind of cluster the equations have to be rewritten. Now one has to keep track of three different transmembrane potentials varying with time, i.e.,  $V_n^1$  denotes the transmembrane potential at the n-th compartment of cell 1,  $V_n^2$  that of the n-th compartment of cell 2 and  $V_n^3$  corresponds to cell 3. Also the ephaptic currents will be denoted in the same manner, i.e.,  $I_{ephap,n}^1$  encodes for the ephaptic current of the n-th compartment of cell 1. Note that within this thesis only for the soma compartment itself ephaptic coupling is considered. Thus the  $n$  only involves the soma index which is 16 for the standard model neuron. For the ephaptic currents of the special three neuron cluster follows as

$$\begin{aligned} I_{ephap,n}^1 &= G_{E,n}^1 \cdot (V_{i,n}^1 - V_{i,n}^2), \\ I_{ephap,n}^2 &= G_{E,n}^1 \cdot (V_{i,n}^2 - V_{i,n}^1) + G_{E,n}^2 \cdot (V_{i,n}^2 - V_{i,n}^3), \\ I_{ephap,n}^3 &= G_{E,n}^2 \cdot (V_{i,n}^3 - V_{i,n}^2). \end{aligned}$$

Therefore, the differential equations have to be adapted according to these equations

$$\begin{aligned} I_{ephap,n}^1 + I_{axR,n}^1 + I_{axL,n}^1 + I_{mem,n}^1 &= 0 \\ I_{ephap,n}^2 + I_{axR,n}^2 + I_{axL,n}^2 + I_{mem,n}^2 &= 0 \\ I_{ephap,n}^3 + I_{axR,n}^3 + I_{axL,n}^3 + I_{mem,n}^3 &= 0. \end{aligned}$$

### 4.2.1 Cluster 1

The first detected cluster contains two cochlear neurons which are both considered to be apical neurons. Fig. 4.7 shows the blue colored nuclei of both neurons in the cluster. Cell 1 has a soma diameter of 17  $\mu\text{m}$  which is the green upper right neuron whereas the larger yellow cell 2 has a diameter of 21.39  $\mu\text{m}$  which is the left neuron at the bottom. The contact area was calculated to be 113.65  $\mu\text{m}^2$  which represents 12.52% of the total area of cell 1 and still 7.9% of the surface of cell 2.

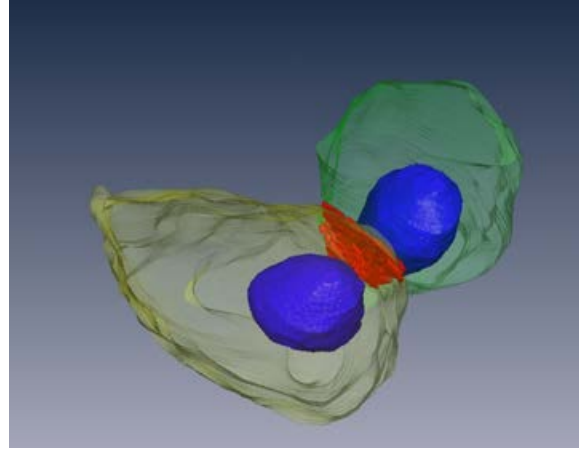


Figure 4.7: Arrangement of the first cluster, with the green cell 1 and yellow cell 2. The nuclei are plotted in blue, the contact area is displayed in red.

When the neurons are stimulated with intracellular current injection at the first dendritic compartment, the threshold value for this type of cell is either 0.06 or 0.07 nA has has been reported before. Again the sensitive parameters at the soma region shall be kept in mind, e.g. the length of the presomatic region  $l_{pre}$  is critical for the larger cell since  $d_{soma}^2 > 19 \mu\text{m}$  which means that the length has to be larger than a certain minimum. If therefore for cell 2  $l_{pre} = 50 \mu\text{m}$  holds, the spike breaks down at the soma region and is unable to successfully conduct the AP to the central end.

In a first experiment both presomatic regions were considered to be very long, 100  $\mu\text{m}$  which was the standard value of [Rattay et al. \(2001\)](#). The first cell received current input with a subthreshold amplitude of 0.05 nA, while the larger second cell was stimulated with 0.07 nA which leads to a successful propagation of an AP. All

the other parameters were held at their standard values, which also means that for both cells the whole soma region was modeled with three myelin layers.

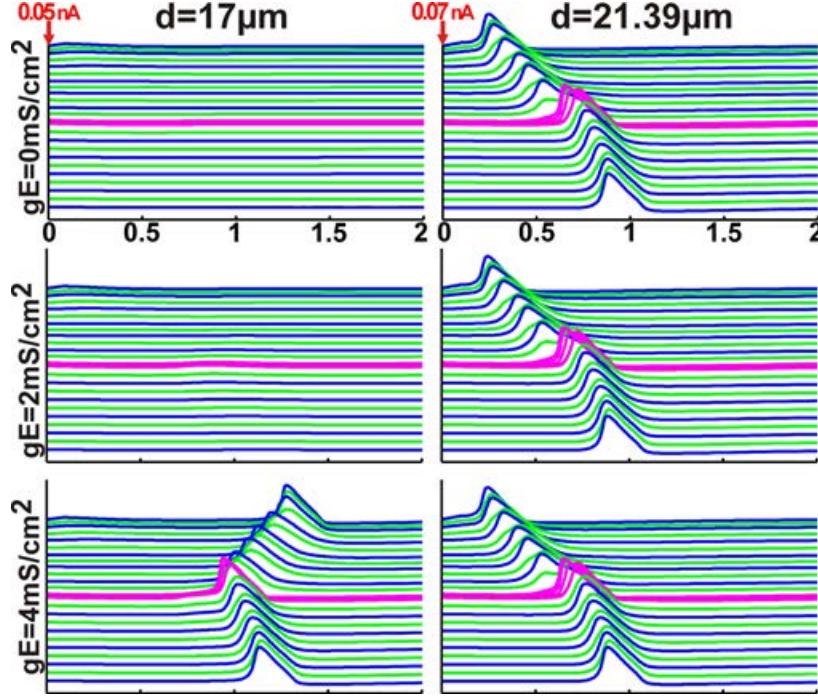


Figure 4.8: Long presomatic compartments  $l_{pre} = 100 \mu\text{m}$ . Cell 1 (left side) receives a 0.05 nA subthreshold stimulus, whereas cell 2 (right side) successfully initiates a spike induced by 0.07 nA current injection into the first compartment (top panels). When ephaptic coupling is considered, cell 1 initiates a spike at its soma for sufficient values of  $g_E$ .

The parameter  $g_E$  was increased step by step starting from 0, which means there is no connection between the two cells. As already mentioned, for this case the first cell fails to initiate a spike which can be seen in the left upper panel of Fig. 4.8. The bigger cell 2 successfully initiates the spike at the first compartment, which then travels along the dendrite with a certain delay over the soma region and then further propagates to the model neuron's central end (upper right panel of Fig. 4.8). The corresponding  $AP_{height}$  at the soma of cell 2 was 102.5 mV which appeared 0.725 ms after spike onset. The AP arrives at compartment 27, which is the last compartment of the short axon model, 0.883 ms after onset.

These values remain almost unchanged when the ephaptic conductance  $g_E$  is increased to 1 mS/cm<sup>2</sup>. When  $g_E = 2 \text{ mS/cm}^2$  the transmembrane potential at the soma of cell 1 starts to get slightly depolarized due to the current flow from the supporting cell 2 soma. As a consequence thereof the  $AP_{height}$  at the soma of cell 2 reduces, although the peak time at the soma and also at the central end are almost unchanged. This effect further increases for  $g_E = 3 \text{ mS/cm}^2$ .

When the value of the ephaptic conductance is increased to  $4 \text{ mS/cm}^2$  the first cell will be excited by the propagating spike of the second one and is able to trigger an AP initiation at the soma compartment, which will then travel to both directions (left bottom panel of Fig. 4.8). This spike of cell 1 has an  $AP_{height}$  at the soma of  $99.39 \text{ mV}$  which appears at  $0.983 \text{ ms}$ , while the AP at the soma of cell 2 is only  $1 \text{ mV}$  decreased with almost unchanged the temporal properties of the spike. The AP of cell 1 is initiated  $0.983 \text{ ms}$  after spike onset which means a delay of  $0.25 \text{ ms}$  compared to cell 2. The spike therefore will arrive at the central end of cell 1 quite late  $1.136 \text{ ms}$  after onset.

When the ephaptic conductance is further increased the  $AP_{height}$  of cell 1 increases while the  $AP_{height}$  of cell 2 decreases and very soon will be smaller than that of cell 1. Still the spike of cell 2 will not suffer of significant delay when it excites cell 1, which by contrast certainly speeds up for increasing values of  $g_E$ . For very large values, it is even possible to obtain almost synchronized spikes. Furthermore it should be noted that the same results are predicted without any stimulating current of cell 1, i.e., if  $IC_{stim}^1 = 0 \text{ nA}$  holds, an ephaptic conductance value of  $g_E = 4 \text{ mS/cm}^2$  will lead to excitation of cell 1 when cell 2 propagates a spike after a current injection of  $IC_{stim}^1 = 0.7 \text{ nA}$  at the first compartment.

Some more interesting results can be obtained, when the amount of myelin layers  $nm^1$  and  $nm^2$  are changed, e.g. if for both somata only one layer is used and only the bigger cell 2 will be stimulated with intracellular current injection, even  $g_E = 3 \text{ mS/cm}^2$  is enough to trigger an AP initiation at the soma of cell 1. This produces an  $AP_{height}$  at the soma of  $95.24 \text{ mV}$  of cell 1 and  $100.7 \text{ mV}$  of cell 2. While the spike of cell 2 appears at the soma  $0.71 \text{ ms}$  after onset, cell 2 initiates certainly later at  $1.23 \text{ ms}$ . The AP arrives at the model end of cell 2 after  $0.87 \text{ ms}$ , but it needs  $1.34 \text{ ms}$  to get to the end of cell 1. On the other hand if 5 layers are used for both somata, the same value of the ephaptic conductance of  $g_E = 4 \text{ mS/cm}^2$  is needed to successfully excite the first cell, but all the spike properties almost remain unchanged compared to the standard case of  $nm = 3$ .

For a second set of experiments both presomatic regions were shortened to  $50 \mu\text{m}$  which certainly changes the excitation profile. When both SGCs are stimulated with  $0.07 \text{ nA}$ , the smaller cell is able to fully conduct the AP over the soma region with the reduced length of the presomatic region, but the spike propagation of the bigger cell breaks down at the soma. The results are displayed in the top panels of Fig. 4.9.

The  $AP_{height}$  at the soma of cell 1 is  $101.5 \text{ mV}$ , whereas the transmembrane potential at the soma of cell 2 only reaches  $4.33 \text{ mV}$ . The spike of cell 1 appears  $0.767 \text{ ms}$  after spike onset and will reach compartment 27 at  $0.924 \text{ ms}$ . If the ephaptic conductance value is increased, the  $AP_{height}$  at the soma of cell 1 reduces since some current is lost to load the soma of cell 2, which further depolarizes. The temporal properties of the spike of cell 1 remain almost unchanged.

But still if the bigger cell 2 is stimulated with a current that displays this behavior,

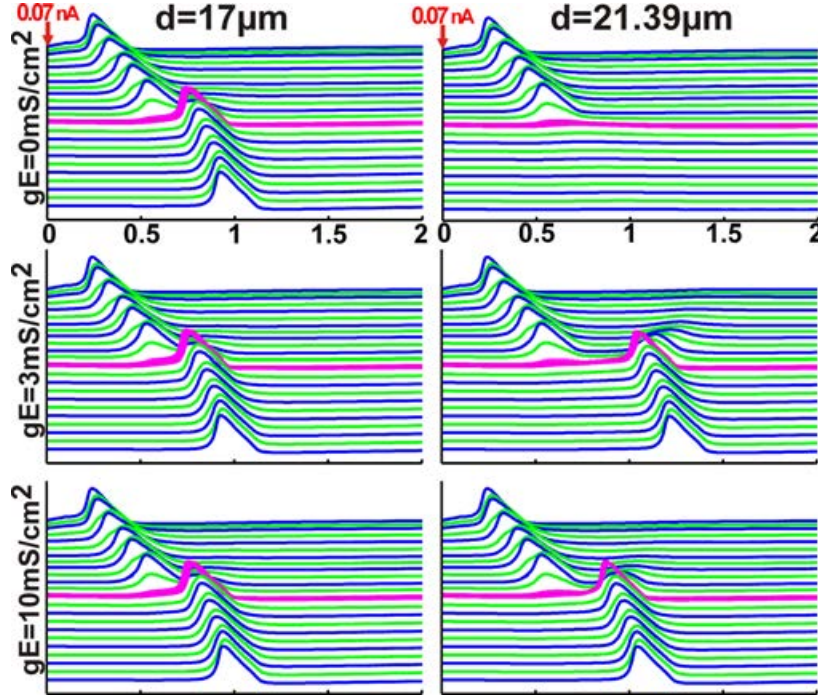


Figure 4.9: Short presomatic compartments  $l_{pre} = 50 \mu\text{m}$ . Both cells are stimulated with  $0.07 \text{ nA}$  current injection into the first compartment, but the spike of the bigger cell 2 breaks down at the soma due to the reduced presomatic length (top right). Still if enough current of the left cell 1 is supplied through ephaptic coupling, cell 2 will be excited with an observed delayed transmission over the soma region.

i.e., the spike breaks down at soma for  $IC_{stim}^1 = 0.07 \text{ nA}$ , it is possible to generate a successful spike with  $g_E \geq 3 \text{ mS/cm}^2$ . The middle panels of Fig. 4.9 represent the results for  $g_E = 3 \text{ mS/cm}^2$ . The spike of cell 2 does not break down but succeeds to overcome the soma region although with a quite long delay. The  $AP_{height}$  of cell 1 is only  $93.47 \text{ mV}$  which appears  $1.069 \text{ ms}$  after spike onset and reaches the model end at  $1.217 \text{ ms}$ .

Further increase of ephaptic conductance results in decreasing spike height at the soma of cell 1 but increasing height for cell 2. The temporal parameters of cell 1 remain almost unchanged but the delay over the soma region and therefore also the traveling time of the spike certainly reduces. For a value of  $g_E = 10 \text{ mS/cm}^2$  the spikes have almost the same height at the somata of both cells, and also the peak times at the model neuron's end are only  $0.099 \text{ ms}$  apart.

Another interesting results can be observed for stimulating the bigger cell 2 only at a subthreshold level, i.e.,  $0.05 \text{ nA}$ . In contrast to the upper experiments, this stimulation mode of cell 2 fails to even initiate an AP (right top panel of Fig. 4.10). Again with the right choice for the ephaptic conductance  $g_E$  a propagating spike of



cell 1 will depolarize the soma region of cell 2 with proceeding spike invasion to both processes. In particular, if  $5 \leq g_E \leq 8$  holds, both cells will conduct an AP to the central end.

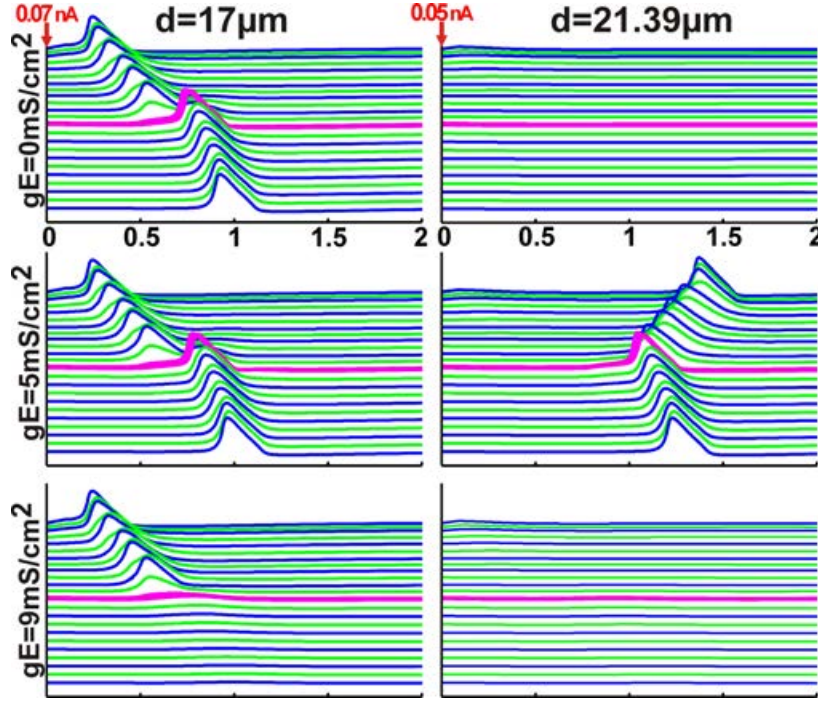


Figure 4.10: Short presomatic compartments  $l_{pre} = 50 \mu\text{m}$ . Contrary to Fig. 4.9 cell 2 only receives 0.05 nA and thus fails to even initiate a spike (top right). For  $5 \leq g_E \leq 8$  both cells propagate the spike to their central ends, but for higher values the spike of cell 1 breaks down at the soma region due to large current loss (bottom left).

The middle panels of Fig. 4.10 display the case of  $g_E = 5 \text{ mS/cm}^2$ , where the  $AP_{height}$  at the soma of cell 1 is reduced to 99.59 mV and a quite similar value for cell 2 of 98.55 mV. For these trials even a small delay of the spike propagation in cell 1 can be observed when it has to support cell 2. Furthermore the AP of cell 2 appears certainly later than that of cell 1, but the gap is not as pronounced as in the previous simulations. Still the striking difference is, that when the conductance gets to big, i.e.,  $g_E \geq 9 \text{ mS/cm}^2$ , the propagation for both cells breaks down, since too much current of cell 1 will escape to the bigger cell 2. This is illustrated in the bottom panels of Fig. 4.10.

Again the observed alteration of the excitation profiles for both cells in cluster 1 remain the same if the amount of myelin layers at the connected somata is changed. If for both cell bodies  $nm = 1$  holds the range for successful excitation of both cells changes to  $4 \leq g_E \leq 20$ . But when both somata have 5 layers of myelin only an ephaptic conductance of either 5 or 6  $\text{mS/cm}^2$  results in spike conduction to the central end of cell 1 and cell 2.

### 4.2.2 Cluster 2

The second detected cluster also contains two apical cochlear neurons which are displayed in Fig. 4.11. But for this cluster both somata are similar concerning their size. Cell 1 has a soma diameter of  $18.3\text{ }\mu\text{m}$  which is displayed in yellow at the left side in the back, cell 2 has almost the same value of soma diameter, i.e.,  $18.35\text{ }\mu\text{m}$  and is shown in green at the right side in the front.

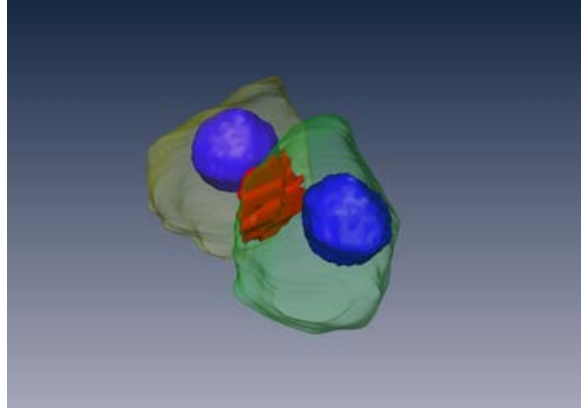


Figure 4.11: Arrangement of the second cluster, with the yellow cell 1 and green cell 2. The nuclei are plotted in blue, the contact area is displayed in red.

The contact area was calculated to be  $83.41\text{ }\mu\text{m}^2$  which represents about 7.9% of the total area. Note contrary to the first cluster, the influence on each other is equal and furthermore cluster 2 is also generally the one with the smallest contact area in terms of the relation to the surface area of the two enclosed neurons. For both cells the threshold value for intracellular current injection is either 0.06 or 0.07 nA, where a presomatic length of  $l_{pre} = 50\text{ }\mu\text{m}$  is of course more sensitive, but since both cells have a soma with a diameter smaller than  $19\text{ }\mu\text{m}$  they are able to successfully transmit a spike over the sensitive soma region.

The first set of experiments again consider both presomatic regions to be very long,  $100\text{ }\mu\text{m}$ . No matter if the first cell only receives subthreshold current input, e.g.,  $IC_{amp}^1 = 0.05\text{ nA}$ , or even no stimulus at all, it is able to initiate a spike at its soma with the help of the second cell. Again the right choice of the ephaptic conductance leads to enough current flow from one soma to the other and therefore also a propagating spike to the neuron's end which is illustrated in Fig. 4.12.

In the upper panel  $g_E = 0\text{ mS/cm}^2$  holds, the slightly smaller cell 1 receives no current input and the current injection of  $IC_{amp}^2 = 0.07\text{ nA}$  into the first compartment of cell 2 leads to a propagating spike with an  $AP_{height}$  at the soma of  $102.8\text{ mV}$  which appears  $0.712\text{ ms}$  after stimulus onset and arrives at  $0.872\text{ ms}$  at compartment 27. For this experiment the corresponding temporal change in transmembrane potential



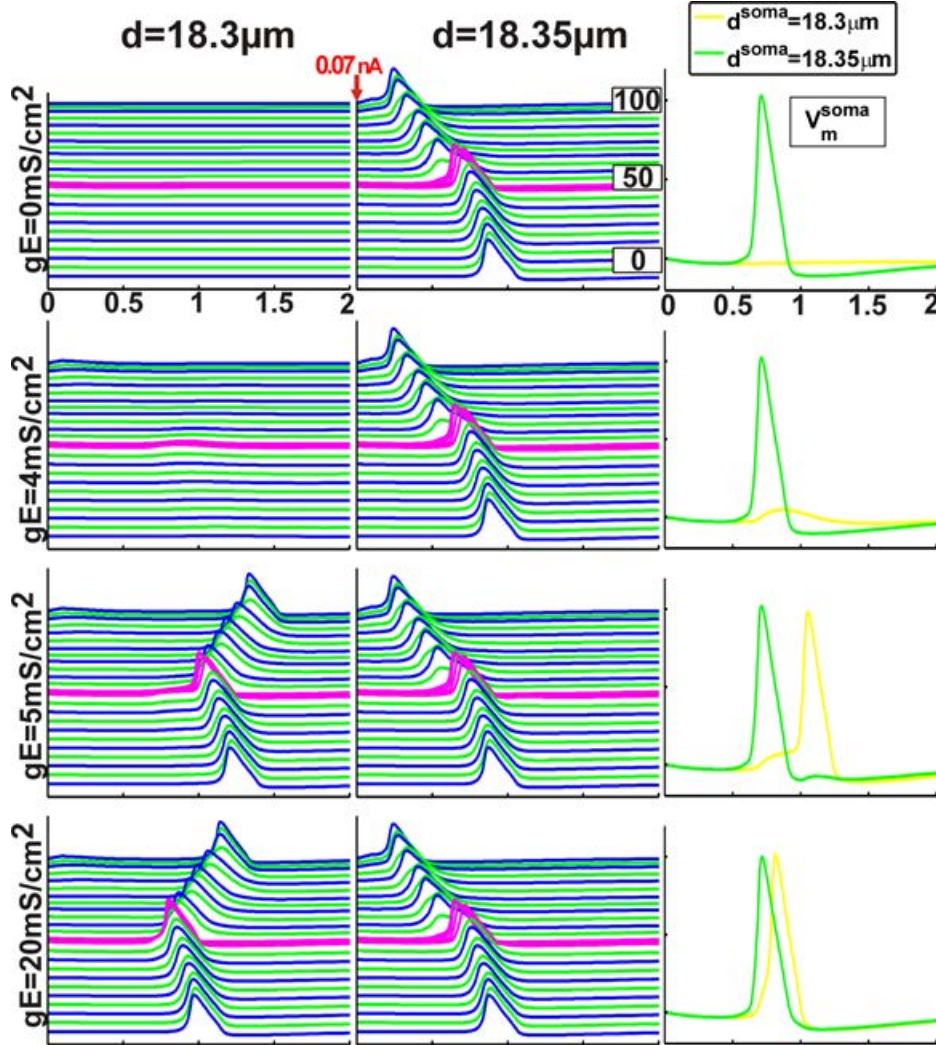


Figure 4.12: Long presomatic compartments  $l_{pre} = 100 \mu\text{m}$ . Only cell 2 (middle panel) is stimulated by  $0.07 \text{ nA}$ . If the ephaptic effect is strong enough, the inactive cell 1 (left panel) initiates a spike at its soma with further synchronization according to the spike of cell 2 for increasing values of  $g_E$ . The right column illustrates the time course of the two transmembrane potentials at the soma compartments.

at the soma compartments are also presented at the right side. The used colors match the representation in Fig. 4.11.

When the ephaptic conductance  $g_E$  is increased, again some current will be lost at the soma of cell 2 which leads to decreasing values of  $AP_{height}$  while the temporal properties almost remain the same. Meanwhile the soma of cell 1 gets further depolarized, e.g., the second row of Fig. 4.12 illustrates the case of  $g_E = 4 \text{ mS/cm}^2$ . The right panel shows that the transmembrane potential reaches a subthreshold level of  $4.595 \text{ mV}$ .

If  $g_E \geq 5$  mS/cm<sup>2</sup> holds, the first cell receives enough current to initiate a spike which will then propagate to both direction, i.e., to the peripheral and the central end. For  $g_E = 5$  mS/cm<sup>2</sup> the  $AP_{height}$  of cell 1 is 98.38 mV which appears quite late 1.053 ms after the stimulus onset of cell 2. This spike then arrives at 1.209 ms at the central end of cell 1 which means a delay of 0.337 ms compared to cell 2. But this difference can be decreased, i.e., the spikes of the cells get synchronized, for higher values of the ephaptic conductance. This can be observed in the bottom row of Fig. 4.12, where a high value of  $g_E = 20$  mS/cm<sup>2</sup> results in a small difference of arrival time at compartment 27 of 0.094 ms. The  $AP_{height}$  of cell 1 which is 101.6 mV now exceeds the corresponding value of 99.95 mV. The yellow and green transmembrane potentials in the right panel show the small difference in peak times at the somata, i.e., the peak of the yellow cell 1 soma appears at 0.814 ms and that of the green cell 2 soma at 0.715 ms.

For all other experiments both presomatic regions were shortened to 50  $\mu$ m. Furthermore the stimulation mode remained the same, i.e., the first cell receives a sub-threshold current of 0.05 nA while the second cell is stimulated by a current injection of 0.07 nA. For this value of  $IC_{amp}^2$  cell 2 usually would trigger an AP which then successfully conducts over the soma region to the central end as long as no ephaptic coupling to a cluster-sharing cell is considered. But for this certain cluster properties, i.e., the quite similar size of somata and the contact area, certainly negative influence of excitation on each other can be observed.

This means that when the standard value of the degree of myelination is chosen for both cell somata, i.e.,  $nm^1 = 3$  and  $nm^2 = 3$ , it is not possible to excite the first cell through ephaptic coupling no matter which value is chosen for  $g_E$ . Even more if  $g_E \geq 5$  mS/cm<sup>2</sup> holds then cell 2 will fail to propagate the spike to its central end, since too much current is lost at the soma. In order to test the influence of the myelin layers, three different values of the parameter  $nm$  were tested, i.e.,  $nm = 1, 3, 5$  as explained in the following text. Additionally Fig. 4.13 illustrates the three different cases of  $nm$  for two selected values of  $g_E$ .

Basically it should be noted that when  $g_E = 0$  mS/cm<sup>2</sup> the spike properties of cell 2 slightly change when the amount of layers is altered. Although the  $AP_{height}$  at the soma almost stays the same, the time at which the AP arrives at the soma and therefore also the time at which the spike arrives at the central end changes. For  $nm = 1$  the time of the peak at compartment 27 is 0.917 ms, whereas for  $nm = 3$  the peak time is 0.981 ms and  $nm = 5$  leads to 1.011 ms.

The striking difference concerning the degree of myelination at the soma is that although for  $nm = 5$  the same suppressing behavior as for  $nm = 3$  can be observed, the effect of ephaptic coupling certainly changes for  $nm = 1$ . As mentioned before, when  $nm = 3$  holds no value of  $g_E$  exists which will lead to a successful spike initiation of cell 1 through current supply of cell 2. Even more, for  $g_E \geq 5$  mS/cm<sup>2</sup> too much current is lost and the spike breaks down at the soma of cell 2 values, so that none

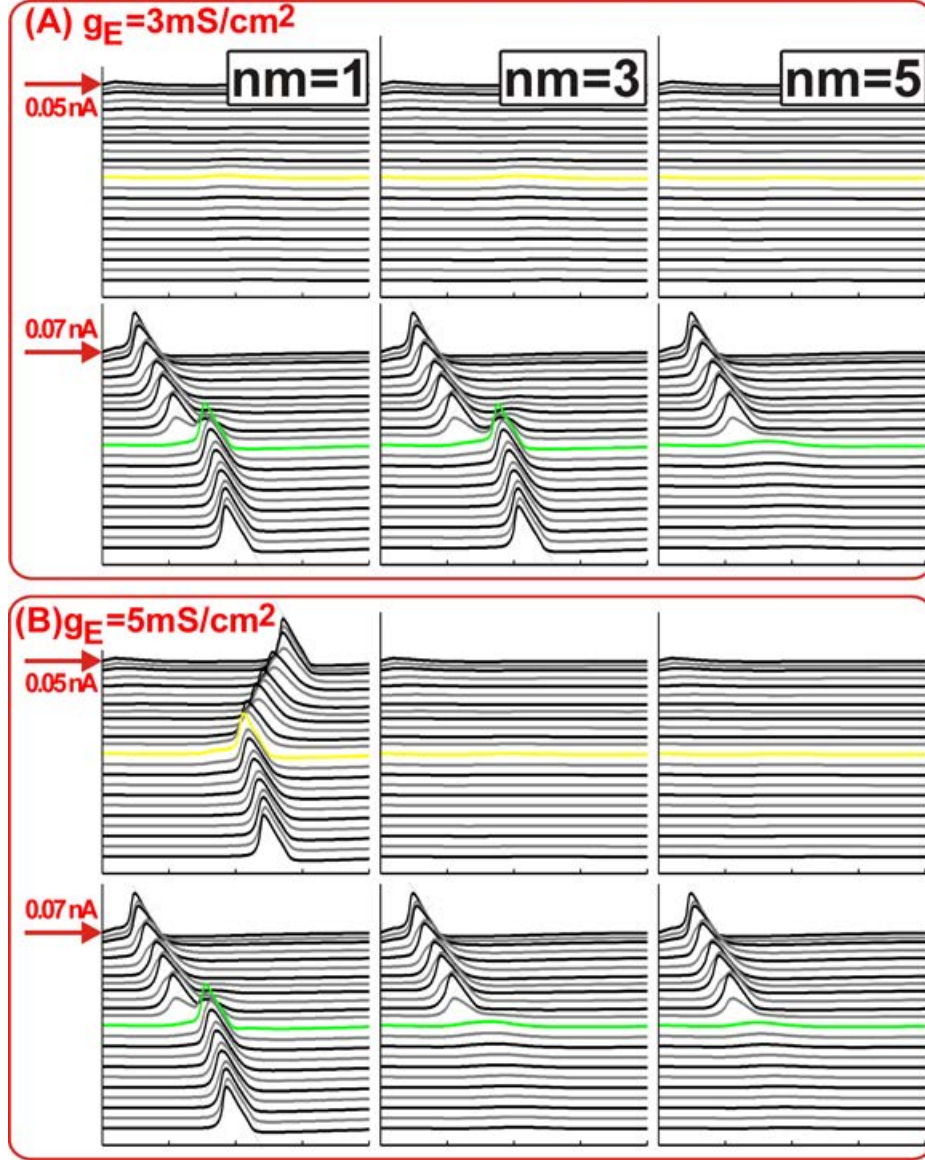


Figure 4.13: Negative influence of clustering for short presomatic lengths  $l_{pre} = 50 \mu\text{m}$ . Results for varying degree of myelination for two selected values of  $g_E$ . (A) The first row shows cell 1 stimulated with subthreshold  $0.05 \text{ nA}$  which is connected to a spiking cell 2 after  $0.07 \text{ nA}$  current injection (second row) with  $g_E = 3 \text{ mS/cm}^2$ . (B) The same pattern for  $g_E = 5 \text{ mS/cm}^2$ . Details are described in the text.

of the cells transmits and AP. But when  $nm = 5$  this break down appears for smaller values of the ephaptic conductance, i.e., for  $g_E \geq 3 \text{ mS/cm}^2$ .

Surprisingly if  $nm = 1$  holds, for ephaptic conductance values of  $5 \leq g_E \leq 18 \text{ mS/cm}^2$  cell 2 is able to depolarize cell 1 leading to successful AP transmission while keeping enough current to itself for an ongoing spike conduction. For higher values,

the spike again breaks down at the soma of cell 2 and no AP is initiated at cell 1. When  $g_E = 5 \text{ mS/cm}^2$  the  $AP_{height}$  at the soma of the excited cell 2 is 99.31 mV and 97.2 mV at the initiating soma of cell 1. The spike arrives at compartment 27 of cell 2 0.934 ms after its current injection and the triggered spike of cell 1 arrives later at 1.211 ms. When the value of  $g_E$  is increased, the  $AP_{height}$  of cell 1 rapidly exceeds that of cell 2 and the spikes get increasingly synchronized. For  $g_E = 18 \text{ mS/cm}^2$  the  $AP_{height}$  at cell 1 is 99.17 mV and that of cell 2 only 93.32 mV, but the difference in the arrival times of the two spikes is reduced to 0.093 ms.

Fig. 4.13A illustrates the case of  $g_E = 3 \text{ mS/cm}^2$  when three different degrees of myelination of both cells are considered. The top panels correspond to cell 1 with its yellow soma which only receives a current injection of a subthreshold value of 0.05 nA. By contrast the green cell 2 presented in the bottom row receives 0.07 nA which leads to successful spike transmission for  $nm = 1$  and also still  $nm = 3$ . Note that since for  $nm = 5$  only  $g_E = 1$  or  $g_E = 2$  allows for an ongoing transmission to the central end of cell 2, the AP breaks down at the green soma which can be seen in the bottom right panel.

In Fig. 4.13B  $g_E = 5 \text{ mS/cm}^2$  holds. This value has been selected because it is the first value of the ephaptic conductance where the AP also breaks down at the soma for  $nm = 3$  illustrated in the top middle panel. Additionally this value of  $g_E$  is also the first where  $nm = 1$  leads to successful excitation of cell 1. Still a certain delay of the yellow cell 1 soma compartment can be observed compared to cell 2 with the green soma presented below.

### 4.2.3 Cluster 3

The third detected cluster also contains two very small cochlear neurons which both are of the middle turn. Their position to each other is presented in Fig. 4.14. Again both somata of the third cluster are of similar size, where cell 1 has a soma diameter of 12.03  $\mu\text{m}$  which is displayed in yellow at the left side in the back, cell 2 has almost the same value of soma diameter, i.e., 12.53  $\mu\text{m}$  and is shown in green at the right side in the front.

The contact area was calculated to be 74.79  $\mu\text{m}^2$  which represents about 16.5% of the total area of cell 1 and still 15.2% of cell 2. Therefore this cluster arrangement leads to the biggest influence of the cells on each other. Nonetheless since both somata are that small, the two neurons are not as restrictive concerning variations in critical parameters. The presomatic length does not affect the safety factor of AP transmission and the threshold values for intracellular current injection are again either 0.06 or 0.07 nA.

Initially again simulations were performed for 100  $\mu\text{m}$  long presomatic regions of both neurons in the third cluster. When cell 2 receives a current injection of 0.07 nA it triggers an AP which conducts to the central end, and also supplies enough

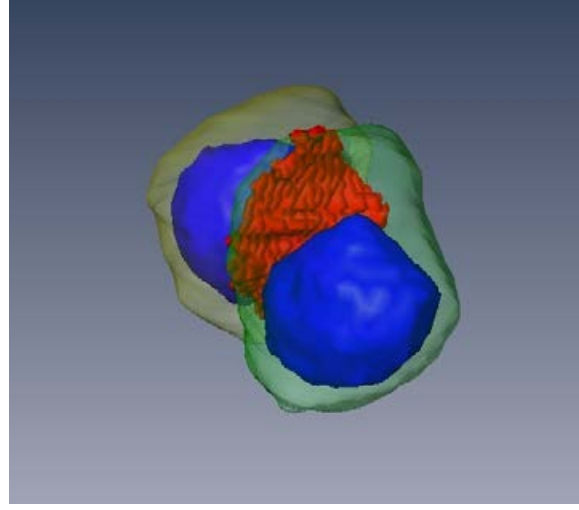


Figure 4.14: Arrangement of the third cluster, with the yellow cell 1 and green cell 2. The nuclei are plotted in blue, the contact area is displayed in red.

current for the excitation of cell 1 at their connected somata if the right value for the ephaptic conductance  $g_E$  is used. This is exactly the same behavior as for the previously discussed neuron clusters, but since both cells are very small and their contact area relatively large, the evaluated spike properties slightly differ.

For  $g_E \geq 4 \text{ mS/cm}^2$  the unstimulated cell 1 initiates a spike at its soma with a height of 100.1 mV at 0.95 ms. Compared to cell 2 which has an  $AP_{height}$  at the soma of 102.8 mV which appears 0.682 ms after stimulus onset, the difference in the peak times at compartment 27 are smaller than for the other clusters. For this value of  $g_E$ , which is the first to allow for a spiking cell 1, the delay at the end of cell 1 compared to cell 2 is 0.258 ms. When  $g_E$  is increased this delay rapidly shrinks and also the  $AP_{height}$ 's and corresponding peak times at the soma assimilate, i.e., the cells get synchronized.

The next step was to decrease both lengths of the presomatic compartments to 50  $\mu\text{m}$  to check if the same behavior as for the previous two clusters can be observed, i.e., that a subthreshold impulse for cell 1 harms a propagating spike of cell 2 resulting in the break-down of the AP at the soma for certain values of  $g_E$ .

Interestingly for these small soma sizes the inhibiting effect of ephaptic coupling seems to be absent at first sight. As for the unmyelinated cell bodies in cluster 2, the right choice of the ephaptic conductance leads to initiation and successful propagating of an AP on cell 1 while cell 2 keeps enough current to transmit its own spike to the central end.

The first value of  $g_E$  to excite cell 1 is again  $4 \text{ mS/cm}^2$  where cell 2 has an  $AP_{height}$  at the soma of 101.8 mV appearing at 0.698 ms, leading to a cell 1  $AP_{height}$  of 100.6 mV at 0.873 ms. Thus a delay of 0.217 ms can be observed at compartment 27



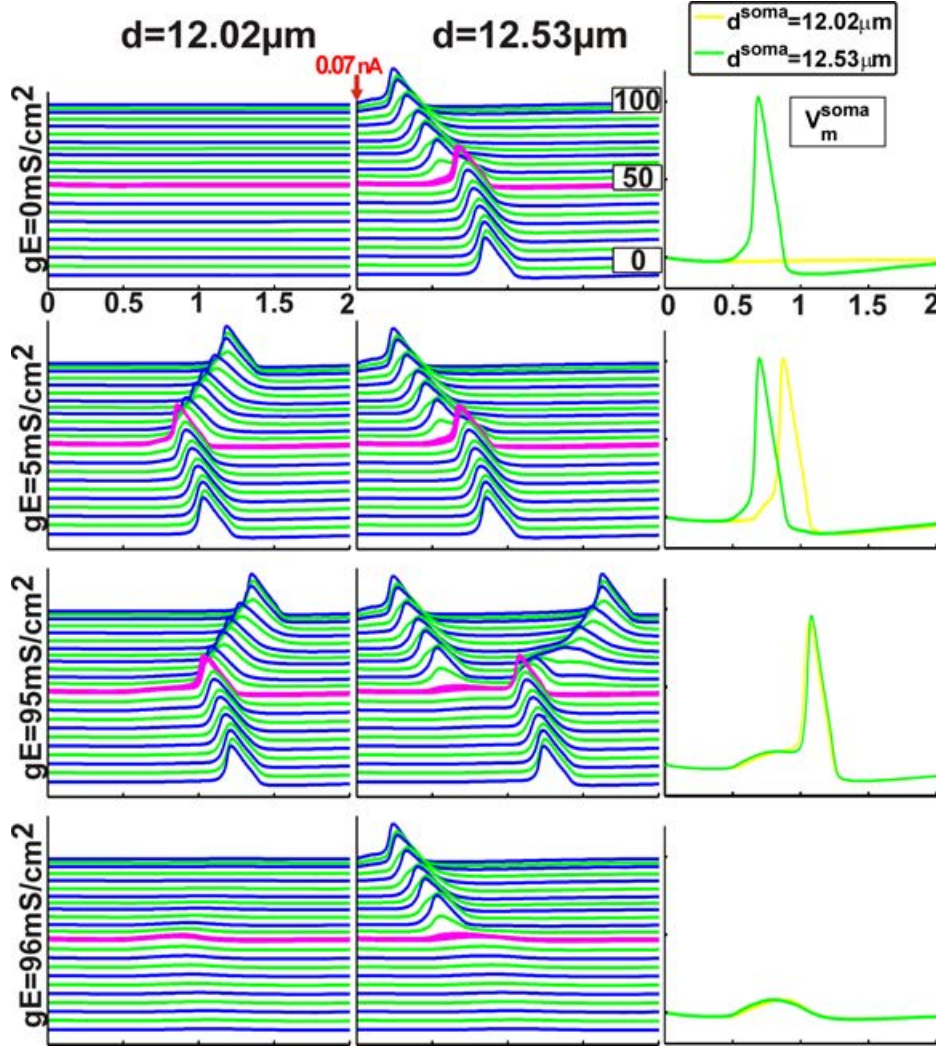


Figure 4.15: Synchronization and inhibiting effect of clustering for short presomatic lengths  $l_{pre} = 50 \mu\text{m}$ . Same stimulus current and figure assembly as in Fig. 4.12 with stronger synchronization for lower values of  $g_E$  compared to cluster 2. The inhibiting effect of cluster 3 appears not until high values of  $g_E$ , i.e., for  $4 \leq g_E \leq 95 \text{ mS/cm}^2$  both cells successfully conduct the AP to the end. Compare smaller range for cluster 2 in Fig. 4.13

between the two cells. The second row of Fig. 4.15 illustrates the case for  $g_E = 5 \text{ mS/cm}^2$ , where again the temporal change in transmembrane potential at the soma of both cells is plotted at the right side. Surprisingly, for this third cluster the ephaptic conductance can be increased to very high theoretical values of about  $100 \text{ mS/cm}^2$ , but then again cell 1 inhibits cell 2 at their connected somata resulting in the absence of any spike transmission.

More precisely, if  $g_E \geq 96 \text{ mS/cm}^2$  both cells are unable to propagate the spike

which is illustrated in the bottom row of Fig. 4.15. But for the last supporting value of  $g_E = 95 \text{ mS/cm}^2$  the appearance of the APs at the somata is almost identical and the spike at cell 2 was held back for such a long time that the peripheral process gets depolarized again and transmits the same spike back to the dendrite ending. This can be observed in the middle panel of the third row in Fig. 4.15.

For this cluster additionally the synchronizing effect of ephaptic coupling was analyzed more precisely. Therefore both cells received a current injection of 0.07 nA into their first compartments but at different times. Cell 1 was stimulated right away, i.e., at  $t = 0 \text{ ms}$ , but for cell 2 the onset of the spike was varied from 0 to 2 ms. But initially the effect of the degree of myelination at the soma was clarified. Thus, a set of experiments was performed, all considered an immediate current of injection of 0.07 nA for cell 1, whereas cell 2 was stimulated with 0.07 nA after  $IC_{delay}^2 = 0.1 \text{ ms}$ .

For the standard case of  $nm^1 = 3$  and  $nm^2 = 3$  the spikes of both neurons have approximately the same height due to similar soma size, but the spike of cell 2 arrives 0.105 ms later at the central end. This delay is reduced when ephaptic coupling is present. When  $g_E = 2.5 \text{ mS/cm}^2$  this delay is reduced to 0.081 ms, for  $g_E = 5 \text{ mS/cm}^2$  to 0.67 ms and for  $g_E = 10 \text{ mS/cm}^2$  to only 0.051 ms. Thus the spikes get synchronized for increasing ephaptic conductance. This simulation trial was repeated for  $nm = 1$  and  $nm = 5$  for both somata. Since only tiny differences could be observed for the subsequent simulations the case of unmyelinated somata within the cluster was used, i.e.,  $nm^1 = 1$  and  $nm^2 = 1$ .

The third cluster with the mentioned parameter values of  $l_{pre} = 50 \text{ }\mu\text{m}$  and  $nm = 1$  and stimulus intensity of 0.07 nA for both cells was then tested for varying delay of current injection into cell 2. For each value the ephaptic conductance was varied in the range of 0 to 20 mS/cm<sup>2</sup>. The results for 4 different values of the delay of stimulus 2 and 4 different values of  $g_E$  are presented in Fig. 4.16 where only the temporal change in transmembrane potential of the two somata are plotted. Again the used colors match the cell representation in Fig. 4.14.

The first row illustrates the case of a very small current injection delay of 0.1 ms for the green cell 2. As it has been mentioned for  $nm = 3$ , the same relation for the reduction of the delay at the neuronal endings can be observed for increasing  $g_E$ , i.e., the delay of 0.101 ms for no connection is reduced to 0.052 ms for  $g_E = 10 \text{ mS/cm}^2$ . It should be noted that for  $g_E = 0$  the AP at the soma of cell 1 appears at  $t = 0.678 \text{ ms}$  and that of cell 2 at  $t = 0.7795 \text{ ms}$ . When  $g_E$  is raised the time at which the peak occurs at the soma of cell 1 only slightly increases whereas the peak of cell 2 will be initiated faster. Thus the synchronization speeds up cell 2 rather than slowing down cell 1.

It is very interesting that regardless of the delay of cell 2 stimulation, the spikes get almost completely synchronized for at least  $g_E = 10 \text{ mS/cm}^2$  which can be seen in the right column of Fig. 4.16. This must be a result of the small soma sizes which



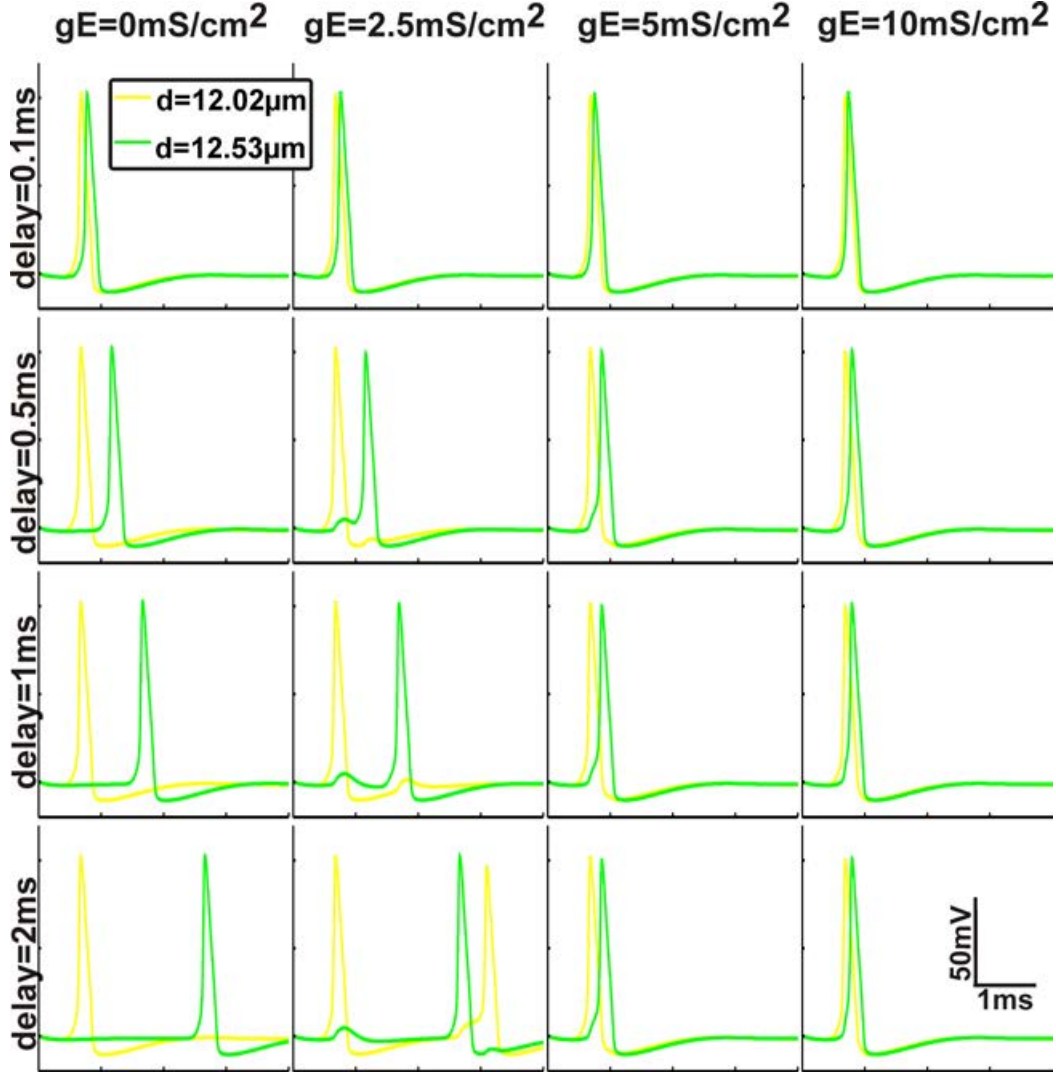


Figure 4.16: Synchronization effect of ephaptic coupling for different delay between  $I_{stim}^1$  and  $I_{stim}^2$  both with  $IC_{amp} = 0.07$  nA. The lines illustrate the time course of the transmembrane potentials at the soma of cell 1 (yellow), always stimulated at  $t = 0$  ms, and cell 2 (green) for different values of  $g_E$  (columns) and increasing delay of current injection of cell 2 (rows). For  $g_E \geq 5$  mS/cm<sup>2</sup> the spikes are synchronized regardless of the time between stimulation (third column).

are insensitive to parameter variations. Additionally the big contact area allows for strong ephaptic coupling effects on each other. When the stimulus of cell 2 is delayed for 1 ms,  $g_E = 2.5$  mS/cm<sup>2</sup> still results in a corresponding delay at the end of the cells, i.e., the spike of cell 2 arrives about 1 ms later at the central end compared to the spike arrival time of cell 1. Still the effect of the clustering is visible at the soma compartments, where current flow between the cells alters the transmembrane

potentials, e.g., compare corresponding yellow and green lines of the first column where no ephaptic coupling is considered to the second column where  $g_E = 2.5 \text{ mS/cm}^2$ . But when  $g_E$  is raised to  $5 \text{ mS/cm}^2$ , immediately the spikes become synchronous at the soma which results in a reduction of the delay between the spike arrival times to only  $0.178 \text{ ms}$ , i.e., the spikes of both cells arrive at the central ends almost at the same time. Generally it can be observed that the  $AP_{height}$ 's at both somata slightly reduce, with a reduction of  $2\text{-}4 \text{ mV}$  for cell 1 and below  $2 \text{ mV}$  for cell 2.

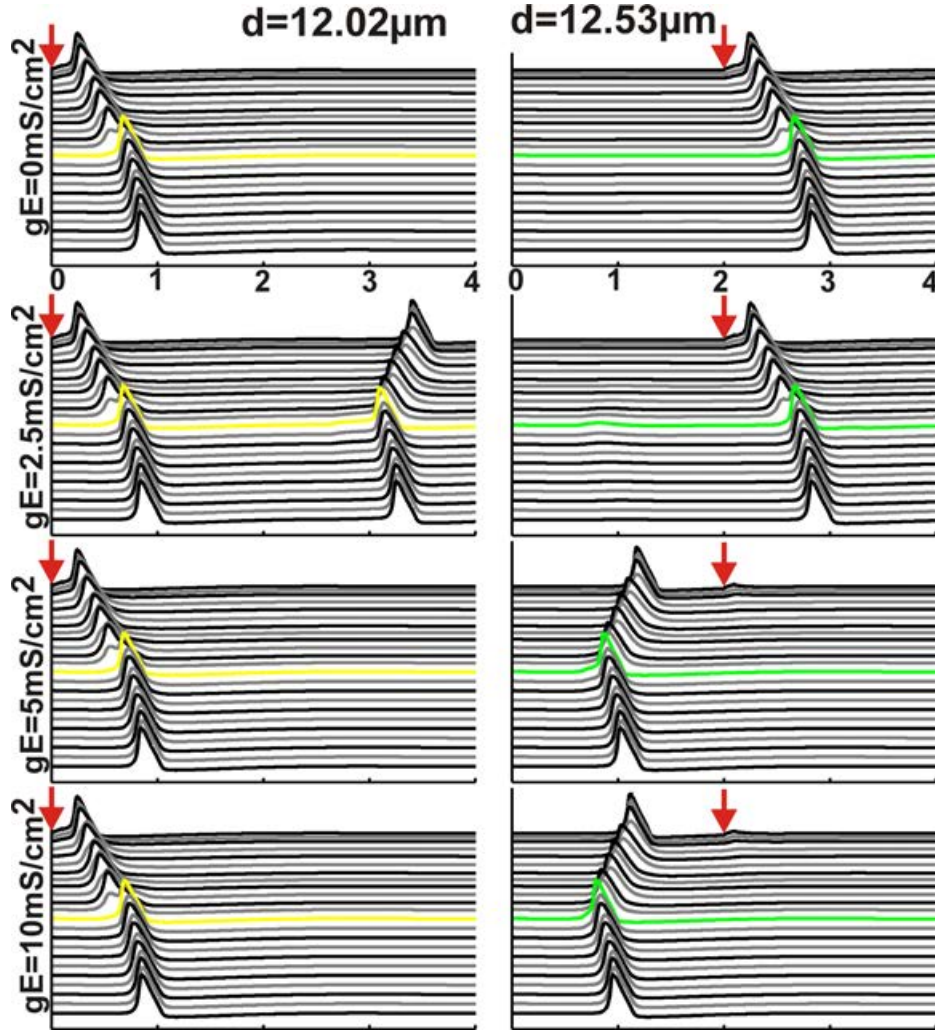


Figure 4.17: Synchronization effect of ephaptic coupling for  $IC_{delay}^2 = 2 \text{ ms}$ . Excitation profiles are plotted for cell 1 which receives  $0.07 \text{ nA}$  at  $t = 0 \text{ ms}$  (left side) and cell 2 which receives  $0.07 \text{ nA}$  at  $t = 2 \text{ ms}$  (right side). Red arrows indicate the time of current injection. Different values of  $g_E$  (rows) are presented which is explained in the text.

A very long delay of  $2 \text{ ms}$  displays a significant behavior which can be seen in the last row of Fig. 4.16, where an ephaptic conductance of  $2.5 \text{ mS/cm}^2$  is too weak to

supply enough current for cell 2 to initiate simultaneously with cell 1, but the later spike of cell 2 again depolarizes the soma of cell 1, which after passing its refractory period will again conduct a spike to both ends. Since this configuration leads to more observation on the refractory behavior of both cells the traveling spikes and thus the whole excitation profiles are plotted in Fig. 4.17.

In Fig. 4.17 the smaller cell 1 which receives 0.07 nA immediate current injection at  $t = 0$  ms is plotted at the left side with its yellow soma. The green cell 2 is stimulated at  $t = 2$  ms. When no ephaptic coupling is considered (top row) the spike of cell 1 arrives 0.843 ms after spike onset, whereas the spike of cell 2 needs 2.83 ms.

In the second row where  $g_E = 2.5$  mS/cm<sup>2</sup> these times do not change significantly, but as mentioned a second spike is initiated at cell 1 by the passing spike of cell 2. But when  $g_E \geq 5$  mS/cm<sup>2</sup> the strong effect of cell 1 on cell 2 will initiate a spike at the soma which travels to both ends. The 'original' spike induced by current injection at  $t = 2$  ms will not be generated and conducted, since cell 2 is still in its refractory period from the backpropagating spike. For  $g_E = 5$  mS/cm<sup>2</sup> the delay of cell 2 at the end is reduced to 0.178 ms and for  $g_E = 10$  mS/cm<sup>2</sup> again the gap only sums up to 0.103 ms, similar to the other cases as discussed previously.

### 4.2.4 Cluster 4

The forth detected cluster contains three neurons which all are considered to be apical cochlear neurons. The cluster arrangement is displayed in Fig. 4.18. This time cell 1 encodes the biggest with  $d_{soma}^1 = 19.13$   $\mu$ m, the middle cell is cell 2 with  $d_{soma}^2 = 16.17$   $\mu$ m and the smallest one is cell 3 with  $d_{soma}^3 = 14.89$   $\mu$ m. The red contact area between the red cell 3 and the yellow cell 2 appears to be quite flat, contrary to the connection to the green cell 3 which somehow entangles the soma of cell 2 at the other side.

This time we have to consider two contact areas, where the first one between cell 1 and cell 2 was calculated to be 135.64  $\mu$ m<sup>2</sup> and the second contact area between cell 2 and cell 3 76.35  $\mu$ m<sup>2</sup>. For the biggest cell 1 the contact area to cell 2 represents 11.8% of the total area and 16.5% of cell 2. Cell 2 also makes contact with cell 3 at 9.3% of its total surface, whereas for cell 3 this contact area represents 11% of the total area. Note that for cell 2 a quarter of its total surface area is connected to other somata.

Another interesting fact concerns the sensitivity to changes in the presomatic length  $l_{pre}$ , since the soma diameter of cell 1 is within the critical range around 19  $\mu$ m where the dependency of the safety factor for successful spike transmission changes. Nonetheless the individual thresholds for intracellular current injection in the first dendritic compartment are either 0.06 or 0.07 nA for all three cells.

Since now three cells with two contact areas have to be considered, the variety of simulation experiments certainly increases. As a first step the ephaptic coupling

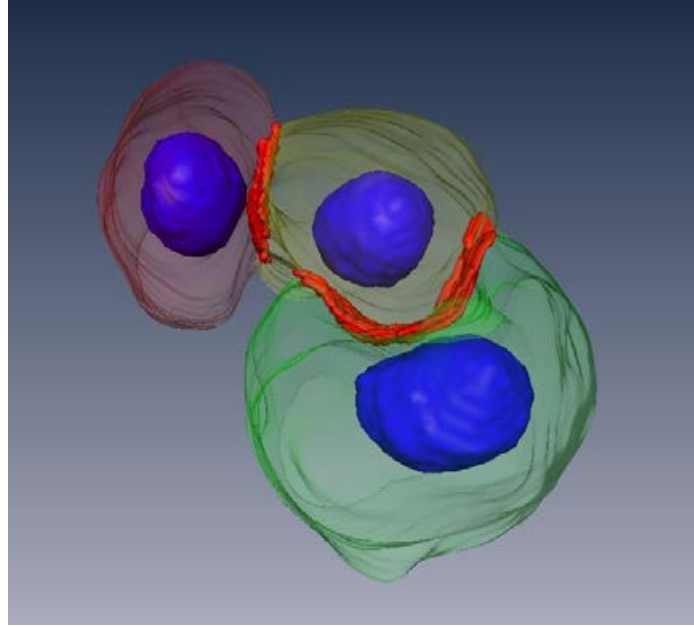


Figure 4.18: Arrangement of the fourth cluster, with the green cell 1, yellow cell 2 and red cell 3. The nuclei are plotted in blue, the contact area is displayed in red.

influence was studied for leaving one cell unstimulated, i.e., no current injection was present, while injecting a subthreshold impulse of 0.07 nA into the first compartment of each of the two other cells. The resulting 3 trials were repeated for either the short presomatic case of  $l_{pre} = 50 \mu\text{m}$  for all 3 cells or the long version, i.e.,  $l_{pre} = 100 \mu\text{m}$ .

If only cell 2 and cell 3 are stimulated with 0.07 nA and no ephaptic coupling is considered ( $g_E^1 = 0 \wedge g_E^2 = 0$ ), the two spikes slightly differ since cell 2 has a bigger soma than cell 3. For the spike height at the soma  $AP_{height}^2 = 101.8 \wedge AP_{height}^3 = 102.3$  mV holds, and the spike of cell 2 arrives later at the central end at 0.905 ms whereas for cell 3 this value is 0.885 ms. Anyway, when the ephaptic conductances of both contact areas are equally raised the soma of cell 1 gets depolarized. For  $g_E^1 = 3 \wedge g_E^2 = 3$  cell 1 will successfully initiate and transmit a spike which arrives 1.325 ms after the current injection of the supporting cells 2 and 3. Further increase in the values of  $g_E^1$  and  $g_E^2$  leads to more synchronized spikes and also to the increase in the  $AP_{height}^1$  of cell 1 and concurrent decrease of that of cell 2. Furthermore if only the value of  $g_E^1$  is increased while  $g_E^2 = 0$  holds, the same results are obtained. Thus the influence of a simultaneously excited cell 3 only has a minor effect on the properties of the three different spikes.

When the long presomatic length is considered, this behavior remains the same. Also a value of  $g_E^1 = 3 \text{ mS/cm}^2$  allows for a spike initiation of cell 1 through current flow from an excited cell 2, regardless of the simultaneously excited cell 3.

If only cell 1 and cell 2 are stimulated with 0.07 nA and cell 3 does not receive any current injection the previously mentioned behavior is very similar. First of all both considered lengths of the presomatic region, i.e., either  $l_{pre} = 50 \mu\text{m}$  for all three cells or  $l_{pre} = 100 \mu\text{m}$ , again display the same excitation profiles for all three cells when the values of the ephaptic conductances are increased. And secondly, now if  $g_E^2 \geq 4 \text{ mS/cm}^2$  holds cell 3 will initiate a spike at its soma with the help of cell 2. This extra  $1 \text{ mS/cm}^2$  might be required because of the smaller contact area between cell 2 and cell 3 compared to that between cell 2 and cell 1. Furthermore again the change of  $g_E^1$  of a simultaneously excited cell 1 does not effect the AP initiation of cell 3 while only slightly changing the spike properties of the three cells sharing the cluster.

It should be noted that when no ephaptic coupling is considered ( $g_E^1 = 0 \wedge g_E^2 = 0$ ), the difference in the two spikes of cell 1 and cell 2 are greater since the difference in soma size is more pronounced. For the spike height at the soma  $AP_{height}^1 = 96.39 \wedge AP_{height}^2 = 101.9 \text{ mV}$  holds, and the spike of cell 1 arrives later at the central end at 1.105 ms whereas for cell 2 this value is 0.905 ms. When  $g_E^1 = 4 \wedge g_E^2 = 4$  the  $AP_{height}$  at the soma of cell 3 is 98.67 mV, but it is delayed at the central end since the spike arrives at 1.245 ms. If the values of the ephaptic conductances are further increased the  $AP_{height}$  at the soma of cell 2 decreases and the propagation is slightly decayed, but cell 3 will increase in height and arrive almost simultaneously at the central end.

The difference in the excitation profiles of the three cells for changing ephaptic conductance is special for not stimulating the middle cell 2 while injecting currents of 0.07 nA into cell 1 and cell 3. First of all the two cases of the length of the presomatic region certainly differ, which is why they are discussed separately. Nonetheless it should be stated that when no ephaptic coupling is considered ( $g_E^1 = 0 \wedge g_E^2 = 0$ ), the difference in the two spikes of cell 1 and cell 3 is the greatest since the soma of cell 1 is the biggest and that if cell 3 is the smallest. The corresponding spike properties have been mentioned before.

For the short presomatic length of  $l_{pre} = 50 \mu\text{m}$  for all three cells and leaving  $g_E^1 = 0$  cell 2 will be excited by cell 3 when  $g_E^2 \geq 5 \text{ mS/cm}^2$  holds (top row of Fig. 4.19). The  $AP_{height}$  at the soma of cell 2 is then (for  $g_E^2 = 5$ ) 99.44 mV and the spike arrives at the end at 1.155 ms which of course is later than cell 3 where the spike arrives 0.895 ms after spike onset, but for this configuration comparable to value of cell 1 which is 1.105 ms. Further increase of  $g_E^2$  increased the  $AP_{height}$  of cell 2 and speeds up the spike conduction whereas having the opposite effect on cell 3.

When only  $g_E^1$  is increased to  $1 \text{ mS/cm}^2$  and  $g_E^2 = 0$ , cell 2 inhibits the excited cell 1 where the AP now breaks down at the soma. This behavior has been reported for the two neuron clusters previously, but this time it is much more pronounced since cell 1 has the biggest of all soma diameters. Especially because it is also bigger than the barrier where the length of the presomatic region is a sensitive parameter, the safety factor of spike transmission is reduced. This behavior is certainly different for the long presomatic region as will be discussed in the following.



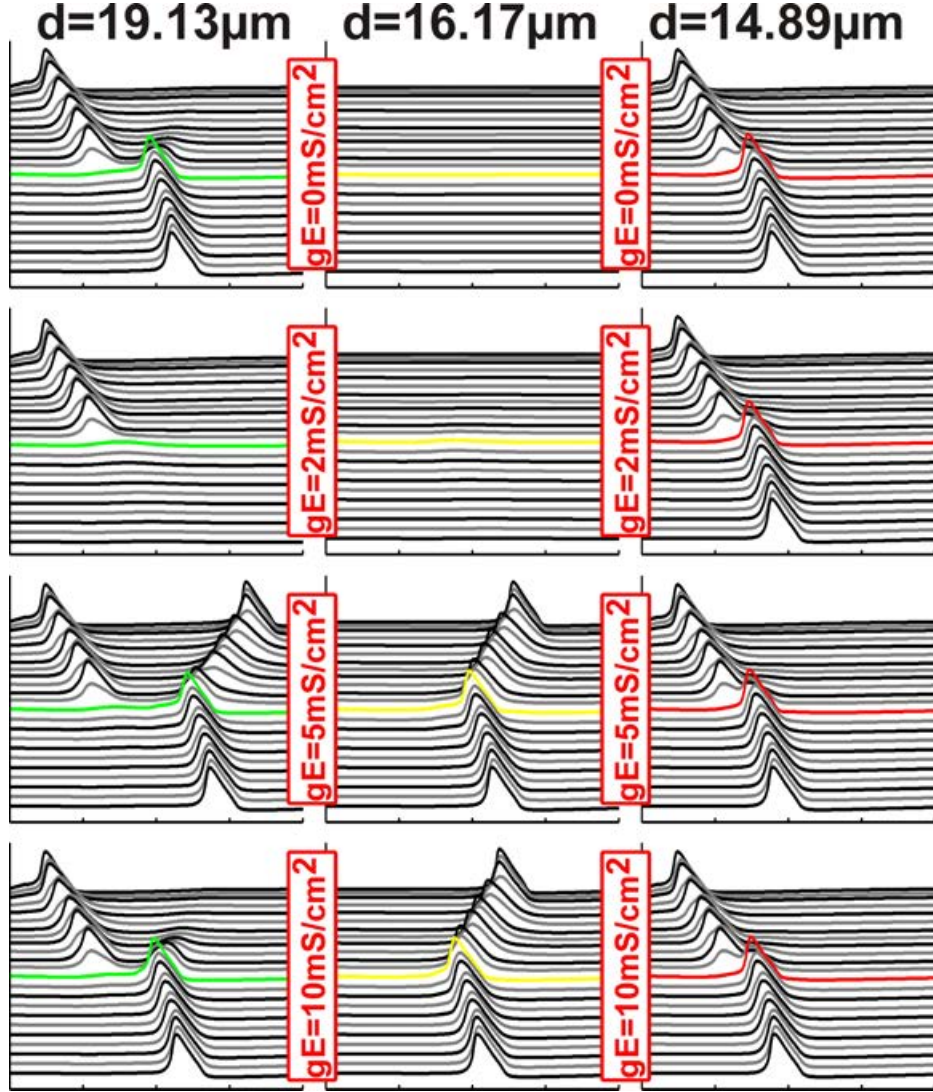


Figure 4.19: Short presomatic lengths  $l_{pre} = 50 \mu\text{m}$  and stimulation of the two outer cells, each with  $0.07 \text{ nA}$  current injection at the first compartment with an inactive middle cell 2. The values of  $g_E^1$  and  $g_E^2$  are simultaneously raised, different configurations are illustrated in rows.

If both ephaptic conductances are equally increased a special behavior can be observed. For  $g_E = 1$  for both conductance values the spike of cell 1 shrinks in size at the soma but conducts faster whereas the spike of cell 3 does not change significantly. For  $2 \leq g_E \leq 4$  for both values the spike at cell 1 interestingly breaks down at the soma since too much current is lost for cell 2 which is still not enough to trigger an AP. This is illustrated in the second row of Fig. 4.19. But still when  $g_E \geq 5 \text{ mS/cm}^2$  for both conductance values cell 2 initiates an AP at its soma which propagates to both ends.

In the third row of Fig. 4.19 the case of  $g_E^1 = 5 \wedge g_E^2 = 5$  is illustrated. The  $AP_{height}$  at the soma of cell 1 is reduced to 93.45 mV which means a reduction of 3 mV although the  $AP_{height}$  at the soma of cell 3 is only 1 mV reduced. The generated AP at the soma of cell 2 has a height of 98 mV. For this case it is interesting that the spike of cell 1 is held back at the soma and certainly delayed, therefore the spike of cell 1 is also the latest at compartment 27 at  $t = 1.365$  ms, compared to 1.135 ms for cell 2 and the smallest and also fastest cell 3 with an arrival time of 0.895 ms after spike onset.

Further simultaneous increase in the values of the two ephaptic conductances leads to spikes of almost equal height at the soma and also to more synchronized arrival times at the end. For the case illustrated in the last row of Fig. 4.19, the spike of cell 1 arrives at 1.135 ms almost at the same time as cell 2 of 1.035 ms and cell 3 slows down to 0.905 ms.

When the presomatic lengths are increased to 100  $\mu\text{m}$ , the safety factor for successful spike conduction over the almost unmyelinated soma region increases, especially for the biggest cell 1. Thus for increasing both values of the ephaptic conductances simultaneously, the break-down at the soma of cell 1 is absent and if  $g_E^1 \geq 2 \wedge g_E^2 \geq 2$  holds, all three cells conduct a spike to the end. Still it should be noted that for this parameter choice the spikes of cell 1 and cell 3 are more similar regarding their height at the soma and the temporal properties compared to the case of short presomatic lengths. When the conductance values are increased cell 1 and cell 3 are only slightly slower than without ephaptic coupling, but cell 2 gets faster and therefore adapts to its companion cells.

If only one of the ephaptic conductance values is increased while leaving the other 0, i.e., only considering ephaptic coupling on one side, the results are quite comparable to the short presomatic length case. When only the smaller cells are connected, i.e.,  $g_E^1 = 0 \wedge g_E^2 \geq 5$ , the middle cell 2 initiates an AP at its soma with ongoing spike transmission. This is exactly the same as for  $l_{pre} = 50$   $\mu\text{m}$ , although the difference in the temporal spike parameters are slightly higher. Since both soma diameters of cell 2 and 3 are beneath the critical value, this is no surprise.

But if only ephaptic coupling between cell 1 and cell 2 is considered, now since the safety factor for the big cell 1 is increased, a combination of  $g_E^2 = 0 \wedge g_E^1 \geq 3$  results in successful spike transmission on all three cells. For  $g_E^1 = 3$  all three spikes arrive within a temporal gap of 0.285 ms, but for an increased value of  $g_E^1 = 10$  this difference is reduced to 0.12 ms.

A second set of experiments considered the case of only stimulating one of the three cells with a current injection of 0.07 nA. It shall be clarified if the influence of ephaptic coupling is strong enough to excite two other cells. Again each of the three trials for one excited cell has been repeated for the long and the short presomatic lengths which show significantly varying behavior for current injection into the big cell 1 while no stimulus was applied for cell 2 and cell 3.



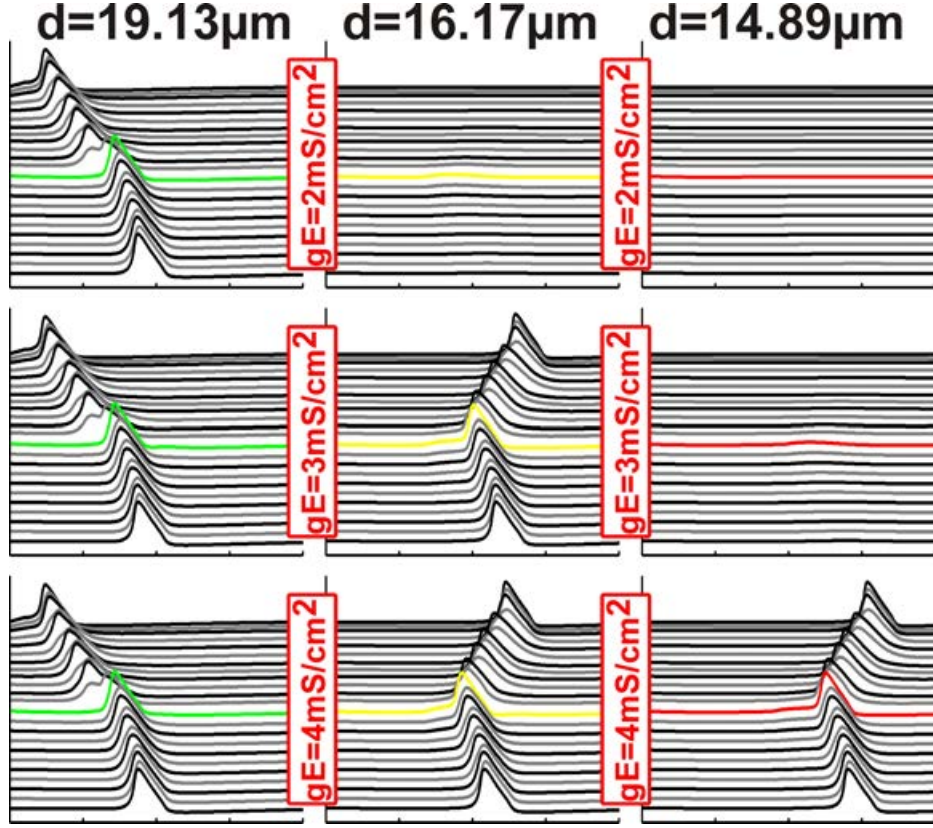


Figure 4.20:  $l_{pre} = 50 \mu\text{m}$ : Stimulated cell 1 (left) with  $0.07 \text{ nA}$  current injection, inactive cell 2 (middle) and cell 3 (right). The values of  $g_E^1$  and  $g_E^2$  are simultaneously raised (rows), where  $3 \text{ mS/cm}^2$  on both sides successfully excites cell 2 but fails to initiate a spike at cell 3 (middle).

Since the spike of cell 1 with  $l_{pre} = 50 \mu\text{m}$  has a very low safety factor for AP transmission over the soma region, only setting  $g_E^1 = 1 \text{ mS/cm}^2$  results in the immediate break-down of the spike at the soma of cell 1 without supplying enough current for cell 2 to initiate a spike. The big contact area between cell 1 and cell 2 also hinders cell 1 to keep enough current to itself.

The behavior again is changed for  $l_{pre} = 100 \mu\text{m}$  which is illustrated in Fig. 4.20. Both ephaptic conductances have been simultaneously raised and again the spike properties have been recorded. The spike of cell 1 arrives at the central end always at the same time, i.e.,  $0.875 \text{ ms}$  after stimulus onset. Even if cell 1 succeeded to stimulate both companion cells this traveling time does not change significantly. If  $g_E^1 = 3 \wedge g_E^2 = 3$  holds cell 2 receives enough current from cell one to initiate a spike at its soma with an  $AP_{height}$  of  $98.53 \text{ mV}$  at the same time the soma of cell 3 gets depolarized as well, but a peak of  $4 \text{ mV}$  is enough to trigger an AP. For these low values of  $g_E^1$  and  $g_E^2$  the spike of cell 2 is still quite long delayed compared to cell 1. The traveling spikes for this case are plotted in the second row of Fig. 4.20.

When the values are further increased to  $g_E^1 = 4 \wedge g_E^2 = 4$  both cells are excited by the stimulated cell 1 which is presented in the bottom row of Fig. 4.20. The values of the  $AP_{height}$ 's are 101.8, 99.13 and 99.23 mV. The peak times at the central end certainly differ, whereas the spike of cell 1 arrives 0.875 ms after onset at its central end, the corresponding values of cell 2 and cell 3 are 1.08 and 1.41 ms.

If the values are further raised the  $AP_{height}$ 's at the somata of cell 2 and 3 will soon exceed that of cell 1 and the conduction velocities of the companion cells are increased. For  $g_E^1 = 10 \wedge g_E^2 = 10$  the spike of cell 2 arrives at 0.98 ms and that of cell 3 at 1.11 ms.

The next trials involve current injection of 0.07 nA into the other outer cell 3 while no stimulation is applied for cell 1 and cell 2. For this case the length of the presomatic compartment does not significantly alter the excitation profiles of the three cells within the cluster. The results for the short length, i.e.,  $l_{pre} = 50 \mu\text{m}$  are summarized in Fig. 4.21. To comprehend the results it should be stated that without ephaptic coupling cell 3 produces a spike which has an  $AP_{height}$  of 102.2 mV at the soma arriving 0.885 ms after spike onset at compartment 27.

Initially both conductance values  $g_E^1$  and  $g_E^2$  are simultaneously raised. For  $g_E^1 = 5 \wedge g_E^2 = 5$  some current is lost on the soma of cell 3 which depolarizes the soma of cell 2 which reaches a maximum of 7.244 mV, which is still not enough for a spike initiation (see the first row of Fig. 4.21). But when  $g_E^1 = 6 \wedge g_E^2 = 6$  holds immediately both cells are excited by the passing spike of cell 3 which is illustrated in the second row. The  $AP_{height}$  at the soma of cell 3 is reduced to 100.9 mV, the corresponding values for cell 2 and 1 are 97.08 mV and 100.7 mV. The spike of cell 3 now arrives at 0.9 ms after current injection at its central end. The spike of cell 2 is the second to arrive at 1.16 ms and then cell 1 at 1.31 ms. Further simultaneous increase of the two ephaptic conductances again leads to faster spike conduction of cell 2 and cell 1.

Since a combination of  $g_E^1 = 6 \wedge g_E^2 = 6$  leads to successful excitation these values have been further analyzed. First it has been clarified that  $g_E^1 = 6 \wedge g_E^2 = 5$  will not lead to a spiking cell 1 without enough depolarization of the middle cell 2. In this case only cell 3 transmits its spike to the end while cell 2 and cell 1 do not produce an AP. Secondly  $g_E^2$  was held constant at 6 mS/cm<sup>2</sup> and it was observed that also lower values of  $g_E^1$  are enough to also excite cell 1. An example is presented in the last row of Fig. 4.21, where the combination of  $g_E^1 = 3 \wedge g_E^2 = 6$  still produces spikes of all three cells. For this configuration the  $AP_{height}$  at the soma of cell 1 shrinks down to critical 97.92 mV and the spike arrival is certainly delayed, i.e., the arrival time now is 1.46 ms.

Summarizing these tests, all three cells are excited if  $g_E^2 \geq 6 \text{ mS/cm}^2$  and  $g_E^1 \geq 3 \text{ mS/cm}^2$ . If the conductance value for the contact area between cell 1 and cell 2 is too small, only cell 2 will initiate a spike with the help of the stimulated cell 3. The current flow required to additionally excite cell 1 is not enough which can be seen in the third row of Fig. 4.21.

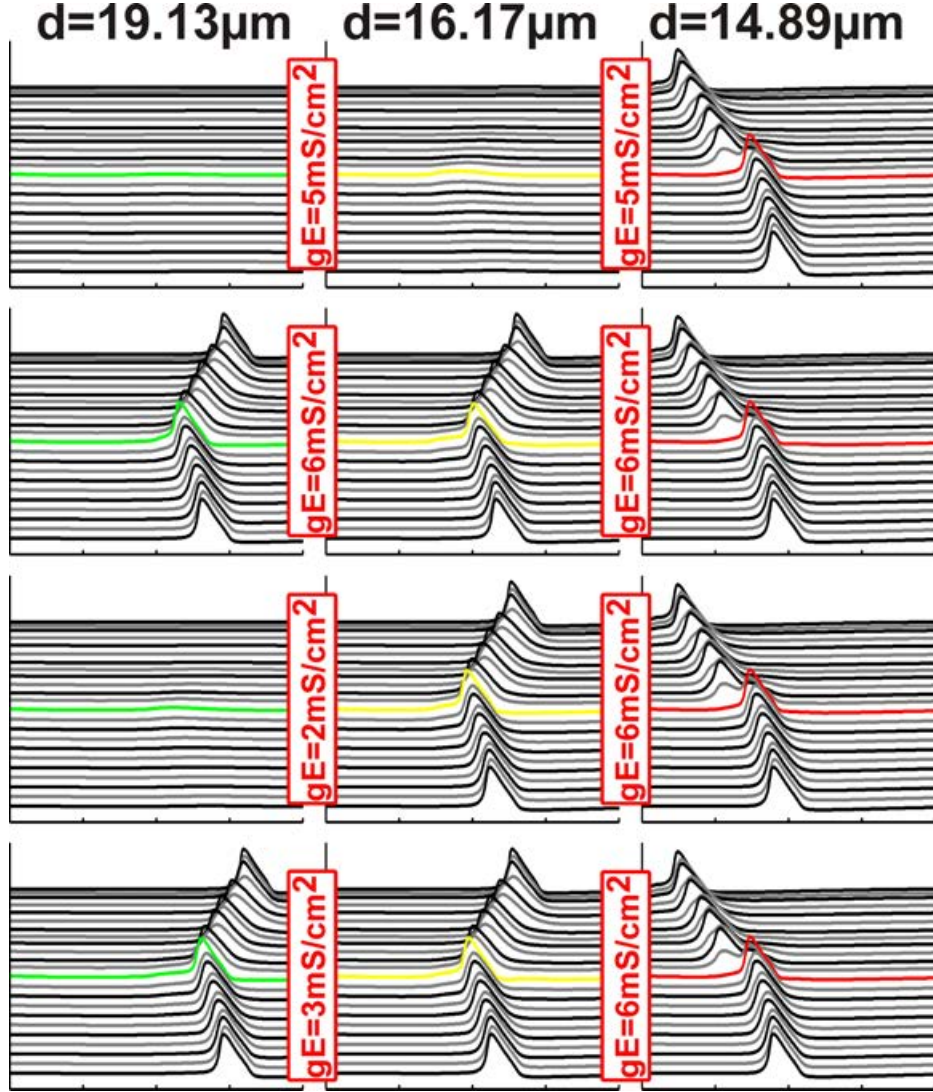


Figure 4.21:  $l_{pre} = 100 \mu\text{m}$ : Stimulated cell 3 (right) with  $0.07 \text{ nA}$  current injection, inactive cell 2 (middle) and cell 1 (left). Different combinations of  $g_E^1$  and  $g_E^2$  (rows) leads to variational excitation pattern.

These reported excitation profiles for changing ephaptic conductance values of  $g_E^1$  and  $g_E^2$  are exactly the same for the long presomatic region. The same combination of values lead to the same amount of induced spikes of the three cells within the cluster, although it should be stated that the peaks at the soma are higher and also slightly earlier.

The third trial is again very interesting since the middle cell 2 is the one that receives a current injection of  $0.07 \text{ nA}$  and again the two cases for the length of the presomatic region displays similar behavior but with some exceptions. In Fig. 4.22 a

variety of results for  $l_{pre} = 100 \mu\text{m}$  is illustrated.

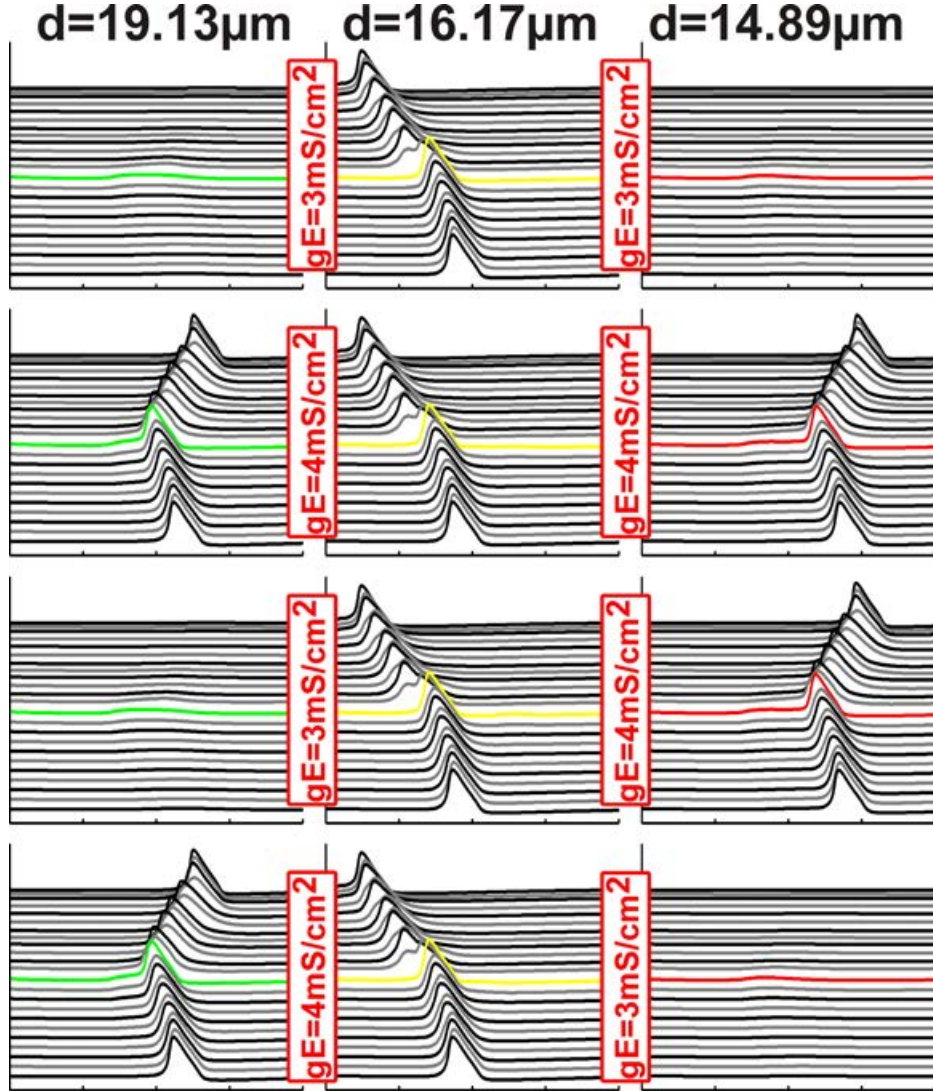


Figure 4.22:  $l_{pre} = 100 \mu\text{m}$ : Stimulated cell 2 (middle) with 0.07 nA current injection, inactive cell 1 (left) and cell 3 (right). Different combinations of  $g_E^1$  and  $g_E^2$  are presented in rows. Although the diameters of the somata and the contact areas essentially differ in magnitude, the same values for  $g_E^1$  and  $g_E^2$  are required for ephaptic excitation of the outer cells.

Again initially simultaneously raising both ephaptic conductance values has been tested. If no ephaptic coupling on either side is considered, cell 2 produces a spike with an  $AP_{height}$  of 103.2 mV at its soma which will arrive at compartment 27 after 0.865 ms. When  $g_E^1$  and  $g_E^2$  are increased the  $AP_{height}$  decreases since some current is lost on both sides, but the velocity remains almost unchanged. Furthermore the bigger contact area to cell 1 is obvious, since for  $g_E^1 = 3 \wedge g_E^2 = 3$  the peak of cell



1 is 6.069 mV and that of cell 3 only 3.36 mV. That means that through the bigger contact area more current flow is possible. This case where the effect of ephaptic coupling is too small to induce spikes at the outer cells is illustrated in the top row of Fig. 4.22.

Still for  $g_E^1 \geq 4 \wedge g_E^2 \geq 4$  the propagating spike of cell 2 depolarizes the somata of cell 1 and cell 3 strongly enough to initiate spikes at both sides as can be seen in the second row of Fig. 4.22. The  $AP_{height}$  at the soma of cell 2 shrinks down to 101.3 mV, the corresponding values of cell 1 and cell 3 are 99.05 mV and 97.23 mV. Still the spike of cell 2 is not at all delayed, but the spikes of cell 1 arrives later at 1.12 ms and that of cell 3 is the latest at 1.35 ms. Further increase of  $g_E^1$  and  $g_E^2$  leads to further reduction of the spike height of cell 2 and faster conduction of cell 1 and cell 3.

Furthermore for this choice of parameters a combination of  $g_E^1 = 3 \wedge g_E^2 = 4$  is enough to excite cell 3 but the depolarization of the cell 1 soma is not enough to trigger an AP. On the other hand the opposing combination of  $g_E^1 = 4 \wedge g_E^2 = 3$  results in the excitation and successful propagation of a spike on cell 3, but does not supply enough current for cell 1. These two cases are presented in the bottom rows of Fig. 4.22.

If the length of the presomatic regions are shortened to 50  $\mu\text{m}$  again the reduced safety factor of the big cell 1 effects the other cells in the cluster. The first difference can be observed for the simultaneous increase of the two conductance values, since for  $g_E^1 = 3 \wedge g_E^2 = 3$  the spike of cell 2 excites the soma of cell 1 which successfully transmits a spike to its end, but cell 3 still remains silent. But it should be noted that not only the  $AP_{height}$  at the soma of cell 2 decreases, the spike of cell 2 also suffers from a very short delay.

When  $g_E^1 = 4 \wedge g_E^2 = 4$  holds both outer cells initiate an AP at their somata which are delayed at the central ends compared to the stimulated cell 2, i.e., the spike of cell 2 is the first to arrive at its central end at  $t = 0.795$  ms, then the spike of cell 1 arrives at  $t = 1.025$  ms and the slowest AP of cell 3 needs  $t = 1.12$  ms. Also a combination of  $g_E^1 = 3 \wedge g_E^2 = 4$  excites all three cells, although the  $AP_{height}$  at the soma of cell 1 is reduced and the spike is further delayed due to less ephaptic influence. Still the difference to the long presomatic region can be observed, since for  $g_E^1 \geq 7 \wedge g_E^2 \geq 7$  the spike of cell 2 now breaks down at its soma and none of the outer cells initiates a spike.

# Chapter 5

## Extracellular stimulation

In contrast to chapter 4 where the natural spiking behavior of cochlear neurons is simulated by intracellular stimulation, this chapter concerns the excitation profile of a model neuron stimulated by an extracellularly placed electrode. Thus the obtained results are of special interest for the simulation of auditory response induced by CI stimulation.

The electrical network has to be extended (compare Fig. 3.4) and the spatial arrangement of the neuron and the placement of the electrode have to be considered in order to simulate the stimulation by an electrode. Sec. 5.1 will give an overview of the modeling approaches in order to calculate the extracellular potentials along the neuron  $V_{e,n}$  which serve as input data to solve the differential equation for the transmembrane potential of each compartment  $V_n$  which has to be applied in its full dimension.

Within a recent study variational soma sizes of SGCs from different tonotopic regions have been reported (Potrusil et al. 2012). These detected soma diameters have been incorporated in the model neuron and tested for differences of the spiking behavior while leaving all other geometrical and electrical parameters to their standard values. The results for different electrode positions and varying pulse shapes are presented in Sec. 5.2.

Our cooperation partners of the MedUni IBK just performed a groundbreaking study which uses recently acquired Micro CT data of a whole human cochlea in order to evaluate traced three-dimensional neuron data. The whole stack includes 7 apical and 7 middle turn neurons as well as 10 basal neurons. Additionally the coordinates of the same amount of electrodes positions have been evaluated which were assumed to be beneath the organ of Corti within the Scala tympani. This new data set is of great relevance, nonetheless initial simulation trials reveal that some of the evaluated spatial coordinates have to be corrected for pending studies. However, Sec. 5.3 points out simulation trials for three different neurons, each representing a model neuron of one cochlear turn. Different electrode positions are analyzed and thresholds as well as temporal spike parameters will be compared.

## 5.1 Extracellular stimulation excitation profiles

If the response induced by stimulation with an electrode of a neuron shall be simulated the model has to be adapted. In this case not only the geometrical and electrical parameter of the neuron are required, also the spatial arrangement of the neuron and the relative placement of the electrode have to be considered. It shall be reminded that for intracellular stimulation, the assumption  $V_{e,n} = 0$  was valid for all compartments, since only changes of a few mV occur on the extracellular side of the membrane when an AP is passing (see e.g., [Rattay 1990](#)).

Nonetheless when extracellular stimulation is considered, the differential equation has to be evaluated in its full dimension. It shall be recalled that with the notation  $V_{m,n} = V_{i,n} - V_{e,n} - E_{rest,n}$  using the reduced membrane potential of the n-th compartment the derived differential equation for this membrane potential can be written as

$$\begin{aligned} \frac{dV_{m,n}}{dt} = & \left[ -I_{ion,n}(t) + \frac{V_{m,n+1}(t) - V_{m,n}(t)}{R_{n+1}/2 + R_n/2} + \frac{V_{m,n-1}(t) - V_{m,n}(t)}{R_{n-1}/2 + R_n/2} \right. \\ & \left. + \frac{V_{e,n+1}(t) - V_{e,n}(t)}{R_{n+1}/2 + R_n/2} + \frac{V_{e,n-1}(t) - V_{e,n}(t)}{R_{n-1}/2 + R_n/2} \right] / C_n. \end{aligned}$$

Since about 97% to 99% of the voltage is carried by the inside of the fiber, the calculation of  $V_{e,n}$  can be done independently from both the geometry and the activity of the fiber. However, for modeling extracellular stimulation the values of  $V_{e,n}(t)$  serve as the input data to solve the electrical network instead of a current injection as  $I_{stim}(t)$ .

Thus assumptions concerning the extracellular potential depend on the degree of accuracy which is demanded of the model approximating a certain setup ([Briaire and Frijns 2000a](#), [Rattay 1990](#)). Beside analytical solutions for the distribution of  $V_e$  used within this thesis, there exist more complex models, which take inhomogeneities of the cochlea into account and numerically calculate the extracellular potentials based on the finite element method (e.g., [Hanekom 2001](#), [Smit et al. 2009a](#)).

The volume conductor models consider different conductivities of various cochlear tissues. The group around Briaire and Frijns first developed a rotationally symmetric mesh algorithm ([Frijns et al. 1995, 1996](#)) and further compared different algorithms including finite element method, finite difference method and boundary element method ([Briaire and Frijns 2000a,b](#)). These meshing algorithms are capable of constructing meshes of different geometries which give potential distributions comparable with their previous results.

However, within the thesis, in order to reduce numerical effort, the complex cochlear geometry is approximated by a medium with constant conductivity. The obtained analytical solutions for  $V_{e,n}$  are applicable in the case of monopolar, dipolar point source and disc electrodes in an infinite homogeneous medium. The point source and the axis of the neuron can be assumed to lie in a plane which results in the possibility to analyze a two-dimensional model. Such a 2D model is used within [Sec. 5.2](#)



## 5.1 Extracellular stimulation excitation profiles

---

where the schematic drawing in Fig. 5.1 illustrates a typical neuron and electrode arrangement adapted by Rattay et al. (2001). As a result the distance  $r_n$  between the electrode with coordinates  $x_{el}|y_{el}$  and the n-th compartment of the neuron with coordinates  $x_n|y_n$  can be calculated via  $r_n = \sqrt{(x_n - x_{el})^2 + (y_n - y_{el})^2}$ .  $V_{e,n}$  therefore is evaluated by

$$V_{e,n} = \frac{\rho_e \cdot I_{el}(t)}{4 \cdot \pi \cdot r_n},$$

where  $\rho_e$  is the extracellular resistivity which is reciprocal to the constant conductivity and considered to be  $300 \Omega \cdot \text{cm}$ .  $I_{el}(t)$  denotes the amplitude of the stimulating current pulse.

Still this calculation can be extended to three dimensions by considering an additional z coordinate. Sec. 5.3 uses recently evaluated 3D traced cochlear neuron data as will be explained subsequently.

The previously mentioned studies which use the volume conductor models compare their results to acquired NRT data. With the measured eCAPs possible application to adjusting device parameters to individual users can be investigated (see Sec. 1). Anyhow, our group currently performs a study about the influence of altering degree of myelination on the excitation profile of a SGC with recently acquired data from the MedUni IBK. Initially we tested if our adapted standard model of the human SGC is able to confirm the same short spike duration predicted by intracochlear recordings when stimulated with a CI.

Within this survey we again use the adapted model of Rattay et al. (2001) (see Sec. 4.1) and the analytical approach for calculating  $V_{e,n}$ . Therefore we used a two dimensional data set of one SGC and an electrode placed at the transition between bony columns and the osseous lamina. The left side of Fig. 5.1 illustrates the spatial arrangement of the compartment model of the standard model SGC. For comparison, the same colors for the compartments have been used as in Fig. 4.1 where the standard geometrical and electrical parameters of the model SGC are described. Although note that in this schematic drawing the spherical yellow soma almost totally overlaps the magenta and violet pre- and postsomatic compartments, since it has been enlarged for better visualization. Four different electrode positions are illustrated which will be used for simulation runs in Sec. 5.2.

Anyway, the original electrode position assumed by Rattay et al. (2001) was E1 which is placed in the scala tympani. If the model SGC with a soma diameter of  $20 \mu\text{m}$  is stimulated by E1 with a biphasic (cathodic-anodic)  $600 \mu\text{A}$  pulse,  $100 \mu\text{s}$  per phase, it will initiate a spike at its first compartment, the green peripheral terminal, and then the AP will propagate orthodromically over the soma region to the central end. This excitation profile is illustrated in panel (A) of Fig. 5.1 where again the rectified model neuron is plotted at the left. The arrowheads mark the active compartments, corresponding voltage lines have again been plotted in the matching color, except the soma which is illustrated in black instead of yellow.

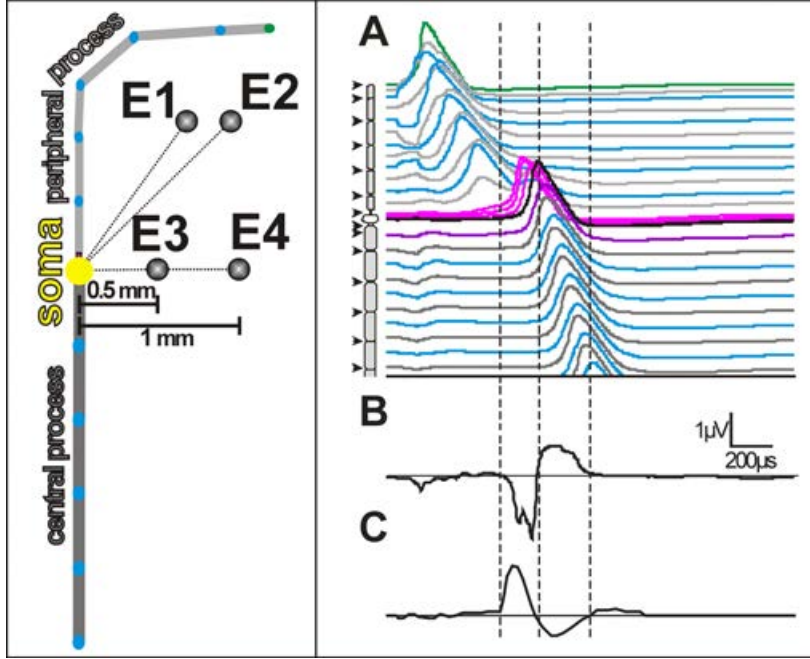


Figure 5.1: The left side illustrated the spatial arrangement and four different electrode positions E1-E4. On the right side (A) shows the excitation profile of the model SGC induced by biphasic stimulation radiated by E1. Simulated extracellular electric potential at the recording electrode,  $I_{rec}$  has the same temporal biphasic characteristic as the recorded one in (C) which is a redrawn version of the -2dB re 1mA case of intracochlear recordings published in [Miller et al. \(2004, Fig. 3\)](#).

In order to compare the simulated excitation profile to NRT measurements, a recording electrode was incorporated into the model. This electrode detects the trans-membrane currents of each compartment of the excited cell which act as local current sources and sum up to a temporal voltage profile of the spike ([Rattay 2004](#)). This potential of the recording electrode can be calculated by

$$V_{rec} = \sum_n \frac{\rho_e \cdot I_n(t)}{4 \cdot \pi \cdot r_n}, \quad \text{with } I_n = I_{ion,n} + C_n \frac{dV_n}{dt}.$$

This summation is presented in Fig. 5.1(B) which corresponds to the field generated by a single neuron in contrast to the recorded eCAP in Fig. 5.1(C) which illustrates the currents from a population of stimulated cells. The vertical dashed lines confine the biphasic main part of the recorded spike, obviously indicating the temporal similarity between the simulated and recorded voltage profiles. Thus, the excitation profile predicted by our simulation emphasizes the reported short SGC spike duration. The soma together with its poorly shielded pre- and postsomatic regions dominate the signal in Fig. 5.1(B) because of their relative large active membrane, compare the dashed lines. In spite of being closer to the electrode the spike in the peripheral axon

contributes poorly to the recorded signal. This is a consequence of the large surface of active membranes at the soma region.

Furthermore the obtained results predict that this conduction time can be divided into four characteristic phases: after a postsynaptic delay of excitation onset, the spike travels with almost constant velocity over the peripheral axon. A postsomatic delay dependent on soma size and degree of myelination (compare Sec. 4.1.1) delays the transmission before the spike again propagates with constant velocity along the central process (compare Sec. 4.1.2).

## 5.2 Soma size

As mentioned previously a recently performed study (Potrusil et al. 2012) revealed varying soma size along the cochlea with some evidence of a tonotopical distribution from high to low frequency regions. Due to improved imaging techniques, the cochleae of two specimens could be systematically scanned and evaluated revealing perikarya and corresponding nuclei in their full dimension. Contrary to the present distinction of two groups of SGCs, agglomerative hierarchical clustering identified four populations of SGCs within the human inner ear, although it should be stated that the most uniform sizes of cell bodies are located in the middle turn representing the majority of phonational frequencies.

Nonetheless the excitation profile of a model neuron is certainly altered for only varying the soma diameter while leaving all other model parameters at their fixed standard values. The simulation results correspond to the standard model SGC of this thesis and uses the 2D representation of the neuron illustrated at the left of Fig. 5.1. Four active electrode positions that correspond to CI situations in the basal turn have been examined and are illustrated in Fig. 5.1. Two electrode positions (E1 and E2) simulate electrodes placed at the transition between bony columns housing nerve fiber bundles ad osseous spiral lamina (E1) and at the distal end of the osseous spiral lamina (E2). E1 was previously introduced by Rattay et al. (2001). Results are presented in Sec. 5.2.1.

E3 and E4 correspond to positions of a cochlear implant electrodes placed at the level of Rosenthal's canal that contain SGC somata orthogonal to the neural axis (Fig. 5.1) in a distance of 0.5 mm (E3) and 1 mm (E4). Therefore E1 and E2 represent typical electrode positions with straight electrode arrays, whereas E3 and E4 illustrate perimodiolar electrode placement investigated in Sec. 5.2.2.

For the following simulation trials four different pulse shapes have been examined of each stimulating electrode. The excitation profile of the model SGC was tested for 0.1 ms long monophasic stimulation, where CAT denotes a cathodic pulse and ANO the anodic one. Additionally the biphasic counterparts have also been tested where 0.05 ms/phase are used. BIC denotes a pulse with a leading 0.05 ms long cathodic phase directly followed by a 0.05 ms long anodic phase of the same amplitude. Thus no interphase gap is considered within this thesis and BIA denotes the exact opposite

pulse pattern with anodic leading phase.

The threshold currents of the electrodes, required to induce an AP on the model neuron which then successfully propagates to the SGC's end, have been evaluated for the different pulse forms. Additionally the *initiation site* (IS) was recorded, i.e., the index of the compartment where the AP is generated and therefore the corresponding transmembrane voltage line shows the first of all peaks. This temporal parameter of the spike, i.e., the time at which the peak occurs at the IS (PT), will also be compared for varying neuron and electrode configuration. Accompanied by the peak time of the soma compartment (PTS) and the last model compartment (ET), the temporal characteristics of the spike can be analyzed. Those peak times correspond to the time where the transmembrane voltage line of the compartment has its maximum.

### 5.2.1 Extracellular stimulation with electrodes E1 and E2

For both electrodes and all four stimulus configurations, the thresholds as well as IS did not change much within the range of all collected soma diameters. Temporal parameters of the spike were collected for threshold stimulation and additionally for pulses of doubled amplitude. These temporal parameters are displayed in Fig. 5.2 which demonstrates different spiking behavior when a selected model cell with  $d = 19.08 \mu\text{m}$  (which is the mean value of all evaluated diameters) is stimulated by electrode E1 with the four different pulse forms. The time courses of membrane potential of this cell are plotted for monophasic and biphasic threshold stimulations.

When stimulated with a 0.1 ms long cathodic pulse, the threshold value for E1 is about 449  $\mu\text{A}$  and 186  $\mu\text{A}$  for E2 regardless of the soma size. Note the difference in magnitude of the two values, although the electrodes are quite close (compare Fig. 5.1). APs were generated in compartment 7 for E1 and in compartment 9 for E2, both pertaining to the peripheral axon. The IS for twice the threshold is changed to compartment 9 for E1 and remains the same for E2. Since for all cases the AP is initiated peripherally, the spike travels orthodromically over the soma to the central end of the neuron. This can be observed in the top left panel of Fig. 5.2, where a threshold current initiates a spike after 0.445 ms at compartment 7, indicated by the blue line. The spike appears later at the yellow soma after 0.812 ms, and then reaches the central end 0.966 ms after stimulus onset, plotted as a red line.

Anodic thresholds slightly decrease with increasing soma size for E1 from 496  $\mu\text{A}$  to 482  $\mu\text{A}$  and cause the spike to start at the central end of the neuron at compartment 27. For E2 the threshold remains constant at 289  $\mu\text{A}$  initiating the spike at the very peripheral end of the neuron in compartment 1. The IS stays the same for both electrodes and all cell sizes when stimulated with twice the threshold value. The spike travels orthodromically as it can be seen in the top right panel of Fig. 5.2, where the AP at the soma (indicated by yellow line) appears later than the graph of the last compartment, indicated by the red line which represents both, the IS and the end of the neuron. Interestingly, the onset of the spike is delayed compared to the cathodic stimulation with a peak time value of 0.558 ms. Still, since it is also the end time of

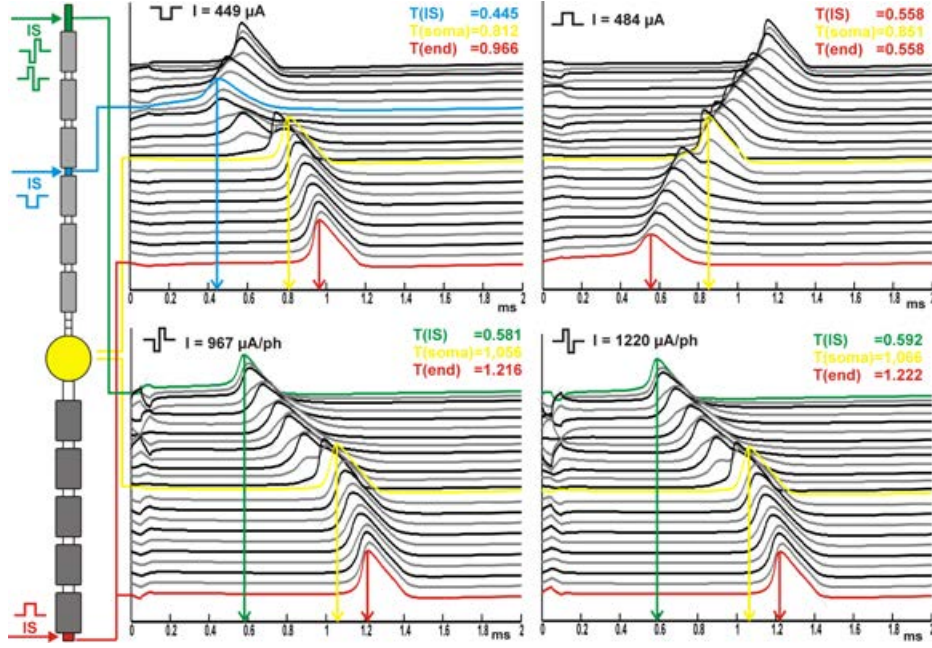


Figure 5.2: Spike initiation sites depend on stimulus pulse type. The left side illustrates the compartment model of a target neuron with spike origin (horizontal arrows) at threshold for four different pulses. Stimulating electrode E1. Traveling APs are plotted at the right. Each line represents the temporal change in transmembrane potential. The top line is the neurons peripheral end, the soma is always plotted in yellow. The values for the time at which the spike occurs at the IS, the soma and the end of the model neuron are given in ms and they are marked by vertical arrows.

the spike, the delay of information processing is certainly reduced.

The thresholds for biphasic pulses from E1 remained constant at  $-967 \mu A$  for cathodic first and  $1220 \mu A$  for anodic first pulses, both initiated the spike at compartment 1 for all cell sizes, indicated by the green lines in the bottom panels of Fig. 5.2. Since the peak time values for both leading phases are quite similar, almost the same value of about 1.2 ms can be observed for the delay of spike transmission, which is certainly longer than for monophasic pulses.

No matter which cell size is observed, when the pulse amplitudes are doubled, the ISs are shifted to compartment 9 for biphasic cathodic first pulses and to multiple sites including compartment 27 and 3 for biphasic anodic first pulses. The corresponding threshold values for E2 are  $483 \mu A$  and  $661 \mu A$ , although it should be stated that the largest cell of the basal turn requires about  $15 \mu A$  more threshold current amplitude compared to the constant values of all other possible cell diameters. Also, the IS is not constant for all cells, but rather switched between compartment 7 and 9 for both biphasic pulse forms of E2. When stimulated with twice the threshold value, the IS was constant for all cell sizes, i.e., compartment 9 for cathodic first and compartment 1 for anodic first biphasic pulses. This behavior demonstrates the overall trend that



temporal fluctuations decrease for increased stimulus amplitudes.

Regardless of the electrode position and pulse form, and despite some fluctuations, it was observed that the peak time values of the spike increased with cell size. No matter which pulse form is chosen, changing the soma diameter alters the temporal spiking behavior and larger soma size delays information processing.

### 5.2.2 Extracellular stimulation with electrodes E3 and E4

These electrode positions were tested for all evaluated soma diameters. Both electrodes are placed normal to the soma at different distances, where E3 denotes the short distance case of 0.5 mm and E4 the longer, doubled distance of 1mm (Fig. 5.1). Initially the individual monophasic and biphasic threshold currents have been determined for varying soma size. While analyzing all soma diameters, the spike is initiated either peripherally at compartment 13, which is the last node of Ranvier before the soma, or at the central end of the model neuron.

Due to the phase duration ratio of 100  $\mu$ s to 50  $\mu$ s, the monophasic threshold currents for both electrode positions are approximately half the values of their biphasic counterparts, as can be seen in Fig. 5.3.

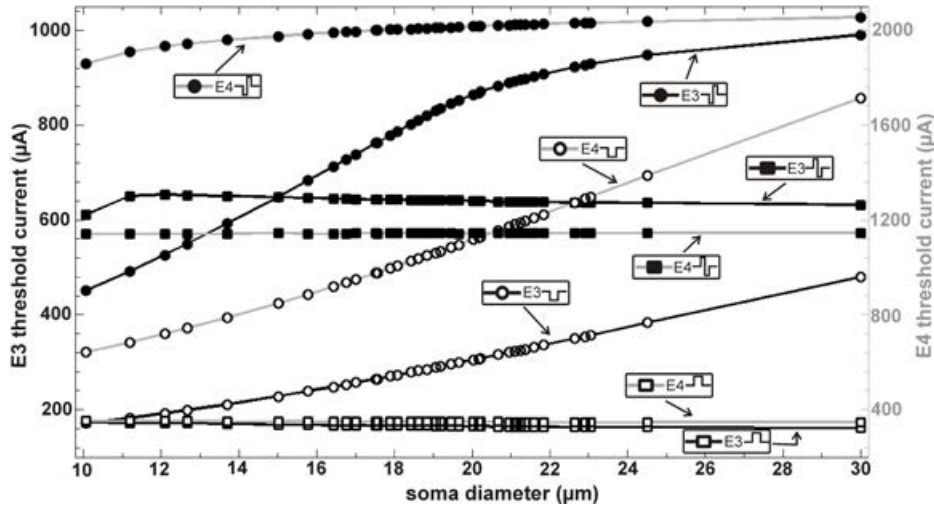


Figure 5.3: Threshold currents of E3 and E4 as function of soma diameter for all detected cells. The black E3 axis on the left is half of the gray E4 axis on the right. Corresponding threshold curves have the same color. For better visualization, the markers display a selection of evaluations.

When the soma-electrode distance is 0.5 mm, the cathodic threshold increases with soma diameter monotonically from 171  $\mu$ A to 393  $\mu$ A, always initiating the AP at compartment 13. Contrarily, the anodic threshold decreases monotonically from 174  $\mu$ A to 162  $\mu$ A with a constant IS at compartment 27. For the biphasic pulses of E3, the thresholds as well as the IS changes with varying soma diameter. When



stimulated with biphasic cathodic first pulses, the thresholds again increase with cell size. The values range from 451  $\mu\text{A}$  to 954  $\mu\text{A}$ , although the slope of the curve decreases for diameters larger than 19.07  $\mu\text{m}$  correlating with the change of IS from compartment 13 to 27 (compare top panel of Fig. 5.4). For biphasic anodic first pulses, this change appears already for diameters above 11.64  $\mu\text{m}$ . As a result, the threshold values ascend steeply at first from 611  $\mu\text{A}$  to 654  $\mu\text{A}$ , but then again decrease to 635  $\mu\text{A}$  (compare bottom panel of Fig. 5.4).

When the electrode is moved further away from the soma to a distance of 1 mm, the application of a cathodic pulse initiates the AP at compartment 13 for each soma diameter. For all other pulse forms and variations in diameter, the IS is the central end of the model neuron (compartment 27). The threshold values for both monophasic and biphasic cathodic pulses increase with cell size, although with a variation between 643  $\mu\text{A}$  to 1420  $\mu\text{A}$ , the monophasic values show a steeper slope than those of biphasic pulses with values ranging from 1858  $\mu\text{A}$  to 2040  $\mu\text{A}$ . For anodic stimulation, the threshold values remain virtually the same (i.e., for monophasic pulses the values decrease only slightly from 353  $\mu\text{A}$  to 348  $\mu\text{A}$ , while the threshold values for biphasic stimulation fluctuate between 1142  $\mu\text{A}$  and 1146  $\mu\text{A}$ , Fig. 5.3).

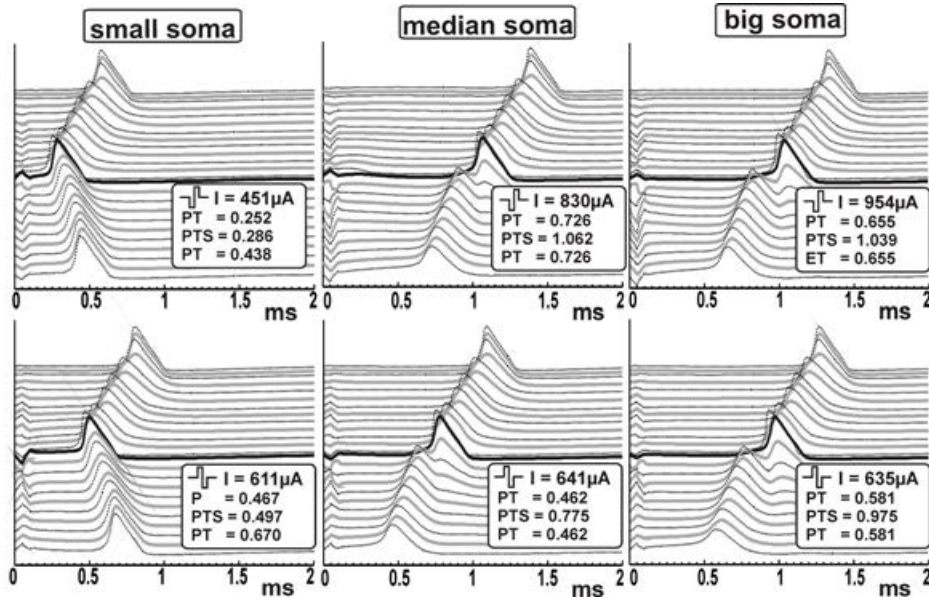


Figure 5.4: Biphasic threshold stimulation by E3 of three neurons with different soma size. The traveling APs (lines from top to bottom correspond to the transmembrane potential of every compartment from the peripheral to the central end) are simulated for the smallest ( $d = 10.05 \mu\text{m}$ ), mean value ( $d = 19.08 \mu\text{m}$ ) and biggest detected cell ( $d = 25.05 \mu\text{m}$ ).

While recording E3 and E4 threshold currents and ISs, we also collected temporal parameters of the spike, namely values of the AP peak time at the IS, the soma and the last model compartment. Corresponding values vary for different soma sizes when

stimulated with the individual thresholds. For monophasic stimulation, the values for the spike onset, the AP peak time at the IS, seem to increase with broad distribution when the soma diameter is raised from its minimum of 10.05  $\mu\text{m}$  to its maximum of 25.05  $\mu\text{m}$ .

The influence of the soma diameter for biphasic stimulation by E3 is illustrated in Fig. 5.4. The shift in IS occurring for altering soma diameter is observed for the biphasic cathodic first pulses radiated by E3. The values jump from a lower level, around 0.25 ms, to a peak time around 0.7 ms at the IS for diameters larger than 19.07  $\mu\text{m}$  (compare top row of Fig. 5.4). For anodic first pulses (bottom row) the latencies, the time at which the AP occurs at the end, are longest for small cells.

Table 5.1 summarizes the results of the whole set of soma diameters and compares different pulse forms for two different electrode-soma distances. Monophasic cathodic pulses lead to smaller E3 values of the AP peak time at the IS compared to their counterparts of E4 with doubled distance. Corresponding anodic values are higher, but the effect of increasing the electrode-soma distance is less pronounced. For biphasic pulses the values of E3 include spikes initiated at two different sites, compartment 13 and 27. Still, the mean value of E3 cathodic first pulses of 0.46 ms is significantly higher than 0.583 ms for E4. By contrast, anodic first pulses by E4 cause a slightly earlier onset. The fastest onset among all pulse forms of the two electrode positions appears for E3 stimulation with monophasic cathodic pulses.

Although changing the pulse shape or electrode position has the same consequences for the peak time at the soma, the variations among corresponding values are now higher. The influence of the soma size is most obvious for this temporal parameter, as the largest values of variance, standard deviation and overall range, appear in the middle part of Table 5.1. Moreover, the results predict that irrespective of the electrode-soma distance, the peak time values at the soma elevate with increasing diameter for each of the four pulse form (data not shown).

The bottom part of Table 5.1 represents the peak time at the end of the model neuron. Since in most cases the spike is initiated at compartment 27, the values of the peak time at the IS and at the end are equal. Spikes which are generated peripherally, as for monophasic cathodic stimulation, need to pass the delaying soma region and therefore have longer latencies than the other pulse forms. The shortest latency appears for E4 stimulation with biphasic anodic first stimulation with a minimum of 0.367 ms.

We not only acquired the volumetric data of a certain amount of SGCs, but also assigned cells to their site within the modiolus. We used this additional information to analyze the distribution of temporal spike parameters along the cochlear turns. Fig. 5.5 shows boxplots of the peak time values of SGCs from the base, the apex and the middle turn which were collected for threshold stimulation of E3 and E4.

Biphasic cathodic first stimulation radiated by E3 leads to the widest variation

		<b>E3</b>				<b>E4</b>			
		CAT	ANO	BIC	BIA	CAT	ANO	BIC	BIA
<b>PT:</b>	<b>min</b>	0.332	0.464	0.252	0.458	0.4	0.494	0.572	0.367
	<b>max</b>	0.36	0.486	0.668	0.467	0.445	0.551	0.594	0.508
	<b>mean</b>	0.346	0.475	0.46	0.462	0.422	0.522	0.583	0.438
	<b>max-min</b>	0.027	0.022	0.416	0.009	0.045	0.057	0.022	0.142
	<b>var</b>	0	0	0.087	0	0.001	0.002	0	0.01
	<b>svd</b>	0.019	0.016	0.294	0.007	0.032	0.04	0.015	0.1
<b>PTS:</b>	<b>min</b>	0.363	0.675	0.286	0.497	0.476	0.747	0.816	0.572
	<b>max</b>	0.454	0.937	1.128	0.948	0.496	0.92	1.007	0.946
	<b>mean</b>	0.408	0.806	0.707	0.723	0.486	0.834	0.912	0.759
	<b>max-min</b>	0.091	0.262	0.843	0.452	0.02	0.174	0.19	0.374
	<b>var</b>	0.004	0.034	0.355	0.102	0	0.015	0.018	0.07
	<b>svd</b>	0.065	0.185	0.596	0.319	0.014	0.123	0.135	0.264
<b>ET:</b>	<b>min</b>	0.526	0.464	0.438	0.458	0.638	0.494	0.572	0.367
	<b>max</b>	0.605	0.486	0.668	0.67	0.649	0.551	0.594	0.508
	<b>mean</b>	0.566	0.475	0.553	0.564	0.643	0.522	0.583	0.438
	<b>max-min</b>	0.079	0.022	0.23	0.213	0.011	0.057	0.022	0.142
	<b>var</b>	0.003	0	0.026	0.023	0	0.002	0	0.01
	<b>svd</b>	0.056	0.016	0.162	0.15	0.008	0.04	0.015	0.1

Table 5.1: Summary of temporal spike parameter values induced by E3 (left) and E4 (right). Values of PT, PTS and ET for each pulse shape are calculated from the whole set of soma diameters and are given in [ms]. Red values correspond to cathodic pulses, green values to anodic pulses, where light colors define monophasic and dark colors corresponding biphasic pulses.

in values of the peak time. Note that this electrode configuration also produces the lowest values of the peak time, although the mean value of apical neurons is certainly higher than those of middle turn and basal neurons. This is also visible for cathodic pulses of E3 and biphasic anodic first pulses of both electrodes, that confirms the trend of increasing values for increasing cell body diameter.

The results for the peak time at the soma are very similar. Since for cathodic pulses the AP is initiated peripherally, and therefore propagates orthodromically, the values of the peak time at the soma are higher than the peak time at the IS. The low outliers for biphasic anodic first pulses of E3 correspond to APs initiated in compartment 13.

Although neurons will respond earlier to cathodic pulses, the delay of information processing to the next cell is lowest for biphasic anodic first pulses (Fig. 5.5, bottom panel), since the spike is initiated at the central end instead of propagating from peripheral sites over the soma. For monophasic and biphasic pulses, longer latencies appear for cathodic pulses. Surprisingly, E3 leads to smaller values than E4 when radiating cathodic pulses, although for biphasic anodic first pulses E4 shows shorter

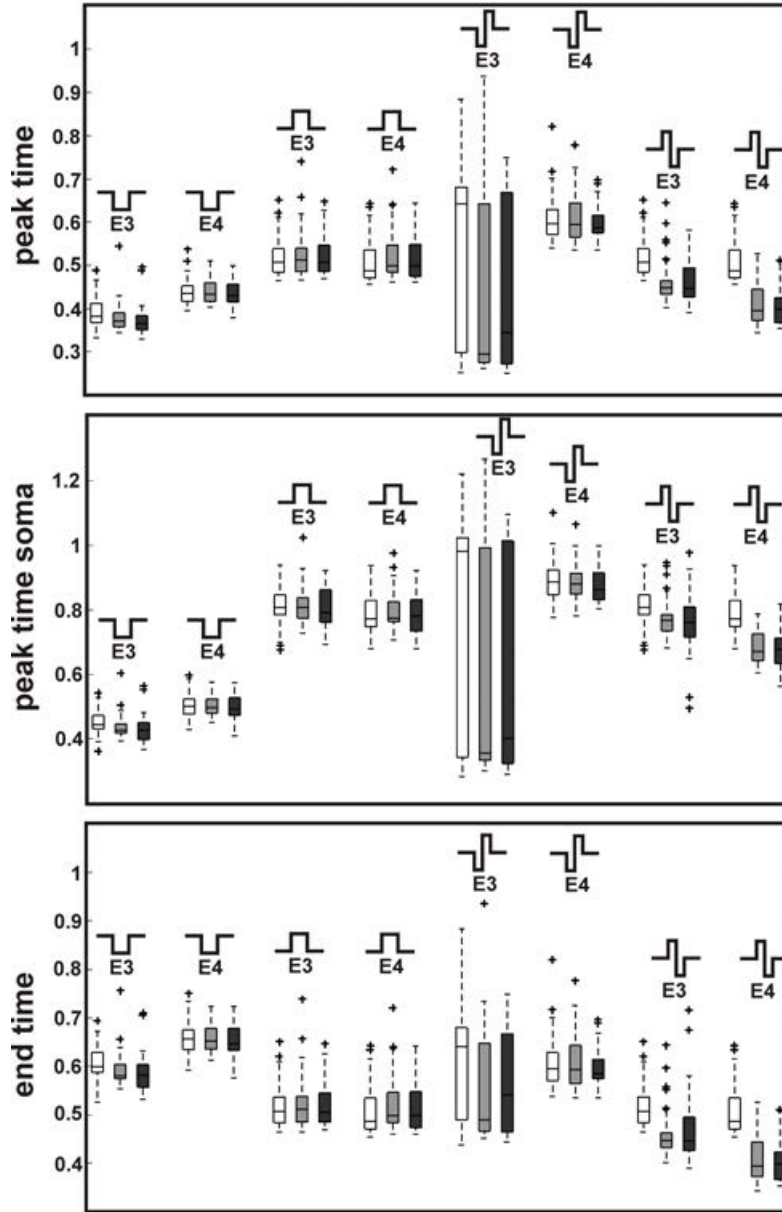


Figure 5.5: Comparison of temporal parameters in the three cochlear regions; Boxplot of temporal parameters of the spike induced by E3 and E4. The peak time at the IS (top) the peak time at the soma (middle) and the end time of the spike (bottom) are compared for apical (white boxes), middle turn (light gray boxes) and basal neurons (dark gray boxes).

latencies.

### 5.3 Micro CT 3D data

The most dominant shortcoming of the previous simulations is the use of a 2 dimensional data set for the spatial arrangement of the model neuron and the stimulating electrode. A just recently performed data evaluation of our partners of the MedUni IBK, reveals a groundbreaking 3D data set of traced cochlear neurons originating from different frequency regions Fig. 5.6.

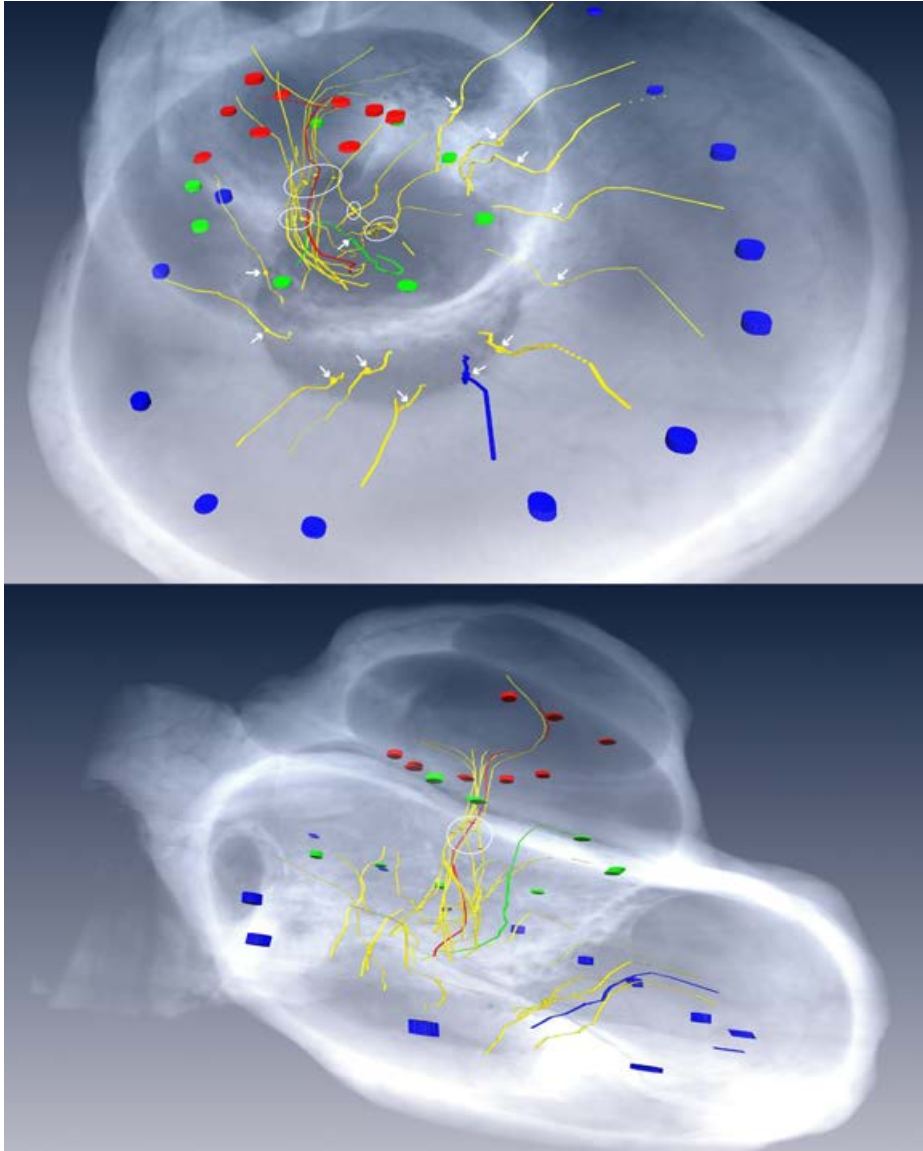


Figure 5.6: 3D data from a MicroCT-imaging of one human cochlea. A total amount of 27 SGCs represented in yellow have been traced. Soma positions are indicated by white arrows or white circle. Red apical 2 SGC, green middle 1 SGC, blue basal 7 SGC. The colors of the evaluated electrode positions correspond to the three turns.

Micro-CT imaging of one human cochlea was performed with a SCANCO Viva 100  $\mu$ CT (Scanco Medical AG, Brüttisellen, Switzerland) yielding an isotropic spatial resolution of 3  $\mu$ m. The tube voltage was set to 70 kV, tube current to 182  $\mu$ A, exposure time to 1600 ms and 2000 projections were used. The acquired image stacks had an average size of 4000\*4000\*2400 volume elements with 16-bit gray value resolution.

A median filter was applied to data prior to segmentation to improve signal-to-noise-ratio. Bundles of nerve fibers (diameter=15  $\mu$ m) as well as possible electrode positions of a CI were manually segmented using Amira 5.3.3 (Mercury Computer Systems Inc., San Diego, CA, USA). The electrode positions were assumed to be beneath the organ of Corti within the Scala tympani.

Segmented structures were saved in a label field which was used to determine the position in space in every slice. For visualization of the cochlea, micro-CT data was resampled and illustrated using digitally reconstructed radiograph method simulating a radiograph display from arbitrary views. Segmentation data was resampled (same output resolution as used previously) and smoothed by producing a surface.

For the following simulation again standard parameters for the model neuron were defined. Three representative neurons of the whole stack of traced cochlear neurons were tested for stimulation by individually selected micro electrodes with different stimulus configurations. From the apical turn, the apical 2 SGC was chosen which is plotted in red in Fig. 5.6, results for five selected electrode positions are presented in Sec. 5.3.1. Results for the green middle 1 neuron are given in Sec. 5.3.2 and those of the blue basal 7 neuron in Sec. 5.3.3.

The trials involve again four different types of pulses, i.e., 0.1 ms long monophasic and 0.05 ms/phase biphasic pulses with both leading polarities, anodic and cathodic, pulses were applied (CAT, ANO, BIC, BIA as explained in Sec. 5.2). Just to be clear, the presomatic lengths of the all three neurons is considered to be of  $l_{pre} = 100$   $\mu$ m, but the soma diameter was slightly varied according to mean values of the three cochlea regions (Potrusil et al. 2012), i.e.,  $d_{soma} = 20.01$   $\mu$ m for the apical 2 neuron,  $d_{soma} = 18.79$   $\mu$ m for the middle 1 neuron and  $d_{soma} = 18.68$   $\mu$ m for the basal 7 neuron.

#### 5.3.1 Apical 2 neuron

The first trials have been performed for the traced apical 2 neuron. For this neuron the length of the whole peripheral process was measured to be 2.8 mm. This measure was used to compute the number of compartments and also the coordinates at their central points which are required to evaluate the extracellular voltage profile  $V_{e,n}$  for each compartment, i.e., the distance of the stimulating electrode to each compartment has to be calculated. This was done by an interpolation method of the traced 3d data of the apical 2 neuron which is represented in Fig. 5.7 and explained in the following. It should be noted that the SGC is actually displayed upside down which will also be



the case for the other selected model SGCs (compare Fig. 5.11 of the middle 1 SGC and Fig. 5.15 of the basal 7 SGC).

By assuming an unmyelinated active dendritic terminal of 100  $\mu\text{m}$  length, a presomatic compartment length of  $l_{pre} = 100 \mu\text{m}$  and two fixed internode length for the first and the last peripheral internode, the total number of peripheral nodes and internodes can be computed. This calculation further includes a fixed length of all other internodes of 450  $\mu\text{m}$  and of 2.5  $\mu\text{m}$  for the nodes of Ranvier. With the total length of the traced neuron including the available central process data, the soma position and also the number of central nodes and internodes can be evaluated. The spherical soma of  $d_{soma} = 20.01 \mu\text{m}$  is followed by a 5  $\mu\text{m}$  long postsomatic compartment and then again an alternating internode (500  $\mu\text{m}$  long) node (2.5  $\mu\text{m}$ ) sequence is interpolated for the available length.

Summing up these considerations, the apical 2 neuron has 27 compartments, whereas compartment 1 refers to the terminal peripheral region (bottom green dot in Fig. 5.7) and compartment 27 to the central end region respectively (top green dot in Fig. 5.7). The peripheral process includes 7 internodes and 6 intersecting nodes, compartment 15 corresponds to the presomatic compartment, the index 16 denotes the soma (yellow dot in Fig. 5.7) and compartment 17 thus is the postsomatic region, leaving 5 internodes with 4 intersecting nodes of the central process.

Furthermore the electrode-neuron distances have been calculated for each of the 27 neuronal compartments. The whole data set includes 6 different electrode positions for apical and also middle turn neurons, additionally corrected coordinates for 5 basal positions could also be evaluated. All the stimulation trials have been repeated for the total amount of 17 electrodes. However, since the tremendous quantity of evaluated results is beyond the scope of this thesis, Fig. 5.7 summarizes the selected electrodes used for the subsequently presented results. The maximum distance of the electrode to the neuron varies, but occurs always for compartment 27 (printed as red dashed lines). The green dashed lines show the minimum electrode-neuron distance which occurs for different sites of the SGC, where the corresponding compartment indices are indicated in brackets.

Four different pulses concerning their polarity have been tested. Initially the threshold values of current amplitude for successful spike transmission to the central end of the apical 2 neuron have been calculated for all electrodes. For cathodic stimulation the lowest threshold current of 65  $\mu\text{A}$  occurs for the api3 electrode which is almost the same value as for electrode api2 which has a threshold of 70  $\mu\text{A}$  (see Table 5.2). These are also the electrodes with lowest values of minimum electrode neuron distance, although note that for api2 the minimum distance of 342.6  $\mu\text{m}$  is reached between the first neuron compartment and the electrode, whereas the minimum of 350.2  $\mu\text{m}$  appears for compartment 7 for the api3 electrode (see Fig. 5.7).

Although the magnitude of the required threshold current of each electrode defi-

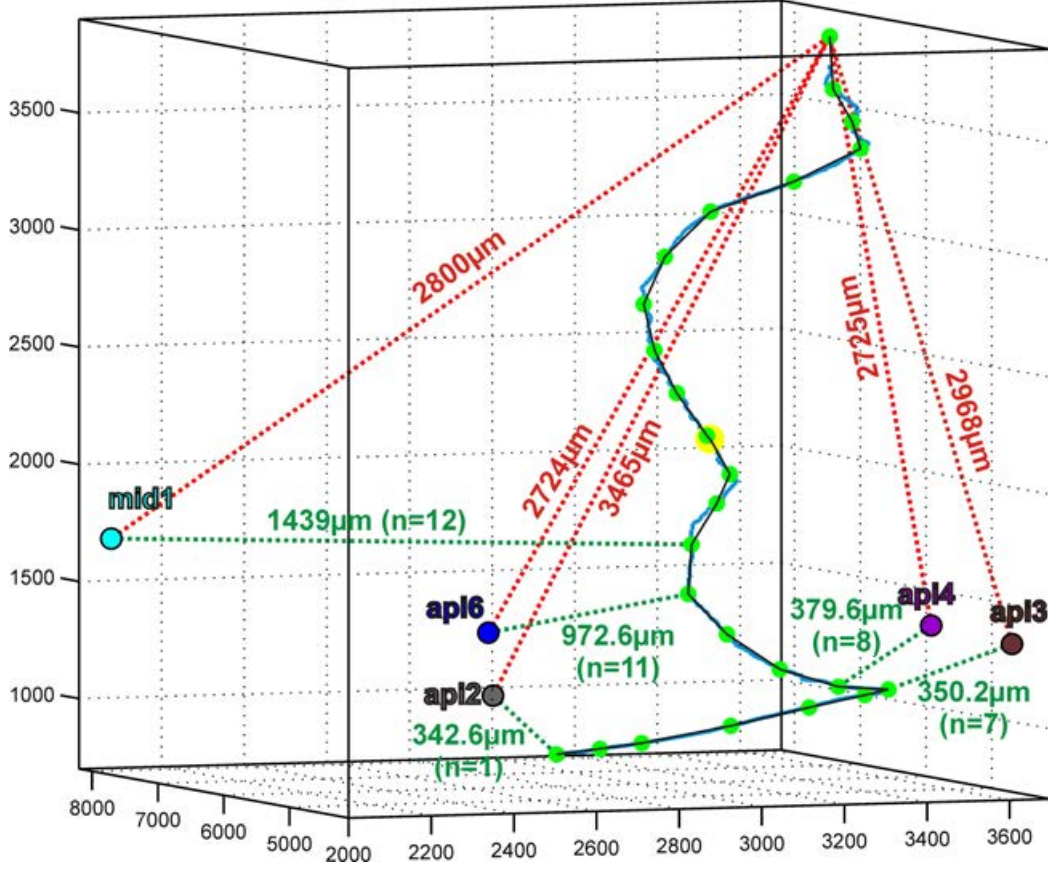


Figure 5.7: Interpolation of apical 2 (black line) traced 3D data (thick blue line) and selected electrode positions. 27 compartments, active nodes are displayed as green dots, the soma yellow. The presented electrodes are used for the stimulation trials, minimum (green lines) and maximum (red lines) electrode-neuron distances are indicated. Since the compartment indices for the minimum distance are not constant, they are presented in brackets.

nitely correlates with the distance to the excited neuron, especially the index of the compartment where the minimum distance appears is crucial. For the *apl1* electrode (data not shown) the minimum distance to compartment 1 of 426.6  $\mu\text{m}$  is quite high, but the threshold value for a successful spike transmission to the neural central end is only 95  $\mu\text{A}$ . This minimum distance is between the corresponding values of electrodes *apl4* ( $\text{min}(\text{dist})=379.9 \mu\text{m}$  for compartment 8) and electrode *apl5* ( $\text{min}(\text{dist})=490.5 \mu\text{m}$  for compartment 10). But these electrodes demand for higher threshold currents, i.e., 130  $\mu\text{A}$  for electrode *apl4* and 185  $\mu\text{A}$  for electrode *apl5*. This must be a consequence of the unmyelinated soma which is closer to the minimum distance sites and demands for a higher current consumption than the sealed peripheral end of the model neuron.

However, the distance significantly increases for all electrodes starting from *apl6*,

which shows a minimum distance value of 972.6  $\mu\text{m}$  appearing for compartment 11 and a corresponding CAT threshold value of 580  $\mu\text{A}$ . For electrodes based in the middle turn the distance values further increase and the site where the minimum appears changes for regions on the peripheral process to the central axon. On the other hand the compartment where the maximum distance appears, which constantly is the central end for all apical and mid1-mid4 electrodes, changes to the first compartment for electrode mid5. The corresponding theoretical threshold values for excitation of the model neuron are between 1 and 1.4 mA. For the far distant basal electrodes again very high threshold currents are needed in the range of 1.8 to almost 5 mA, but the distance behavior again changes (more details omitted).

Not only the threshold values of CAT stimulation varies for different electrodes according to their sites and magnitude of minimum distance, also the induced excitation profiles of the spike propagating on the model neuron certainly differ. The consequence of altering site of minimum distance also influences the IS of the spike. Fig. 5.8 illustrates the stimulation of the apical 2 model neuron with 5 different electrodes.

For each trial the electrode stimulates with a 0.1 ms long CAT impulse with the individual threshold current. The api2 and api3 electrode (first row panels) almost have the same threshold value, but the initiation site of the spike is changed from compartment 1 to compartment 7, which is the third node of Ranvier on the peripheral process. The delay of spike onset after stimulation can be defined as the time at which the peak of transmembrane potential appears at the IS compartment. These two values did not significantly differ for both electrodes, i.e., the first peak on the neuron appears 0.23-0.28 ms after stimulus onset.

Another temporal parameter of the spike is the peak time at the soma, i.e., the time at which the soma shows the maximum of transmembrane potential. For both electrodes the AP is initiated on peripheral sites, and thus also travels orthodromically over the soma region to the central end, but since for the api3 electrode the spike is generated closer to the soma these two peak times differ. Compare the values in Table. 5.2: the spike induced by stimulation with electrode api2 will appear at the soma 0.859 ms after spike onset, whereas the spike from electrode api3 reaches the soma earlier at 0.638 ms. This results in comparable differences for values of the peak time where the spike arrives at the central end which is compartment 27. The corresponding transmembrane potential curves of the last neuron compartment for each electrode are plotted in the last panel in order to compare the delay of information processing to the next target cells.

Results for electrodes api4 and api6 are plotted in the middle row of Fig. 5.8. Larger threshold values are needed for the current amplitude of these electrodes. Furthermore the ISs are correlating with the sites of minimum electrode-neuron distance. For electrode api4 the spike is induced at the fourth peripheral node 0.319 ms after spike onset. Although this causes a delay of spike initiation compared to the previ-

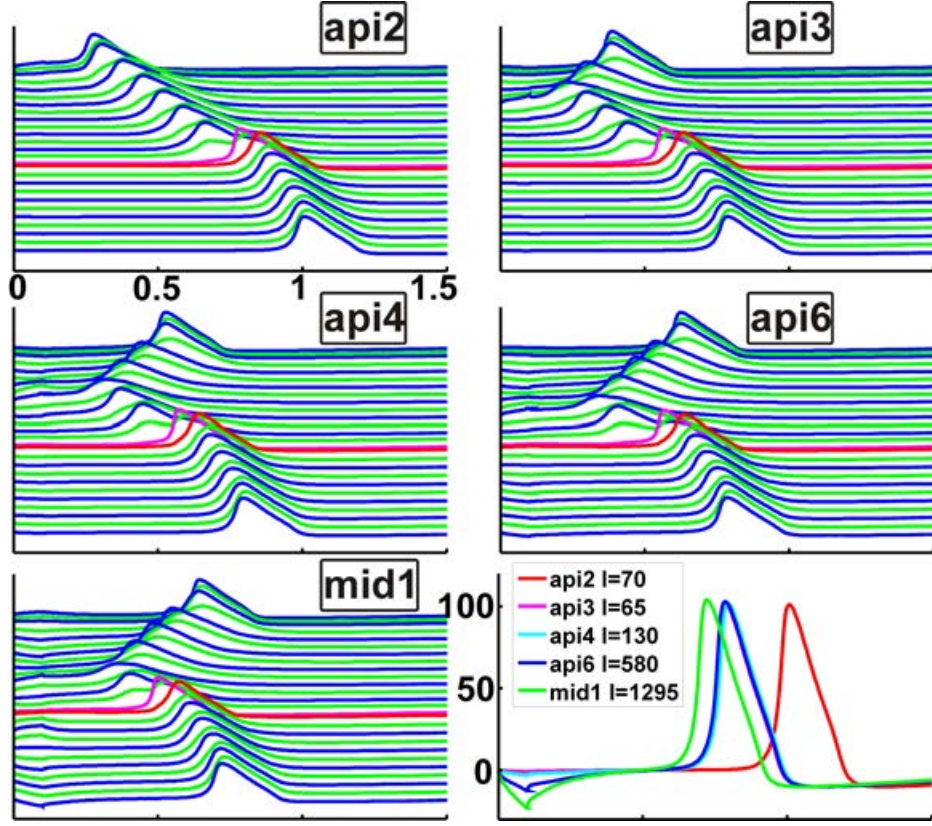


Figure 5.8: CAT stimulation of apical 2 SGC with 5 selected electrodes as indicated in the panel titles. Transmembrane voltages of nodes of Ranvier are blue lines, the internodes green. The presomatic compartment is the magenta line and the soma is displayed in red. The transmembrane potentials of the last model neuron compartment are plotted in the bottom right panel. Threshold values are given in  $\mu\text{A}$  in the legend for 0.1 ms long CAT stimulation.

ously mentioned electrodes, the spike appears at the soma at approximately the same time at 0.65 ms which is a result of the shorter distance to the soma. Thus the spike is also not delayed at the central end and arrives almost simultaneously (compare transmembrane potentials of the last compartment in the bottom right of Fig. 5.8).

The same pattern is valid for electrode api6. Although the larger minimum distance of 972.6  $\mu\text{m}$  results in higher current threshold and 0.345 ms delayed spike onset, the spike will be at the central end almost at the same time as the spikes induced by electrodes api3 and api4. Furthermore the stimulation by the closest electrode in the middle turn has almost the same temporal spike properties. Still it should be noted, that the 400  $\mu\text{m}$  longer distance results in doubled threshold current. Corresponding peak time values are presented in Table 5.2.

The same trials have been repeated for the biphasic version of a cathodic pulse



denoted as BIC pulse, i.e., a 0.05 ms cathodic phase is followed by a 0.05 ms long anodic phase of the same current amplitude. Results for the BIC stimulation are presented in Fig. 5.9. The same electrodes have been compared as for the CAT stimulation.

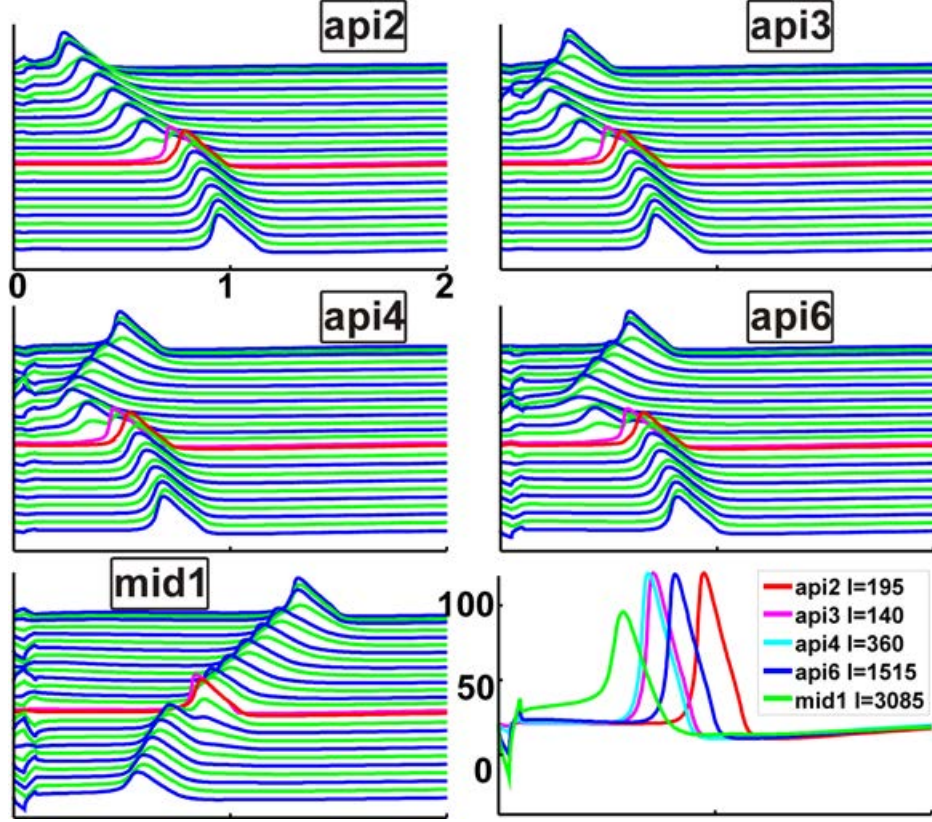


Figure 5.9: BIC stimulation of apical 2 SGC with the same electrodes as in Fig. 5.8. In comparison, threshold values for biphasic stimulation are higher than monophasic counterparts. The IS of the apical electrodes did not change significantly, but for mid1 stimulation the AP is generated at the SGC's model end at compartment 27, resulting in the shortest delay represented by the green line in the bottom right.

For both cathodic pulse forms the results are comparable concerning the ISs for each electrode and generally also for the temporal spike parameters with certain variations as will be pointed out. However, although again electrode api3 shows the lowest threshold value of current amplitude, the magnitude is certainly altered, i.e., the threshold value for BIC stimulation by electrode api3 is now 140  $\mu\text{A}$  which is more than doubled compared to the corresponding monophasic value. Nonetheless, the relation between increasing threshold values and electrode position remains the same with about doubled amplitude compared to the monophasic counterpart.

The IS for the api2 electrode (upper right panel in Fig. 5.9) remains compartment 1 where the AP appears 0.235 ms after spike onset. This spike travels orthodromically

from the beginning over the soma where the spike appears at 0.797 ms to the central end where it arrives at 0.953 ms. Note that this is a reduction in delay of 0.5 ms compared to the CAT stimulation by the same electrode (values are presented in Table 5.2). Also for the api3 electrode the IS remains compartment 7 and the temporal spike properties are slightly smaller.

For stimulation with electrode api4 the IS is changed to compartment 11 which is the fifth peripheral node. The delay of the spike onset on the IS is reduced to 0.272 ms for BIC pulses and the shift closer to the soma results in over 0.1 ms acceleration compared to the monophasic CAT stimulation. The farthest mid1 electrode which needs a high threshold value of 3 mA initiates a spike at the central end of the model neuron. Since the IS now is compartment 27 which is also the central end the spike propagates antidromically back to the soma. This results in a higher value of the peak time for the soma compared to the IS value. This value now equals the peak time at the end which appears only 0.78 ms after spike onset (bottom right panel).

At this point it should be noted that an IS at compartment 27 indicates that the model neuron should have a longer central axon as excitation conditions are not correct for the central boundary. The axon should be extrapolated in direction of the cochlea axis, which could not yet been evaluated correctly and thus will be done for pending studies (see chapter 6).

Again the transmembrane potentials of the last compartments are plotted for each electrode in the bottom left panel of Fig. 5.9. The green line corresponds to the stimulation of electrode mid1 which is the earliest, because it is also the site where the spike is first generated. For the apical electrodes, api2 stimulation causes the longest delay of information processing, because the spike has to travel from the very beginning to the central end. This distance is reduced for the other apical electrodes according to their IS. Still although electrodes api4 and api6 both induce the spike at compartment 11, the longer delay of spike onset of electrode api6 also results in a corresponding delay at the central end.

The same trials have been performed for anodic stimulation, i.e., either a 0.1 ms long monophasic pulse which is denoted as ANO or a biphasic pulse with leading anodic phase of 0.05 ms duration, abbreviated as BIA, was used. For ANO stimulation of the target apical 2 neuron, among all different electrode positions only two possible ISs occur. For electrodes which have their minimum electrode-neuron distance before compartment 8, the spike will be generated at the peripheral terminal at compartment 1. This is valid for almost all apical electrodes, namely api1-api5. The last two apical electrodes and all middle turn electrodes contrary lead to a spike initiation at the central ending at compartment 27. Even for the very distant basal electrodes and theoretical high threshold values greater than 4 mA, only these two ISs occur. This discrepancy is certainly reflected in the temporal spike properties, especially the delay of information processing to the next cell, i.e., the peak time of the AP at the central end shows two groups of values. If the IS is compartment 1 the spike has to travel



over the whole neuron resulting in end times between 1.13 and 1.4 ms (compare values in Table 5.2). For all other electrodes the spike is directly initiated at the central end about 0.34 to 0.5 ms after spike onset, although note that compartment 27 is the site with the maximum electrode-neuron distance in many cases.

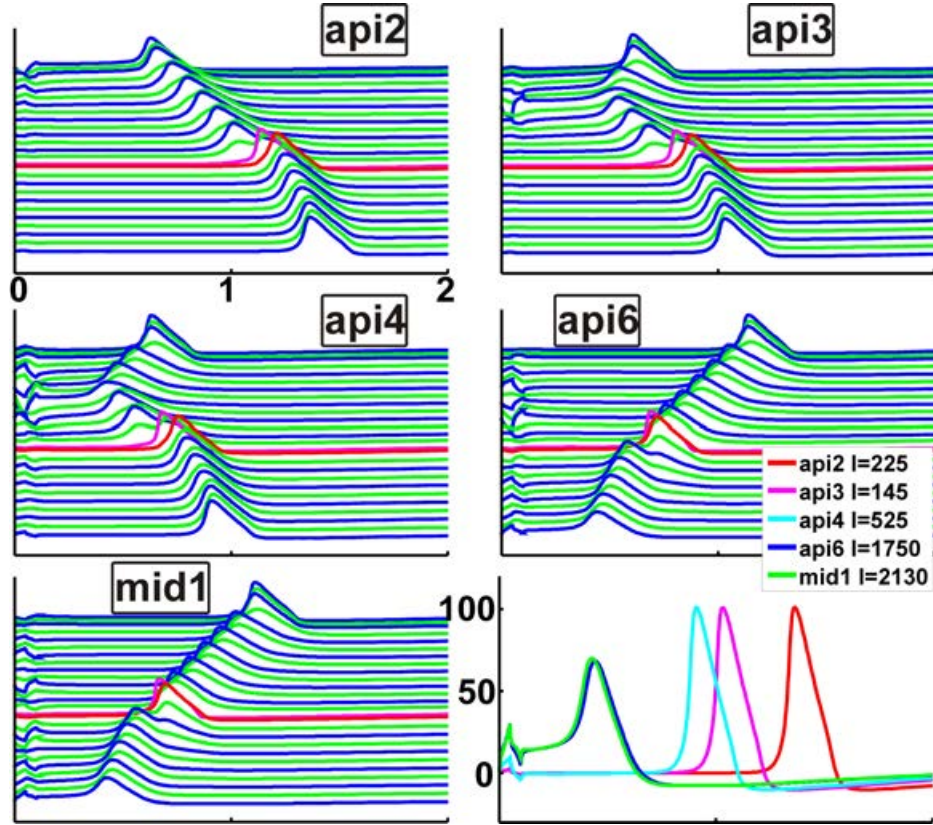


Figure 5.10: BIA stimulation of apical 2 SGC with the same electrodes as in Fig. 5.9. In comparison BIA thresholds are higher than corresponding BIC threshold with the exception of the api3 electrode which is almost the same as for BIC and the mid1 electrode has a lower value compared to BIC stimulation. Also the api6 electrode generates the AP at the end causing shortest delays at compartment 27 as represented in the bottom right.

Another interesting disparity compared to cathodic stimulation is the relation between the threshold currents of monophasic and biphasic pulses. For cathodic stimulation, the biphasic pulses are less efficient as they demand for more than doubled current amplitudes compared to their monophasic counterparts. When anodic pulses are used, electrodes api2-api3 have almost the same threshold values (compare corresponding values in Table 5.2). Electrode api3 needs 145  $\mu\text{A}$  for an ANO pulse to initiate a spike at compartment 1 0.402 ms after spike onset which will then arrive at the end at 1.136 ms, and also a threshold current of 145  $\mu\text{A}$  of a BIA pulse will generate a spike a bit later 0.537 ms after spike onset. Still for this configuration the

spike is initiated at a more distal site (5\* in Table 5.2 means three simultaneous ISs, namely compartment 5, 7 and 9), so that the spike arrives slightly earlier at the end compared to the ANO pulse with a delay of 1.03 ms.

However, for all other electrodes, except api2-api3, again more than doubled current amplitudes are needed to induce a spike followed by biphasic stimulation compared to the anodic counterpart. The excitation profiles for BIA stimulation of the same electrodes as discussed previously, are presented in Fig. 5.10. For this type of stimulation multiple ISs occur, e.g., a threshold current of 225  $\mu\text{A}$  for a BIA pulse of electrode api2 induces a spike at the first compartment 0.63 ms after spike onset which will reach the central end quite late at 1.367 ms which is the longest delay, illustrated by the red line in the bottom right panel of Fig. 5.10.

		threshold	IS	PT	PTS	ET
CAT:	api2	70	1	0.278	0.859	1.013
	api3	65	7	0.228	0.638	0.794
	api4	130	9	0.319	0.650	0.804
	api6	580	11	0.345	0.652	0.798
	mid1	1295	11	0.382	0.634	0.782
BIC:	api2	195	1	0.235	0.797	0.953
	api3	140	7	0.204	0.568	0.721
	api4	360	11	0.272	0.539	0.693
	api6	1515	11	0.369	0.658	0.816
	mid1	3085	27	0.577	0.868	0.577
ANO:	api2	220	1	0.606	1.252	1.406
	api3	145	1	0.402	0.981	1.136
	api4	195	1	0.391	0.968	1.125
	api6	510	27	0.502	0.775	0.502
	mid1	650	27	0.433	0.701	0.433
BIA:	api2	225	1	0.630	1.211	1.367
	api3	145	5*	0.537	0.881	1.032
	api4	525	9	0.429	0.754	0.910
	api6	1750	27	0.446	0.719	0.446
	mid1	2130	27	0.426	0.694	0.426

Table 5.2: Summary of stimulation trials for the apical 2 neuron and five selected electrode positions. Values of the threshold are given in [ $\mu\text{A}$ ], the IS compartment index is listed and the collected temporal spike properties are given in [ms].

For electrode api4 which is illustrated in the middle row at the left, the IS is compartment 9 and since the threshold value of 525  $\mu\text{A}$  is quite high the onset of the spike appears early 0.429 ms after stimulus onset. This spike will reach the central end after 0.91 ms indicated as cyan line. The remaining two electrode positions generate the spike at compartment 27 after about  $0.43 \pm 0.01$  ms. Still note, that the

corresponding threshold currents are very high.

Although extensive testing was performed for the stimulation of the apical 2 model neuron, a summary of computed spike properties is presented in Table 5.2. The presented values include only the electrodes which are also used for the presented results in the previous figures. Still evaluated values of the IS and corresponding temporal spike properties, i.e., PT, PTS and ET, are presented for all four pulse forms.

#### 5.3.2 Middle 1 neuron

The whole stack of traced neuron data includes 6 different middle turn neurons, but compared to the apical neurons their accessible traced length was quite short. Especially the central process is very often cut off to a very short length of only 0.373 mm for the middle 6 neuron. The data has to be extended with the cochlea axis and central processes have to be extrapolated in the right direction. However the middle 1 neuron has a total length of 3.71 mm including 2.479 mm for the central axon. Consequently this model neuron was used for the following simulations as presented in Fig. 5.11.

As a first step again the traced neuronal data of the middle 1 neuron was interpolated to evaluate the total number of model neuron compartments. The same considerations as for the apical 2 neuron, but with incorporating the detected length of the peripheral process of the middle 1 neuron, i.e.,  $l_{peripher} = 1.231$  mm, reveals only 19 compartments. This time only 3 peripheral internodes all of a different length with 2 intersecting nodes could be incorporated. The soma compartment therefore has the index 8. For the central process 5 internodes with corresponding 5 nodes have been interpolated along the traced neuron data.

For this model neuron again all theoretical electrode positions have been tested, but only 5 relevant positions have been selected to be presented in detail within this thesis. Initially the neuron-electrode distances have been calculated for each model compartment for electrode positions api5, mid2 and mid4-mid6 (see Fig. 5.11). The closest electrode to the middle 1 neuron is electrode mid4 which shows a distance of 325.56  $\mu\text{m}$  to compartment 1. Another interesting fact is the change of the site of maximal electrode-neuron distance. Although for all apical electrodes and positions mid1-mid4 the central process is the farthest site, this changes for electrode positions mid5 and mid6 where the maximal distance to the neuron occurs for the first neuron compartment.

Although the results are not presented, it should be noted that some basal electrode positions would be closer to the middle 1 neuron than some of the middle turn electrodes. The bas5 electrode is only about 1 mm away from compartment 1 of the middle 1 neuron, but still the maximal distance of more than 3.5 mm to compartment 19 is very far.

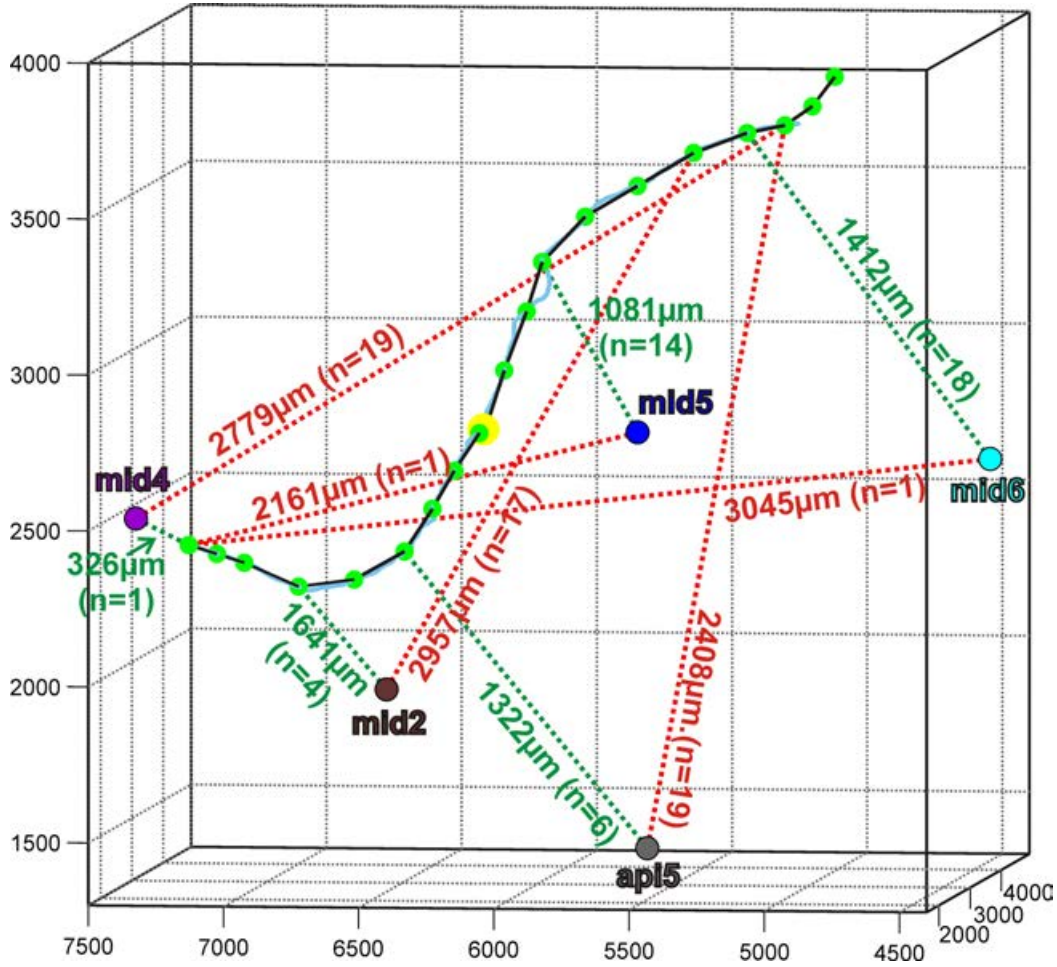


Figure 5.11: Interpolation of middle 1 (black line) traced 3D data (thick blue line) and selected electrode positions. 19 compartments, active nodes are displayed as green dots, the soma yellow. The presented electrodes are used for the stimulation trials, minimum (green lines) and maximum (red lines) electrode-neuron distances are indicated with the corresponding compartment indices in brackets.

Again all four pulse forms, i.e., CAT, BIC, ANO and BIA stimulation have been tested and the individual threshold currents for successful generation and transmission of an AP were calculated. As for the apical 2 neuron the spread of threshold values is enormous and depending on the electrode position the middle 1 neuron either favors cathodic or anodic pulses with usually higher values for biphasic stimulation. Fig. 5.12 illustrates the excitation profiles of the middle 1 neuron resulting from CAT stimulation by 5 different electrodes.

If the middle 1 neuron is stimulated by the api6 electrode, the threshold current of 780  $\mu\text{A}$  initiates a spike at compartment 7 which is the neighboring node of Ranvier closest to the minimum neuron-electrode distance site, which is compartment 6. This



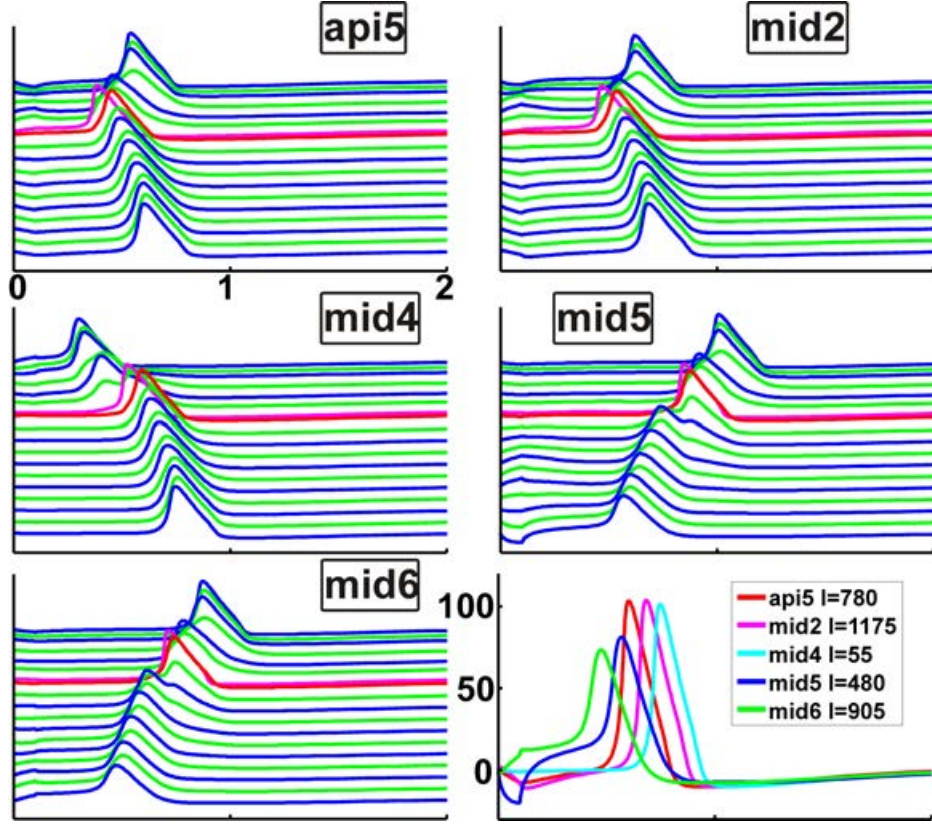


Figure 5.12: CAT stimulation of middle 1 SGC with 5 selected electrodes as represented in Sec. 5.3.1. The api5, mid2 and mid4 electrodes have peripheral ISs, contrary to the spikes induced at the model neurons end for mid5 and mid6. The lowest threshold value (given in  $\mu\text{A}$ ) in the bottom right) of the mid4 electrode causes the longest delay at the end, cyan line.

spike initiates 0.387 ms after stimulus onset and travels orthodromically and reaches the central end at 0.602 ms. The mid2 electrode has the same IS but the threshold current is essentially higher with a value of 1775  $\mu\text{A}$  and therefore the spike onset is also delayed, which results in a small difference in the end time value of 0.683 ms. The corresponding voltage profiles are plotted in the first row of Fig. 5.12.

The smallest electrode-neuron distance is observed for the mid4 electrode, which is only 325.56  $\mu\text{m}$  to compartment 1. As a first consequence the lowest threshold value of 55  $\mu\text{A}$  is satisfactory for AP initiation with a very short delay of spike onset of 0.299 ms. Still the spike has to travel along the whole neuron and therefore also is the last to reach the central end 0.75 ms after spike onset. Obviously the peak of the cyan line in the bottom right panel of Fig. 5.12 is the latest, which corresponds to the transmembrane potentials at the last compartment.

For the two remaining middle turn electrodes, mid5 and mid6, the relation of maximum and minimum site of electrode-neuron sites is reversed, i.e., now the closest

compartments to the electrodes are located centrally. This results in an IS on compartment 19 for threshold stimulation of both electrodes, although mid6 needs almost doubled current of 905  $\mu\text{A}$  compared to mid5 with a threshold of 480  $\mu\text{A}$ . The higher current of the mid6 electrode initiates the spike earlier and therefore also leads to the shortest delay of information processing at the central end. The corresponding green line in the bottom right panel of Fig. 5.12 has the earliest peak at 0.472 ms followed by the blue peak of the mid5 electrode at 0.567 ms.

The next trials have been performed for monophasic anodic currents of the 5 selected electrodes, and again three different ISs occur, but with a different distribution among the electrodes compared to the cathodic counterparts. Whereas electrodes api5 and mid6 initiate the spike at compartment 1 and electrodes mid2 and mid5 lead to an IS at compartment 19, the only exception is the spike initiated at compartment 5 for ANO stimulation by electrode mid4. This is not the only disparity, only for two electrode positions, api5 and mid5, the ANO threshold values are lower than the corresponding CAT values. However, Fig. 5.13 illustrates the excitation profiles of the same electrodes but now for ANO stimulation.

The lowest threshold value is again reached by ANO stimulation of electrode mid4, which is 265  $\mu\text{A}$  leading to the shortest delay of spike onset 0.289 ms after stimulus onset. But the spike has to travel from compartment 5 to the central end where it appears at 0.663 ms which is only the third fastest transmission to the next cell (see cyan line in the bottom right of Fig. 5.13).

The second lowest threshold value of 315  $\mu\text{A}$  holds for electrode mid5 which has the same short delay of spike onset as induced by electrode mid4. But for this electrode the spike is initiated at compartment 19 which is the central ending of the model neuron, and therefore the earliest peak appearing at 0.289 ms is the blue line.

By comparing the left panels which illustrate the excitation profiles it is obvious that also electrode mid2 generates the spike at compartment 19, but the threshold value is surprisingly high with a current demand of more than 1.1 mA which leads to a long delay of spike onset of 0.587 ms. Therefore although the spike is initiated at the central end, the peak at compartment 19 appears quite late at 0.587 ms.

The most distant mid6 electrode needs the highest threshold value of 1345  $\mu\text{A}$  and even more the IS is again compartment 1. Thus this electrode results in the longest delay of information processing to the next cell, since the peak of the green line in the bottom right of Fig. 5.13 is not reached until almost 1 ms after spike onset.

The trials for the biphasic counterparts reveal that BIC and BIA stimulation show certain similarities among their excitation profiles of each electrode. For all apical electrodes the IS is compartment 1 no matter which polarity is the leading phase. Also the far distant biphasic stimulation with basal electrodes leads to uniform ISs for each electrode, although for some the IS is compartment 1, but for most positions the spike is initiated at compartment 19. These two sites also occur for stimulation



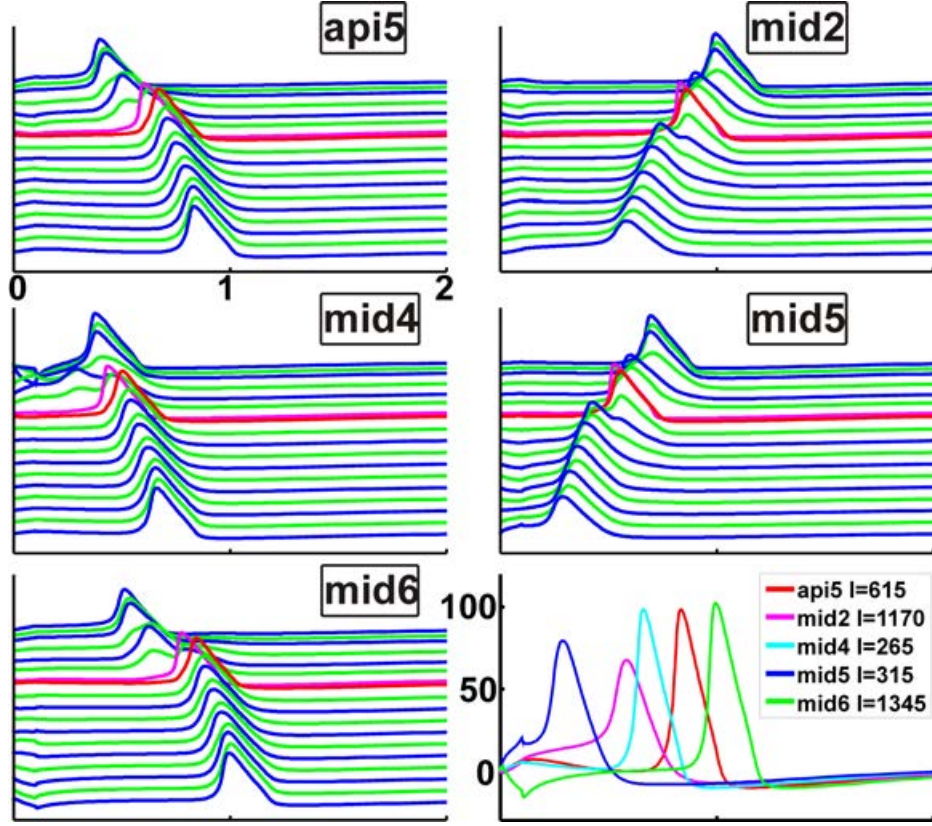


Figure 5.13: ANO stimulation of middle 1 SGC with the same 5 selected electrodes as in Fig. 5.12. For the mid2 and mid6 electrode the IS changes to the last compartment in contrast to CAT stimulation resulting in stronger variations of the transmembrane potentials at the end (bottom right) among different electrodes. The threshold value of the mid2 electrode remains almost the same as BIC stimulation. While the corresponding ANO values of api5 and mid5 are lower, mid4 and mid6 ANO stimulation demands for higher threshold values than CAT pulses.

with middle turn neurons. Interestingly for electrodes mid1-mid3 BIC pulses initiate the spike at compartment 1 whereas BIA pulses of the same electrodes have their IS at compartment 19. For the remaining electrodes mid4-mid6 the ISs again are the same for BIC and BIA stimulation, namely compartment 1 for the mid4 electrode and 19 for mid5 and mid6.

In Fig. 5.14 each row corresponds to one electrode position and compares the excitation profiles induced by BIC (left column) and BIA (middle column) stimulation. Thus only three electrode positions are presented, whereas the mid2 electrode is the only position leading to different ISs for the two different leading pulse polarities. Still the threshold of both pulses are of similar magnitude, i.e. BIC current stimulation needs 4160  $\mu\text{A}/\text{phase}$  to initiate a spike at compartment 1 after 0.553 ms whereas 4065  $\mu\text{A}$  are sufficient for AP generating at compartment 19 earlier at 0.458 ms.

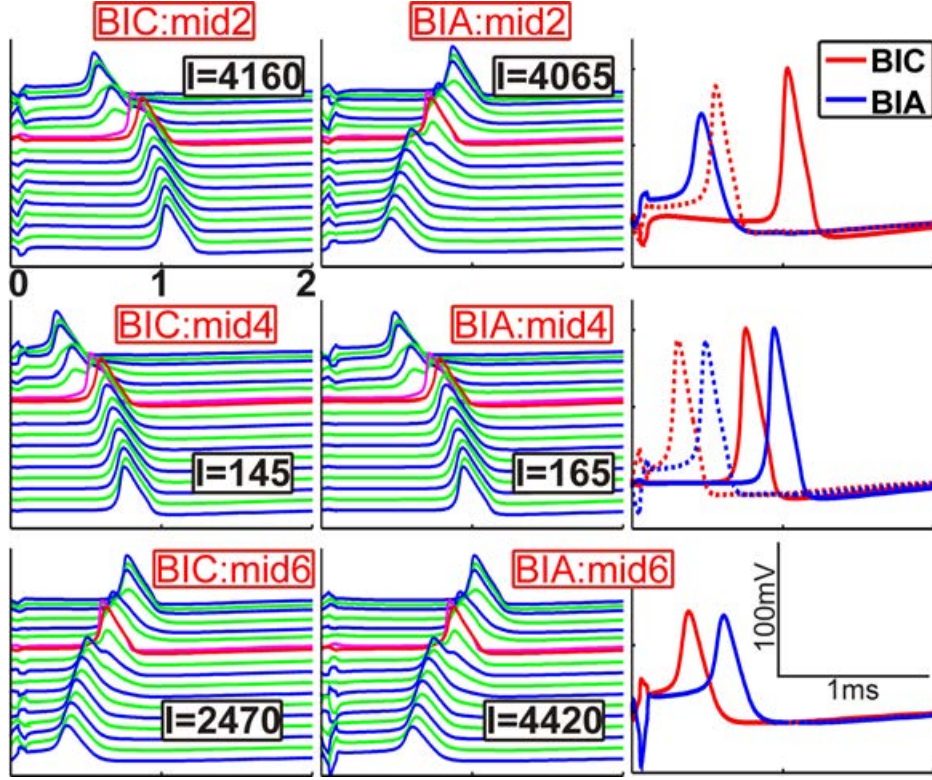


Figure 5.14: Biphasic threshold stimulation of middle 1 neuron. Three electrodes are selected (rows), where the result for the BIC pulse is presented on the left and the corresponding BIA pulse of the same electrode is plotted in the middle. The right panels indicate the transmembrane potentials of the last compartment, dotted lines correspond to those of the IS, which are congruent for initiation at the model neurons end.

Since this is also the time when the AP appears at the end BIA stimulation causes essentially shorter delay of information processing to the next cell. The spike induced by BIC stimulation still has to propagate to the central end where it appears 1.031 ms after stimulus onset. This is illustrated at the right side of the first row, where the transmembrane potentials of compartment 19 are plotted as blue line for the BIA pulse and as red thick line. Additionally the transmembrane potential of the IS for BIC stimulation is represented by the red dotted line, the short delay of onset of the spike compared to BIA stimulation is also obvious.

The two other presented electrodes have the same IS for both pulse forms, as it appears to be the case in most of the cases. Still it is interesting to note that generally for all electrodes, except the mid6 electrode the corresponding threshold values of BIC and BIA stimulation are of similar magnitude. For the mid4 electrode BIC stimulation needs 145  $\mu\text{A}$  and BIA stimulation only slightly higher 165  $\mu\text{A}/\text{phase}$  to initiate a spike. This is again also the electrode with the lowest threshold values. Although the

ISs are identical and the thresholds are almost the same, BIC stimulation initiates the spike 0.304 ms after spike onset, whereas excitation caused by BIA threshold stimulation is delayed to 0.479 ms. Therefore the spikes arrive at different times at the central end which are illustrated as thick lines at the right middle panel. The dotted lines represent again the voltage profile of the first compartment, which in this case is the IS.

The bottom row shows the exceptional mid6 electrode concerning the different threshold values for BIC and BIA stimulation. Both pulses lead to spike initiation at the last compartment. A high threshold value for BIC stimulation of about 2.5 mA initiates the spike quite early at 0.374 ms whereas the high value of 4.4 mA of the BIA pulse needs 0.607 ms to initiate the spike at compartment 19. In both cases the spike travels antidromically backwards to the soma. Also note the different initial excitation phases at the IS represented by the red and blue lines at the right side.

Again as for the apical 2 model neuron stimulation trials, the temporal spike properties of the middle 1 neuron induced by the 5 discussed electrodes are summarized in Table 5.3. Values for the four different pulse forms are given in ms.

#### 5.3.3 Basal 7 neuron

As mentioned before, the just recently obtained data set of the whole stack of cochlear neurons still has to be adapted. Especially the neurons of the basal turn are cut off at unfavorably sites which have to be extended in direction of the cochlea axis. These problems are dealt with at the moment and will soon be resolved in order to perform more appropriate simulations for the basal neurons and the corresponding electrode positions. However, since the spatial arrangement of the neurons along the cochlear show such strong diversity, one neuron was chosen to perform initial tests.

Thus, the basal 7 neuron was selected because it is the longest of all traced basal neurons. As a first step again the traced neuronal data of the basal 7 neuron was interpolated to evaluate the total number of model neuron compartments (Fig. 5.15). The same considerations as for the apical 2 neuron, but with incorporating the detected length of the peripheral process of the basal 7 neuron, i.e.,  $l_{peripher} = 2.287$  mm, reveals 23 compartments. The soma compartment now has the index 14, since 6 peripheral internodes with 5 intersecting nodes of Ranvier could be applied. Still only 4 central internodes with 3 nodes could be inserted which definitely has to be extrapolated for future simulations as will be discussed in the following. Note that the last internode (top green dot in Fig. 5.15) actually was extrapolated since the thick blue line, representing the original 3D traced data, ends between the last two nodes.

Again all electrode positions have been evaluated during the testing period, including all 6 apical and all 6 basal positions, whereas only 5 basal electrodes with correct coordinates were accessible. Interestingly among all those electrodes the high-

		threshold	IS	PT	PTS	ET
CAT:	api5	780	7	0.388	0.451	0.602
	mid2	1775	7	0.468	0.536	0.683
	mid4	55	1	0.299	0.595	0.750
	mid5	480	19	0.567	0.875	0.567
	mid6	905	19	0.472	0.740	0.472
BIC:	api5	2110	1	0.597	0.919	1.076
	mid2	4160	1	0.553	0.870	1.031
	mid4	145	1	0.303	0.599	0.756
	mid5	675	19	0.400	0.659	0.400
	mid6	2470	19	0.374	0.634	0.373
ANO:	api5	615	1	0.401	0.672	0.837
	mid2	1170	19	0.587	0.859	0.587
	mid4	265	5	0.289	0.501	0.662
	mid5	315	19	0.289	0.549	0.289
	mid6	1345	1	0.512	0.844	0.996
BIA:	api5	1880	1	0.358	0.659	0.816
	mid2	4065	19	0.458	0.726	0.458
	mid4	165	1	0.488	0.784	0.944
	mid5	705	19	0.359	0.594	0.359
	mid6	4420	19	0.607	0.874	0.607

Table 5.3: Summary of stimulation trials for the middle 1 neuron and five selected electrode positions. Values of the threshold are given in [ $\mu\text{A}$ ], the IS compartment index is listed and the collected temporal spike properties are given in [ms].

est value for the minimum neuron-electrode positions of 520.58  $\mu\text{m}$  occurs for the bas4 electrode, the lowest of all these values, 113.45  $\mu\text{m}$ , appears between the mid6 electrode and the 12<sup>th</sup> compartment of the basal 7 neuron. Anyway, the values show a surprisingly small spread, i.e., the distribution of distance values between the basal 7 neuron to the electrodes is more uniform than that of the previously used model neurons, apical 2 and middle 1.

Still among all trials, very high threshold currents are required to initiate a spike on the basal 7 model neuron. Even more, if either ANO, BIA or BIC pulses are used the IS is the last compartment 23 and therefore the central ending. Nonetheless for CAT stimulation three different ISs can be observed. For presentation the five electrodes with the lowest threshold have been chosen. Their maximum and minimum distances to the neuron including the corresponding compartment index are presented in the boxes of Fig. 5.15 with corresponding colors according to the different positions.

Among all electrodes only the mid1 electrode (data not shown) has its minimum distance at a central site, although compartment 15 actually is the postsomatic compartment. The bas8 electrode which is the third closest electrode to the model neuron



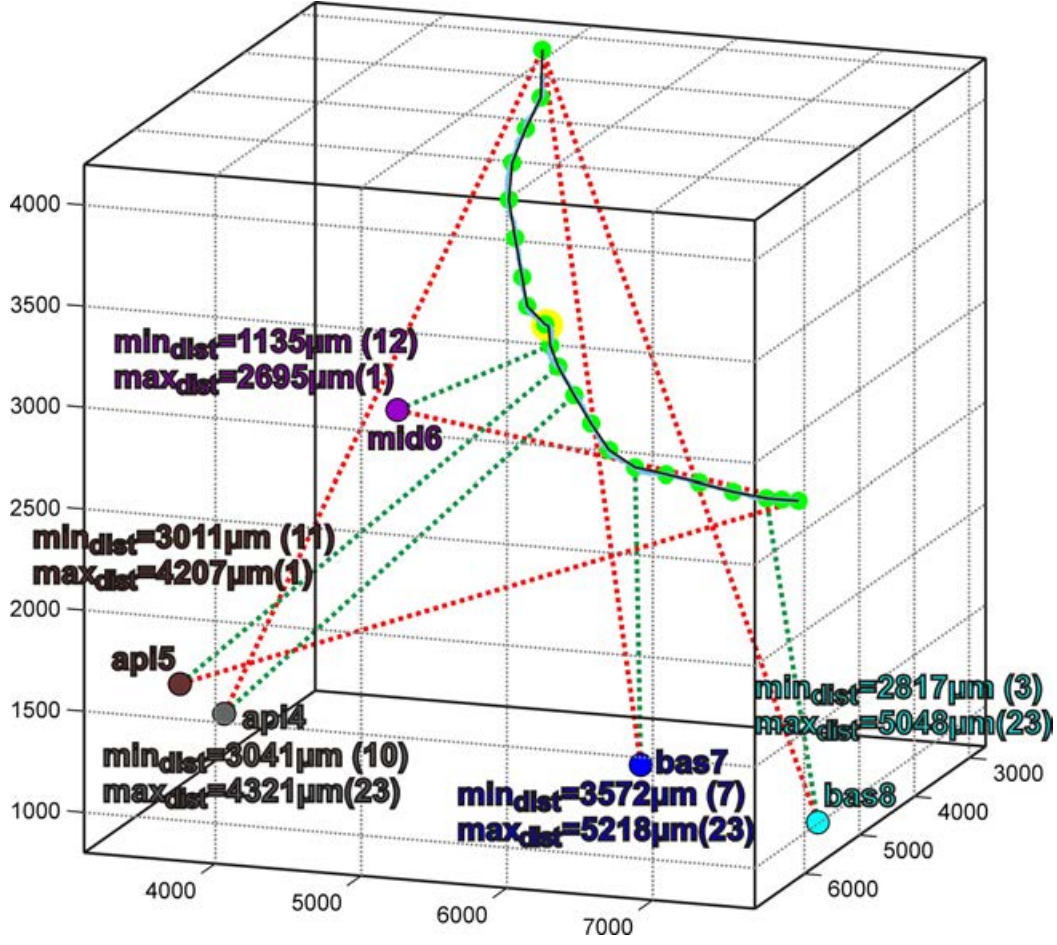


Figure 5.15: Interpolation of basal 7 (black line) traced 3D data (thick blue line) and selected electrode positions. 23 compartments, active nodes are displayed as green dots, the soma yellow. The presented electrodes are used for the stimulation trials, minimum (green lines) and maximum (red lines) electrode-neuron distances are indicated. Corresponding values and indices of the compartment are presented in boxes of the same color as the electrode.

with a distance of 281.7  $\mu\text{m}$  to compartment 3 is the only electrode having its minimum at such a peripheral site. On the other hand the maximum electrode-neuron distance is the last compartment for all basal positions with one exception, most of the apical neurons and a single middle turn electrode. For all others the maximum distance occurs for the first compartment.

As already mentioned, only CAT stimulation leads to variational ISs, all other pulse forms of the whole set of electrodes lead to spike initiation at the central end. The excitation profiles of the basal 7 neuron for the 5 chosen electrodes are presented in Fig. 5.16. The only electrode that leads to a IS at compartment 9 is the api4

electrode. Still for this CAT stimulation a high threshold value of 5.485 mA is required to generate the spike 0.425 ms after stimulus onset. This spike will arrive at the central end at 0.746 ms which is the latest peak time of compartment 23, illustrated as red line in the bottom right of Fig. 5.16.

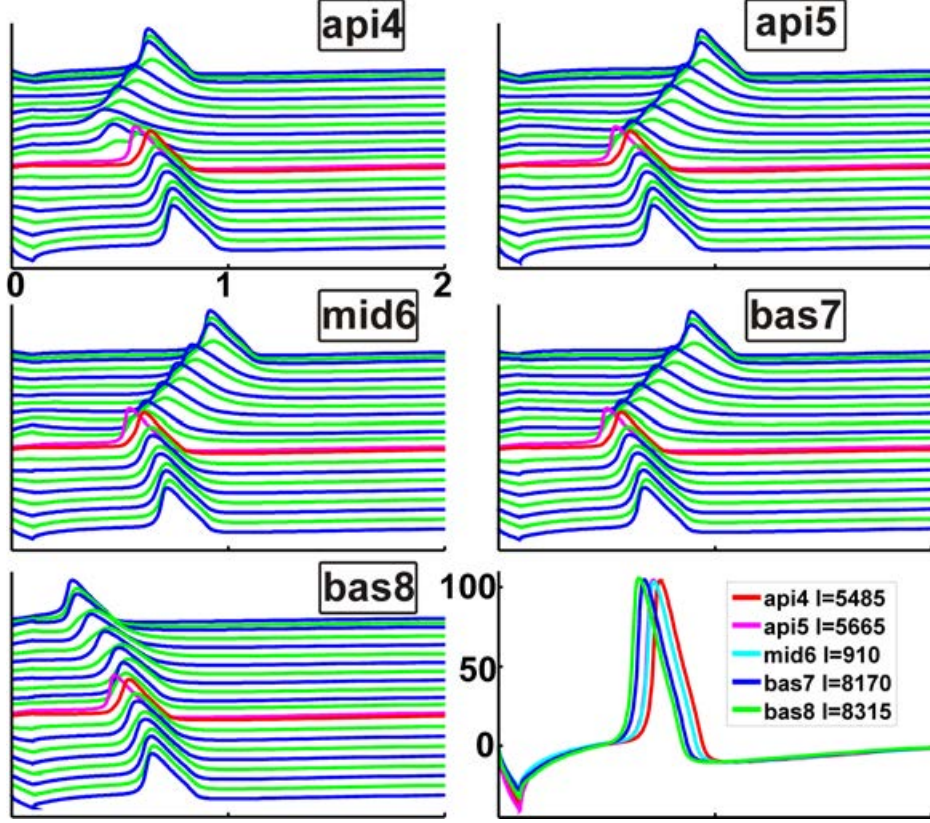


Figure 5.16: CAT stimulation of basal 7 SGC with 5 selected electrodes. Although the IS is not constant for the electrodes, the induced spikes arrive almost simultaneous at the last compartment of the model neuron, illustrated in the bottom right with the corresponding threshold values in  $\mu\text{A}$ .

The other tested apical electrode induces a spike at compartment 13 after 0.541 ms followed by a high 5.665 mA CAT impulse. Although this represents a small delay of spike onset compared to the api4 electrode, the spike generated by stimulation with api5 will arrive slightly earlier at the central end 0.771 ms after stimulus onset.

The lowest threshold for CAT stimulation occurs for the mid1 electrode, i.e., 910  $\mu\text{A}$  are required to initiate a spike at compartment 13 after 0.544 ms, arriving almost synchronously with the spike of the api5 electrode at 0.719 ms. Note that the magenta and cyan lines in the bottom right of Fig. 5.16 are congruent except for the stronger hyperpolarization for the api5 electrode in the beginning.

Also the bas7 electrode generates the spike at compartment 13 just a bit earlier 0.501 ms after stimulus onset. Thus the spike will also arrive just a bit earlier at the



end, although it should be noted that almost a 10 fold threshold value is required for the bas7 electrode compared to the mid6 value (compare corresponding values in Table 5.4).

	threshold	IS	PT(IS)	PT(S)	PT(E)
api4	5485	9	0.425	0.642	0.746
api5	5665	13	0.541	0.608	0.771
mid6	910	13	0.544	0.612	0.719
bas7	8170	13	0.501	0.565	0.673
bas8	8315	1	0.280	0.543	0.649

Table 5.4: Summary of CAT stimulation trials for the basal 7 neuron and five selected electrode positions. Values of the threshold are given in [ $\mu\text{A}$ ], the IS compartment index is listed and the collected temporal spike properties are given in [ms].

Another exception is the bas8 electrode since it is the only one that induces the spike at the beginning, i.e., a high CAT threshold current of 8.315 mA generates a spike at compartment 1 very shortly after 0.28 ms. Nonetheless, since this spike has to travel along the whole neuron, the arrival time at the end is similar to the other excitation profiles. Still the green peak in the bottom right is the earliest which appears at 0.649 ms.

Although the high evaluated threshold values show large disparity among the whole stack of electrodes, the strong uniformity of spike arrival times at the central end is surprising. Especially for the CAT stimulation where although initiated at different sites surprisingly synchronous end times are detected. But still for all other pulse forms very different threshold values for the current amplitude result in relatively uniformity of this temporal property.

Still it should be noted, that for all basal electrodes and the last middle turn positions the BIC threshold is almost doubled compared to the corresponding CAT value, whereas for the other neurons less increase is observed. This time all the ANO threshold values are lower than the CAT values with a reduction to a quarter or a third of the CAT amplitude, with a single exception, the mid6 electrode with the lowest ANO threshold of 420  $\mu\text{A}$  which is about half the corresponding CAT value. Again the corresponding BIA threshold values are about 3-fold compared to the ANO values of the corresponding electrode.

# Chapter 6

## Discussion

Within this thesis a model of a typical human SGC is carefully analyzed in order to compare the single neuron response induced by either intracellular current injection or the application of an extracellularly placed electrode. An established model was adapted according to new anatomical and histological findings (partly provided by MedUni IBK) and was used in order to examine variations of the SGC's excitation profile. Beside the investigation of the unmyelinated soma region which is unique for humans, also other recently determined geometrical and electrical properties were considered. Furthermore an approach is presented for modeling the possible ephaptic or electric interactions between neurons which are connected at their somata which are shielded by common satellite glial cells. An extensive study on the influence of changing soma size on the SGC's excitation profile induced by extracellularly stimulation was performed with a previously used 2D data set. Since our partners of the MedUni IBK are just working on groundbreaking Micro-CT data of a human cochlea and were able to provide first traced 3D data of SGCs along the whole cochlea, initial results were collected for three selected neurons, each representing one turn.

Chapter 3 illustrates how the electrical behavior of nerve cells can be modeled, i.e., how a nerve impulse can be represented as temporal change of transmembrane potential described by the solution of a system of differential equations. Since a large variety of different model approaches exist, it is very hard to compare different simulation studies even for models which all follow a deterministic approach and the HH ansatz for channel kinetics. Thus the most crucial decision concerns the selected ion channel representation, since other model parameters, e.g., the resting membrane potential  $V_{rest}$  or the membrane's capacitance or resistance  $C_{mem}$  and  $R_{mem}$  can be directly measured.

The available data of patch-clamp recordings and immunochemistry studies is overwhelming. Still there is a gap between theoretical investigations and experimental results. No uniform representations of distinct ion channel isoforms are available, which is the biggest shortcoming of contemporary modeling investigations. Due to

improved immunostaining techniques, more and more studies reveal the distinct distribution of different ion channel isoforms along neural elements. On the other hand with the single channel recordings, the voltage-dependency and temporal parameters of the channel kinetics can be deduced. Thus in order to derive a valid biophysical model of the spiking behavior of a neuron, the present ion channels of the nervous structure of interest should be identified and described with uniform equations for the gating kinetics. It would be satisfactory if contemporary modeling studies would follow this approach, in order to compare obtained results.

Sec. 3.4 elucidates the great differences between model approaches, where especially the representation of the  $K$  channel is critical. Although older studies focus on one potassium channel, newer modeling studies include a variety of different  $K$  channels since they are responsible for various specific spiking pattern which is extensively discussed in scientific publications, but beyond the scope of this thesis. Anyhow, especially for potassium currents there is an urgent need for a uniform representation.

Furthermore the modeling of unmyelinated neural elements shall be reconsidered. Ever since HH presented the first mathematical model of unmyelinated cell membrane, all further investigations were concerned with myelinated fibers of different specimen concluding experiments of human nodes of Ranvier. Not much attention has been paid to modeling the unmyelinated structure although thin, unmyelinated fibers are numerous both in the peripheral and central nervous system. Improved recording techniques revealed different AP shapes of different sites along the neuron what strengthens the expected divergent spike properties of myelinated and unmyelinated regions.

Many authors report strong variations in geometrical and electrical parameters among different SGCs additionally with tonotopic specialization. Furthermore the two human peculiarities concerning the specific properties of the soma region are said to essentially effect the SGCs excitation profile. The results of chapter 4 further emphasize the strong need for adaption of contemporary models according to the specific human anatomy.

Although Miller et al. (2001) state interspecies difference in spiking behavior, the morphologically distinct soma region of human SGCs often remains unaccounted for. Thus the first part of chapter 4, i.e., the sections 4.1.1, 4.1.2 and 4.1.3 point out the difference in the spiking behavior of a SGC when the geometrical and electrical properties of different regions of the neurons are varied within the range of reported values. Previously observed delay of spike transmission over the soma region as well as certain sensitive parameters could be confirmed. Additionally conduction velocity values for varying diameter and degree of myelination of cell processes were obtained which are well within reported ranges (Esteves et al. 2009, Miller et al. 2004).

Still the biggest shortcoming is the use of the adapted model of Rattay et al. (2001) which used the modified HH model for all active compartments. Still the model correctly predicts many specific spiking properties of human SGCs and is also used by the group around Smit and Hanekom. Still, e.g., Woo et al. (2009b) also state

that the HH model does not simulate the significant changes in auditory nerve fiber responses to sustained stimulation that are associated with neural adaptation.

In order to derive a new model, our partners at the MedUni IBK tried to identify the densities of specific channel isoforms along human SGCs. Up to present day we were only able to apply a cross-staining technique on animal neurons, but human data is still not available. With the densities and single channel recordings a valid biophysical model of the human SGC could be completed, since especially for the unmyelinated soma region a specific combination of  $Na_v1.1$ ,  $Na_v1.2$ ,  $Na_v1.6$  and  $K$  isoforms is expected. Even more, [Davis and Liu \(2011\)](#) and [Rusznák and Szücs \(2009\)](#) predict variational distribution with tonotopic arrangement. If the missing properties could be obtained it would be satisfactory to compare results with similar studies performed for the type I neurons of guinea pig ([Santos-Sacchi 1993](#)) and different type I and type II mouse SGCs ([Hossain et al. 2005](#)).

In section 4.2 a new model approach for the inclusion of ephaptic coupling at SGC somata is considered. Two basic consequences could be observed while comparing the excitation profiles of cluster-sharing SGCs for suggesting different degrees of coupling impact. This was done by altering the introduced ephaptic conductance  $g_E$  what shall represent a measure of possible electric and ephaptic interactions. First, for successful ephaptic stimulation the spikes of adjacent neurons get synchronized. Second, some inhibiting effects can also be observed due to large current loss on the sensitive human soma region.

Both observations have been reported in previous studies, e.g., [Binczak et al. \(2001\)](#) discussed the phenomena of impulse synchronization due to ephaptic interactions and found the formation of synchronized pulses on neighboring fibers. Furthermore they also compared the ratio of the conduction velocity of such coupled impulses to the corresponding velocity of an uncoupled (free) impulse and observed changes in the onset of failure. Also [Anastassiou et al. \(2011\)](#) support the notion that ephaptic potentials serve to synchronize neuronal activity with little regard to whether excitatory or inhibitory. They further suggest that such synchronization may have a substantial effect on neural information processing and plasticity.

The study of [Holt and Koch \(1999\)](#) on extracellular potentials near cell bodies reports that in extreme cases an AP can be induced in an inactive axon by a nearby one, whereas the investigations of [Anastassiou et al. \(2011\)](#) from pyramidal neurons suggest that ephaptically induced changes in  $V_m$  under physiological conditions cannot give rise to APs when  $V_m$  is around rest. The presented modeling approach suggests strong interactions between adjacent SGCs which is why the ephaptic excitation of a neuron at rest can be observed, i.e., an inactive SGC will initiate a spike at its soma when enough current is supplied by a passing AP of the other cell.

The special case of ephaptic interactions of SGCs has already been investigated by [Jönsson et al. \(2008\)](#). Still their calculation of the extracellular potential only includes the ionic currents of all the compartments, by contrast within this thesis

the total membrane current  $I_{mem}$  is considered to constitute to the ephaptic current released from one SGC. Their investigations suggest that ephaptic excitation could be important at stimulus intensities close to threshold, which is consistent with the obtained findings.

As [Davis and Liu \(2011\)](#) properly summarize the SGCs are notable in that the soma is part of the AP conduction pathway, meaning that, in addition to reflecting structural specializations such as axonal diameter or extent of the axonal arbor, differences in soma size could regulate signaling parameters as well. Furthermore changes of soma diameter essentially changes the excitation pattern of a SGC stimulated by an extracellularly placed electrode, as has been extensively tested in section 5.2 with a previously used 2D model. Previous studies also predict consequences for CI stimulation, e.g., [Goldwyn et al. \(2010\)](#) suggest that the varying soma diameter may contribute to channel-to-channel variability of implants.

[Potrusil et al. \(2012\)](#) acquired volumetric data of SGCs from different cochlea regions which has been tested systematically by only changing the soma diameter of the model neuron while leaving all other parameters at their standard values. The results of all four electrode positions E1-E4 indicate that forthcoming studies should include varying soma sizes according to detected data, since thresholds and temporal parameters change significantly under certain circumstances (CAT pulses for E3). Still the threshold investigations for E1-E4 support common findings of previous studies. They consider different electrode configurations concerning their position ([Mino et al. 2004](#)) and pulse forms, including monophasic ([Miller et al. 1999](#)), biphasic ([van Wieringen et al. 2006](#), [Miller et al. 2001](#)) and triphasic pulses ([Bierer 2007](#), [Goldwyn et al. 2010](#)) as well as pulse trains ([Miller et al. 1997](#), [Woo et al. 2009a](#)).

The obtained results are in accordance with [Miller et al. \(2004\)](#) who reported that anodic monophasic stimuli lead to antidromic APs resulting from a relatively central site of excitation which was predicted by the unique positive-to-negative morphology of the recorded eCAP. Greater latencies appear for cathodic stimulation ([Miller et al. 1999](#), [Shepard and Javel 1999](#)) which also leads to lower thresholds compared to anodic pulses ([Miller et al. 1999](#)) and also to their biphasic counterparts ([Shepard and Javel 1999](#), [Miller et al. 2001](#)). In accordance with the detected ISs, the results of [Miller et al. \(1999\)](#) also support the fact that neurons are mainly stimulated at central processes and that only a minority of fibers close to the electrode is excitable at the respective peripheral axons. This is of special interest for retrograde degeneration of peripheral processes following loss of sensory cells reported in humans ([Spoendlin 1984](#), [Glueckert et al. 2005b](#)). [van Wieringen et al. \(2006\)](#) also state that the trend of lower monophasic thresholds is also valuable for pulse trains and it will occur for different CI devices, different electrode configurations, and generally, for different phase duration.

Since recordings in cats may not be valid for humans, the neural response induced by extracellular stimulation can alternatively be studied with recordings of eCAPs.

Briaire and Frijns (2005) compared one model including a myelinated cell body with the unmyelinated cell body case. They also reported a delay caused by the lack of myelin layers and examined the difference in excitation by biphasic pulses of both leading phases. With the inclusion of our new morphological analysis, more precise results might be obtained. Macherey et al. (2008) not only studied the eCAP, they also report that the human auditory system is more sensitive to anodic stimulation, yielding larger response at an equal stimulus level compared to cathodic pulses. The presented results, which predict a quite uniform anodic threshold value for all soma diameters, are in accordance with this finding. Therefore, one anodic impulse might excite a larger number of SGCs compared to cathodic pulses with highly changing threshold current amplitude for varying soma size.

Many more parameters which affect the neurons excitability vary along the length of the cochlea. For pending studies about electrode position and pulse configuration, three-dimensional data from a greater amount of traced cochlear neurons is crucial. Although the obtained results clearly show divergent single fiber response for different soma sizes, the model would certainly benefit from further adjustments.

The last part of chapter 5 uses just recently provided 3D data of traced SGCs of a Micro-CT imaging of one human cochlea. Unfortunately still some corrections of the coordinate evaluation have to be done, since some basal positions could not be calculated. Furthermore all central processes of the SGCs have to be extended with extrapolation in direction of the cochlea axis, which still has to be incorporated. As a result of too short axons, the spike induced by an electrode is initiated at the last model neuron's compartment. This is an artifact which needs to be extracted. Anyhow, these problems are dealt with at the moment, and certainly obtained results with the new data set will be published in the near future.

The results certainly predict varying excitation profiles for neurons of different cochlea turns, since their 3D spatial arrangement are highly divergent (compare Fig. 5.7, Fig. 5.11 and Fig. 5.15). As a first result the maximum and minimum distances to possible electrode positions have different magnitude and the corresponding sites along the neuron vary. The excitation pattern is significantly altered when the minimum electrode-neuron distance is changed from peripheral to central sites. Still the influence of electrode position on the IS is not consist among different pulse polarities. Furthermore no monotony in favoring either anodic or cathodic pulses could be observed for the different three selected SGCs. In exceptional cases some circumstances even lead to higher monophasic threshold values than for biphasic stimulation.

Anyhow, the possibilities to perform realistic simulations of the auditory response induced by CI stimulation with this groundbreaking data set are numerous. Complex CI strategies could be mimicked which might provide further insight in the variational performance of individual CI users for different frequencies.



# Bibliography

- H. Alle, A. Roth, and J.R.P. Geiger. Energy-efficient action potential in hippocampal mossy fibers. *Science*, 325:1405–1408, 2009. doi: 10.1126/science.1174331. 3.1
- C.A. Anastassiou, R. Perin, H. Markram, and C. Koch. Ephaptic coupling of cortical neurons. *Nature Neuroscience*, 14(2):217–224, 2011. doi: doi:10.1038/nn.2727. 1, 6
- A. Bahmer, M. Polak, and U. Baumann. Recording of electrically evoked auditory brainstem responses after electrical stimulation with biphasic, triphasic and precision triphasic pulses. *Hearing Research*, 259:2010, 2010. 1
- B.P. Bean. The action potential in mammalian central neurons. *Nature Reviews Neuroscience*, 8:451–465, 2007. 3.1, 3.1
- J.A. Bierer. Threshold and channel interaction in cochlear implant users: evaluation of the tripolar electrode configuration. *J Acoust Soc Am*, 121:1642–1653, 2007. 1, 6
- S. Binczak, J.C. Eilbeck, and A.C. Scott. Ephaptic coupling of myelinated nerve fibers. *Physica D*, 148(1-2):159–174, 2001. 1, 6
- J.J. Briaire and J.H. Frijns. 3d mesh generation to solve the electrical volume conduction problem in the implanted inner ear. *Simulation Practice and Theory*, 8: 57–73, 2000a. 5.1
- J.J. Briaire and J.H. Frijns. Field patterns in a 3d tapered spiral model of the electrically stimulated cochlea. *Hearing Research*, 148:18–30, 2000b. 5.1
- J.J. Briaire and J.H. Frijns. Unraveling the electrically evoked compound action potential. *Hearing Research*, 205:143–156, 2005. 1, 6
- I.C. Bruce, M.W. White, L.S. Irlicht, S.J. O’Leary, S. Dynes, E. Javel, and G.M. Clark. A stochastic model of the electrically stimulated auditory nerve: Single-pulse response. *IEEE Transactions on Biomedical Engineering*, 46(6):617–629, 1999. 4.1
- J.F. Brugge, D.J. Anderson, and J.E. Hind. Time structure of discharge in single auditory nerve fibers of the squirrel monkey in response to complex periodic sounds. *J Neurophysiol*, 32:386–401, 1969. 1

## BIBLIOGRAPHY

---

- K.G. Chandy. Simplified gene nomenclature. *Nature*, 352:26, 1991. doi: 10.1038/352026b0. 3.3
- K.G. Chandy and G.A. Gutman. Nomenclature for mammalian potassium channel genes. *Trends Pharmacol. Sci.*, 14:434, 1993. 3.3
- F. Chen and Y.-T. Zhang. An integrate-and-fire-based auditory nerve model and its response to high-rate pulse train. *Neurocomputing*, 70:1051–1055, 2007. 4.1
- J. Chen, X. Wu, L. Li, and H. Chi. Simulated phase-locking stimulation: An improved speech processing strategy for cochlear implants. *J Otorhinolaryngol Relat Spec*, 71(4):221–227, 2009. doi: SimulatedPhase-LockingStimulation: AnImprovedSpeechProcessingStrategyforCochlearImplants. 1
- W.A. Coetzee, Y. Amarillo, J. Chiu, A. Chow, D. Lau, T. McCormack, H. Moreno, M.S. Nadal, A. Ozaita, D. Pountney, M. Saganich, E. Vega-Saenz de Miera, and B. Rudy. Molecular diversity of K<sup>+</sup> channels. *Annals of the New York Academy of Sciences*, 868:233–85, 1999. doi: 10.1111/j.1749-6632.1999.tb11293.x. 3.3
- T.R. Cummins, Y. Xia, and G.G. Haddad. Functional properties of rat and human neocortical voltage-sensitive sodium currents. *Journal of Neurophysiology*, 71(3): 1052–1064, 1994. 3.3
- R.L. Davis and Q. Liu. Complex primary afferents: What the distribution of electrophysiologically-relevant phenotypes within the spiral ganglion tells us about peripheral neural coding. *Hearing Research*, 276:34–43, 2011. 2, 2.1, 2.2, 6
- W.R. Drennan, J.H. Won, V.K. Dasika, and J.T. Rubinstein. Effects of temporal fine structure on the lateralization of speech and on speech understanding in noise. *J Assoc Res Otolaryngol*, 8:373–383, 2007. 1
- J.M. Dubois, G. Ouanounou, and B. Rouzaille-Dubois. The boltzmann equation in molecular biology. *Progress in Biophysics and Molecular Biology*, 99:87–93, 2009. doi: 10.1016/j.pbiomolbio.2009.07.001. 3.3
- Online Encyclopædia Britannica. structures of the human ear. Art. <http://www.britannica.com/EBchecked/media/115575/In-human-hearing-sound-waves-enter-the-outer-ear-and>, March 2012a. 2.1
- Online Encyclopædia Britannica. basilar membrane. Art. <http://www.britannica.com/EBchecked/media/18100/Model-showing-the-distribution-of-frequencies-along-the-basilar-membrane>, April 2012b. 2.2
- Online Encyclopædia Britannica. cochlea:cross section. Art. <http://www.britannica.com/EBchecked/media/534/A-cross-section-through-one-of-the-turns-of-the>, April 2012c. 2.2

## BIBLIOGRAPHY

---

- D. Engel and P. Jonas. Presynaptic action potential amplification by voltage-gated Na<sup>+</sup> channels in hippocampal mossy fiber boutons. *Neuron*, 45:405–417, 2005. 3.3
- E. Erixon, H. Högstorp, and H. Wadin, K. Rask-Andersen. Variational anatomy of the human cochlea: Implications for cochlear implantation. *Otology & Neurotology*, 30(1):14–22, 2009. doi: 10.1097/MAO.0b013e31818a08e8. 2, 2.1
- M.C. Esteves, A.H. Dell’ Aringa, G.V. Arruda, A.R. Dell’ Aringa, and J.C. Nardi. Brainstem evoked response audiometry in normal hearing subjects. *Braz J Otorhinolaryngol.*, 75(3):420–425, 2009. 6
- E. Felder, G. Kanonier, A. Scholtz, H. Rask-Andersen, and A. Schrott-Fischer. Quantitative evaluation of cochlear neurons and computer-aided three-dimensional reconstruction of spiral ganglion cells in humans with a peripheral loss of nerve fibres. *Hearing Research*, 105:183–190, 1997. 1
- J.F. Fohlmeister. A nerve model of greatly increased energy-efficiency and encoding flexibility over the hodgkin-huxley model. *Brain Research*, 1296:225–233, 2009. 3.3
- J.F. Fohlmeister, E.D. Cohen, and E.A. Newman. Mechanisms and distribution of ion channels in retinal ganglion cells: Using temperature as an independent variable. *J Neurophysiol*, 103:1357–1374, 2010. doi: 10.1152/jn.00123.2009. 3.1, 3.3, 3.3
- F. Francis, M.R. Garca, O. Mason, and R.H. Middleton. A mathematical model for voltage gated ion-channel stationary conductance. *Journal of Theoretical Biology*, 2010. 3.3
- J.H. Frijns, J. Mooij, and J.H. ten Kate. A quantitative approach to modeling mammalian myelinated nerve fibers for electrical prosthesis design. *IEEE Trans Biomed Eng*, 41:556–566, 1994. 1, 4.1
- J.H. Frijns, S.L. de Snoo, and R. Schoonhoven. Potential distributions and neural excitation patterns in a rotationally symmetric model of the electrically stimulated cochlea. *Hearing Research*, 87:170–186, 1995. 5.1
- J.H. Frijns, S.L. de Snoo, and J.H. ten Kate. Spatial selectivity in a rotationally symmetric model of the electrically stimulated cochlea. *Hearing Research*, 95:33–48, 1996. 5.1
- R. Glueckert, K. Pfaller, A. Kinnefors, H. Rask-Anderson, and A. Schrott-Fischer. Ultrastructure of the normal human organ of corti. new anatomical findings in surgical specimens. *Acta oto-laryngologica*, 125:534–539, 2005a. 2.1
- R. Glueckert, K. Pfaller, A. Kinnefors, H. Rask-Anderson, and A. Schrott-Fischer. The human spiral ganglion: New insights into ultrastructure, survival rate and implications for cochlear implants. *Audio Neurothology*, 10:258–273, 2005b. 1, 2.3, 2.1, 2.2, 2.4, 6

## BIBLIOGRAPHY

---

- R. Glueckert, K. Pfaller, A. Kinnefors, H. Rask-Anderson, and A. Schrott-Fischer. High resolution scanning electron microscopy of the human organ of corti. a study using freshly fixed surgical specimens. *Hearing Research*, 199:40–56, 2005c. [2.1](#)
- A.L. Goldin, R.L. Barchi, J.H. Caldwell, F. Hofmann, J.R. Howe, Hunter J.C., R.G. Kallen, G. Mandel, Meisler M.H., Netter Y.B., M. Noda, M.M. Tamkun, S.G. Waxman, J.N. Wood, and W.A. Catterall. Nomenclature of voltage-gated sodium channels. *Neuron*, 28:365–368, 2000. [3.3](#)
- J.H. Goldwyn, S.M. Bierer, and J.A. Bierer. Modeling the electrode-neuron interface of cochlear implants: effects of neural survival, electrode placement, and the partial tripolar configuration. *Hearing Research*, 268:93–104, 2010. [1](#), [6](#)
- Y. Gutfreund, Y. Yarom, and I. Segev. Subthreshold oscillations and resonant frequency in guinea-pig cortical neurons: physiology and modelling. *Journal of Physiology*, 483:621–640, 1995. [3.1](#)
- T. Hanekom. Three-dimensional spiraling finite element model of the electrically stimulated cochlea. *Ear Hear.*, 22(4):300–15, 2001. [5.1](#)
- M.G. Heinz, X. Zhang, I.C. Bruce, and L.H. Carney. Auditory nerve model for predicting performance limits of normal and impaired listeners. *Acoustics Research Letters Online*, 2(3):91–96, 2001. doi: DOI10.1121/1.1387155]. [4.1](#)
- M. Hill. UNSW cell biology. <http://cellbiology.med.unsw.edu.au/cellbiology.htm>, April 2008. [3.1](#)
- A.L. Hodgkin and A.F. Huxley. A quantitative description of membrane current and its application to conduction and excitation in nerve. *The Journal of Physiology*, 117:500–544, 1952. [1](#), [3.1](#), [3.3](#), [3.3](#)
- D.A. Hoffman, J.C. Magee, C.M. Colbert, and D. Johnston. K<sup>+</sup> channel regulation of signal propagation in dendrites of hippocampal pyramidal neurons. *Nature*, 387:869–875, 1997. [3.3](#)
- G.R. Holt and C. Koch. Electrical interactions via the extracellular potential near cell bodies. *Journal of Computational Neuroscience*, 6:169–184, 1999. [1](#), [6](#)
- W.A. Hossain, S.D. Antic, Y. Yang, M.N. Rasband, and D.K. Morest. Where is the spike generator of the cochlear nerve? voltage-gated sodium channels in the mouse cochlea. *The Journal of Neuroscience*, 25(29):6857–6868, July 2005. [2.1](#), [2.2](#), [6](#)
- W. Hu, C. Tian, T. Li, M. Yang, H. Hou, and Y. Shu. Distinct contributions of nav1.6 and nav1.2 in action potential initiation and backpropagation. *Nature Neuroscience*, 12(8):996–1002, August 2009. [3.3](#), [3.3.1](#)

## BIBLIOGRAPHY

---

- N. Imennov and J.T. Rubinstein. Stochastic population model for electrical stimulation of the auditory nerve. *IEEE Trans Biomed Eng*, 56(10):2493–2501, 2009. [4.1](#)
- E. Javel. Shapes of cat auditory nerve fiber tuning curves. *Hearing Research*, 81:167–88, 1994. [1](#)
- R. Jönsson, T. Hanekom, and J.J. Hanekom. Initial results from a model of ephaptic excitation in the electrically excited peripheral auditory nervous system. *Hearing Research*, 237:49–56, 2008. [6](#)
- N.Y.S. Kiang. Discharge pattern of single fibres in the cats auditory nerve. MIT press, Cambridge, MA, 1965. [1](#)
- P. Kienker. Equivalence of aggregated markov models of ion-channel gating. *Proceedings of the Royal Society of London. B. Biological Science*, 236(1284):269–309, 1989. [3.3](#)
- M.H.P. Kole, J.J. Letzkus, and G.J. Stuart. Axon initial segment kv1 channels control axonal action potential waveform and synaptic efficacy. *Neuron*, 55:633–647, 2007. [3.3](#)
- D.M. Landsberger and A.G. Srinivasan. Virtual channel discrimination is improved by current focusing in cochlear implant recipients. *Hearing Research*, 254:34–41, 2009. [1](#)
- M.C. Liberman and M.E. Oliver. Morphometry of intracellularly labeled neurons in the auditory nerve: correlations with functional properties. *The Journal of comparative neurology*, 223:163–176, 1984. [1](#)
- L.S. Liebovitch, D. Scheurle, M. Rusek, and M. Zochowski. Fractal methods to analyze ion channel kinetics. *Methods*, 24:359–375, 2001. doi: 10.1006/meth.2001.1206,. [3.3](#)
- W. Liu, M. Böstrom, and H. Kinnefors, A. and Rask-Andersen. Unique expression of connexins in the human cochlea. *Hearing Research*, 250:55–62, 2009. [1](#), [2.2](#), [4.2](#)
- W. Liu, M. Böstrom, A. Kinnefors, F. Linthicum, and H. Rask-Andersen. Expression of myelin basic protein in the human auditory nerve-an immunohistochemical and comparative study. *Auris Nasus Larynx*, 39(1):18–24, 2012. doi: 10.1016/j.anl.2011.04.007. [1](#), [2.2](#), [2.2](#), [4.2](#)
- B. Lütkenhöner. Threshold and beyond: Modeling the intensity dependence of auditory responses. *JARO*, 9:102–121, 2008. doi: 10.1007/s10162-007-0102-y. [4.1](#)
- O. Macherey, R.P. Carlyon, A. van Wieringen, J.M. Deeks, and J. Wouters. Higher sensitivity of human auditory nerve fibers to positive electrical currents. *Journal of the Association for Research in Otolaryngology : JARO*, 9(2):241–251, 2008. [6](#)

## BIBLIOGRAPHY

---

- Z.F. Mainen and T.J. Sejnowski. Influence of dendritic structure on firing pattern in model neocortical neurons. *Nature*, 382:363–366, 1996. [3.3](#), [3.3.2](#), [3.4](#)
- Z.F. Mainen, J. Joerges, J.R. Huguenard, and T.J. Sejnowski. A model of spike initiation in neocortical pyramidal neurons. *Neuron*, 15:1427–1439, 1995. [3.3](#)
- J. Malmivuo and R. Plonsey. *Bioelectromagnetism - Principles and Applications of Bioelectric and Biomagnetic Fields*. Oxford University Press, 1995. [3.1](#), [3.1](#)
- J.P. Meeks and S. Mennerick. Action potential initiation and propagation in ca3 pyramidal axons. *J Neurophysiol*, 97:3460–3472, 2007. doi: 10.1152/jn.01288.2006. [3.3](#), [3.4](#)
- A.L. Miller, D.J. Morris, and B.E. Pfingst. Interactions between pulse separation and pulse polarity order in cochlear implants. *Hearing Research*, 109:21–33, 1997. [6](#)
- C.A. Miller, P.J. Abbas, B.K. Robinson, J.T. Rubinstein, and A.J. Matsuoka. Electrically evoked single-fiber action potentials from cat: responses to monopolar, monophasic stimulation. *Hearing Research*, 130:197–218, 1999. [6](#)
- C.A. Miller, B.K. Robinson, J.T. Rubinstein, P.J. Abbas, and C.L. Runge-Samuelson. Auditory nerve responses to monophasic and biphasic electric stimuli. *Hearing Research*, 151:79–94, 2001. [6](#)
- C.A. Miller, P.J. Abbas, M.J. Hay-McCutcheon, B. Robinson, K.V. Nourski, and F.C. Jeng. Intracochlear and extracochlear ecaps suggest antidromic action potentials. *Hearing Research*, 198:75–86, 2004. [1](#), [3.1](#), [5.1](#), [6](#)
- H. Mino, J.T. Rubinstein, C.A. Miller, and P.J. Abbas. Effects of electrode-to-fiber distance on temporal neural response with electrical stimulation. *IEEE Trans Biomed Eng*, 51:13–20, 2004. [1](#), [4.1](#), [6](#)
- J.B. Jr. Nadal. Comparative anatomy of the cochlea and auditory nerve in mammals. *Hearing Research*, 34:253–266, 1988. [1](#), [2.2](#)
- B.A. Nayagam, M.A. Muniak, and D.K. Ryugo. The spiral ganglion: Connecting the peripheral and central auditory systems. *Hearing Research*, 278:2–20, 2011. doi: doi:10.1016/j.heares.2011.04.003. [2.1](#)
- G. Neske and J. Rinzel. A coupled compartmental model of ephaptic coupling in avian nucleus laminaris and its effect on auditory coincidence detection. NYU, Center for Neural Science [working paper], 2010. [1](#)
- N Osorio, L Cathala, MH Meisler, M Crest, J Magistretti, and P Delmas. Persistent nav1.6 current at axon initial segments tunes spike timing of cerebellar granule cells. *J Ohysiol*, 588:651669, 2010. [3.3](#)



## BIBLIOGRAPHY

---

- C.Y. Ota and R.S. Kimura. Ultrastructural study of the human spiral ganglion. *Acta oto-laryngologica*, 89:53–62, 1980. [1](#), [2.2](#)
- J. Otte, H.F. Schunknecht, and A.G. Kerr. Ganglion cell populations in normal and pathological human cochleae. implications for cochlear implantation. *The Laryngoscope*, 88:1231–1246, 1978. [1](#), [2.1](#)
- L. Pamulova, B. Linder, and H. Rask-Andersen. Innervation of the apical turn of the human cochlea: a light microscopic and transmission electron microscopic investigation. *Otology & Neurotology*, 27:270–5, 2006. [2.2](#)
- B.E. Pfungst, S.A. Bowling, D.J. Colesa, S.N. Garadat, Y. Raphael, S.B. Shibata, G.L. Strahl, S.B. Su, and Zhou N. Cochlear infrastructure for electrical hearing. *Hearing Research*, 281:65–73, 2011. [1](#)
- T. Potrusil, C. Wenger, R. Glueckert, A. Schrott-Fischer, and F. Rattay. Morphometric classification and spatial organization of spiral ganglion neurons in the human cochlea: Consequences for single fiber response to electrical stimulation. *Neuroscience*, 2012. in press: Ms. No.: NSC-11-1617R1. [1](#), [2.1](#), [4.1.1](#), [4.1](#), [5](#), [5.2](#), [5.3](#), [6](#)
- F. Rattay. *Electrical Nerve Stimulation. Theory, Experiments and Applications*. Springer-Verlag, Wien, 1990. [4.1.2](#), [5.1](#)
- F. Rattay. Propagation and distribution of neural signals: A modeling study of axonal transport. *Phys Alive*, 3:60–66, 1995. [1](#)
- F. Rattay. Central nervous system stimulation. In KW Horch and GS Dhillon, editors, *Neuroprosthetics: Theory and Practice*, volume 2 of *Series on Bioengineering & Biomedical Engineering*, chapter Central nervous system stimulation, pages 429–447. World Scientific Publishing, 2004. ISBN 981-238-022-1. [3.1](#), [5.1](#)
- F. Rattay and P. Lutter. Speech sound representation in the auditory nerve: computer simulation studies on inner ear mechanisms. *Zeitschrift für angewandte Mathematik und Mechanik*, 77:935–943, 1997. [1](#)
- F. Rattay, P. Lutter, and H. Felix. A model of the electrically excited human cochlear neuron: 1. contribution of neural substructures to the generation and propagation of spikes. *Hearing Research*, 153:43–63, 2001. [1](#), [2.2](#), [3.1](#), [3.4](#), [3.3](#), [4.1](#), [4.1](#), [4.1.1](#), [4.1.1](#), [4.1.2](#), [4.1.3](#), [4.2.1](#), [5.1](#), [5.1](#), [5.2](#), [6](#)
- F. Rattay, R.J. Greenberg, and S. Resatz. Neuron modeling. In Warren E. Finn and Peter G. LoPresti, editors, *Handbook of Neuroprosthetic Methods*, chapter Neuron modeling, pages 39–74. CRC Press LLC, 2003. [3.2.1](#)
- M.A. Reid, J. Flores-Otero, and R.L. Davis. Firing patterns of type ii spiral ganglion neurons in vitro. *The Journal of Neuroscience*, 24(3):733–742, 2004. [3.1](#)

## BIBLIOGRAPHY

---

- J.M. Ritchie. Physiology of axons. In S.G. Waxman, J.D. Kocsis, and P.K. Stys, editors, *The Axon - Structure, Function and Pathophysiology*, chapter Physiology of axons, pages 68–96. Oxford University Press, 1995. [3.1](#)
- Z. Rusznák and G. Szücs. Spiral ganglion neurones: an overview of morphology, firing behaviour, ionic channels and function. *Pflugers Arch - Eur J Physiol*, 457: 1303–1325, 2009. [1](#), [2.1](#), [2.2](#), [3.1](#), [6](#)
- M.B. Sachs and P.J. Abbas. Rate versus level functions for auditory-nerve fibers in cats: tone-burst stimuli. *The Journal of the Acoustical Society of America*, 56(6): 1835–47, 1974. [1](#), [4.1](#)
- S. Santos-Sacchi. Voltage-dependent ionic conductances of type i spiral ganglion cells from the guinea pig inner ear. *The Journal of Neuroscience*, 13(8):3599–3611, 1993. [3.1](#), [6](#)
- C. Schmidt-Hieber, P. Jonas, and J. Bischofshofer. Action potential initiation and propagation in hippocampal mossy fibre axons. *J Physiol*, 586:1849–1857, 2008. [3.3](#)
- B. Sengupta, M. Stemmler, S.B. Laughlin, and J.E. Niven. Action potential energy efficiency varies among neuron types in vertebrates and invertebrates. *PLoS Comput Biol*, 6(7):1–16, 2010. doi: 10.1371/journal.pcbi.1000840. [3.2](#), [3.1](#)
- S.A. Shamma. Speech processing in the auditory system. i: The representation of speech sounds in the responses of the auditory nerve. *The Journal of the Acoustical Society of America*, 78(5):1612–21, 1985. [1](#)
- R. Shepard, K. Verhoeven, J. Xu, F. Risi, J. Fallon, and A. Wise. An improved cochlear implant electrode array for use in experimental studies. *Hearing Research*, 277:20–27, 2011. [1](#)
- R.K. Shepard and E. Javel. Electrical stimulation of the auditory nerve: Ii. effect of stimulus waveshape on single fibre response properties. *Hearing Research*, 130: 171–188, 1999. [6](#)
- J.E. Smit, T. Hanekom, and J.J. Hanekom. Predicting action potential characteristics of human auditory nerve fibres through modification of the hodgkinhuxley equations. *South African Journal of Science*, 104:284–292, 2008. [4.1](#)
- J.E. Smit, T. Hanekom, and J.J. Hanekom. Estimation of stimulus attenuation in cochlear implants. *J Neurosci Methods*, 180:363–373, 2009a. [1](#), [4.1](#), [5.1](#)
- J.E. Smit, T. Hanekom, and J.J. Hanekom. Modelled temperature-dependent excitability behaviour of a generalised human peripheral sensory nerve fibre. *Biol Cybern*, 101:115–130, 2009b. doi: 10.1007/s00422-009-0324-7. [3.3](#)

## BIBLIOGRAPHY

---

- J.E. Smit, T. Hanekom, and J.J. Hanekom. Modelled temperature-dependent excitability behaviour of a single ranvier node for a human peripheral sensory nerve fibre. *Biol Cybern*, 100:49–58, 2009c. doi: 10.1007/s00422-009-0324-7. [3.3](#)
- H. Spoendlin. Factors inducing retrograde degeneration of the cochlear nerve. *Ann Otol Rhinol Laryngol Suppl*, 112:76–82, 1984. [6](#)
- H. Spoendlin and A. Schrott. Analysis of the human auditory nerve. *Hearing Research*, 43:25–38, 1989. [1](#), [2.1](#), [2.1](#), [2.2](#)
- H. Spoendlin and A. Schrott. Quantitative evaluation of the human cochlear nerve. *Acta Otolaryngol Suppl*, 470:61–69, 1990. [1](#), [2.1](#)
- C.J. Sumner, E.A. Lopez-Poveda, L.P. O’Mard, and R. Meddis. A revised model of the inner-hair cell and auditory-nerve complex. *J. Acoust. Soc. Am.*, 111(5): 2178–2188, 2002. doi: 10.1121/1.1453451. [4.1](#)
- A. Trevino, T.P. Coleman, and J. Allen. A dynamical point process model of auditory nerve spiking in response to complex sounds. *J Comput Neurosci*, 26(1-2):193–201, 2010. doi: 10.1007/s10827-009-0146-6. [4.1](#)
- S. Tylstedt and H. Rask-Andersen. A 3-d model of membrane specializations between human auditory spiral ganglion cells. *Journal of Neurocytology*, 30:465–473, 2001. [1](#), [2.2](#), [2.2](#), [4.2](#)
- S. Tylstedt, A. Kinnefors, and H. Rask-Anderson. Neural interaction in the human spiral ganglion: A tem study. *Acta oto-laryngologica*, 117:505–512, 1997. [1](#), [2.2](#), [2.2](#), [4.2](#)
- A. van Wieringen, R.P. Carlyon, O. Macherey, and J. Wouters. Effects of pulse rate on thresholds and loudness of biphasic and alternating monophasic pulse trains in electrical hearing. *Hearing Research*, 220:49–60, 2006. [6](#)
- A.A. Westen, D.M.T. Dekker, J.J. Briaire, and J.H.M. Frijns. Stimulus level effects on neural excitation and ecap amplitude. *Hearing Research*, 280(1-2):166–176, 2011. doi: doi:10.1016/j.heares.2011.05.014. [1](#)
- B.S. Wilson and M.F. Dorman. Cochlear implants: Current designs and future possibilities. *Journal of Rehabilitation Research & Developement*, 45:695–730, 2008. [1](#)
- J. Woo, C.A. Miller, and P.J. Abbas. Biophysical model of an auditory nerve fiber with a novel adaptation component. *IEEE Trans Biomed Eng*, 56:2177–2180, 2009a. [6](#)

## BIBLIOGRAPHY

---

- J. Woo, C.A. Miller, and P.J. Abbas. Simulation of the electrically stimulated cochlear neuron: modeling adaptation to trains of electric pulses. *IEEE Trans Biomed Eng*, 56:1348–1359, 2009b. [1](#), [4.1](#), [6](#)
- F.H. Yu and W.A. Catterall. Overview of the voltage-gated sodium channel family. *Genome Biology*, 4:207.1–207.7, 2003. [3.3](#)
- F. Zhang, C.A. Miller, B.K. Robinson, P.J. Abbas, and N. Hu. Changes across time in spike rate and spike amplitude of auditory nerve fibers stimulated by electric pulse trains. *JARO*, 8:356–372, 2007. doi: 10.1007/s10162-007-0086-7. [3.1](#)
- X. Zhang, M.G. Heinz, I.C. Bruce, and L.H. Carney. A phenomenological model for the responses of auditory-nerve fibers: I. nonlinear tuning with compression and suppression. *J. Acoust. Soc. Am.*, 109(2):648–670, 2001. doi: 10.1121/1.1336503. [4.1](#)

# Curriculum Vitae

## Personal Data

Name: Cornelia Wenger  
Nationality: Austria  
Date of birth: 13.03.1985  
Place of birth: Krems a.d. Donau, Austria  
Private address: Pramergasse 1/17B  
1090 Vienna  
Email: cornelia.wenger@tuwien.ac.at

## Education

June 2003 Graduate with honor from Secondary school BRG Ringstrasse  
Krems  
October 2008 Graduate with honor from Vienna University of Technology  
Degree in Technical Mathematics with emphasis on Natural Science (Dipl.-Ing.)

## Professional Experience

since 2009 Project Assistant (FWF), Department of Analysis and Scientific  
Computer,  
Vienna University of Technology, Vienna, Austria  
Project: Human Cochlea Nerve Model  
10/2010-06/2011 Shop Assistant,  
Blue Tomato Shop Wien, Vienna, Austria  
2008 Scientific Coworker for Modeling and Simulation as well as Risk  
Analysis,  
Secure Business Austria, Vienna, Austria  
2006-2007 Project Management and Controlling,  
Secure Business Austria, Vienna, Austria

## BIBLIOGRAPHY

---

- 2006-2007 Tutor for „Internet Security“,  
Vienna University of Technology, Vienna, Austria
- 2004-2005 Project Management, Accounting, Budgeting and Ticketing,  
LS Konzertagentur GmbH, Vienna, Austria
- 2004 Summer Internship at the Financial Department,  
Johnson & Johnson, Vienna, Austria
- 2004 Internship as Promotion Assistance and Accountant,  
Wiesen Festivals GmbH, Austria
- 2003, 2001 Summer Internship Nursery,  
Privatklinik Döbling, Vienna, Austria

- Publications** T. Potrusil, C. Wenger, R. Glueckert, A. Schrott-Fischer and F. Rattay. Morphometric Classification and Spatial Organization of Spiral Ganglion Neurons in the Human Cochlea: Consequences for Single Fiber Response to Electrical Stimulation. *Neuroscience* (in press), 2012.
- S. Danner, C. Wenger and F. Rattay. *Electrical stimulation of myelinated axons*. VDM Verlag Dr. Müller, 2011. ISBN: 978-3-639-37082-9.
- T. Potrusil, C. Wenger, R. Glueckert, A. Schrott-Fischer and F. Rattay. Morphological differences and distributions of spiral ganglion cells in the human cochlea and simulation of single neuron response to microstimulation. *48th Inner Ear Biology Workshop*, Lisbon, 2011.
- C. Wenger, L. Paredes and F. Rattay. Current-distance relations for microelectrode stimulation of pyramidal cells. *Artificial Organs*, 35:263-266. 2011.
- F. Rattay and C. Wenger. Which elements of the mammalian central nervous system are excited by low current stimulation with microelectrodes? *Neuroscience*, 170:399-407.2010
- F. Rattay, C. Wenger and L. Paredes. Neuron Modeling for Neuroprosthetic Applications. *Pre conference Workshop at 10th Vienna International Workshop on FES and 15th IFESS Annual Conference*. Vienna, 2010.
- C. Wenger, L. Paredes and F. Rattay. Current-distance relations for microelectrode stimulation of pyramidal cells. *Proc. 10th Vi-*



## BIBLIOGRAPHY

---

*enna International Workshop on FES and 15th IFESS Annual Conference*, 10:170-172. 2010. ISBN: 978-3-900928-09-4.

L. Paredes, C. Wenger and F. Rattay. Enhancement of vowel encoding for cochlear implants by adding a high frequency signal: a modelling study. *Proc. Center for Medical Physics and Biomedical Engineering, 10th International Conference Vienna*, 10:167-169. 2010. ISBN: 978-3-900928-09-4.

C. Wenger and F. Rattay. Communication Specialties between Ear and Brain: Analysis of the Cluster Functions in the Human Cochlea. *Proc. of the 8th Junior Scientist Conference*. 295-296. Vienna, 2008.